5-2011

APPLICATIONS OF MODERATE-RESOLUTION REMOTE SENSING TECHNOLOGIES FOR SURFACE AIR POLLUTION MONITORING IN SOUTHEAST ASIA

Arika Bridhikitti
Clemson University, arika_bridhikitti@hotmail.com

APPLICATIONS OF MODERATE-RESOLUTION REMOTE SENSING TECHNOLOGIES FOR SURFACE AIR POLLUTION MONITORING IN SOUTHEAST ASIA

A Dissertation
Presented to
The Graduate School of
Clemson University

In Partial Fulfillment
of the Requirements for the Degree
Doctor of Philosophy
Environmental Engineering and Science

---

by
Arika Bridhikitti
May 2011

Accepted by
Dr. Thomas J. Overcamp, Committee Chair
Dr. Patrick D. Gerard
Dr. Gerald Lehmacher
Dr. Stephen Moysey
Dr. Elizabeth R. Carraway

ABSTRACT

Retrievals from Earth observation satellites are widely used for many applications, including analyzing dynamic lands and measuring atmospheric components. This research aims to evaluate appropriateness of using satellite retrievals to facilitate understanding characteristics of Southeast Asian (SEA) surface air pollution, attributed to regional biomass burnings and urban activities. The studies in this dissertation focused on using satellite retrievals for 1) mapping potential SEA air pollution sources; which are forests, rice paddies, and urban areas, 2) understanding dynamic optical characteristics of SEA biomass-burning aerosols, and 3) inferring surface ozone level. Data used in this study were from three NASA's Earth Observing System (EOS) satellites, which are Terra, Aqua, and Aura. These retrievals have spatial resolution ranging from hundred meters to ten kilometers.

Algorithms used for the SEA land cover classification were developed using time-series analyses of surface reflectance in multiple wavelength bands from Moderate Resolution Imaging Spectroradiometer (MODIS) on the Terra satellite. Comparing the results to national statistical databases, good agreement was obtained for spatial estimation of forest areas after correction with plantation areas. For estimation of rice paddies areas, the agreement depended on the rice ecosystems. It was good for rainfed rice and poor for deepwater rice. Models for irrigated and upland rice areas showed overall high coefficients of determination, suggesting that they effectively simulated the spatial distribution of those rice paddies; but were prone to underestimate and overestimate,

respectively. Estimated SEA regional rice area was 42×10^6 ha, which agrees with previous published values. Analysis of the satellite retrieval could identify large urban areas. However, the satellite-derived urban areas also incorrectly included large sandy beaches.

Optical properties of SEA background aerosols were investigated through the multivariate analyses of long-term ground-based aerosol measurements acquired from Aerosol Robotic Network (AERONET). The results in this study showed that from mid-September to December, the aerosol had both fine size and high light scattering efficiency. It was assumed to be largely urban/industrial aerosols, possibly coming from eastern China. From January to April, the aerosol had fine size and had single scattering albedo (*SSA* at 440 nm) of approximately 0.9. It was assumed to be smoke from local biomass burning. From October to January, when seasonal winds are strongest, more SEA urban aerosol was observed. This aerosol had coarser size and had *SSA* of ~0.9 or less.

The appropriateness of using Ozone Monitoring Instrument (OMI) aerosol retrieval to facilitate understanding SEA biomass-burning aerosol properties was evaluated through three lines of evidence. These are 1) comparisons between the results obtained from multivariate analyses of the OMI aerosol retrieval and those obtained from the ground-measured AERONET data, 2) from Atmospheric Infrared Sounder (AIRS) total column CO product, and 3) from MODIS active fire detections. The results showed that the OMI retrieval used for large-scale SEA biomass-burning aerosol characterization was

consistent with these alternative measures only when 1 < OMI aerosol optical depth (442 nm) < 3.

The OMI aerosol retrieval was then used for the study on dynamic characteristics of biomass burning aerosol. This study considered the aerosols from two forest-fire episodes, 2007 SEA continent and 2008 Indonesian fires. Dependence of the aerosol optical properties on four variables was investigated. These variables were 1) wind speed/direction, 2) relative humidity (RH), 3) land use/cover as a surrogate of fuel type estimated from time-series analysis of MODIS surface reflectance, and 4) age of aerosol estimated from spatial-temporal analysis of MODIS active fire and the wind characteristics. Results from Pearson Chi-square test for independence showed that the dependence between aerosol group memberships with different optical properties and the limiting variables was significant for most cases, except for Indonesian aerosol age factor. These results agree with prior knowledge on regional burning conditions (types of fuel and relative humidity) and aerosol chemical/physical properties (chemical composition related to aerosol optical properties and hygroscopicity).

Using EOS-Aura tropospheric column ozone (TCO) to infer surface ozone level was evaluated through analyses of linear relationships between TCO estimated from OMI and Microwave Limb Sounder (MLS) retrievals and coincident TCO from balloon-based ozonesonde measurements. This evaluation was for different tropospheric ozone profile shapes and for different geographical regions (for low, mid, and high latitudes and for Pacific and Atlantic regions). Results indicate that inference on ozone level derived from

the satellite-based TCO requires corresponding information about tropospheric ozone profile shape. The use of satellite-based TCO was more appropriate for polluted low-latitude locations where upper troposphere ozone is rare and surface enhanced ozone is high.

ACKNOWLEDGEMENTS

My Advisor, Prof. Overcamp, is the one behind every single step to the completion of this dissertation. He and I started working on this project from nothing to something. He kindly opens his heart to a whole new entity and spent numerous hours reviewing my papers and advising me. I am wholeheartedly grateful for his being my guardian during the way to my degree. I am also thankful Lynda, his wife, for her time reading and checking my writing and help me to have a first impeccable publication.

I especially thank Dr. Lehmacher from the Department of Physics and Astronomy and Dr. Gerard from the Department of Applied Economics and Statistics for giving me insightful suggestions and sharing me your experiences and professions. I also thank Dr. Moysey, Dr. Carraway, Dr. Shelie Miller, former faculty member of Clemson University in the Environmental Engineering and Earth Science department, for providing me time and feedback.

Thank the Department of Environmental Engineering and Earth Science, Clemson University for welcoming me to be a part of "Clemson Tigers." This community is small enough to warm me up and is big enough to fulfill my PhD student life. There are always lights here.

My parents, Bancherd and Vipada Bridhikitti, are my everything. They always find the best for me. If you can find something good out of me, please give credit to my parents. My life is completed because of them.

Last but not least, I would like to thank Mahasarakram University who provides me an opportunity to study aboard. Especially thank the Royal Thai Government for supporting me financially for my master's degree at the Asian Institute Technology continuously through my doctoral study at the Clemson University.

TABLE OF CONTENTS

LIST OF TABLES

LIST OF FIGURES

LIST OF ABBREVIATIONS

AAOD	Absorbing Aerosol Optical Depth
AAR	*AAOD* to *AOD* Ratio
AERONET	Aerosol Robotic Network
AIRS	Atmospheric Infrared Sounder
AOD	Aerosol Optical Depth
BL	Boundary Layer
BMR	Bangkok Metropolitan Region
CALIPSO	Could-Aerosol Lidar and Infrared Pathfinder Satellite Observation
CAN	Canonical Function
CCD	Convective Cloud Differential
CO	Carbon monoxide
DEM	Digital Elevation Model
DJF	December, January, and February
DOAS	Differential Optical Absorption Spectroscopy
DU	Dobson Unit
EEC	Electrochemical Concentration Cell
EOS	Earth Observing System
EVI	Enhanced Vegetation Index
FT	Flooding and Transplanting
g	Asymmetry Factor
GOME	Global Ozone Monitoring Experiment
HDF	Hierarchical Data Format
HS	Histosol
IR	Infrared
JJA	June, July, and August
k	Imaginary-part Refractive Index
LSWI	Land Surface Water Index
MAM	March, April, and May
MLS	Microwave Limb Sounder

MODIS	Moderate Resolution Imaging Spectroradiometer
n	Real-part Refractive Index
NCEP	National Centers for Environmental Prediction
NDBI	Normalized Build-up Index
NDVI	Normalized Difference Vegetation Index
NIR	Near-Infrared
NO	Nitrogen Oxide
NO_2	Nitrogen Dioxide
NO_x	Oxides of Nitrogen
OMI	Ozone Monitoring Instrument
PCD	Pollution Control Department of Thailand
RH	Relative Humidity
RO	Residual Layer Ozone
r_{eff}	Effective Radii
r_v	Volume Mean Radii
SCO	Stratospheric Column Ozone
SEA	Southeast Asia(n)
SO	Surface Enhanced Ozone
SON	September, October, and November
SSA	Single Scattering Albedo
SWIR	Shortwave-Infrared
TCO	Tropospheric Column Ozone
TOMS	Total Ozone Mapping Spectrometer
UO	Upper Troposphere Ozone
VIS	Visible
VOC	Volatile Organic Compounds
WOUDC	World Ozone and Ultraviolet Radiation Data Centre
α_a	Absorbing Angström Exponent
α_e	Extinction Angström Exponent
ρ	Surface Reflectance

CHAPTER ONE

INTRODUCTION

This research aims to evaluate appropriateness of using moderate-resolution satellite data to facilitate understanding characteristics of Southeast Asia (SEA) surface air pollution attributed to forest fires, agricultural fires, and urban activities. Massive forest fires in SEA occur often in the dry season and have been recognized as one of the important global air pollution sources. Many of these fires are caused by agricultural burning that is widely practiced over the region. SEA rice paddy areas were approximately thirty percent of the world total (Hays et al., 2005).The emissions from burning rice residues contribute large amount of air pollutants, including greenhouse gases, into the global atmosphere. Urban pollution is significant in many SEA urban cities and air pollutant concentrations, especially particulate pollutants and anthropogenic ozone, frequently exceeds the EPA ambient air quality standard level (Oanh et al., 2006).

In this study, the moderate-resolution satellite retrievals were first validated with either ground measurements or other commensurate satellite retrievals. After passing the validation, they were used for three applications. The first application is mapping SEA land cover, including the major air pollution sources. The second is understanding SEA biomass-burning aerosol properties, and the third is evaluating appropriateness of using satellite-based tropospheric column ozone to infer surface ozone level. The scope for the last application extends beyond SEA because observations used in the investigation are from many places in the world.

1.1. BACKGROUND AND SIGNIFICANCE

Satellite remote sensing is widely used for Earth observations to collect information about global dynamic systems, including both natural and anthropogenic environments. Among Earth observation satellites currently active, the satellites launched under NASA's Earth Observing System (EOS) have been well recognized by their applications. These applications include monitoring and modeling of air quality, water management, agricultural planning, land-use planning, and monitoring abundance of natural resources and their changes. In this work, we focus on using retrievals from three satellites, Terra, Aqua, and Aura. These satellites are positioned at an altitude of 705 km and have a near-polar orbit in synchronization with the Sun. Their paths cross the same location at the same local time every day. The satellite retrievals used in this study are moderate resolution, with spatial resolutions ranging from hundred meters to ten kilometers. Details on the satellite retrieval products used in this study are in Table 1.1.

In the following paragraph, general applications and advantages of moderate-resolution satellite retrievals applied in previous land use/cover and air quality studies together with the limitations associated with technical configurations of the satellite sensors are first reviewed. Then, the methodologies adopted for this study are introduced.

Table 1.1. Characterizations of satellite retrievals used in this study

Sensors/Satellites	Products	Spectra used for retrievals	Spatial/Temporal resolutions	Orbit
Land Use/Cover Studies				
Moderate Resolution Imaging Spectroradiometer (MODIS)/Terra	Surface Reflectance	Visible to near infrared	500 m/ 8-day (selected from the best daily observation)	Ascending orbit, crossing equator at 10:30 pm, and descending orbit, crossing equator at 10:30 am
Air Quality Studies				
Moderate Resolution Imaging Spectroradiometer (MODIS)/Terra	Aerosol Optical Depth, Angström Exponent, Aerosol type	Visible to near infrared	10 km/ daily (level 2)	Ascending orbit, crossing equator at 10:30 pm, and descending orbit, crossing equator at 10:30 am
	Thermal Anomalies/Fire	4 and 11 μm (infrared)	1 km/ daily (level 3)	
Atmospheric Infrared Sounder (AIRS)/Aqua	Surface air temperature, Surface skin temperature, Tropospause height, Relative humidity profile	4.2 and 15 μm (CO_2 bands) and 6.3 μm (water band)	~100 to 111 km/ daily (level 3)	Ascending orbit, crossing equator at 1:30 pm
	Total column CO	4.50 to 4.58 μm (infrared)	~100 to 111 km/ daily (level 3)	
Ozone Monitoring Instrument (OMI)/Aura	Absorbing/Extinction Aerosol Optical Depth, Aerosol Single Scattering Albedo	Near UV to mid-visible	~13 to 24 km/ daily (level 2) and ~25 to 27 km/daily (level 3)	Ascending orbit, crossing equator at 1:45 pm
	Total column ozone	317.5 to 336.1 nm (Harley and Huggins bands in UV)		
	Tropospheric column NO_2	405 to 465 nm		
	Total column formaldehyde	327.5 to 356.5 nm		
Microwave Limb Sounder (MLS)/Aura	Atmospheric Ozone vertical profile	~1249 μm (240 GHz)	Vertical resolution is 3 km from upper troposphere to stratosphere and 4 to 6 km in the upper mesosphere/ daily	Ascending orbit, crossing equator at ~1:38 pm (7 minute before OMI views)

1.1.1. Land use/cover studies

Investigating observations over time allows dynamic land cover analysis to be performed. High-resolution satellite data may be desired, but their spatial coverage is limited, the number of time-series observations is small, and data analyses require expensive advanced computational resources. Moderate-resolution satellite sensors are appropriate for larger-scale dynamic system studies. The moderate-resolution sensors include Moderate Resolution Imaging Spectroradiometer (MODIS) on Terra and Aqua satellites. This instrument provides global coverage information with 250- and 500-m spatial resolutions in visible and near-infrared wavelengths at nadir every one to two days. With these characteristics, retrievals from MODIS have been widely used for vegetation detection and its changes (Huete et al., 2002; Xiao et al., 2005; Xiao et al., 2006; Hayes and Cohen, 2007; Wardlow and Egbert, 2008).

In this study, algorithms using time-series analysis of MODIS surface reflectance data for mapping the SEA land cover have been developed and assessed for their accuracy. Forests are identified from temporal profiles of vegetation indices, which are normalized red-visible and near-infrared spectral reflectance. The indices are widely used in satellite-based land analyses. The algorithm for rice paddy identification is modified from Xiao (2005, 2006) based on the temporal profiles of vegetation and water indices which respond to rice canopy development patterns. Urban land analyses using moderate-resolution satellite retrieval have not widely implemented by others. In this study, an

algorithm for urban land mapping was developed by using the build-up index introduced by Zha et al. (2003) for high-resolution imagery.

1.1.2. Air quality studies

Satellite remote sensing of air quality has evolved since 1959 when the first TIROS I satellite was launched for cloud detection (Hoff and Christopher, 2009). Currently, many air pollutants are retrieved including aerosols, tropospheric O_3, NO_2, CO, and formaldehyde (HCHO). However, there are many physical processes that could affect their accuracy and precision. For aerosol remote sensing using solar backscattering, the major interferences are from cloud and surface reflectance (Martin, 2008). For trace gas remote sensing using both solar backscattering and thermal infrared emission, an appropriate radiative transfer calculation associated with selection of fitting spectra window, solar/molecular reference spectra has to be done, and these largely affect accuracy on detection of species (Martin, 2008). Because atmospheric scattering and absorption can attenuate the radiation passing through the boundary layer, the ability of individual satellite instruments to detect trace gases can be limited near the ground (Martin, 2008). Therefore, remote sensing of surface air pollution monitoring has been associated with some uncertainties that need to be evaluated.

Even though the satellite measurement of tropospheric aerosol may never achieve the accuracy needed for measuring regulated surface air pollutant concentrations, satellite observations are useful for emission characterization and support assessment of long-range pollutant transport and background concentration using global-scale models (Hidy

et al., 2009). Estimating the strength of wildfires or other high pollution events is another advantage from satellite retrievals (Hidy et al., 2009).

In this study, appropriateness of using the moderate-resolution satellite sensors for SEA air pollution monitoring will be evaluated. To build strong evidence on the evaluation, results obtained from the analyses will be compared with those from other analyses using comparable satellite retrievals or with ground-measured data, including that obtained from the Aerosol Robotic Network (AERONET) from NASA/Goddard Space Flight Center. Secondly, if the evaluations from this first step yield satisfactory agreement with the validating data sets, then the satellite data sets will be used to improve understanding surface air pollution characterizations.

Biomass-burning aerosol characterization was investigated in this study. Biomass burnings are defined as forest fires and agricultural open burnings. The appropriateness of using Ozone Monitoring Instrument (OMI/Aura) sensors for biomass-burning aerosol property determination was evaluated by comparison to ground measurements and other satellite retrievals, including Atmospheric Infrared Sounder (AIRS/Aqua) total atmospheric column CO, and MODIS active fire detections. The OMI aerosol properties products were then used in a study on factors limiting biomass-burning aerosol properties. The factors considered in this analysis are the type of burning fuels obtained from the previous MODIS land cover analysis, meteorological factors (wind speed/direction, humidity), background aerosol, and aerosol age. The results obtained from this study provide more understanding on what causes different biomass-burning

aerosol properties corresponding to their various radiative forcing potentials reported in previous studies conducted in different environments (Dubovik et al., 2002; Jeong, et al., 2008; Podgorny et al., 2003; Santos et al., 2008) and how these factors affect aerosol properties.

The last issue that was investigated is the performance of using the moderate-resolution satellite retrievals to infer daily changes of surface ozone level. Urban activities increase surface ozone concentrations by complex photochemical reactions. Ozone OMI and MLS in Aura mission are designed especially for assessment of total column ozone and vertical ozone profile, respectively. There was an attempt to validate tropospheric column ozone (TCO) derived from these satellite measurements with seasonal average of the measurements from balloon-based ozonesonde and with the results obtained from global-scale model (Ziemke et al. 2006). Some attempted to apply this TCO as urban signature (Kar et al. 2010) or even used it to evaluate mechanisms driving surface ozone production (Duncan et al., 2010; Martin et al., 2004). However, implications of these satellite-based retrievals to surface ozone concentration are still problematical because there is no evidence showing sufficient sensitivity of the satellite retrievals of the daily variation of surface ozone concentration. This study evaluates, for the first time, the sensitivity of the TCO-derived from OMI and MLS retrievals on the daily changes of surface ozone level. Concurrent measurements from balloon-based ozonesonde were used for the evaluation. This quantitative satellite sensitivity helps us to gain more understanding from the satellite retrievals on surface ozone behavior.

1.2. HYPOTHESES

This study used retrievals from moderate-resolution satellites to facilitate monitoring air pollution in SEA by focusing on three main parts. Hypotheses drawn under each part serve as sub-objectives to be tested in order to fulfill the research goal.

1.2.1. Using surface reflectance from MODIS onboard Terra satellite to map potential air pollution sources, including forests, rice paddies, and high-intensity urban areas.

The hypothesis drawn under this part is that the MODIS surface reflectance used for mapping of SEA forests, rice paddies, and high-intensity urban areas provide consistent results with national statistical databases or with the high-resolution satellite imagery. Testing this hypothesis and completed results are in Chapter 2, titled *Algorithms for Mapping Forests, Rice Ecosystems, and High-Intensity Urban Areas over Southeast Asia Using Moderate-Resolution Satellite Imagery*.

1.2.2. Using aerosol optical products from OMI onboard Aura satellite incorporated with spatial information from the first task and retrievals from other remote sensors to facilitate understanding dynamic optical characteristics of biomass-burning aerosols.

There are three hypotheses drawn from this part.

I. SEA background aerosols determined from the ground-based AERONET measurements are seasonally dependent and their properties are consistent with the land activity and seasonal prevailing winds. Testing this hypothesis and completed

results are detailed in Chapter 3, titled *Optical Characteristics of the Southeast Asia's Regional Aerosols and Their Sources*. Chapter 3 is accepted for publication in the Journal of Air and Waste Management Association (JAWMA).

II. The OMI aerosol variables used for studying SEA biomass-burning aerosol properties provide satisfactory results which are consistent with ground-measured AERONET and other satellite observations; including MODIS active fire detections, and AIRS total atmospheric column CO. Testing this hypothesis and completed results are detailed in Chapter 4, titled *Ozone Monitoring Instrument (OMI) Sensor for Biomass-Burning Aerosol Optical Properties*. Chapter 4 was published in proceedings of the Air and Waste Management Association's 103rd Annual Conference and Exhibition, Calgary, AB, Canada.

III. The factors limiting the biomass-burning aerosol properties are 1) type of fuels (forests and vegetation), 2) wind speed/direction, 3) relative humidity, 4) background aerosol, and 5) age of aerosols. Testing this hypothesis and completed results are detailed in Chapter 5, titled *Remote Sensing Observations of the Optical Properties of Southeast Asian Forest-Fire Aerosols***.** Chapter 5 was published in proceedings of the Air and Waste Management Association's 103rd Annual Conference and Exhibition, Calgary, AB, Canada.

1.2.3 Using TCO estimated using retrievals from OMI and MLS, both on Aura satellite, to infer surface ozone level.

Hypothesis drawn under this part is that linear relationships between the OMI/MLS-based TCO and its coincident measurements taken from balloon-based ozonesonde are dependent on vertical ozone profile shapes and good linear relationships, characterized by high linear slopes, low intercept values, and high coefficient of determination (R^2) are found for the observations with presences of surface enhanced ozone. The ozone profile shape identifies the altitude which ozone-rich air masses existed. In addition, OMI and MLS ozone retrievals are based on *a priori* knowledge of ozone profiles. Therefore the ozone profile shape should be one factor limiting the effectiveness of the satellite-based ozone retrieval algorithm. Testing this hypothesis and completed results are detailed in Chapter 6, titled *Tropospheric Ozone Profiles and Their Effects on EOS-Aura Column Ozone for Surface Ozone Implication*.

CHAPTER TWO

ALGORITHMS FOR MAPPING FORESTS, RICE ECOSYSTEMS, AND HIGH-INTENSITY URBAN AREAS OVER SOUTHEAST ASIA USING MODERATE-RESOLUTION SATELLITE IMAGERY

2.1. ABSTRACT

Multi-temporal satellite imagery from the Moderate Resolution Imaging Spectrometer, MODIS, were used for mapping Southeast Asian (SEA) forest, high-intensity urban areas, and rice paddies. Algorithms developed for the analyses are based on temporal changes of vegetation strength and/or water content, which is indicated by intensity distribution of 8-day MODIS reflectance in visible to near-IR range. The algorithms were extended from small-scale observations of SEA land cover characteristics. For rice-paddy mapping, the algorithm was extended from prior studies to identify rice ecosystems. The results obtained from the forest and rice analyses were compared to national statistics. The urban areas were qualitatively evaluated for agreement with high-resolution satellite imagery. For forests, good linear relationships between the MODIS-derived forest areas, corrected by plantation areas, and the provincial national statistics were obtained. For the rice paddy areas, model performance was dependent on rice ecosystems. Good linear relationships between the model results and the national statistics were observed for rainfed rice. High correlations were also found for irrigated rice and upland rice. These high correlations indicated that the model effectively simulated spatial distribution of these rice areas. However the model tended to underestimate irrigated rice and

overestimate upland rice. Poor correlation was observed for deepwater rice. For the high-intensity urban areas, identification of the large MODIS-urban areas spatially corresponded with the observations from high-resolution satellite imagery.

2.2. INTRODUCTION

The Moderate Resolution Imaging Spectrometer, MODIS, is one of the instruments onboard the Terra and Aqua satellites. After the first MODIS flight instrument was launched in December 1999, land analyses using time-series MODIS retrievals have been conducted for detecting changes in vegetation (Xiao et al., 2005; Xiao et al., 2006; Hayes and Cohen, 2007; Wardlow and Egbert, 2008). Currently, an accuracy assessment of the use of MODIS data and further development of its algorithms are being investigated.

This research applies the MODIS multi-temporal satellite imagery for mapping over Southeast Asia (SEA): forests, rice paddies, and high-intensity urban areas. Massive forest fires are usually caused by shifting cultivation occur every year in this region. SE Asian rice paddy areas are approximately thirty percent of the world total (Hays et al., 2005, Huke and Huke, 1997), natural methane emissions and toxic air pollutants emissions from growing rice and burning its residues over this region are significant. Their magnitudes strongly depend on type of rice ecosystem (Hays et al., 2005; Wassmann et al., 2000). Particulate matter over urban cities in Asia frequently reported exceeding US EPA ambient air quality standard level. These particles have been attributed to traffic emission, secondary aerosol formation, biomass burning, and soil dust (Kim Oanh et al., 2006). The results obtained from this study indicated performance and

limitations of using the moderate-resolution satellite retrievals for regional land use/cover analysis.

2.3. METHODOLOGY

2.3.1. Description of study area

SEA can be divided into two geographic regions: the mainland and the islands. The mainland consists of the countries of Cambodia, Lao PDR, Myanmar, Thailand, and Vietnam. The larger islands are the countries of Brunei, East Timor, Indonesia, Malaysia, Philippines, and Singapore. The latitude of this region ranges from 7° S to 20° N, and its longitude is from 95° to 130° E.

The climate of the SEA is tropical, hot and humid year round. NE winds bring in dry, colder air from mainland China causing a dry season from November to mid-March for most of SEA mainland. These NE winds bring severe weather to the SEA islands. The milder SW prevailing winds are from mid-May to September. These winds bring wet air masses from Indian Ocean causing a wet season over the entire region.

A tropical rainforest, or evergreen forest, dominates SEA. Some tropical deciduous forest can be found in mountainous areas that have a dry-wet seasonal pattern. There are also small mangrove forests around shorelines.

2.3.2. Description of MODIS image data used in this study

The MODIS surface reflectance 8-day L3 Global 500 m SIN Grid V005, or MOD09A1, data set from 2006 to 2007 was acquired for this study. Each grid value gives the

percentage of the radiation energy in the specific bandwidth from the total energy integrated over entire spectrum. In this study, the MODIS surface reflectance at four spectral bands, lying from visible to near-infrared, were considered. These are band 1: 620 to 670 nm (visible-red: VISR), band 2: 841 to 876 nm (near-infrared: NIR), band 3: 459 to 479 nm (visible-blue: VISB), and band 6: 1628 to 1652 nm (shortwave-infrared: SWIR). The products were downloaded from the USGS Land Processes Distributed Active Achieve Center (LPDAAC, 2008).

These reflectance products are reported at a 500-meter resolution in a level 3, grid projection. Each pixel contains the best possible L2G (daily) observation during an 8-day period. These version 5 reflectance products are validated stage 1, meaning that accuracy has been estimated using a small number of independent measurements obtained from selected locations and time periods and ground-truth/field program efforts (LPDAAC, 2008). The products are in HDF-EOS format. Prior to the analysis, these data were reprojected to GeoTIFF format, referencing the UTM zone 48 projected coordination system with WGS1984 (the World Geodetic Survey system of 1984) datum, by using MODIS Reprojection Tool (MRT) from the USGS/LPDAAC (LPDAAC, 2008). These reprojected data sets were used in the land classification analyses running on the Modelbuilder in ArcGIS 9.2 software with Python scripts interfered. The algorithms used for these analyses are detailed in section 2.3.5 to 2.3.7.

2.3.3. Description of ancillary data

Global 30 Arc-Second Elevation Data Set, GTOPO30

The GTOPO30 data set was acquired from the U.S. Geological Survey (USGS) website (http://edc.usgs.gov/products/elevation/gtopo30.html). This is a global raster Digital Elevation Model (DEM) with a horizontal grid spacing of 30 arc seconds (approximately 1 km). These data are expressed in geographic coordinates and referenced to WGS1984 datum. This DEM was used to generate a mask of the elevation above 2,500 m or regions having a slope greater than 30^{o}. Since rice is not usually grown at these high elevations or steep slopes (IRRI, 1975), these were excluded from the rice paddy map.

SEA Administrative Boundary Coverage map

The country administrative base maps were downloaded from the International Potato Center data server (CIP, 2008). These maps are polygon shapefiles expressed in geographic coordinates and referenced to WGS1984 datum. The maps provide the administrative boundary coverage in provincial/state levels which were used to mask raster maps to generate raster data compatible to the national statistics databases.

2.3.4. Surface reflectance enhancement techniques

After eliminating the effects from atmospheric gases, aerosols, and clouds, the multispectral electromagnetic signals retrieved from the satellites were strongly dependent on light reflectivity and absorptivity of land surfaces. Liquid water is a good absorber of solar irradiance, especially in the infrared region. Vegetation leaves have

chlorophyll which strongly absorbs visible light for use in photosynthesis. On the other hand, its cell structure strongly reflects near-infrared spectra. Bare soils have electromagnetic characteristics depending on soil moisture content, organic matter, and particle size (Bowers and Hanks, 1965). However, this research was interested in the wavelengths from visible to near-infrared in which soil moisture plays a major role. Paved surfaces and buildings consisting of dark asphalt and concrete behave like blackbodies which absorb nearly all irradiance energy and reemits back to space in longer wavelength, mainly 8 to 13 μm.

The normalized difference vegetation index (NDVI), the enhanced vegetation index (EVI), the normalized build-up index (NDBI), and the land surface water index (LSWI: negative NDBI) are calculated from the surface reflectance, ρ, in visible-red (VISR; MODIS-band 1), near-infrared (NIR; MODIS-band 2), visible-blue (VISB; MODIS-band 3), and shortwave-infrared (SWIR; MODIS-band 6) using the following equations (Xiao et al., 2005; Xiao et al., 2006; Zha et al., 2003).

$$\text{NDVI} = \frac{\rho_{NIR}-\rho_{VISR}}{\rho_{NIR}+\rho_{VISR}} \quad \text{(Eq.1)}$$

$$\text{EVI} = 2.5 \times \frac{\rho_{NIR}-\rho_{VISR}}{\rho_{NIR}+6\rho_{VISR}-7.5\rho_{VISB}+1} \quad \text{(Eq.2)}$$

$$\text{NDBI} = \frac{\rho_{SWIR}-\rho_{NIR}}{\rho_{SWIR}+\rho_{NIR}} \quad \text{(Eq.3)}$$

NDVI and EVI were used in this study to enhance vegetation detection sensitivity of the MODIS electromagnetic signals. Both indices are estimated from normalizing the

difference between the radiances in near-infrared spectra and in red-visible spectra. In addition, EVI incorporates the additional blue band to diminish residual atmosphere contamination caused by smoke and sub-pixel thin clouds to minimize canopy background variation and to maintain sensitivity over dense vegetation conditions (Huete et al., 2002). In this study, the time-series NDVIs were used to distinguish deciduous forests from evergreen forests, which include some perennial plantations. The time-series EVIs were used to distinguish rice paddies with different ecosystems because of its higher sensitivity to canopy structural variation.

Zha et al. (2003) introduced NDBI to automate the process of mapping built-up areas. NDBI is the negative of LSWI. Both indices are calculated from the normalized difference between the radiance in shortwave-infrared spectra and in near-infrared spectra. From the plots of NDVI versus NDBI shown in Figure 2.1, NDBI provided better urban land and soil separation. In the dry season, soils exhibited higher NDBI than urban surfaces but these soils exhibited lower NDBI in wet seasons. Therefore, by the analysis of the temporal NDBI variation, urban surfaces and soils should be differentiated.

The time-series NDVI, EVI, NDBI or LSWI raster maps were then imported to the rice paddy analysis model to create the flooding and transplanting (FT) binary maps from the math algebra of either $LSWI + 0.05 \geq EVI$ (Xiao et al., 2005; Xiao et al., 2006) or $LSWI \geq 0.18$.

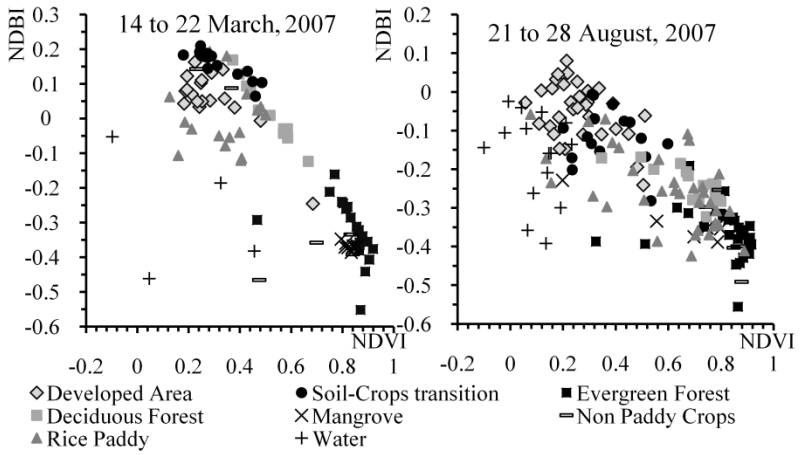

Figure 2.1. Plots of NDBI versus NDVI for different land covers in the dry period in March and the wet period in August. These parameters were calculated from MODIS surface reflectance retrieved over selected areas in SEA

2.3.5. Algorithm for mapping SEA forests (forest mask)

As seen in Figure 2.2, evergreen forests and perennial plantations (mainly rubber, oil palm, and coconut plantations) were consistently observed having NDVI > 0.7. Deciduous forests exhibited lower mean NDVIs with higher annual variation from 0.55 to 0.75 due to interference by high annual soil moisture variations. Mangrove forests, with wetland backgrounds, exhibited high NDVI variation ranging from < 0.1 to > 0.8.

The logical schematic diagram for the forest type classification, developed for this study, is shown in Figure 2.3. Evergreen forests and perennial plantations were identified as any pixel having NDVI ≥ 0.7 for at least half of total annual 46 consecutive maps [= 23 – number of day having a missing tile (3 for this study) = 20]. Deciduous forests and seasonal plantations were identified as any pixel having NDVI ≥ 0.7 for at least one third [= 12] and flooding and transplanting, FT, was observed for less than half of the

observations. Wetland and mangrove forests were identified as any the pixel having NDVI ≥ 0.7 for at least one third and FT for at least half of the observations.

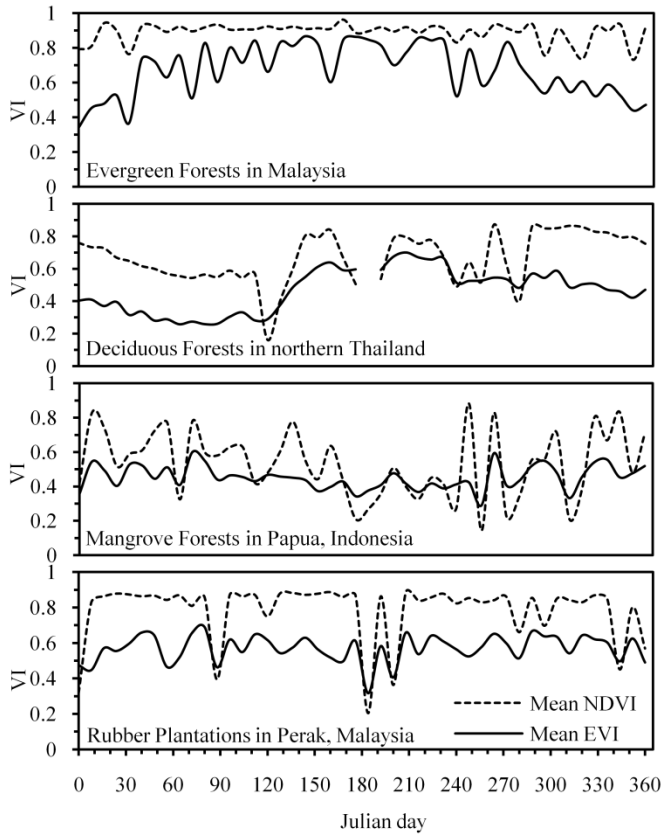

Figure 2.2. Temporal NDVI and EVI profiles over different types of forests and plantations

2.3.6. Algorithm for mapping high-intensity developed areas (urban mask)

Built-up surfaces were identified from any pixel having 0.1 < NDVI < 0.5 and NDBI > − 0.15 for at least half of the total 46 consecutive maps. By using these criteria, built-up surfaces and also highly light-reflecting soils were determined, as observed from the plots in Figure 2.1. These soils are predominantly found over the central dry zone in Myanmar,

and over northeastern Thailand. The soils are actually used for growing rainfed rice, wheat, and other short-growing-season crops. Annual NDBI variance, calculated using Equation 4, was used to differentiate built-up surfaces from these soils. From the time-series NDBI plots in Figure 2.4, high NDBI variation was found for the soils due to soil-vegetation transition, and lesser variation was found over the built-up surfaces.

$$\text{NDBI variance} = \frac{\sum_1^{46} \text{NDBI}^2 - 46 \times (\overline{\text{NDBI}})^2}{46} \quad \text{(Eq.4)}$$

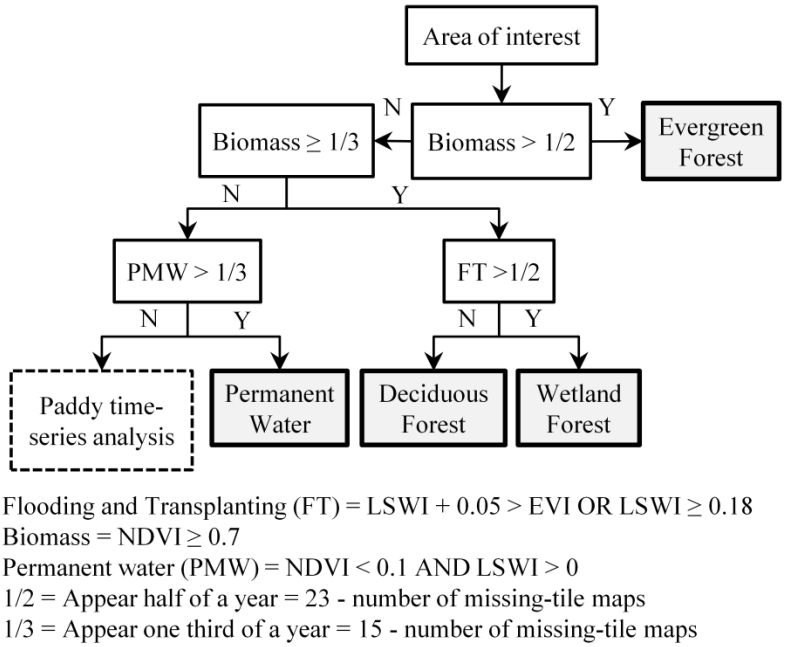

Figure 2.3. The schematic diagram showing the forest types classification methodology used in this study

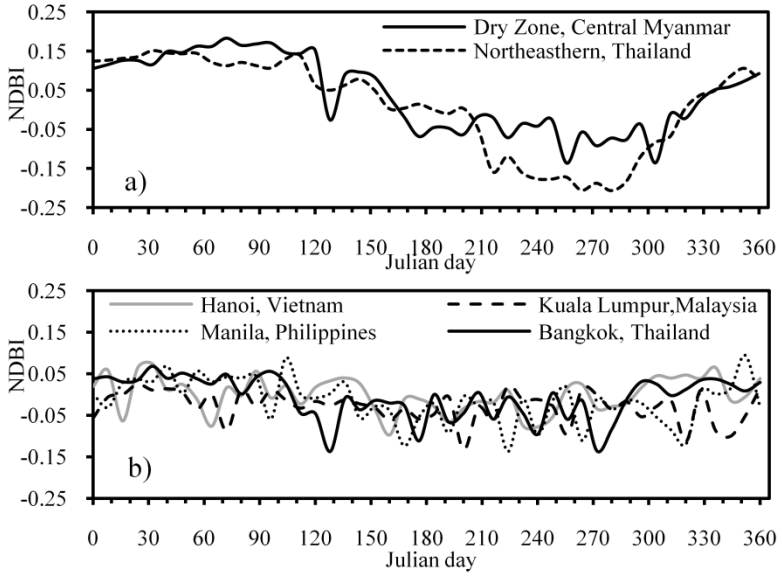

Figure 2.4. Time-series NDBI profiles over the high light-reflecting soil surfaces and the major urban land surfaces calculated from the MODIS 8-day composite surface reflectance

The histogram of the annual NDBI variance shown in Figure 2.5 revealed three peaks which the first peak (P1: < 0.0086) primarily found over built-up areas, second peak (P2: 0.0086 to 0.031) primarily found over the northeastern Thailand, and the third peak (P3: 0.037 to 0.05) was over the central Myanmar. In this study, the areas with NDBI variance less than P1 plus one standard error (0.0086) was assigned to built-up surfaces. In the case of low- to medium-intensity developed areas or urban areas having large green area combination, this analysis tends to have high omission error which can be minimized by merging the results from two consecutive years (2006 and 2007 for this study).

This NDBI variance relates to soil moisture content. In the dry zone of Myanmar, which showed the highest NDBI variance's peak (P3) in Figure 2.5, the soil is naturally dry with deep cracks in dry season, but it is cultivated in the wet season.

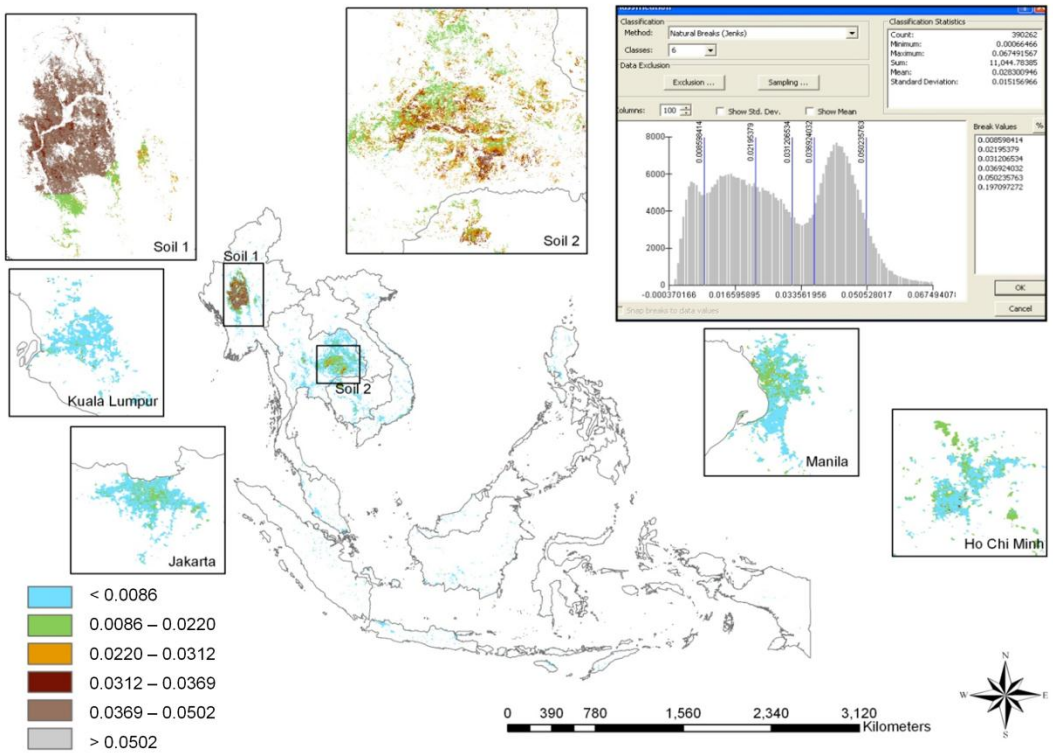

Figure 2.5. NDBI variance (unitless) map showing paved surfaces of urban lands and high light-reflecting soils over SEA. Note: P1 represents the first peak (shown in light blue) indicating the paved surfaces, P2 represents the second peak (shown in green) indicating the soil in northeastern Thailand (Soil 2), and P3 represents the third peak (shown in light brown) indicating the soil in dry zone, central Myanmar (Soil 1) Note: the colors shown on the zoom-in maps are true color. However, the color shown on the regional map is false color resulted from insufficient memory of computational resources to illustrate high-resolution true color on the large scale map.

2.3.7. Algorithm for mapping SEA rice paddy

In this study, different rice ecosystems and annual cropping frequency are identified from rice canopy development patterns. There are major four rice ecosystems: irrigated, rainfed lowland, upland, and flood-prone, as categorized by International Rice Research

Institute (IRRI). These ecosystems can be found in SEA as their characteristics are detailed in the following:

Irrigated rice is grown in fields with assured irrigation for one or more crops a year. It is planted in leveled, diked fields with water control. Rice can be either transplanted from nursery mats or directly seeded in puddled soil. Intermediate fallow periods range from a few days to three months.

Rainfed lowland rice is only grown once a year during the wet season when there is sufficient water from rain. It is planted in leveled to slightly sloping, diked fields with non-continuous flooding. The water level does not exceed 50 cm for more than ten consecutive days. Rice can be either transplanted in puddled soil or directly seeded on puddled or plowed dry soil.

Deepwater rice or *flood-prone rice* only has one crop per year during the wet season when natural flooding occurs. It is planted in leveled to slightly sloping or depressed fields. Water level ranges from 50 to more than 300 cm for more than ten consecutive days in growth stage. Rice can be either transplanted in puddled soil or directly seeded on plowed dry soil.

Upland rice can grow in both flat and sloping fields, which rarely flood and are not diked. This rice is prepared and directly seeded on plowed dry soil or dibbled in wet soil that depends on rainfall for moisture (IRRI, 1975).

A rice-cropping cycle takes three to six months depending on the rice ecosystems. Rice canopy development is generally divided into three phases:

1) Vegetative phase. This period occurs around 60 days after sowing. Generally, germination and early seeding stages are prepared in nursery mats and then transplanted into puddled, leveled field. The water signature dominates during transplanting.
2) Productive phase starts around 60 days after sowing or 30 days after transplanting and lasts until the 90^{th} day. Plants rapidly grow and reach fully developed height. The plant canopies cover most of water surface, intensifying the vegetation signature.
3) Ripening phase is from 90^{th} day to about 120^{th} day. Golden grains start developing. The vegetation signature is still dominant but lessens due to drying leaves. This period could be extended to six months in the case of deepwater rice.

The algorithm for mapping rice paddies used in this study is the first contribution using MODIS retrievals to identify SEA rice paddy areas with different ecosystems. This algorithm is a modification of research conducted by Xiao et al. (2005, 2006) estimating rice paddy areas for Southern China, and South and Southeast Asia, respectively, using multi-temporal MODIS images analysis. Major modifications from the work of Xiao et al. (2005, 2006) in this study are 1) different constraints for terrain mask that allows for steeper slopes and higher altitudes, 2) temporal patterns and strengths of the vegetation-water signals that are more adaptive to specific vegetation-canopy developments in different rice ecosystems, and 3) including deciduous forests/seasonal plantations and

urban masks. The brief schematic diagram used for mapping the rice paddy areas in this study is shown in Figure 2.6. The 55 data sets of the 8-day composite (440 days) surface reflectance band 1, 2, 3, and 6 were used to create 55 consecutive NDVI, EVI, LSWI or NDBI, and FT raster maps. These series maps were then used to create the rice paddy area masks, which include the forest, the built-up areas, the permanent water, and the terrain. The algorithms for creating the forests and the built-up areas masks were given in sections 2.3.5 and 2.3.6, respectively. The algorithms for water, permanent water, and terrain are detailed below.

- The permanent water mask is the mask of pixels having NDVI < 0.1 and LSWI > 0 for at least one-third of the total 46 consecutive maps (368 days). This algorithm provided sufficient sensitivity for identifying the major water resources, such as Mekong River; Irrawaddy River in Myanmar; Red River in Vietnam; Tonlé Sap Lake in Cambodia; Songkhla Lake in Thailand; Inle Lake in Myanmar; and Laguna de Bay in Philippines.
- Upland rice which can be found on slopes up to 30^{o} (Ahmadi et al., 2004) and elevations up to 2,500 m (IRRI, 1975). To allow for upland rice in this study, the terrain mask is restricted to areas having elevation greater than 2,500 m or slope greater than 30^{o}. Xiao et al. (2005, 2006) defined the terrain mask as elevations greater than 2,000 m or slopes greater than 2^{o}.

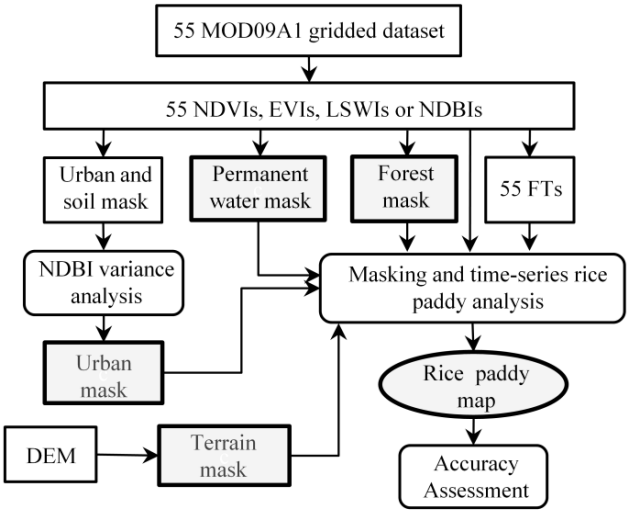

Figure 2.6. Schematic diagram showing the methodology used for mapping rice paddy in this study Note: NDVI = Normalized difference vegetation index; EVI = Enhanced vegetation index; LSWI = Land surface water index; NDBI = Normalized build-up index; FT = flooding and transplanting binary; DEM = Digital elevation model

Constraints for evaluating rice ecosystems used in this study are the solutions providing the best agreement with the SEA rice ecosystems. A total of 55 EVI consecutive maps were used to complete one-year analysis. After masking, the time-series analysis was performed using the following algorithms in order.

- The deepwater rice candidates are assumed to be the pixels having FT for more than 38 of the total 55 consecutive maps, slopes $\leq 2^{o}$, and elevations < 600 m. The true deepwater rice pixels are the candidates that have EVI higher than half of maximum EVI in the next five 8-day (40 days) composites following the date appearing FT. The EVI must continue rising to higher than 0.6 of EVI maximum in the next nine 8-day composites.

- The rainfed rice candidates are assumed to be the pixels having FT for 4 to 20 maps of the total, and slope $\leq 2^{o}$. The true rainfed rice pixels are the candidates that have EVI higher than half of maximum EVI in the next six 8-day composites following the date appearing FT. Then EVI must continue rising higher than 0.7 of EVI maximum in the next eight composites.

- The irrigated rice candidates are assumed to be the pixels having FT for 16 to 38 maps of the total, and slope $\leq 2^{o}$. The true irrigated rice pixels are the candidates that have the EVI higher than half of maximum EVI in the next five 8-day composites following the date observing FT. This EVI continues rising to higher 0.6 than EVI maximum in the next six composites.

- The true upland rice pixels are identified using the same algorithms with the ones for rainfed rice and irrigated rice but allows slope $> 2^{o}$.

2.3.8. Accuracy Assessment

The national statistics of forest, perennial plantation, and rice paddy areas were acquired from the sources listed in Table 2.1 to compare with the results obtained from the MODIS time-series models. These comparisons were done on a provincial/state level.

2.4. RESULTS AND DISCUSSION

The land use/cover map generated from the model is shown in Figure 2.7. The result showed that approximately 75% of the total SEA land is forests and plantations. Rice paddy area accounted for 8.7% of the total land area. Approximately 14% was not

classifiable in this study including non-rice crop lands, grasslands, and medium/low-intensity developed areas.

Table 2.1. The sources of the national statistical databases used in this study for accuracy assessment

Country	National forest/perennial plantation area database	National rice paddy area database
Cambodia	2002/03 national forest areas acquired from the Forest Administration of Cambodia (Forest Administration of Cambodia web page, 2008)	No data available
Indonesia	2005 national estate areas acquired from Badan Pusat Statistik (BPS, 2008) 2002 forest areas by selected province was acquired from the Forest Watch Indonesia and Global Forest Watch (FWI/GFW, 2002)	2007 national rice paddy areas acquired from Badan Pusat Statistik (BPS, 2008)
Lao PDR	No data available	2006 rice paddy areas acquired from the National Statistics Center of the Lao PDR (NSC, 2008)
Philippines	2005 forest areas acquired from the Forest Management Bureau of Philippines (FMBP, 2008) 2007 coconut plantation areas acquired from the Philippines Coconut Authority (PCA, 2008)	2006 rice paddy areas acquired from the National Statistics Office of Philippines (NSOP, 2008)
Thailand	2004 national forest areas acquired from the National Statistical Office of Thailand (NSOT, 2008) Perennial plantation areas acquired from the provincial statistics center (Provincial statistics center of Thailand web page, 2008)	2003 national rice paddy areas acquired from the National Statistical Office of Thailand (NSOT, 2008)
Vietnam	2006 national forest areas acquired from the General Statistics Office of Vietnam (GSO, 2008) Perennial plantation areas estimated from subtracting 2006 total agricultural production areas with 2006 cereal cropping lands areas. Those acquired from the General Statistics Office of Vietnam (GSO, 2008)	2006 rice paddy areas acquired from the General Statistics Office of Vietnam (GSO, 2008)

Note: No data available for Myanmar, Brunei, East Timor, Malaysia, and Singapore

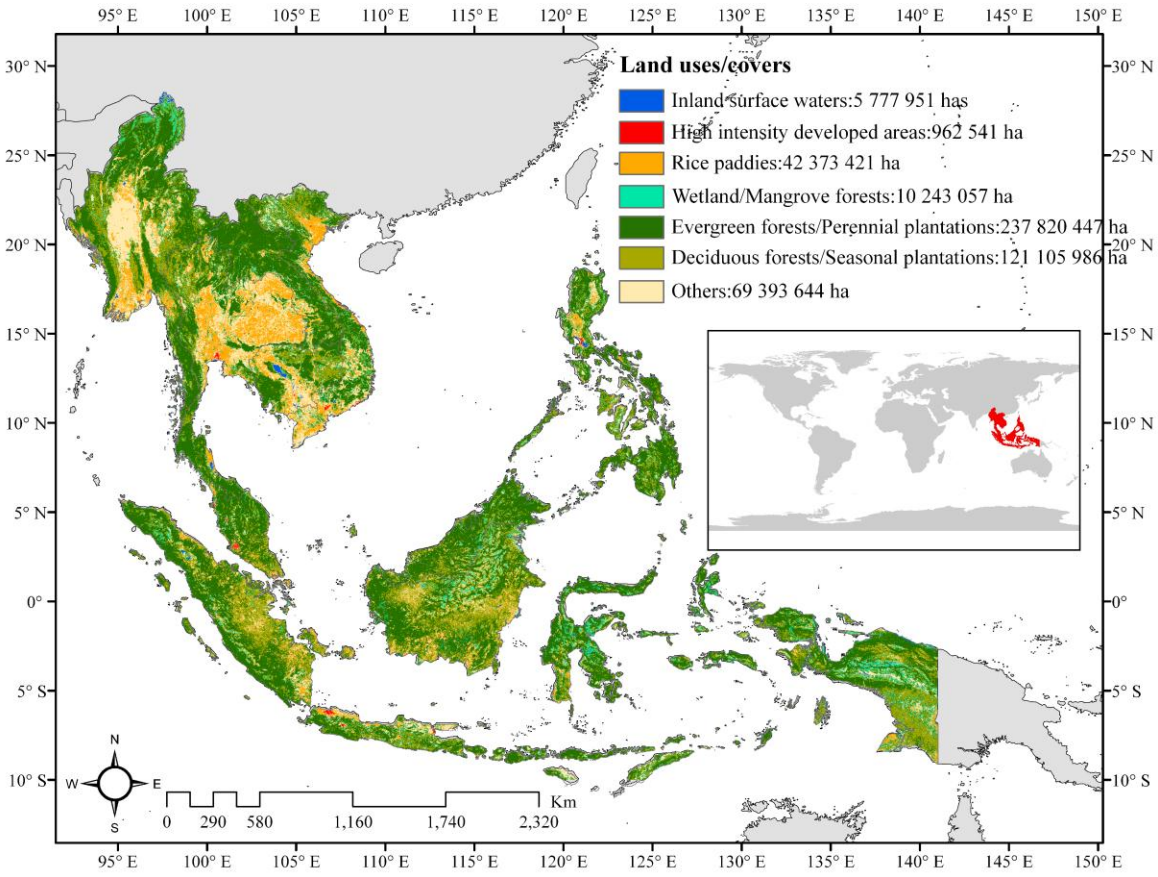

Figure 2.7. SEA land uses/covers map in 2007 generated from the MODIS-derived model

2.4.1. Spatial distribution of the SEA forests and the accuracy assessment

Figure 2.7 shows the spatial distribution of the SEA forests obtained from the model. Forests covered 370 million hectares of SEA. They were primarily distributed over the islands and the northern mainland. Approximately 64% percent of this area was evergreen forests and perennial plantations and 33% was deciduous forests and seasonal plantations.

The estimated areas by type of forests and plantations are reported in Table 2.2. Except for Cambodia and Brunei, the estimated evergreen forest combination, including forests and plantations, areas (column 1) were in the similar magnitude with the total forest area acquired from the FAOSTAT (column 6) and/or the national statistics (column 8). The estimate was somewhat greater in the case of Philippines, Malaysia, and Indonesia. However, this model estimated twice as much forest/perennial plantation areas for Brunei as the reported in the national database. In the case of Cambodia, using the MODIS total forest areas for estimating the Cambodia's forest areas provided better agreement with the national forest statistics than the using MODIS evergreen forest area alone. Unlike the other SEA countries that have mainly evergreen forests, Cambodian deciduous forests account for approximately half of the total forest area (Mayaux et al., 1998), and it was estimated to be 41% by the model (see Table 2.2). Therefore, the MODIS evergreen forest area alone underestimated the total Cambodian forest area.

Table 2.2. Forest areas by forest type by country

Country	Estimated MODIS forest area, 10^3 ha				FAOSTAT 2005 Permanent crops area[j], 10^3 ha (5)	FAOSTAT 2005 Forest area[j], 10^3 ha (6)	(5) + (6) (7)	NFS , 10^3 ha (8)
	Evergreen Forest + Perennial plantation (1)	Deciduous forest + Seasonal plantation (2)	Wetland forests (3)	(1)+(2)+(3) (4)				
Myanmar	31722	13341	390	45453	888	32222	33110	33447[a](2003/04)
Vietnam	11932	7627	447	20006	2350	12931	15281	12418[b](2006)
Philippines	19837	8094	607	28538	5000	7162	12162	15792[c](2005)
Lao PDR	17441	2817	65	20323	81	16142	16223	11177[d](1992)
Thailand	14974	8461	80	23515	3600	14520	18120	16759[e](2004)
Cambodia	6272	4411	82	10765	156	10447	10603	11392[f](2002/03)
Malaysia	23941	6714	647	31302	5785	20890	26675	19420[g](2005)
Indonesia	111188	69569	7916	188673	13600	88495	102095	113975[h](1997)
Brunei	513	65	7	585	5	278	283	236[i](2008)
Singapore	1	8	1	10	0.2	2	2	NR
Total	237820	121106	10243	369169	31465	203089	234554	234649

NFS = National Forest Statistics; NR = Not reported

Source: [a]Ministry of Agricultural and Irrigation Union of Myanmar web page (2010); [b]General Statistics Office of Vietnam (GSO, 2008); [c]Forest Management Bureau of Philippines (FMBP, 2008); [d]International Centre for Environmental Management (ICEM, 2003); [e]National Statistical Office of Thailand (NSOT, 2008); [f]Forest Administration of Cambodia web page (2008); [g]Malaysia Timber Council (MTC, 2008); [h]Forest Watch Indonesia and Global Forest Watch (FWI/GFW, 2002);[i]Forestry Department Brunet Darussalam web page (2008); [j]FAOSTAT (2006)

Due to their similar temporal greenness features, this model could not distinguish evergreen forests from perennial plantations. The same was true for deciduous forests and seasonal plantations. The major perennial plantations in this region are rubber, oil palm, and coconut plantations. The major seasonal plantations are fruit plantations (growing longan, durian, rambutan, and mango). Figure 2.8 shows the linear regression plots between the estimated total forest areas obtained from the model (y) and that acquired from the national forest and major plantation area databases by province/state (x). These total forest areas on the y-axis include the estimated areas of the evergreen forest, deciduous forest, wetland forest, perennial plantation, and seasonal plantation. The results for Indonesia, Philippines, Thailand, Vietnam, and Cambodia showed that the estimated forest areas were larger than the national statistics. However, after including the national plantation areas statistics into the national forest areas statistics, both data sets show better 1:1 relationships for all five cases (slope = 1.34, 1.02, 1.10, 1.05, 0.94 for Indonesia, Philippines, Thailand, Vietnam, and Cambodia, respectively) with coefficient of determination (R^2) of 0.86, 0.78, 0.97, 0.82, and 0.95, respectively. It is concluded that the accuracy of the forest mapping from this model was improved by subtracting plantation areas. In case of Indonesia, the estimated forest area was still larger than the national data after this correction (see Figure 2.8). This correction, however, was not applied in the Papua province and Maluku island of Indonesia due to the lack of national estate area information. Both regions are large remote areas which could account for this inconsistency.

Even though moderate-resolution satellite retrievals have not been widely used to perform local land-cover classification, unsupervised forest-cover classification from MODIS imagery conducted by Fu et al. (2008) shows promising agreement with local classification using high-resolution satellite retrievals. Several time-series MODIS imagery analyses have been previously proposed and these suggest appropriateness of using the imagery for vegetation-cover classification (Yui et al., 2004) and for land-cover classification (Guo et al., 2008). Time-series MODIS imagery analysis proposed in this study is simpler than the previous proposed methods using amplitude/phase analysis (Yui et al., 2004) and statistical relationship analysis (Guo et al., 2008). The results obtained from this model had good agreement with the national database at provincial level with the correction for plantation areas.

2.4.2. Spatial distribution of the SEA high-intensity developed areas

Figure 2.9 shows the map generated from the model for high-intensity developed areas determination over the ten capital cities in SEA compared the high-resolution satellite imagery acquired from Google Earth. This model clearly identified the urban areas in major cities in SEA countries: (1) Bangkok, Thailand; (2) Kuala Lumpur, Malaysia; (3) Manila, Philippines; (4) Jakarta, Indonesia; (5) Ho Chi Minh City, Vietnam; (6) Bandung, Indonesia; and (7) Surabaya, Indonesia. These cities have dense populations and their MODIS urban areas were larger than 80 km^2.

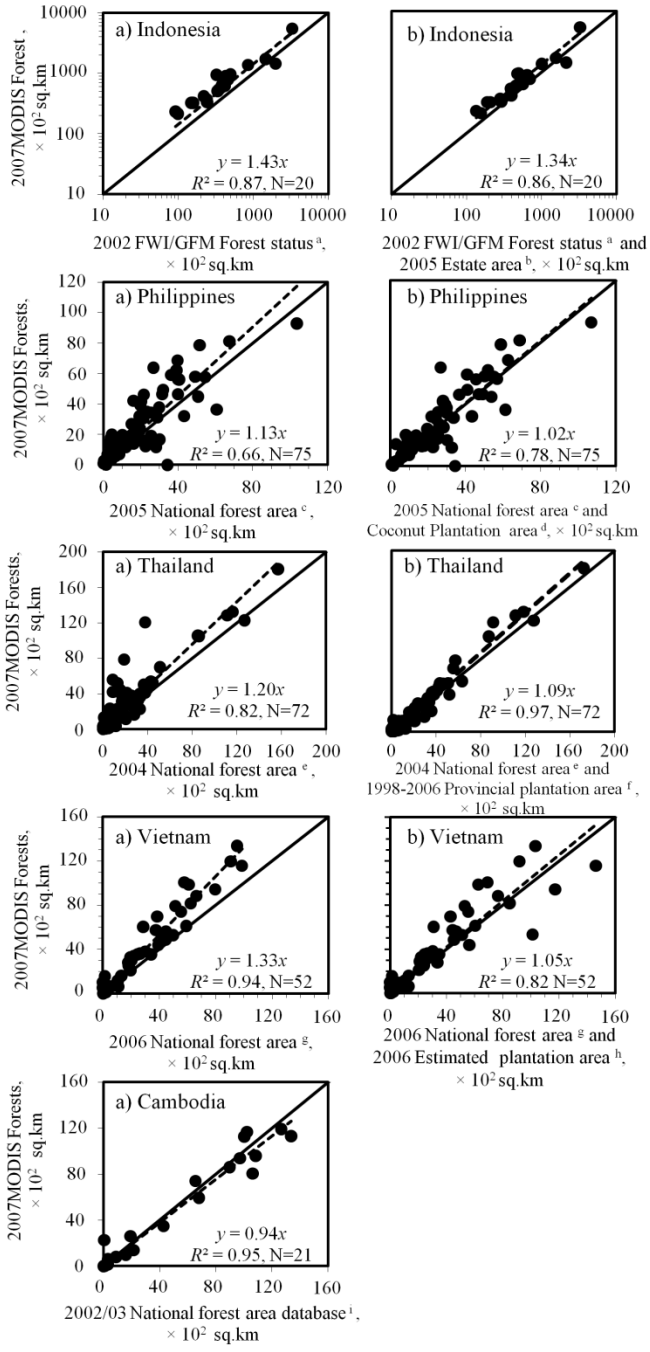

Figure 2.8. Linear regression plots (a: left hand) between the estimated MODIS forest areas and the national forest area database by province (or state), and (b: right hand) between the estimated MODIS forest areas and the corrected national forest areas with the major perennial plantation areas, for Indonesia, Philippines, Thailand, Vietnam, and Cambodia (only a)

Note: N = number of observation

Source: [a]FWI/GFM (2002); [b]BPS (2008) (no estate area reported for Papua and Maluku region); [c]FMBP (2008); [d]PCA (2008); [e]NSOT (2008); [f]Provincial statistics center of Thailand (2008); [g]GSO (2008); [h]GSO (2008) with estimating the plantation areas by subtracting the total agricultural production areas with the total cereal cropping lands; [i]Forestry Administration of Cambodia (2008)

Besides these cities, there were low-developed cities that were identified as urban areas on the MODIS-derived map. These are (8) Phong Dien and Quang Dien in Thua Thien-Hue, Vietnam. Both appeared as bright white areas on the satellite map indicating high surface reflectance, probably from sandy beaches. This urban MODIS-derived model could include other high light reflectance areas, such as desert or permanent bare soils that do not occur in SEA.

The map shown in Figure 2.9 also illustrates the urban areas over (9) Phnom Penh, Cambodia, (10) Singapore, (11) Hanoi, Vietnam and (12) Vientiane, Lao PDR. Their MODIS estimated urban areas, however, are smaller than 80 km^2. The model, however, did not represent the urban areas of Banda Seri Begawan, Brunei and Yangon, Myanmar very well. Both capital cities have urban-green combinations, enhancing light absorbability.

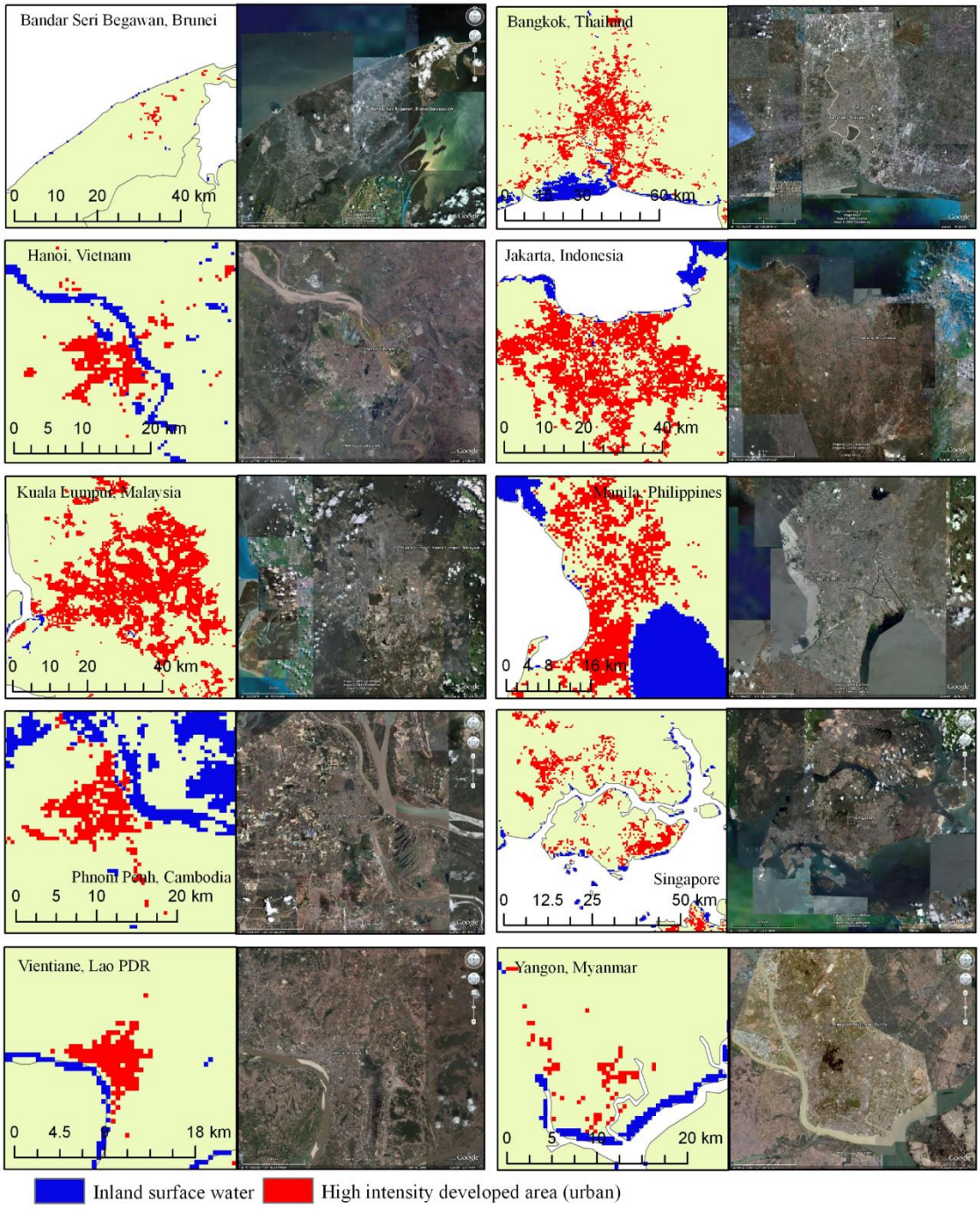

Figure 2.9. The urban maps generated in this study using the MODIS time-series analysis (left hand maps) over 10 capital cities in SEA in compared with the very high resolution satellite imagery from Google Earth acquired on July 18, 2008 (right hand images)

2.4.3. Spatial distribution of the SEA rice paddies and the accuracy assessment

Figure 2.10 shows the spatial distributions of the predicted rice ecosystem over SEA. As seen from this map, rainfed rice ecosystem dominated over NE Thailand, central Myanmar, and Cambodia. The irrigated rice ecosystem dominated the central Thailand; Red River Delta, Vietnam; Irrawaddy River Delta, Myanmar; Central Luzon, Philippines; Songkhla Lake, Thailand; and Mekong River drainages in both Cambodia and Vietnam. The deepwater rice ecosystem was primarily observed over Mekong River Delta, Vietnam; and Papua, Indonesia. The single rice crops were approximately 32×10^6 ha for SEA. Approximately 10×10^6 ha were double- and multiple-rice crops, which were found in the major irrigated rice ecosystems.

As shown in Table 2.3, the estimated total regional rice paddy area is 42.4×10^6 ha, consistent with the areas reported in FAOSTAT (2006), 42.2×10^6 ha, and by Huke and Huke (1997), 40.1×10^6 ha. Considering paddy areas by country, good agreement between the estimated values and the published values was found for Myanmar, Cambodia, Thailand, and Indonesia. The estimates for Vietnam and Philippines were low. Rice paddy area was overestimated for Lao PDR and Malaysia.

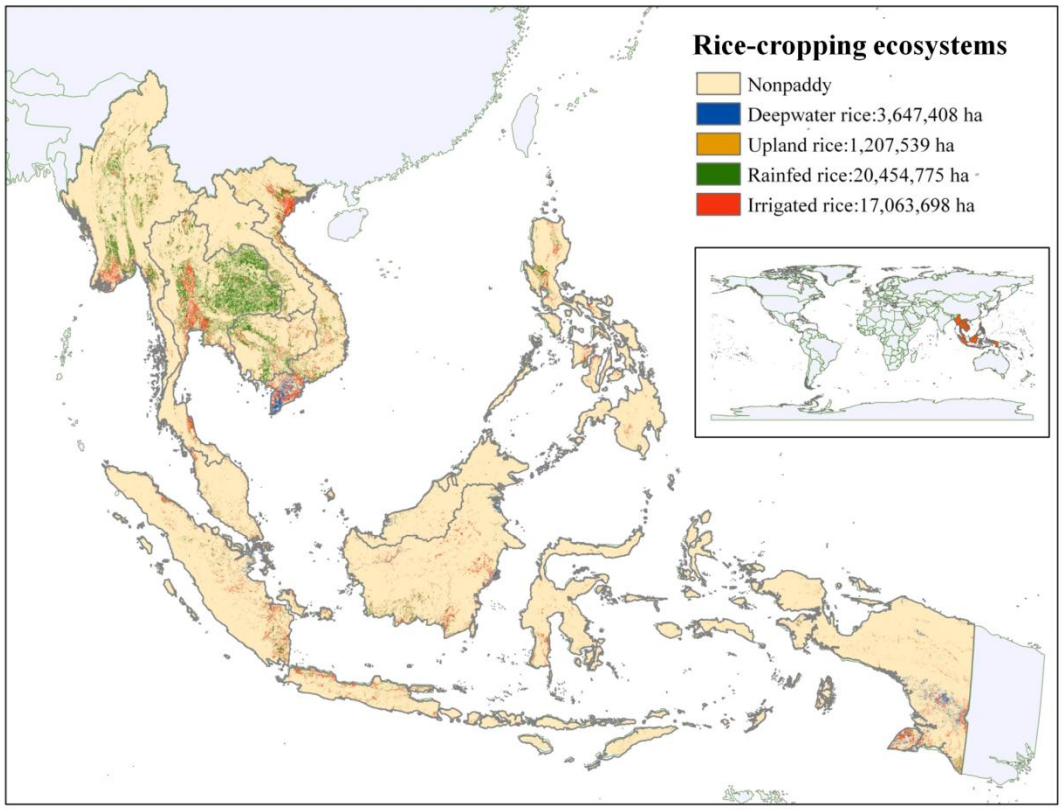

Figure 2.10. Spatial rice paddy distribution map over SEA by rice ecosystem generated from time-series MODIS imagery analysis

The rainfed rice ecosystem dominated in Myanmar (62%), Cambodia (61%), Lao PDR (75%), Thailand (75%), and Philippines (70%), as indicated from Table 2.3. The values obtained from this model for Myanmar and Philippines were significantly higher than that reported by Huke and Huke (1997) of 40% and 35%, respectively. This might be a result of misclassifying multiple-irrigated rice as single-rainfed rice, which is discussed later. Figure 2.11 shows the plots between the MODIS-estimated paddy areas (y) and the national rice paddy area statistics by province (x) for Indonesia, Philippines, Thailand, Lao PDR, and Vietnam. These plots suggest the good correlations for Thailand with R^2 of 0.83 and for Lao PDR with R^2 of 0.93. The estimated rainfed rice ecosystem is

approximately 75% of the total rice paddy area in both countries. Under this ecosystem, the temporal EVI and the water logic profiles, as seen in Figure 2.12 for northeastern Thailand and Phnom Penh, Cambodia, clearly illustrate single rice canopy development (single annual cycle of EVI after the presence of water logic of unity), which can be easily predicted by the model.

The national rice statistics of Lao PDR reported that 13.6% of the total rice paddy area was upland rice (NSC, 2008). The ratio is higher than that estimated from the model, which was only 4.7% of the total. High uncertainty on the upland rice area estimation using a MODIS-derived model was also found in related studies (Xiao et al., 2005; Xiao et al., 2006). As seen in Figure 2.11, the results over the major upland rice provinces in Lao PDR, and in the North West and the Central Highlands regions in Vietnam showed that the MODIS rice areas were 2.2 times and 3.6 times, respectively, larger than the reported in the national statistics. The overestimation for upland case was not only found for the rice paddy areas, but it also found for general upland crops fields. Tingting and Chuang (2010) used MODIS NDVI to separate crop and non-crop areas in the Chao Phraya Basin, Thailand and their upland crops area was greater than that from statistic data. They attributed this area discrepancy to similarity of the NDVI signals between the crops and adjacent grass or deciduous shrub.

As indicated from the model's results in Table 2.3, irrigated rice paddies were predominant in Vietnam (49%), Malaysia (59%), and Indonesia (59%). These areas were in similar magnitude with that reported in Huke and Huke (1997) except for the case of

Philippines. Their work showed the prevalence of irrigated rice in Philippines, which differed from this work. The EVI and the water logic profiles in Figure 2.12 over the selected irrigated rice paddy pixels in Hanoi, Vietnam clearly indicated double-rice crops; however, the profiles observed in South Kalimantan, Indonesia and Bataan, Philippines are not clearly indicated. In an irrigated ecosystem, there are sufficient water resources for multiple-rice cropping and each holder of rice paddies can have different rice cropping calendar. This causes inconsistent temporal patterns of rice canopy development over large spatial scale. For this reason, the model tends to not include irrigated rice areas or misclassifies this rice as single rice in a rainfed ecosystem. Over the irrigated rice dominated provinces in region 1 Vietnam; including Red River Delta, North East, North Central Coast, and South Central Coast, and Philippines (see Figure 2.11), the MODIS rice areas were 0.68 and 0.47 times, respectively, smaller than the reported in the national databases with R^2 of 0.78 and 0.66, respectively.

Table 2.3. The percentage of area by rice ecosystem, and by rice cropping frequency, and the total rice paddy areas acquired from FAOSTAT Database and estimated from the MODIS-derived model by country

Country	MODIS-derived model								Total areas mid-1990s [Δ], 10^3 Ha	FAO total areas 2005[*],10^3 Ha
	Rice ecosystem, %				Cropping Frequency, %			Total areas, 10^3 Ha		
	Deepwater	Upland	Rainfed	Irrigated	Single	Double	Multi			
Myanmar	0.97	6.40	61.71	30.91	78.51	19.12	2.37	6157	6285	6270
Vietnam	15.58	6.86	28.75	48.81	78.86	17.91	3.23	5762	6375	7340
Cambodia	4.71	3.41	60.96	30.93	72.26	22.35	5.40	1961	1899	2150
Lao PDR	0.00	4.73	75.38	19.89	83.49	15.02	1.48	1129	611	736
Thailand	0.97	1.43	75.07	22.54	81.39	16.44	2.18	11994	9644	10200
Philippines	1.32	0.52	70.10	28.06	76.60	20.27	3.13	2827	3620	4000
Malaysia	13.99	0.83	26.04	59.14	68.27	23.66	8.06	994	668	660
Indonesia	19.99	0.90	19.79	59.31	67.92	22.20	9.88	11511	11015	11801
Brunei	17.31	0.38	28.86	53.45	74.03	21.20	4.77	17	-	-
Singapore	4.20	0.00	65.52	30.28	58.62	30.93	10.45	20	-	-
							Total	42373	40117	43157

[Δ] Huke and Huke (1997)

[*] FAOSTAT (2006)

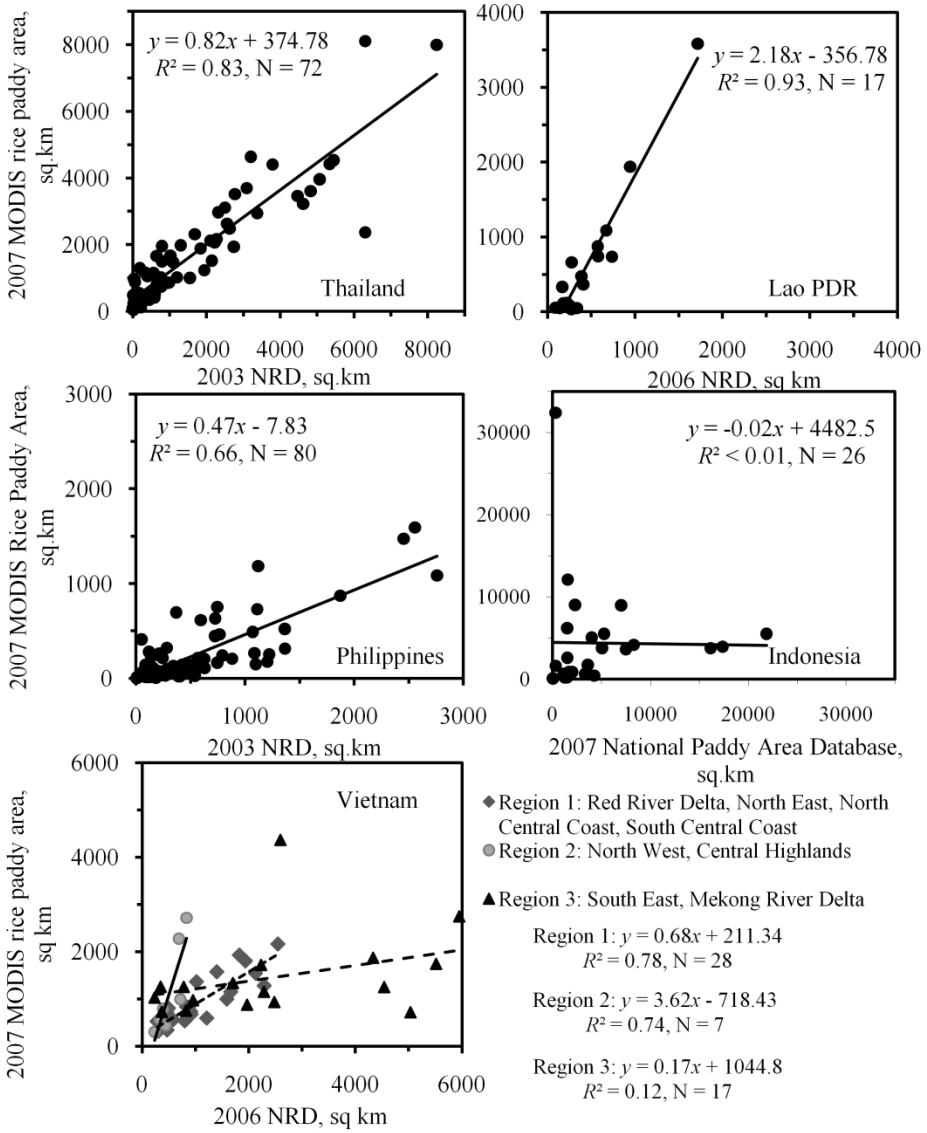

Figure 2.11. Linear regression plots of the MODIS rice paddy areas and the rice paddy areas acquired from the national rice database by province (or state) for Indonesia, Philippines, Thailand, Lao PDR, and Vietnam

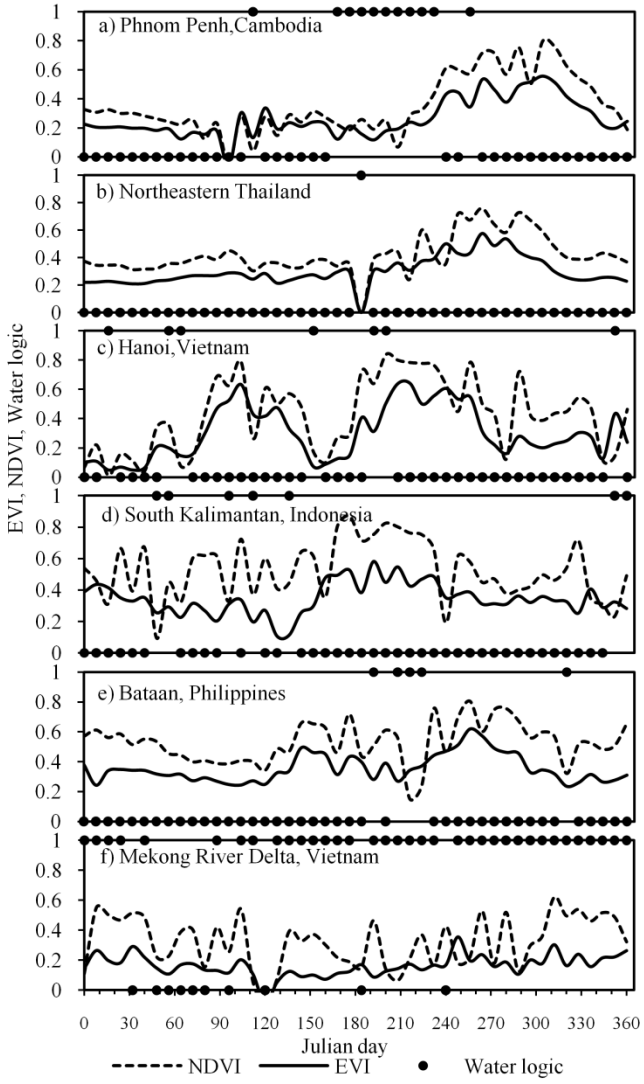

Figure 2.12. Temporal EVI, NDVI, and water logic profiles at the selected rice paddy pixels

In case of Indonesia, there was poor correlation between the estimated rice areas and the national rice statistics. One of the outlier estimates was observed in Papua region. The model reported 3×10^6 ha rice paddies over this region, while the national rice statistics were only 22,957 ha. What causes this discrepancy is not understood. This model predicted that deepwater and irrigated rice was dominant in southern Papua, where the actual major farming system is root and tuber and the principal crops are yam, taro, sweet potato, vegetables, and fruits (Dixon et al., 2001). The poor correlations for the deepwater ecosystem were also observed in the South East and Mekong River Delta regions in Vietnam from the correlation coefficients shown in Figure 2.11.

From Figure 2.12, temporal EVI and the water logic profiles observed over a deepwater rice paddy grid in Mekong River Delta in Vietnam exhibited similar to long-term wetlands. Thus this rice ecosystem could be easily misclassified as natural wetlands and vice versa. Mekong River Delta in Vietnam has heterogeneous characteristics of deepwater rice paddies, irrigated rice paddies, and aquaculture farms (Pingali and Xuan, 1992; Sakamoto et al., 2009). MODIS data have coarse spatial resolution which could respond to its poor efficiency to distinguish among these land types. There are attempts to reduce the noise component in the time-series MODIS data collected over this region. Several mathematical techniques had been proposed which include wavelet-based filter (Sakamoto et al. 2005) and empirical mode decomposition (Chen et al. 2011). The techniques provided good results which suggest that they are capable of resolving the heterogeneity of this mixed rice land (Sakamoto et al. 2009, Chen et al. 2011). However,

efficiency and accuracy of using these noise reduction techniques in regional scale land analysis had not yet been proven.

2.5. CONCLUSION

The land cover classification using the time-series satellite imagery analysis was performed for mapping forest areas, high-intensity developed areas, and rice paddies over SEA region. These imagery were generated from the 500-m resolution MODIS/Terra spectral surface reflectance (MOD09A1) acquired from 2006 to 2007.

The estimated forest combination areas, including forests and plantations, resulted in the similar magnitude with the provincial forest areas reported in the national forest statisitical databases after corrected plantation areas. The linear regression slopes between the MODIS forest areas (y) and the national database by province (x) ranged from 0.94 to 1.34 with R^2 of 0.78 to 0.97 for the five countries.

The estimated urban areas were determined from the areas which had constantly high surface reflectance in the shortwave infrared over time. With except for beaches, deserts, and permanent bare soils, large urban areas can be easily identified. In this study, the MODIS urban areas greater than 80 km^2 were observed over seven cities. These were 1) Bangkok, Thailand; 2) Kuala Lumpur, Malaysia; 3) Manila, Philippines; 4) Jakarta, Indonesia; 5) Ho Chi Minh City, Vietnam; 6) Bandung, Indonesia; and 7) Surabaya, Indonesia.

The algorithm for mapping rice paddy area was developed based on the observed temporal SEA rice canopy developments. This algorithm distinguishes different rice

ecosystems and provides rice-cropping frequency. The total estimated rice area for SEA was 42×10^6 ha, which is consistent with published values. Comparison of the estimated rice paddy area (y) and the national rice statistics (x) on the provincial or state level showed high correlations over the areas dominated by rainfed rice (i.e. Thailand: R^2 = 0.83, slope = 0.82 and Lao PDR: R^2 = 0.93, slope = 2.2). The high correlations were also found in irrigated rice but the model tended to under estimate the paddy areas (i.e. Red River delta in Vietnam: R^2 = 0.78, slope = 0.68, and Philippines: R^2 = 0.66, slope = 0.47). This could be resulted from inconsistency of temporal rice canopy development pattern over large-scale areas. For the areas dominated by upland rice, the correlations were good but the MODIS rice areas were overestimated (i.e. Lao PDR, and the highland regions in Vietnam: R^2 = 0.74, slope = 3.6). Overall high R^2 values indicate that spatial distribution of the MODIS rice areas was consistent with the actual distribution. In addition, These R^2 values are either in the similar magnitude or better than those reported in literature, regardless the rice ecosystem extraction. The poor correlation was observed for deepwater rice (i.e. Mekong River Delta in Vietnam: R^2 = 0.12) because this rice ecosystem could easily be misclassified as wetlands and vice versa and area heterogeneity, one case of the Mekong River Delta in Vietnam, caused high uncertainties associated with interpreting the MODIS data.

CHAPTER THREE

OPTICAL CHARACTERISTICS OF SOUTHEAST ASIA'S REGIONAL AEROSOLS AND THEIR SOURCES

3.1. ABSTRACT

The dominant optical characteristics of Southeast Asia (SEA)'s regional aerosols were determined from the cluster analysis of the twenty-six AERONET aerosol inversion products, including aerosol light scattering/absorption indicators and aerosol size/shape parameters. The data sets were measured at four stations: Bac Giang in Vietnam and Mukdahan, Pimai, and Silpakorn University in Thailand from 2003 to 2007. We investigated agreement among the aerosol optical characteristics, land cover/uses, season as the surrogate of the prevailing winds, and observations from the literature. The results of this study showed that during the NE prevailing winds from mid-September to December, the high aerosol exposure events were most frequently observed over the upwind station and less often over the downwind stations. This aerosol exhibited a single scattering albedo, *SSA*, of approximately 0.95 (440 nm), a relatively low refractive index, and a larger fine-mode size, suggesting it had the characteristics of urban/industrial aerosols reported in the literature. These aerosol sources were upwind from Bac Giang, probably in eastern China. From January to April, the aerosol exhibited a lower *SSA* of approximately 0.90, a higher refractive index, and a smaller fine-mode size, suggesting biomass burning smoke reported in the literature. The SEA urban aerosol exhibited a mean *SSA* of approximately 0.90 (440 nm) or lower and the coarse-mode aerosol,

possibly road dust or soil dust, played a role from October to January when seasonal winds are strongest. The results from a canonical discriminant function analysis suggest that the dominant SEA aerosol clusters tended to be separated by a canonical function positively correlated to *SSA*, the fine-mode asymmetry factor, and the overall fine-mode size, and negatively correlated to the refractive index.

3.2. INTRODUCTION

Various sources of Southeast Asian aerosol were reported in previous studies. One study conducted by Remer et al. (2005) used cluster analysis of the AERONET level 2 data for each AERONET site and each season. AERONET (AErosol RObotic NETwork) program is a federation of ground-based remote sensing aerosol networks established by NASA and LOA-PHOTONS (CNRS). One of Remer's findings was that aerosol having a single scattering albedo (*SSA*) of approximately 0.95 (670 nm) played a major role over the SEA region. This aerosol was presumed to be urban/industrial aerosol, but the source of this aerosol was not determined in their study. Another study was conducted by Wangkiat et al. (2004) using the chemical mass balance analysis of the total suspended particulate matter from the Bangkok metropolitan area. They concluded that soil and road dust were the major contributors to aerosol loading. Cohen et al. (2010) presented work on fine particle ($PM_{2.5}$) characterizations and source apportionment in Hanoi during 2001-2008 using nuclear techniques. Their result suggested that automobile emissions were the most significant aerosol contributor. These studies are among previous SEA aerosol contribution studies focusing on urbanized areas. All agreed that biomass burning

was less significant, contradicting the previous understanding that smoke should play a role over this region, especially in the dry season (Liu et al., 1999; Pochanart et al., 2001; Tipayarom, 2004). Traditional aerosol contribution studies using mass balance or positive matrix factorization analysis were limited to local urban sources and their results may not represent SEA regional aerosols.

This study reports the optical characteristics of the dominant SEA aerosols based on the results from cluster analysis. The assignment of the sources of these aerosols were based on their optical properties and their temporal occurrences related to typical air trajectory pathways from prevailing wind directions and back trajectory analysis. The aerosol data sets acquired from AERONET used in this study have the time-series, regional-distributed characteristics which are suitable for a study of the seasonal characteristics of the SEA regional aerosols.

3.3. METHODOLOGY

3.3.1. AERONET level 2 data descriptions

The level 2 (cloud-screened and quality-assured) daily average aerosol optical depth (*AOD*), the Angström exponent (α), and other aerosol optical properties were used in this study. The data were taken from the AERONET website (http://aeronet.gsfc.nasa.gov/) for 2003 to 2007, with the exception of the Silpakorn University site for which the only data available were from November 2006 to April 2007. Only observations from the days with complete aerosol variables were used. The number of observations in each month was given in Table 3.1. There were relatively few observations during the rainy season

from June to August. The aerosol during these months, therefore, was not equally weighted in this study.

Table 3.1. Monthly number of observations used in this study

	Bac Giang					Mukdahan					Pimai					Silpakorn U.	
	2003	2004	2005	2006	2007	2003	2004	2005	2006	2007	2003	2004	2005	2006	2007	2006	2007
Jan	0	2	5	0	8	0	8	15	10	10	0	0	0	14	11	0	16
Feb	0	8	0	0	9	0	14	12	6	17	7	10	0	11	17	0	21
Mar	4	3	3	0	1	0	23	9	20	21	6	7	0	24	21	0	18
Apr	8	5	1	0	2	0	18	11	7	10	17	0	0	6	8	0	7
May	5	4	0	2	2	0	1	3	3	2	2	0	0	3	0	0	0
Jun	7	5	0	0	0	0	0	0	0	0	0	1	0	0	0	0	0
Jul	0	0	0	1	0	0	0	1	0	0	0	0	0	0	0	0	0
Aug	2	1	0	1	0	0	0	0	0	0	0	0	0	0	0	0	0
Sep	6	10	0	8	2	0	3	0	3	2	0	0	0	0	0	0	0
Oct	14	17	0	16	0	0	3	1	9	6	0	1	1	3	0	0	0
Nov	11	13	0	14	0	3	5	4	8	2	0	0	3	14	0	10	0
Dec	9	13	0	11	0	4	10	3	6	0	0	0	3	10	0	13	0
Total	233					293					200					85	

AOD is a quantitative measure of the extinction of solar radiation caused by aerosol scattering and absorption between the top of the atmosphere and the point of the observation. An *AOD* of unity means that the atmospheric aerosol decreases solar radiance to 0.368 of the total atmospheric gaseous-corrected radiance from the sun. The Angström exponent is an aerosol-size-related parameter, calculated from a spectral pair of *AOD* measurements (870 and 440 nm for this study).

AERONET Cimel sun/sky-radiometers measure both the direct and diffuse radiation. These radiance measurements, in combination with aerosol optical depth measurements and estimations of land and water surface reflectance, were inverted to estimate various aerosol optical properties (AERONET, 2010), called aerosol inversion products, using the inversion algorithm developed by Dubovik and King (2000). Twenty-six aerosol inversion products were used for the cluster analysis in this study: two volume mean radii (r_v: fine and coarse fraction, F/C), two effective radii (r_{eff}: F/C), four single-scattering albedos (*SSA*: 440, 675, 870, 1,020 nm), four real-part refractive indices (*n*: 440, 675, 870, 1,020 nm), four imaginary-part refractive indices (*k*: 440, 675, 870, 1,020 nm), an Angström exponent (α: for 870-440 nm), a total water column, and eight asymmetry factors (*g*: 440, 675, 870, 1,020 nm, F/C). The asymmetry factor is the fraction of the incident radiation scattered forward after striking an aerosol to total incident incoming radiation. The asymmetry factor can be used to infer nonsphericity of the particle.

3.3.2. Back trajectory result

Back trajectories were used to characterize the transport of the Chinese urban aerosol to SEA. These were based on a kinematic trajectory analysis using NASA GMAO (Global Modeling Assimilation Office) assimilated gridded analysis data and NCEP (National Centers for Environmental Prediction) analyses. The results were retrieved from the AERONET website.

3.3.3. AERONET site description

The data from four SEA AERONET stations were acquired for the study: Bac Giang in northern Vietnam; Pimai in northeastern Thailand; Mukdahan in northeastern Thailand; and Silpakorn University in central Thailand. Bac Giang, Pimai, and Mukdahan are characterized as rural environments, surrounded by agricultural fields, primarily rice paddies. Silpakorn University is more urban and located about 50 km west of Bangkok, the capital of Thailand. Two prevailing winds dominate these areas: northeasterly winds from mid-September to April, which includes the dry season, and southwesterly winds from May to September, which includes the rainy season. The locations of the four sites are shown in Figure 3.1.

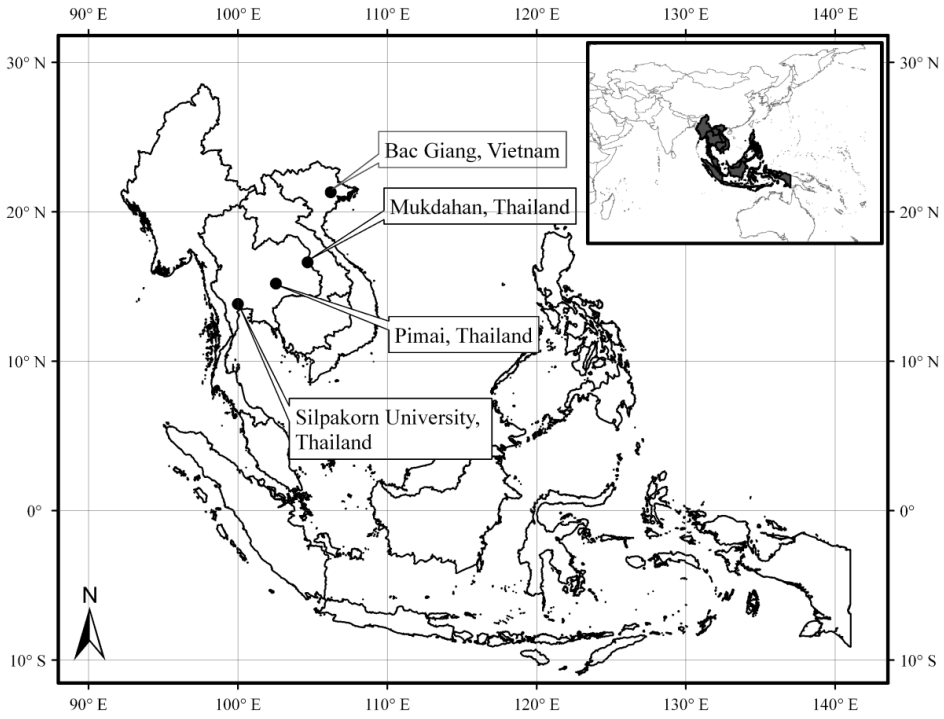

Figure 3.1. The locations of the four AERONET stations considered for this study

3.3.4. Research methodology

A schematic diagram of the methodology applied in this study is shown in Figure 3.2. An *AOD* at 500 nm exceeding unity was chosen for this study as an aerosol exposure episode. Cluster analysis grouped aerosol observations into classes with similar optical properties. This type of analysis is useful for solving problems with unknown number of classes (Manly, 1994). For this study, the analysis was done on standardized variables using the agglomerative hierarchical method with group average linkage. Two groups merge if the average of all pairwise differences between observations from each group is small enough. This method tends to be less influenced by the extreme values and joins clusters with small variances (SAS Institute Inc., 2002). The number of clusters was selected from the minimum number yielding the relatively high pseudo-*F* statistic compared with the nearby upper and lower cluster numbers. The results from the cluster analysis indicated the optical characteristics of the major SEA aerosol clusters.

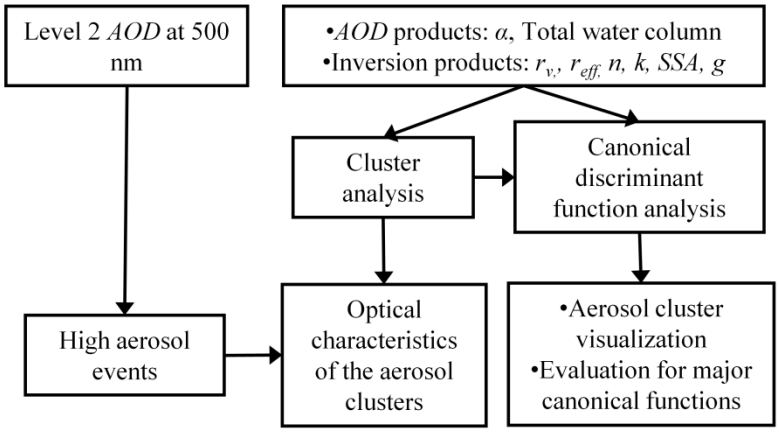

Figure 3.2. Summary of research methodology

In addition, canonical discriminant function analysis was conducted for each station to generate linear combinations of variables, called canonical functions, from the original twenty-six variables to maximize the *F*-ratio (ratio of the between clusters mean square and the within clusters mean square) for a one-way analysis of variance. The analysis helps to visualize the separation between the aerosol clusters. The correlations between the canonical functions and the set of original variables are reported. This correlation suggests which of the original variables play a role in describing the canonical function characteristics. The first canonical function, CAN1, is the linear combination that reflects the largest cluster differences. The second function, CAN2, captures as much as possible of the cluster differences not displayed by CAN1. The third function, CAN3, captures as much as possible of the group differences not displayed by CAN1 and CAN2, and so on (Manly, 1994). Both statistical analyses were done via SAS 9.2 software (SAS Institute Inc., Cary, NC).

3.4. RESULTS AND DISCUSSION

The aerosol cluster names begin with a letter: B for Bac Giang, M for Mukdahan, P for Pimai, S for Silpakorn University, and then are followed by the cluster numbers. In this study, an appropriate number for a cluster was chosen from the peak of its pseudo-*F* statistics. Four were chosen for Bac Giang, eight for Mukdahan, four for Pimai, and seven for Silpakorn University. Optical properties of the dominant aerosol clusters, having the majority of the observations at each site, are shown in Table 3.2.

Table 3.2. Results of the cluster analysis for the dominant aerosol clusters at four SEA stations

Total number of observation ; Total aerosol exposure events	233; 79		293; 37		200; 18		85; 2		
Cluster	B1	B2	M1	M2	P1	P2	S1	S2	S3
Number of observations	121	109	214	48	157	31	37	22	14
Number of aerosol exposure events	58	20	28	8	14	3	1	1	0
r_{eff}-F/C, μm	0.226/2.465	0.167/2.264	0.172/2.453	0.216/2.789	0.168/2.472	0.203/2.794	0.156/2.386	0.170/2.257	0.192/2.990
r_v-F/C, μm	0.257/2.892	0.187/2.719	0.192/2.970	0.247/3.260	0.186/3.023	0.229/3.284	0.173/2.986	0.187/2.796	0.224/3.467
α for 870-440 nm	1.268	1.409	1.544	1.328	1.541	1.365	1.560	1.536	1.274
g-F*	0.755/0.691/ 0.639/0.605	0.704/0.606/ 0.541/0.501	0.711/0.618/ 0.553/0.510	0.751/0.684/ 0.633/0.599	0.710/0.609/ 0.538/0.491	0.740/0.664/ 0.606/0.567	0.684/0.588/ 0.521/0.476	0.718/0.622/ 0.549/0.499	0.724/0.658/ 0.611/0.584
g-C*	0.877/0.824/ 0.795/0.787	0.891/0.831/ 0.797/0.785	0.894/0.839/ 0.807/0.797	0.888/0.837/ 0.808/0.798	0.891/0.837/ 0.805/0.796	0.879/0.827/ 0.799/0.789	0.897/0.835/ 0.808/0.801	0.875/0.819/ 0.798/0.795	0.918/0.866/ 0.837/0.824
SSA*	0.951/0.952/ 0.951/0.950	0.900/0.899/ 0.899/0.897	0.911/0.896/ 0.885/0.872	0.950/0.943/ 0.937/0.931	0.905/0.891/ 0.886/0.878	0.950/0.946/ 0.945/0.942	0.884/0.873/ 0.850/0.830	0.917/0.906/ 0.886/0.870	0.908/0.905/ 0.889/0.874
n*	1.403/1.416/ 1.423/1.418	1.428/1.448/ 1.462/1.458	1.433/1.448/ 1.454/1.451	1.402/1.416/ 1.423/1.420	1.423/1.437/1 .450/1.445	1.409/1.423/ 1.432/1.434	1.469/1.480/ 1.487/1.480	1.413/1.426/ 1.437/1.433	1.443/1.452/ 1.462/1.458
k*	0.007/0.006/ 0.005/0.005	0.014/0.011/ 0.010/0.009	0.014/0.013/ 0.012/0.013	0.007/0.007/ 0.007/0.007	0.014/0.013/ 0.011/0.011	0.006/0.006/ 0.005/0.005	0.019/0.017/ 0.017/0.017	0.012/0.011/ 0.011/0.012	0.013/0.012/ 0.013/0.013
Total water column, cm	3.706	2.473	3.130	3.381	3.305	3.116	3.092	4.050	3.435

* at 440/675/870/1020 nm

3.4.1. SEA aerosol cluster analysis

Daily observation frequency of the aerosol clusters seen in Table 3.2 indicated that Cluster B1 (52%) and B2 (47%) were dominant at Bac Giang; M1 (73%) and M2 (16%) were dominant at Mukdahan; P1 (78.5%) and P2 (15.5%) were dominant at Pimai; and S1 (44%), S2 (26%), and S3 (16%) were dominant at Silpakorn University. Based on their mean properties and the literature, the major SEA aerosol types were divided into three types: long-range transport urban/industrial aerosol, SEA biomass burning smoke, and SEA local urban/industrial aerosol.

Long-range Transport Urban/Industrial Aerosol

Cluster B1 had a mean *SSA* of 0.95 (440 nm); a mean $r_{eff,}$ r_v of 0.23, 0.26 and 2.46, 2.89 μm (for a fine- and a coarse-mode, respectively); an α of 1.27; and a mean refractive index of 1.403 - 0.007*i* (440 nm). This cluster is similar to urban/industrial aerosol as described by Dubuvik et al. (2002). High *SSA* found for this aerosol suggests a high organic carbon fraction (Mallet et al., 2003). Although sea salt also has a high *SSA* of about 0.994 (Remer et al., 2005), B1 was probably not sea salt because an aerosol similar to the B1 was also found at the inland sites, Mukdahan (M2) and Pimai (P2).

B1 and M2 often occurred from September to December when prevailing northeasterly winds frequently had trajectories from inland eastern China. P2 was also observed sporadically over this period. The high aerosol episodes, *AOD* > 1, accounted for 48%, 17%, and 9.6% of the total B1, M2, and P2 observations, respectively. Bac Giang, Mukdahan, and Pimai are rural, agricultural sites located away from highly developed

areas and are not urban/industrial sites, traditionally associated with urban/industrial aerosols. From the evidence that the occurrence of these high level aerosol episodes were more frequent at the Bac Giang site than at Mukdahan and Pimai sites, it is plausible that some of these aerosols originated from urbanized areas upwind from the Bac Giang, probably in eastern Asia.

While moving from China to SEA, a secondary aerosol could develop in the B1, M2, and P2 aerosols. This secondary aerosol increases the radiative scattering, resulting in a higher *SSA* and a lower *k* as in one case observed in the SEA aerosol optical properties along the air trajectory shown in Figure 3.3. Such a significant contribution of secondary aerosols in the plume downwind of mega-cities in China has been reported in previous studies (Chan and Yao, 2008; Chuang et al., 2008). Chuang et al. (2008) performed a simulation and founded a significant secondary sulfate aerosol formation in NE Chinese polluted air masses during their transport southward to Taiwan. The same formation could have occurred over SEA as well.

From these findings, we agree with the conclusion drawn by Remer et al. (2005) on the dominance of the urban/industrial-like aerosol over SEA during the dry season from September to December.

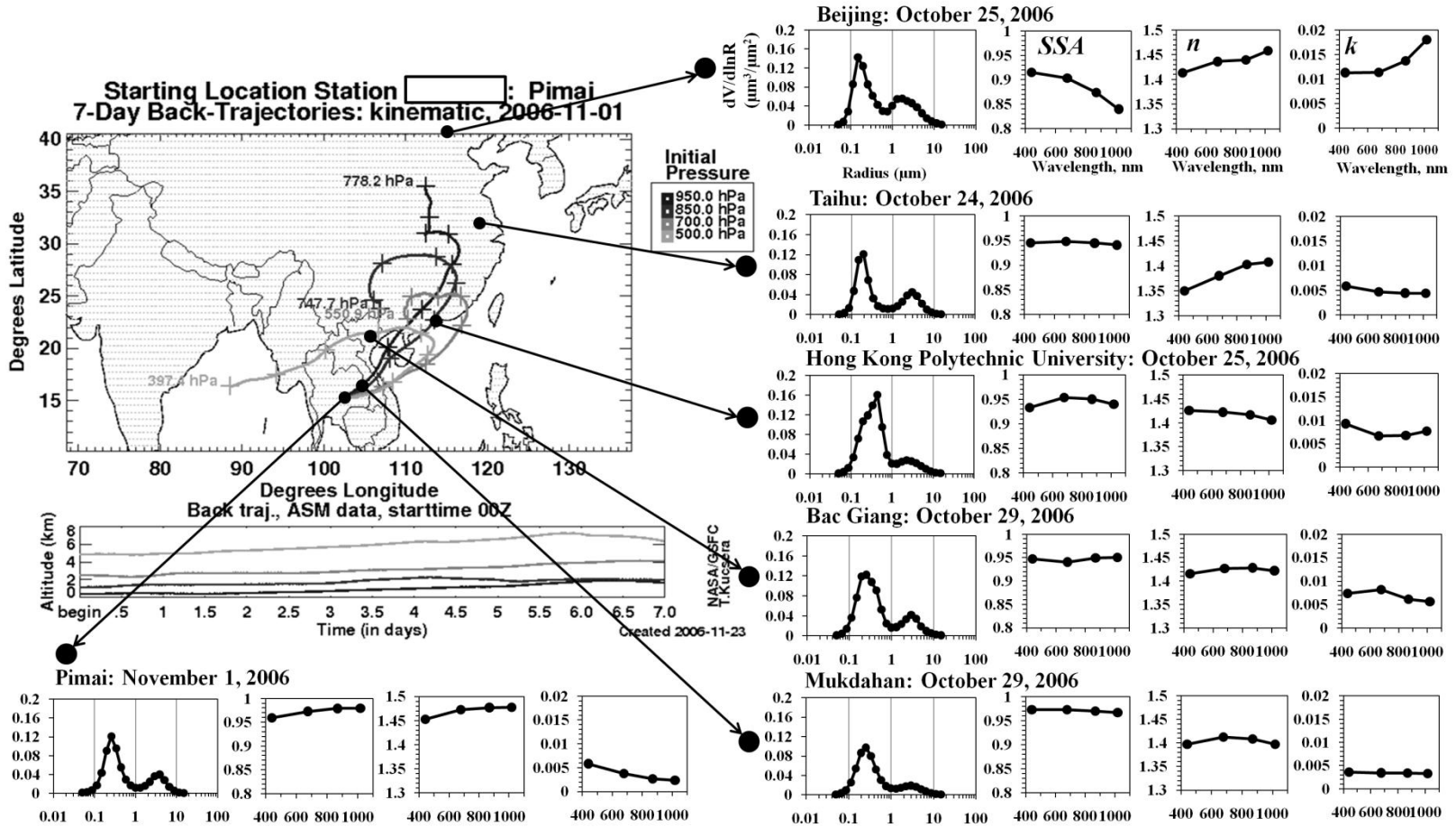

Figure 3.3. 7-day back trajectories at Pimai station on November 1, 2006, acquired from http://aeronet.gsfc.nasa.gov/, and the aerosol size distribution (dV(volume)/dlnR(radius); $\mu m^3/\mu m^2$), spectral *SSA* (unitless), real–part of refractive index (*n*-unitless), and imagery–part of refractive index (*k*-unitless) observed at the different stations along the trajectory pathway

Southeast Asian Biomass Burning Smoke

For B2, M1, P1, and S2, *SSA*s were similar to biomass burning smoke observed over the South American Cerrado, in Brazil [0.91, 440 nm] and over the African savanna, in Zambia [0.88, 440 nm] (Dubovik et al., 2002). These *SSA*s also agreed with the biomass burning smoke reported over South Korea [0.89 ± 0.01, 550 nm (Kim et al., 2006)] and over Thessaloniki, Greece [0.9, 340 nm (Balis et al., 2003)]. Their r_v [~0.19 μm: fine, ~3 μm: coarse] also agree with the smoke reported in Dubovik et al. (2002). This aerosol type exhibited a lower *SSA* and a higher refractive index (especially in the imaginary-part, ranging from 0.012 to 0.014 at 440 nm) than the previous long-range urban/industrial cluster, probably due to a higher portion of soot (Mallet et al., 2003). The aerosol occurred in the dry season from November to mid-May, which is dominated by northeasterly winds. The aerosol accounted for 25%, 76%, 78%, and 26% of the total observations at Bac Giang, Mukdahan, Pimai, and Silpakorn University, respectively.

Southeast Asian Local Urban/Industrial Aerosol

Cluster S1 was observed from December to April, when elevated black carbon concentration, mainly from agricultural burning emissions, has been observed over SEA continent (Uno et al., 2003). This aerosol, however, was not previously assigned in this study to the biomass burning smoke because it exhibited a significant lower mean *SSA* of 0.88 (440 nm) and a higher refractive index of 1.470 - 0.02*i* (440 nm). These implied that S1 had a significantly high portion of soot (Mallet et al., 2003). These values were similar to the ones of the urban/industrial aerosol from Mexico City [*SSA* = 0.90 ± 0.02, *n* = 1.47

± 0.03, k = 0.014 ± 0.06 all at 440 nm (Dubovik et al., 2002)]. Dubovik et al. (2002) indicated that this real-part of refractive index, n, of the aerosol from Mexico City was higher than those from GSFC, Greenbelt (MD) and Crete-Paris (France) and they related this finding to higher concentrations of black carbon over Mexico City. In comparison with the major aerosol clusters, S1 aerosol was the smallest and roughest in fine-mode as indicated from the smallest mean fine-mode r_{eff} and r_v and mean fine-mode asymmetry factor. Currently, studies on the optical properties of the urban aerosol from central Thailand are not available for comparison. Due to its exclusive appearance at the site adjacent to an urban area and its properties resembling those of the aerosol from Mexico City, S1 aerosol is more likely to be a local urban/industrial aerosol. This aerosol, however, was not usually found in high aerosol events.

Chueinta et al. (2000) conducted positive matrix factorization on elemental compositions of atmospheric aerosols from urban and suburban areas in central Thailand. Their results show that soil, vehicle emissions, and sea salt are the major sources of the aerosols for December to April and biomass burning (stated as charcoal/wood burning in Chueinta et al. (2000)) is more dominant in the suburban area. Silpakorn University is more suburban. Based on the findings from the literature, S1 aerosol could be a mixture of biomass burning emissions, soil, vehicle emissions, and sea salt.

Cluster S3 exhibited similar light scattering properties to S1 but was different in size/shape. Cluster S3 aerosol exhibited a higher coarse-mode fraction, as indicated by a lower α (1.274) and a larger fine-mode size (0.192 and 0.224 µm for a mean r_{eff} and r_v,

respectively), and it was fairly round as shown by asymmetry factor of 0.92 (440 nm). Road dust/soil dust plays a major role in a coarse-mode fraction of a typical urban/industrial dust, such as that observed in the Bangkok metropolitan area in central Thailand (Wangkiat et al., 2004). The highest monthly wind speeds were 4 to 5 m/s observed from October to January (Pongkiatkul and Oanh, 2007), occurring when S3 was found as shown in Figure 3.4. Cluster S3, therefore, was plausibly a local urban/industrial aerosol with a higher fraction of road dust/soil dust. This hypothesis agrees with the conclusion from the aerosol study conducted in Bangkok by Wangkiat et al. (2004).

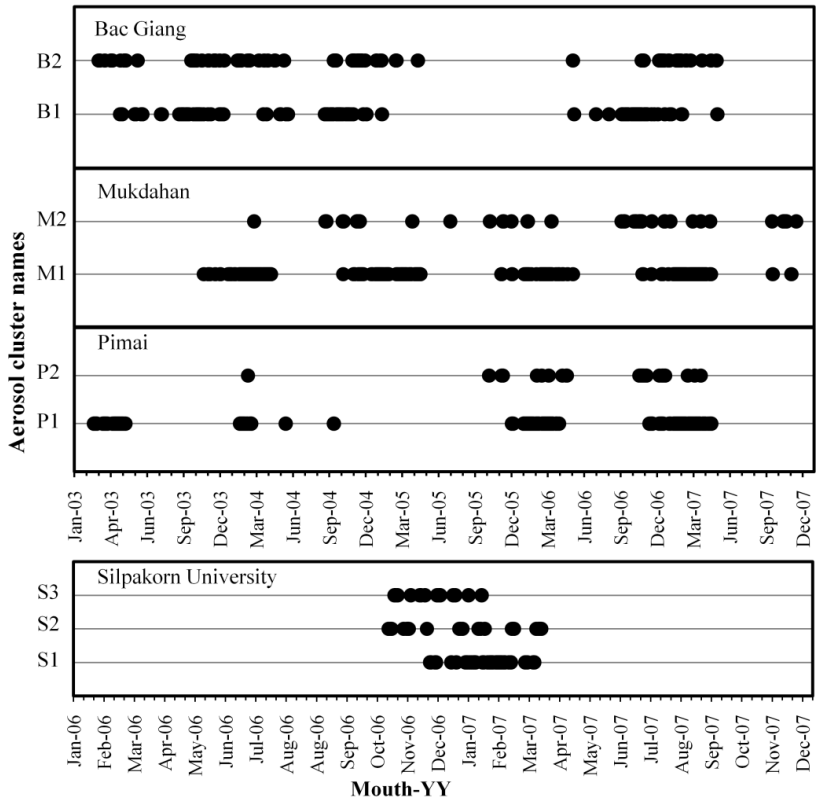

Figure 3.4. Temporal distribution of the aerosol clusters observed over the four sites

3.4.2. Canonical discriminant function analysis

In cases where there are a few outliers accounting for a large portion of the total variability in the data set, the first canonical function tends to discriminate against these outliners from the rest and shows small variability among observations in the majority group. Therefore, this function is not always useful to discriminate the major clusters; whereas, the second and/or third functions might be (a) better discriminator(s). Figure 3.5 shows the plots of the pairs of the selected canonical functions for each site. These plots show that two dominant aerosol clusters for Bac Giang (B1 and B2) were well separated by CAN2-B. Two dominant aerosol clusters for Mukdahan (M1 and M2) were also observed and those were well separated by CAN2-M. At Pimai station, two dominant aerosol clusters (P1 and P2) were well separated by both CAN1-P and CAN3-P. Aerosol clusters at Silpakorn University were observed in three or more groups, and those were well separated by CAN1-S and CAN2-S. The total sample correlations between the canonical functions and the original variables are presented in Table 3.3. By considering the high correlations (those outside the range -0.5 to 0.5) shown in Table 3.3, it appeared these the canonical functions can be described as following;

- CAN2-B: High *SSA*, high fine-mode *g*, large fine-mode r_{eff} and r_v, and low *n* and *k*,
- CAN2-M: High *SSA*, high fine-mode *g*, large fine-mode r_{eff} and r_v, and low *k* (particularly for short visible wavelengths), low α,

- CAN1-P: High α, high k (particularly for short visible wavelengths), and low *SSA*,
- CAN3-P: High *SSA*, high fine-mode g (particularly for short visible wavelengths), large fine-mode r_{eff} and r_v, and low n (particularly for near infrared wavelengths),
- CAN1-S: High *SSA*, high fine-mode g, large fine-mode r_{eff} and r_v, and low n and k,
- CAN2-S: High coarse-mode g, large coarse-mode r_{eff} and r_v, and low α.

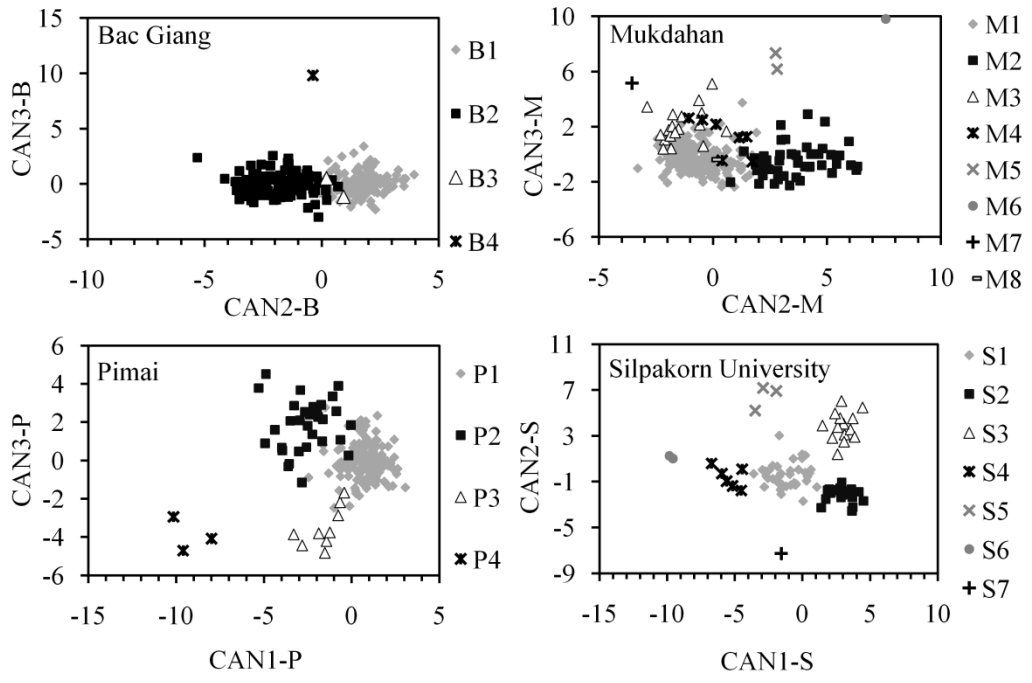

Figure 3.5. The plots of values from two dominant canonical functions for each site. The CAN variables are in arbitrary unit

Table 3.3. Total-sample correlations between the selected canonical functions, which gave the well dominant aerosol clusters separation, and the original twenty-six variables for each site

	Bac Giang	Mukdahan	Pimai		Silpakorn U.	
Variables	CAN2-B	CAN2-M	CAN1-P	CAN3-P	CAN1-S	CAN2-S
Total water column	0.62	0.15	0.00	-0.07	0.38	-0.06
α for 870-440 nm	-0.46	-0.62	0.69	0.19	-0.28	-0.53
SSA at 440 nm	0.89	0.63	-0.52	0.55	0.80	-0.20
SSA at 675 nm	0.85	0.63	-0.50	0.63	0.79	-0.15
SSA at 870 nm	0.77	0.60	-0.49	0.63	0.76	-0.12
SSA at 1020 nm	0.72	0.60	-0.50	0.61	0.74	-0.10
n at 440 nm	-0.35	-0.30	-0.07	-0.40	-0.62	0.26
n at 675 nm	-0.52	-0.38	-0.10	-0.47	-0.72	0.25
n at 870 nm	-0.62	-0.38	-0.10	-0.51	-0.74	0.25
n at 1020 nm	-0.62	-0.37	-0.19	-0.53	-0.73	0.25
k at 470 nm	-0.81	-0.63	0.57	-0.36	-0.79	0.12
k at 675 nm	-0.66	-0.55	0.55	-0.43	-0.79	0.19
k at 870 nm	-0.55	-0.44	0.49	-0.47	-0.77	0.21
k at 1020 nm	-0.47	-0.40	0.45	-0.48	-0.75	0.23
g-F at 440 nm	0.87	0.61	-0.09	0.73	0.83	0.10
g-F at 670 nm	0.81	0.67	-0.24	0.54	0.74	0.42
g-F at 870 nm	0.76	0.68	-0.31	0.41	0.66	0.57
g-F at 1020 nm	0.73	0.69	-0.34	0.31	0.60	0.64
g-C at 440 nm	-0.34	-0.16	0.34	-0.21	-0.02	0.65
g-C at 675 nm	-0.17	-0.04	0.20	-0.33	0.07	0.68
g-C at 870 nm	-0.03	0.02	0.12	-0.39	0.08	0.65
g-C at 1020 nm	0.08	0.02	0.14	-0.39	0.08	0.60
r_{eff}-F	0.78	0.72	-0.34	0.56	0.66	0.46
r_v-F	0.77	0.73	-0.36	0.46	0.63	0.58
r_{eff}-C	0.36	0.44	-0.40	-0.31	0.16	0.66
r_v-C	0.30	0.37	-0.46	-0.40	0.00	0.62

Note: The canonical function can be described by the original variables which exhibit high positive (close to 1) or negative correlation (close to -1).

There were similarities among CAN2-B, CAN2-M, CAN3-P, and CAN1-S, suggesting that these canonical functions were key in distinguishing the dominant SEA aerosol clusters. Their higher value for these canonical variables indicates the dominance of the aerosol exhibiting a high *SSA*, a high fine-mode *g*, a large fine-mode r_{eff} and $r_{v,}$, and a low refractive index. CAN1-P and CAN2-S were the additional canonical functions, useful for distinguishing the aerosol clusters at the Pimai station and at the Silpakorn University station, respectively. CAN1-P related to the fraction of black carbon in the aerosol, indicated by its high correlation with a high imaginary-part refractive index, a low *SSA*, and a large fine-mode fraction (Mallet et al., 2003). CAN2-S was sensitive to size, shape, and magnitude of the coarse-mode aerosols. The high value of this CAN2-S was observed for S3, as seen in Figure 3.5, indicating to coarse-mode dominant aerosol, probably road dust and soil dust which are the typical coarse-mode aerosol observed in urban areas (Mallet et al., 2003; Chow et al., 2004).

3.5. CONCLUSION

During NE prevailing winds from mid-September to December, the aerosol exposure events were most frequently observed over the upwind station, Bac Giang, and less often over the downwind stations, Mukdahan, Pimai, and Silpakorn University. The aerosols observed during this time at Bac Giang, Mukdahan, and Pimai exhibited a *SSA* of about 0.95 (440 nm), a lower refractive index, and a larger fine-mode size. These optical properties were similar to the urban/industrial aerosol reported in literature. Based on

observing frequency and air back trajectory analyses, this aerosol could be from urbanized areas upwind from Bac Giang, probably in eastern China.

From January to April, a biomass-burning aerosol dominated at all four stations. Compared to the previous aerosol cluster, this aerosol exhibited a lower *SSA* of about 0.90, a higher refractive index, and a lower fine-mode size. These optical properties were similar to the aerosols from biomass burning reported in the literature.

The SEA urbanized aerosol, as represented by the aerosol from Silpakorn University, exhibited a mean *SSA* of about 0.90 (440 nm) or lower. This *SSA* was similar to that previously found in Mexico City (Dubovik et al., 2002). Coarse-mode aerosol, possibly road dust or soil dust, played a role at this site from October to January during high wind speed conditions.

The aerosol clustering can be visualized from the plots between the two selected canonical functions. The canonical functions having positively high *SSA*, high fine-mode *g*, large fine-mode r_{eff} and r_v, and low refractive index, were the key for distinguishing the dominant SEA aerosol clusters. In addition, a black carbon fraction and a coarse-mode size were additional factors for distinguishing the aerosol clusters at Pimai and the suburban station, respectively.

CHAPTER FOUR

OZONE MONITORING INSTRUMENT (OMI) SENSOR FOR BIOMASS-BURNING AEROSOL OPTICAL PROPERTIES

4.1. ABSTRACT

In this study, two small spatial-scale Greek forest fires (in 2007 and 2009) and two large-scale Southeast Asia continent fires (in 2005 and 2007) were investigated. Appropriateness of using Ozone Monitoring Instrument (OMI) aerosol products was evaluated for each fire episode from comparisons between the results obtained from multivariate analyses of the OMI products and those obtained from collocated ground-measured Aerosol Robotic Network (AERONET) data, from the Atmospheric Infrared Sounder (AIRS) total column CO, and from the Moderate Resolution Imaging Spectroradiometer (MODIS) active fire detections. OMI aerosol optical depth (*AOD*) tended to overestimate the AERONET *AOD* up to nearly four times. For the small-scale fires, OMI single-scattering albedo (*SSA*) values provide contradictory conclusions on radiative forcing potential of the aerosol to the AERONET *SSA*. For the large-scale fires, the OMI absorbing Angström exponent (α_a), corresponding to aerosol size, and *SSA* from both OMI and AERONET data sets were largely comparable. Positive correlation between OMI *AOD* and AIRS CO was found for one large-scale fire. Good relations between the MODIS active fire detection and OMI aerosol properties were observed for both large-scale fires. The good agreement, however, was limited for 1 < OMI *AOD* (442 nm) < 3.

4.2. INTRODUCTION

The Ozone Monitoring Instrument (OMI) is onboard the Aura satellite. Its aerosol products, including absorbing aerosol optical depth (*AAOD*) and UV-absorbing aerosol index, have been said to be useful in determining intrinsic aerosol properties and have been used to detect biomass burning smoke plumes (Jeong and Hsu, 2008; Badarinath et al., 2009; Hoff and Christopher, 2009). However, the OMI products have a relatively coarse spatial resolution of 13 × 24 km^2, which might be more susceptible to sub-pixel cloud contamination (Jeong and Hsu, 2008). These might decrease its sensitivity for biomass-burning aerosol detections and characterizations in some circumstances, such as small fire-affected areas contributing low aerosol loading over large spatial scale (Christopher et al., 2008; Jeong and Hsu, 2008).

The appropriateness of using the OMI aerosol products for biomass-burning aerosol detection and characterization was evaluated in this study using three lines of evidence. The first line is the comparison between the results from multivariate analyses of these products with the results obtained using ground-based AERONET measurements. The second line is the correlation between OMI *AOD* and the total atmospheric column CO acquired from Atmospheric Infrared Sounder (AIRS) onboard the AQUA satellite. The last line is spatial agreement between the biomass-burning aerosols determined from the OMI aerosol products and the Moderate Resolution Imaging Spectroradiometer (MODIS) active fire detections.

4.3. METHODOLOGY

4.3.1. Site description

Four forest fire/biomass burning episodes were considered in this study. These included two Greek forest fires in 2007 and 2009, and two SE Asian continent (SEA) biomass burnings and forest fires in 2005 and 2007. According to spatial coverage, the Greek fires were small-scale fires. The AERONET aerosol variables were acquired from Thessaloniki and Athens_NOA (the National Observatory of Athens) stations for the 2007 and 2009 events, respectively. The SEA fires were large-scale fires. The AERONET data were from the Mukdahan station for both 2005 and 2007 fire events; whereas, the data from Pimai station were also used for the 2007 fire. Locations of these four stations are shown in Figure 4.1. These AERONET stations are located adjacent to the hot spot grids, but they were not in the grids. Therefore, their data might not represent fresh biomass-burning aerosol. OMI aerosol variables and the MODIS active fire product were acquired over the grids covering biomass burning-affected areas and the AERONET stations.

Athens_NOA is located in Athens, Greece. Athens is central to economic, financial, political and cultural life in Greece. Thessaloniki is the second major city in Greece. Mukdahan is located in the Mekong valley in Northeast (NE) Thailand, which is surrounded by the agricultural lands, primarily rice paddies, and is adjacent to dense forests. Pimai is located in NE Thailand and surrounded by agricultural lands, primarily rice paddies.

In a typical summer, Mediterranean shrublands are often affected by wildfires (Dimitrakopoulos, 2002). In summer 2007, wildfires were more extensive and aggressive due to a stable heat wave and dry conditions (Xanthopoulos, 2009; Kaskaoutis et al., 2011). Burned areas included the parts of Greece, Albania, and southern Italy (Kaskaoutis et al., 2011). More than 270,000 ha of vegetation lands were affected by the fire (Xanthopoulos, 2009). Compared to the 2007 Greek fire, Greek wildfires in summer 2009 burned smaller areas, ~20,000 ha, and were shorter in duration, 4 days (Xanthopoulos, 2009). The fires, however, were important because it caused significant impact in Athens.

In the mainland SEA region, fires from agricultural land clearing and slash-and-burn are widely and often observed during the late-dry season, February to April, covering the two SEA fire episodes. Many of these fires occur within forest ecosystems. Land covers relating to SEA forest fire activities include open savanna woodlands, grasslands, rice paddies, and other permanent crop lands (Jones, 1998; Johnson and Dearden, 2009).

4.3.2. Data description

Four data sets used in this study include AERONET aerosol inversion products, the aerosol products from OMI, the total atmospheric column CO from AIRS, and active fire detection from MODIS. The AERONET aerosol variables at the four AERONET stations were acquired from the web-based data surgery tool available in the Aerosol Robotic Network website (http://aeronet.gsfc.nasa.gov/). The OMI aerosol variables and the AIRS total column CO were acquired from the Giovanni web-based database developed by

Goddard Earth Sciences Data and Information Services Center, GES DISC (available at http://disc.sci.gsfc.nasa.gov/giovanni/giovanni/overview). The time-series MODIS active fire products were from the Land Processes Distributed Active Archive Center, LA DAAC, website (https://lpdaac.usgs.gov/lpdaac/get_data/data_pool).

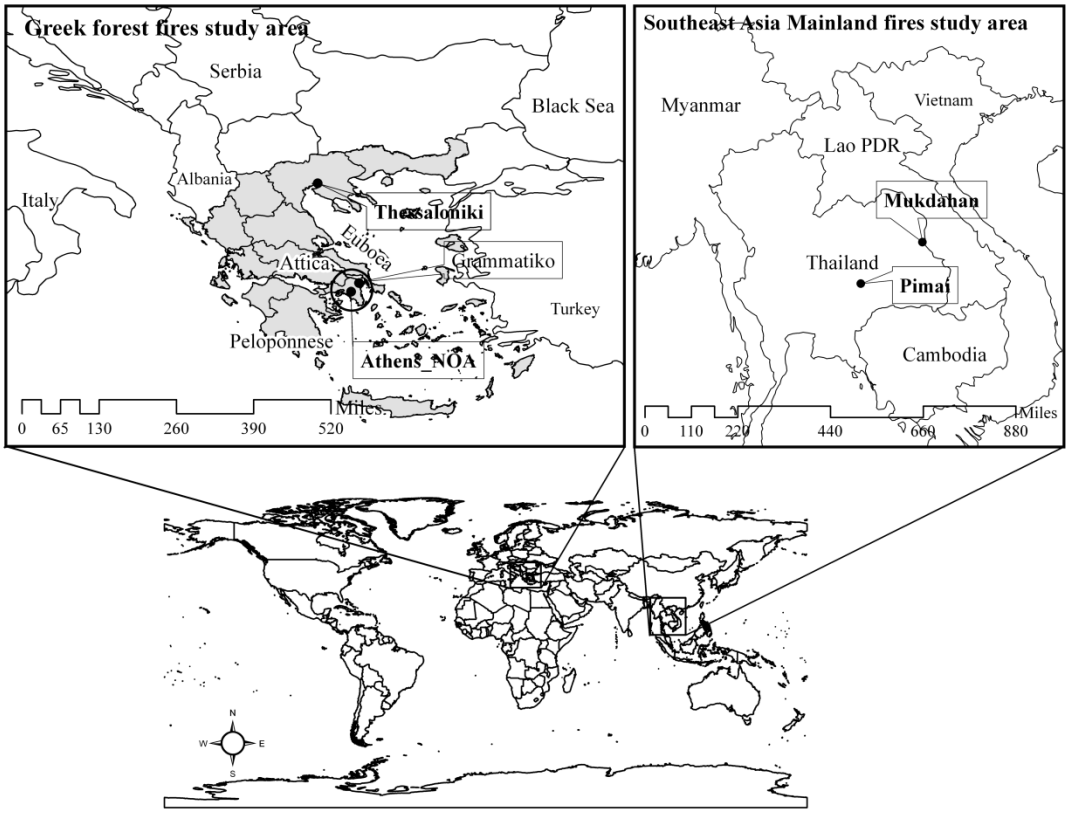

Figure 4.1. The Greek and SEA fires affected areas and locations of the four AERONET stations considered in this study

AERONET Cimel sun/sky-radiometers measure both the direct and diffuse radiation. These measurements and estimates of land and water surface reflectance were used in the inversion analysis to determine aerosol optical properties, called aerosol inversion

products (Dubovik and King, 2000). Seventeen AERONET variables were used in this study, including seven aerosol optical depths (*AOD*) at 340, 380, 440, 500, 675, 870, and 1020 nm, four absorbing *AOD*s (*AAOD*) at 440, 675, 870, and 1020 nm, four aerosol single-scattering albedos (*SSA*) at 440, 675, 870, 1020 nm, the extinction Angström exponent, α_e, and the absorbing Angström exponent, α_a. Both Angström exponents were evaluated for 870:440 nm. This data set features point measurements having the temporal resolution of fifteen minutes giving many measurements during the daytime.

OMI is a nadir-viewing spectrometer. The sensor is onboard the Aura satellite orbiting at 705 km and crossing the equator in an ascending orbit at 1:45 pm local time. The data represented daytime observation and were compared with all possible daily AERONET daytime measurements. It provides information on atmospheric composition, including aerosols, with a spatial resolution of 13 × 24 km^2 (level 2, swath) at nadir and daily global coverage. The OMI data sets used in this study are the daily $0.25^o \times 0.25^o$ (level 3e, ~25 km for longitude and 27.8 km for latitude) aerosol product version 3. Each grid cell has *AOD*, *AAOD*, and *SSA* for five wavelengths; 342.5, 388, 442, 463, and 483.5 nm. These products are estimated from the measured backscattering in seventeen selected wavelength bands between 330 and 500 nm, from near UV to visible. The UV absorbability of aerosol is enhanced due to increasing Rayleigh scattering by atmospheric gases. In the version 3 data retrieval algorithm, a set of two to three aerosol sub-type models was selected from the aerosol indices (a measure of the change in spectral contrast), geographic location, and season. Then, an appropriate model, providing least square error with observed radiation, was chosen (Torres et al., 2002).

The total atmospheric column CO acquired from AIRS, on Aqua satellite, was correlated with the OMI *AOD* in this study. AIRS estimates CO using radiative transmittance in the 4.50 to 4.58 μm band. The data are averaged and binned into $1^{o}\times1^{o}$ grid cells (~100 km for longitude, 111.2 km for latitude). Only the data for the daytime ascending orbit, crossing an equator at 1:30 pm from Southern Hemisphere to Northern Hemisphere (Olsen, 2007), were used in this study. These products are contained in the AIRS level 3 daily gridded standard retrieval product using combined infrared and microwave retrievals.

The active fire detection product in the MODIS Thermal Anomalies/Fire Daily Level 3 Global products, under the Terra mission, was acquired for this study. This is a 1-km gridded composite of fire pixels detected in each grid cell over each daily period. Active fires were evaluated from the variability of surface brightness temperature, derived MODIS radiances at 4 and 11 μm, compared to its background value. These fire observations are made twice a day at 10:30 am and 10:30 pm from Terra (Justice et al., 2006). Both daytime and nighttime measurements were used to evaluate the daily active fires.

4.3.3. Data processing

Angström exponents, both extinction and absorbing, indicate spectral sensitivity of aerosols and can be considered as aerosol size-related variables. Extinction Angström exponents smaller than unity usually indicate coarse-mode aerosols (Cheng et al., 2006). In this study for OMI retrievals, these variables are calculated from a spectral pair of

AOD and *AAOD* measurements for extinction and absorbing, respectively using equation 1.

$$\alpha_{483.5:442} = -\frac{\ln\left[\frac{(A)AOD_{483.5}}{(A)AOD_{442}}\right]}{\ln\left(\frac{483.5\,\text{nm}}{442\,\text{nm}}\right)} \qquad \text{(Eq.1)}$$

OMI α_e was calculated using OMI *AOD* at 442 and 483.5 nm, and OMI α_a was similarly calculated using OMI *AAOD*. The spectral *AAOD* to *AOD* ratio, *AAR*, was calculated and used for multivariate analyses. Higher *AAR* indicates higher radiative absorption of the aerosol and more potential for global warming.

Multivariate statistical analysis methods applied in this study are 1) factor analysis of aerosol variables obtained from AERONET and OMI/Aura, and 2) cluster analysis of aerosol factor scores obtained from the previous factor analysis of the aerosol factors. The analyses were done via SAS 9.2 software (SAS Institute Inc., Cary, NC).

Factor analyses using the Varimax rotation method on the correlation matrix of all the AERONET and separately on all the OMI/Aura aerosol variables, including *AOD*s, *AAR*s, *SSA*s, and *α*s, were performed to find a smaller number of uncorrelated functions, or underlying factors, that explain the relationship among the original aerosol variables. The analyses were run for each fire event. In Varimax rotation, a new orthogonal matrix is determined by maximizing sum of variance of squared loading vectors for all columns in this loading matrix. Each underlying factor has a theoretical mean of zero, variance of

unity, and is orthogonal to the others. These factors are significant aerosol characteristics capturing major variation of all aerosol variables observed in the systems.

Hierarchical cluster analysis using the Ward-minimum variance method was used in this study to identify the groups of different aerosol types dominating during the fire episodes. In this method, the distance between clusters is obtained from squaring the distance between cluster means and divided by the reciprocals of the number of points in each cluster. The observations are assigned to the clusters in which cluster sum of squares is minimized. The number of clusters was selected as yielding a relatively high pseudo-F statistic together with relatively low pseudo-T^2 statistic compared to among the nearby higher and lower cluster numbers.

The cluster analyses were run twice. First, the cluster analyses of aerosol factors were done separately for OMI and AERONET aerosol variables at commensurate locations and days. Each of the cluster results obtained from this analysis for both OMI and AERONET data sets were paired on the basis of temporal correspondence to evaluate their agreement on aerosol type classification. Second, a cluster analysis of those OMI aerosol variables was done using the spatial observations acquired over the biomass burning affected areas on selected fire days with significant data available. Then, the aerosol clusters obtained from the second analysis were associated with the commensurate MODIS active fire detections.

4.4. RESULTS AND DISCUSSION

4.4.1. Factor analysis of AERONET and OMI aerosol variables

Three underlying factors were identified in the factor analysis. The factor loading patterns of these three factors for both the AERONET and the OMI data sets were similar, which indicates similar variation and relationships among aerosol variables from both data sets. Considering high factor loading values (> 0.6), the first factor, having eigenvalues of 7.73 and 9.81 for the AERONET and OMI, respectively, loaded positively on the *SSA*s and negatively on the *AAR*s. The second factor, having eigenvalues of 6.9 and 5.2 for AERONET and OMI, respectively, loaded positively on the *AOD*s. The third factor, having eigenvalues of 1.44 for both data sets, loaded positively on α_e and α_a. Total communalities were 16.1 and 16.4 out of total 17 variables used in the analyses for AERONET and OMI data sets, respectively. These indicate similarly high overall-performance of using these three factors to explain both aerosol data sets.

4.4.2. Comparison between the biomass-burning aerosol properties estimated from the multivariate analyses of AERONET and OMI/Aura aerosol products

The mean aerosol variables for each aerosol cluster obtained from the cluster analyses of OMI aerosol factor scores and AERONET aerosol factor scores are shown in Table 4.1 and their corresponding temporal distributions are in Figure 4.2. The aerosol properties discussed here are the mean AERONET aerosol variables at 440 nm and the mean OMI aerosol variables at 442 nm. *AOD* greater than unity was used in this study to indicate high aerosol levels, potentially contributed from biomass burnings or forest fires. In Table 4.1 for the 2007 Greek aerosols, for example, the cluster analysis of the AERONET aerosol variables resulted in four aerosol clusters, which are AER7-G1

through AER7-G4. The separate analysis of the OMI variables resulted in three clusters, which are OMI7-G1 through OMI7-G3. There is no *a priori* correspondence of AER7-G1 and OMI7-G1, etc.

Both Angström exponents (α_e and α_a) from AERONET and OMI were based on different spectral pairs (870:440 nm and 483.5:442 nm, respectively). There was no significant correlation between the Angström exponents obtained from both data sets in the same day. Analysis of variance, however, failed to reject a hypothesis of equal mean α_a from both data sets with 0.05 significance level for most fire episodes, except for the 2009 Greek fire; but it resulted the all cases being rejected for α_e. Therefore, the comparisons on Angström exponents and aerosol size used in this study are referred on α_a and coarse-mode dominant aerosols were assumed to have $\alpha_a < 0.75$.

2007 Greek Forest-fire Aerosol

The 2007 Greek forest-fire episode occurred in summer months covering July and August. The fires broke out in the Peloponnese region of Greece (Kaskaoutis et al., 2011). Three high AOD days on August 1, 20, and September 1 were observed at the Thessaloniki AERONET station located quite far away from the hot spot areas. Therefore, these aerosols with high AOD were less associated with the Greek fire, but they were more associated with biomass-burning aerosols from inland Europe flowing into Greece due to the prevailing N to NE winds (Liu et al., 2009). Additionally, on September 1, prevailing westerly winds blew urban/industrial pollution from Italy and Western Europe to Greece (Liu et al., 2009).

Table 4.2 shows frequencies of coincidence for each reciprocal pair between the OMI clusters and the AERONET clusters. Based on the results obtained from Table 4.2 and the temporal analysis, three areas of agreement between the OMI and the AERONET aerosol clusters were observed.

Table 4.1. The mean value of the optical properties of the aerosol clusters obtained from cluster analyses of time-series OMI and AERONET aerosol variables

	2007 Greek forest-fire episode				2009 Greek forest-fire episode				
AERONET *	AER7-G1	AER7-G2	AER7-G3	AER7-G4	AER9-G1	AER9-G2	AER9-G3	AER9-G4	AER9-G5
No. Obs.	16	11	10	9	69	44	17	13	13
AOD	0.57	0.83	0.45	0.46	0.24	0.17	0.44	0.31	0.13
SSA	0.96	0.94	0.92	0.92	0.86	0.79	0.87	0.81	0.71
AAR	0.04	0.06	0.08	0.08	0.14	0.21	0.13	0.19	0.29
α_e, α_a	1.85, 1.24	1.62, 1.33	0.90, 1.56	1.76, 1.11	1.57, 1.03	1.41, 0.93	1.71, 1.08	1.04, 1.21	1.26, 0.90
OMI **	OMI7-G1	OMI7-G2	OMI7-G3		OMI9-G1	OMI9-G2	OMI9-G3		
No. Obs.	17	24	6		43	58	55		
AOD	1.08	0.58	0.46		0.2	0.66	0.33		
SSA	0.97	0.97	0.96		0.96	0.97	0.97		
AAR	0.03	0.03	0.04		0.04	0.03	0.03		
α_e, α_a	1.27, 1.22	1.27, 1.35	1.81, 1.26		1.91, 2.04	1.27, 1.24	1.27, 1.54		
	2005 SEA biomass-burning episode				2007 SEA biomass-burning episode				
AERONET *	AER5-SEA1	AER5-SEA2	AER5-SEA3	AER5-SEA4	AER7-SEA1	AER7-SEA2	AER7-SEA3	AER7-SEA4	AER7-SEA5
No. Obs.	39	45	43	11	93	136	54	17	45
AOD	0.42	1.07	0.9	1.86	0.6	0.64	0.49	0.31	1.42
SSA	0.89	0.91	0.87	0.89	0.88	0.9	0.92	0.87	0.91
AAR	0.11	0.09	0.13	0.11	0.12	0.09	0.08	0.14	0.09
α_e, α_a	1.30, 0.86	1.49, 1.15	1.59, 1.20	1.63, 1.37	1.58, 1.16	1.49, 1.24	1.11, 0.99	1.09, 0.44	1.54, 1.32
OMI **	OMI5-SEA1	OMI5-SEA2	OMI5-SEA3	OMI5-SEA4	OMI7-SEA1	OMI7-SEA2	OMI7-SEA3	OMI7-SEA4	OMI7-SEA5
No. Obs.	40	44	44	16	89	98	81	31	48
AOD	0.74	1.8	1.57	3.8	1.23	1.11	0.67	0.33	3.12
SSA	0.95	0.89	0.88	0.93	0.87	0.87	0.95	0.94	0.93
AAR	0.05	0.11	0.12	0.07	0.14	0.13	0.05	0.06	0.07
α_e, α_a	1.04, 1.15	1.71, 1.14	0.96, 1.05	1.40, 1.17	1.64, 1.18	0.96, 1.00	1.10, 1.18	1.82, 1.74	1.56, 1.17

* *AOD*, *SSA*, and *AAR* at 440 nm; α_e and α_a for 870: 440 nm

** *AOD*, *SSA*, and *AAR* at 442 nm; α_e and α_a for 483.5: 442 nm

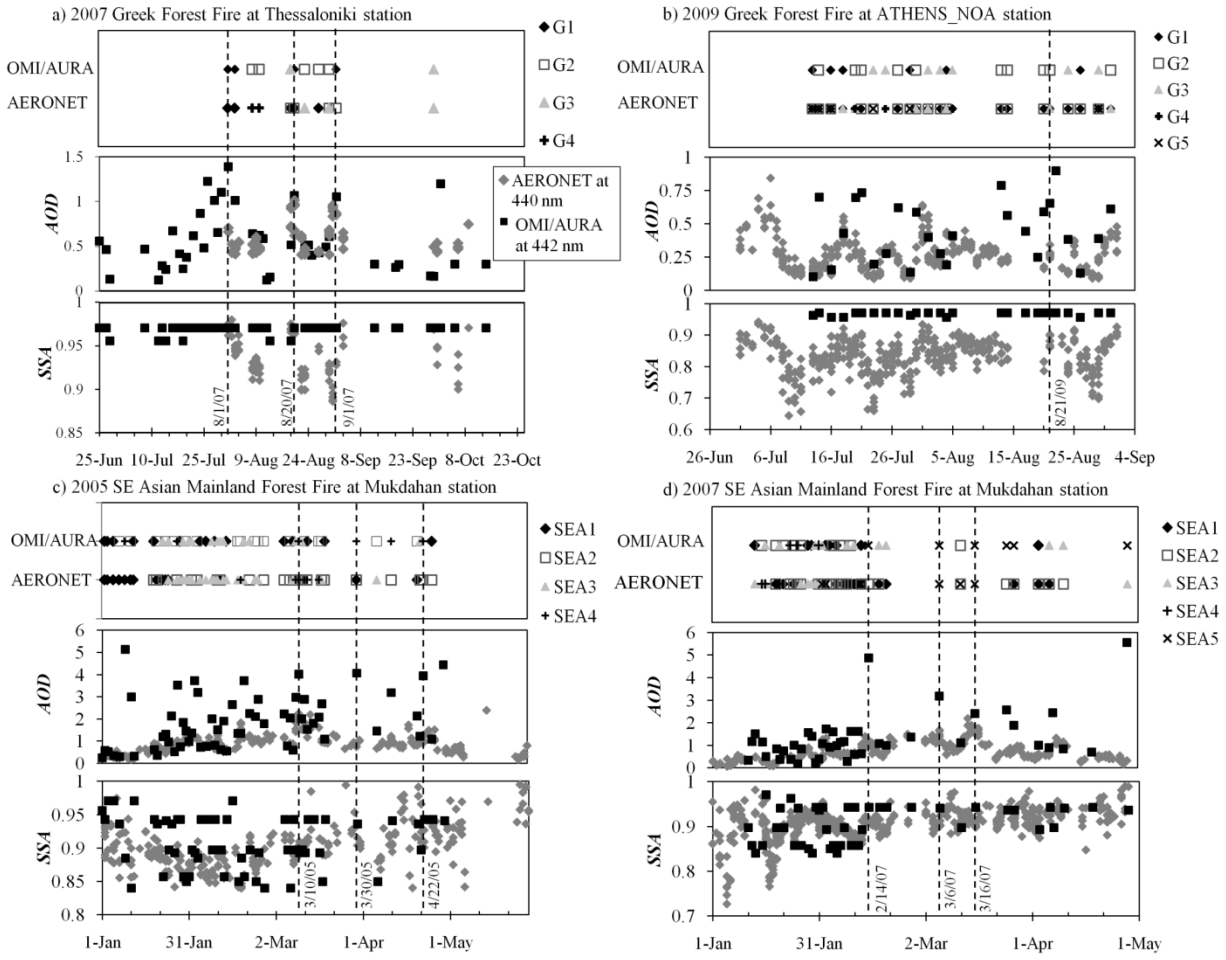

Figure. 4.2. Time-series plots of the aerosol clusters and their selected optical properties for each fire episode

First, 69% and 50% of the OMI clusters, OMI7-G1 and -G3, respectively, were classified with AERONET cluster AER7-G1. With comparatively high aerosol loadings, these aerosol clusters were assumed to be aerosol attributed to 2007 Greek forest fire. Both OMI clusters, OMI7-G1 and -G3, exhibited similar high light scattering properties (*SSA* of 0.97 and 0.96) and similar size characteristics (α_a of 1.22 and 1.26, respectively). OMI7-G1, however, had significant higher aerosol loading than the OMI7-G3; with *AOD* of 1.08 and 0.46, respectively. AER7-G1 (*AOD* = 0.57, *SSA* = 0.96, and α_a = 1.24) were

more similar to OMI7-G3. The temporal distribution of the 2007 Greek forest-fire aerosol clusters shows that correspondences among these AERONET and OMI aerosol clusters were found early in the fire episode, corresponding with prevailing N to NE winds (Liu et al., 2009).

Second, late in the fire episode, OMI7-G1 corresponded with AER7-G2. Based on temporal occurrences, these aerosol clusters had been attributed to the 2007 Greek forest fire mixed with urban/industrial pollution (Liu et al., 2009). Both aerosol clusters had slightly different properties. The cluster from AERONET (*AOD* = 0.83, *SSA* = 0.94, and α_a = 1.33) had lower aerosol loading, lower scattering, and higher α_a.

Third, the frequencies of coincidence also show that 75% of OMI7-G2 was classified with either AER7-G3 or -G4. These aerosol clusters exhibited *AOD* lower than unity. The radiative scattering potential obtained from the AERONET (*SSA* = 0.92 for both AER7-G3 and -G4) was significantly lower than the one from OMI (*SSA* = 0.97).

Kaskaoutis et al. (2010) observed long-term spatial distributions of OMI UV-absorbing aerosol index (*AI*), which is the residue between the measured radiance and the calculated one using the Lambert equivalent reflectivity assumption (Badarinath et al., 2009), over Greece. They found strong south-to-north gradients but insignificant west-to-east gradients. The dominance of negative *AI* values, suggesting non-absorbing aerosols, was found over northern Greece in the typical summer months (not during fire episodes). Based on the OMI *AI* values, they hypothesized that these aerosols were sulfate and sea salt (Badarinath et al., 2009). This finding was consistent with the observing consistently

high OMI *SSA* over the Thessaloniki station in this study. However, this OMI *SSA* value did not correspond well with those from AERONET measured on high *AOD* days during the 2007 Greek fire episode. This suggests that the OMI aerosol retrievals were influenced by the presence of biomass-burning aerosols from the fire.

Table 4.2. Frequencies of coincidence between the clusters evaluated from the OMI and the AERONET aerosol variables observing in the same day

Row %, Col. %	2007 Greek biomass burning episode		
	OMI7-G1	OMI7-G2	OMI7-G3
AER7-G1	69, 69	12, 8	19, 50
AER7-G2	46, 31	36, 17	18, 33
AER7-G3	0, 0	90, 37	10, 17
AER7-G4	0, 0	100, 38	0, 0

Row %, Col. %	2009 Greek biomass burning episode		
	OMI9-G1	OMI9-G2	OMI9-G3
AER9-G1	23, 37	57, 67	20, 25
AER9-G2	30, 30	27, 21	43, 35
AER9-G3	47, 19	29, 8	24, 7
AER9-G4	0, 0	8, 2	92, 22
AER9-G5	46, 14	8, 2	46, 11

Row %, Col. %	2005 SEA biomass burning episode			
	OMI5-SEA1	OMI5-SEA2	OMI5-SEA3	OMI5-SEA4
AER5-SEA1	31, 32	38, 36	26, 23	5, 13
AER5-SEA2	22, 27	22, 24	36, 36	20, 60
AER5-SEA3	32, 38	26, 26	40, 39	2, 7
AER5-SEA4	9, 3	55, 14	9, 2	27, 20

Row %, Col. %	2007 SEA biomass burning episode				
	OMI7-SEA1	OMI7-SEA2	OMI7-SEA3	OMI7-SEA4	OMI7-SEA5
AER7-SEA1	23, 23	40, 38	31, 36	2, 6	4, 8
AER7-SEA2	24, 36	27, 38	21, 36	15, 65	13, 38
AER7-SEA3	39, 24	20, 12	22, 15	17, 29	2, 2
AER7-SEA4	0, 0	59, 10	35, 8	0, 0	6, 2
AER7-SEA5	33, 17	5, 2	9, 5	0, 0	53, 50

2009 Greek Forest-fire Aerosol

The 2009 Greek wildfires started in June and then faded away. The fires, however, reoccurred in Grammatik, approximately 35 km northeast of Athens on August 21 and spread quickly towards the suburbs of Athens. The fire episode ended on August 25 (Xanthopoulos, 2009). AERONET observation of high aerosol levels on August 21 should be attributed to the fire. This observation was classified with OMI9-G2 and with AER9-G1 together with -G3 (see Figure 4.2).

The frequency of coincidence shows that 67% of OMI9-G2 was classified with AER9-G1. The aerosol properties acquired from the OMI and the AERONET were significantly different. The OMI exhibited higher *AOD* (0.66), *SSA* (0.97), and α_a (1.24) than AERONET (*AOD* = 0.24, *SSA* = 0.86, α_a = 1.03). From the temporal distribution of aerosol variables, the AERONET *AOD* did not significantly increase during the fire; whereas the OMI *AOD* increased due to the fire. Similar to the 2007 Greek fire, the OMI *SSA*s were 0.96 or 0.97 across the clusters; whereas the AERONET *SSA*s indicated strongly absorbing aerosols, with mean *SSA* ranging from 0.71 to 0.87, dominating throughout the fire episode. These similar highly absorbing aerosols were previously found over Peloponnese region during the 2007 Greek fire (Kaskaoutis et al., 2011). Therefore, they should be the biomass-burning aerosol from the 2009 Greek fires.

Even though temporal OMI *AOD* profiles related to the appearances of both Greek fires, OMI *SSA* was not. The OMI *SSA* over the Greek stations had only two values, 0.96 and 0.97, for entire study period. These values did not always agree with the ground observations during the Greek fires. This probably resulted from poor sensitivity of the sensor to detect the small-scale fire aerosols and/or ineffectiveness of aerosol models in the OMI aerosol algorithm to represent the actual biomass-burning aerosol properties. This inconsistency in *SSA* values results in contradictory conclusions on radiative forcing potential of the Greek forest fire aerosols based on OMI versus AERONET.

Kaskaoutis et al. (2011) used spatial OMI aerosol retrieval products, including *AOD*, *AAOD*, *SSA*, and UV *AI*, to simulate large-scale climatology effects associated with

aerosols from the 2007 Greek fire. However the results from our study showed that interpreting aerosol radiative forcing potential from OMI data was not always consistent with those from the ground measurement for this fire. Therefore, the conclusion drawn by Kaskaoutis et al. (2011) may have large uncertainty.

2005 SEA Biomass-burning Aerosol

From the temporal plots of 2005 SEA aerosol properties, the OMI *AOD* peak coincided with the AERONET *AOD* peak on March 10. The cluster analysis revealed the aerosol on this day was OMI5-SEA4 and AER5-SEA4. Both aerosol clusters exhibited high *AOD* (3.80 and 1.86 for these acquired from OMI and AERONET, respectively). They were assumed to be aerosol from the 2005 SEA fires. OMI5-SEA4 had an *SSA* of 0.93, and an α_a of 1.17; whereas AER5-SEA4 had an *SSA* of 0.89, and an α_a of 1.37. The optical properties of both clusters differed but were in the range of neutral (corresponding to *SSA* of ~0.9) to slightly negative (corresponding to *SSA* of greater than 0.9) radiative forcing potential and were fine-mode aerosol. Only 20% of OMI5-SEA4 was classified with AER5-SEA4. Three additional pairs of OMI and AERONET aerosol clusters exhibited relatively high coincidence percentages and are discussed below:

1) The majority of OMI5-SEA4 observations (60%) were classified with AER5-SEA2. Mean *AOD* for the cluster from OMI was 3.5 times higher than the one from AERONET; however, both had a high-aerosol level, which is potentially attributable to the SEA fires. In addition, both exhibited slightly negative radiative forcing

potential and similar size characteristic (*SSA* = 0.93 and 0.91; α_a =1.17 and 1.15, for OMI5-SEA4 and AER5-SEA2, respectively)

2) The majority of the AER5-SEA4 observations (55%) were classified with OMI5-SEA2, and both had comparatively high aerosol loading (*AOD* = 1.86 and 1.80, respectively) and similar radiative scattering properties; with *SSA* of 0.89 and 0.89, respectively, indicating positive radiative forcing potential. The clusters had different size characteristics, but were dominated by fine particles (α_a = 1.37 and 1.14 for AER5-SEA4 and OMI5-SEA2, respectively). In addition, these aerosols were frequently observed from March to April 2005 during late biomass-burning episode (see Figure 4.2).

3) The frequencies of coincidence also show approximately forty percent correspondence between OMI5-SEA3 and AER5-SEA3. These aerosol clusters were frequently observed in the early fire episode from mid-January to February 2005. The low radiative scattering property acquired from OMI was similar to that from AERONET (*SSA* = 0.88 and 0.87, respectively), indicating radiative absorbing or positive radiative forcing potential. The cluster from OMI had a lower α_a than the one from AERONET (1.05 and 1.20, respectively), which indicates a coarser aerosol.

The 2005 SEA clusters showing high coincidence percentages also had mean *AOD* greater than unity. OMI5-SEA1 clusters having mean *AOD* < 1 were likely associated with either AER5-SEA1 (32%) or AER5-SEA3 (38%). However, *SSA*, which indicates radiative scattering potential, obtained from OMI (0.95) was significantly higher than the

ones from AERONET (0.89 and 0.87, for AER5-SEA1 and-SEA3, respectively). This difference in *SSA* leads to opposite conclusions on aerosol radiative forcing potential.

2007 SEA Biomass-burning Aerosol

Similar biomass-burning aerosol properties found in the 2005 SEA fire were also found here as described below:

- There was good agreement on aerosol properties for high-*AOD* clusters. For the 2007 aerosol clusters exhibiting the highest *AOD*, OMI7-SEA5 and AER7-SEA5, the frequency of coincidence shows that 50% of this OMI cluster was associated with the AERONET cluster. Similar with what was observed in the 2005 SEA fire, both aerosol clusters exhibited neutral to slightly non-absorbing and fine-mode size (*SSA* = 0.93 and 0.91; α_a = 1.17 and 1.32 for OMI7-SEA5 and AER7-SEA5, respectively). However, the *AOD* from the OMI was approximately 2.2 times higher than the *AOD* from the AERONET. This aerosol was frequently found late in a fire episode.
- There was good agreement on aerosol properties for strong radiative absorbing aerosol observed in the early fire event from January to mid-February. The aerosol properties acquired from OMI, OMI7-SEA2, and from AERONET, AER7-SEA1, had similar aerosol loadings (*AOD* = 1.11 and 0.60, respectively), radiative scattering properties (*SSA* = 0.87 and 0.88, respectively) and size characteristic (α_a = 1.00 and 1.16, respectively). The frequencies of coincidence show 38% of OMI7-SEA2 was associated with AER7-SEA1, and similarly vice versa.

The OMI7-SEA2 cluster also corresponded to the AERONET absorbing coarse-mode aerosol, assigned to AER7-SEA4 (*SSA* = 0.87 and α_a = 0.44). Fifty-nine percent of the AER7-SEA4 was classified with the OMI7-SEA2; however, the mean *AOD* from the OMI was 3.6 times higher than the mean *AOD* from the AERONET. Both AERONET clusters (AER7-SEA1 and AER7-SEA4) corresponding to OMI7-SEA2 exhibited different size characteristics based on their α_a values. Size dissimilarity was also occasionally found for other high coincidence pairs for the SEA aerosol clusters as shown earlier. Since the AERONET data are taken many times over daytime period, they can show more temporal aerosol size variations resulting from aerosol growth/production processes; whereas the OMI data, providing one daytime observation daily, cannot. Therefore, it is possible that the size inconsistency was from different temporal-resolution of the sensors.

- There was poor agreement on aerosol properties for low-*AOD* clusters. For OMI7-SEA4 exhibiting *AOD* lower than unity, 65% of observations were classified with AER7-SEA2. The cluster from OMI exhibited significant higher *SSA* and higher α_a than the cluster from AERONET (*SSA* = 0.94 and 0.90; α_a = 1.74 and 1.24, respectively).

From our findings, the OMI aerosol retrievals were often inconsistent with those from AERONET when aerosol loading is small. Christopher et al. (2008) also found that OMI aerosol retrievals showed poor agreement with daily *AOD* retrieved from the Multiangle Imaging Spectroradiometer (MISR) when MISR *AOD* is small, especially when it was

less than 0.2. Based on these findings, we suggest using OMI aerosol retrievals with OMI *AOD* > 1 for the studies concerning biomass-burning aerosol characterization.

4.4.3. Correlations between the OMI aerosol loading and the AIRS total column CO

Correlations between the AIRS total atmospheric column CO (x) and the coincident OMI *AOD* at 442 nm (y) were analyzed for each biomass-burning aerosol type. These correlations, however, were evaluated from small number observations ($4 \leq N \leq 14$) that were available during the fire episodes. Two aerosol clusters, assumed to be the Greek forest-fire aerosols (OMI7-G1 and OMI9-G2) due to their relatively high *AOD*, showed negative linear correlations between OMI *AOD* and AIRS total column CO, which was not expected for biomass-burning plumes.

For the 2005 SEA biomass-burning aerosols, significant positive correlations (Pearson correlation coefficient, $r_p = 0.77$; Spearman correlation coefficient, $r_s = 0.62$; N = 13; $p < 0.0001$) between the OMI *AOD* and the AIRS total column CO were found for OMI5-SEA3, but were negatively correlated for OMI5-SEA4 ($r_p = -0.49$; $r_s = -0.80$; N = 4; $p < 0.0001$). There was not a significant positive correlation between the OMI *AOD* and total column CO observed in the clusters assigned to the 2007 biomass-burning aerosols, OMI7-SEA2 and OMI7-SEA5. This indicates that using only the CO level from AIRS to identify biomass-burning aerosols may not be warranted.

The negative or poor correlations found in OMI5-SEA4 and OMI7-SEA5, which is assumed to be biomass-burning aerosol based on their very high *AOD* levels (OMI *AOD* = 3.80 and 3.12, respectively), could have resulted from a limitation of satellite detection

of surface air pollutants. High aerosol loading, especially from non-absorbing aerosols (*SSA* > 0.9), could prevent incoming radiative IR from transmitting through the aerosol layer and minimize the IR absorption by the CO within the layer. Although the dominant size of typical biomass-burning aerosol is fine mode (< 2.5 μm), these optically thick aerosols could prevent transmission of IR (4.5 to 4.58 μm) used for the CO sounding. Therefore, high aerosol loading plumes at hot spots or adjacent areas potentially affect the accuracy of surface gaseous and particulate pollutant retrieval. To avoid possible effects of the satellite sensor limitation, OMI *AOD* (440 nm) < 3 is tentatively suggested for uses in studies on the aerosol optical properties. This *AOD* < 3 was typically observed during many biomass burning episodes (Dubovik et al., 2002).

4.4.4. Spatio-temporal evaluations of biomass-burning aerosol estimated from OMI/Aura retrievals comparing with the MODIS active fire detection products

The MODIS active fire did not show many hot spots during both Greek forest fire episodes. Therefore, a comparison of OMI data with the MODIS active fire detections for these small-scale fire cases in Greece will not be discussed. Conclusions on the appropriateness of using the OMI aerosol products to represent the aerosol from small-scale fire are based solely on indications from the previous two lines of evidence.

Cluster analyses of OMI aerosol factors were done across the SEA biomass burning-affected areas on the selected days. For the 2005 SEA fire, these days are on February 12, 17, and 18. For the 2007 SEA fire, these days are February 10, 19, and March 7. The mean OMI aerosol variables for each aerosol cluster are given in Table 4.3 and the spatial

maps of the SEA aerosol clusters overlaid with the MODIS active fire detections are shown in Figure. 4.3.

Table 4.3. The mean value of the optical properties of the SEA aerosol clusters obtained from cluster analyses of the spatial OMI aerosol variables*

	2005 SEA biomass-burning aerosol					2007 SEA biomass-burning aerosol				
	SEA5-1	SEA5-2	SEA5-3	SEA5-4	SEA5-5	SEA7-1	SEA7-2	SEA7-3	SEA7-4	SEA7-5
No. Obs.	2096	843	2378	2130	137	2416	5560	3106	559	1154
AOD	0.63	2.28	0.55	0.6	0.13	0.81	0.65	0.73	3	0.31
SSA	0.96	0.89	0.87	0.88	0.94	0.88	0.87	0.95	0.91	0.94
AAR	0.04	0.11	0.13	0.12	0.07	0.12	0.13	0.05	0.09	0.06
α_e, α_a	1.27, 1.23	1.32, 1.09	1.66, 1.17	0.97, 1.02	1.81, 2.71	0.96, 1.01	1.67, 1.17	1.17, 1.19	1.51, 1.17	1.83, 1.80

* *AOD*, *SSA*, and *AAR* at 442 nm; α_e and α_a for 483.5: 442 nm

2005 SEA Biomass-burning Aerosol

Detection of MODIS active fire was scattered over Cambodia and NE Thailand, primarily in rice paddy areas, and northern Thailand, primarily in forests. On February 17, 2005 (see Figure. 4.3), the highest mean OMI *AOD* (2.28) aerosol cluster, SEA5-2, corresponded or was adjacent to the MODIS fire grids. This aerosol cluster was also associated with observations on February 12 and 18 over the areas adjacent to the MODIS fire grids. This aerosol exhibited radiative absorbing properties (OMI *SSA* = 0.89) and fine-mode size (OMI α_a = 1.09). In addition, SEA5-3 (OMI *AOD* = 0.55; OMI *SSA* = 0.87; OMI α_a = 1.17) and SEA5-4 (OMI *AOD* = 0.60; OMI *SSA*= 0.88; OMI α_a = 1.02) exhibiting similar radiative forcing and size properties compared to SEA5-2.

There was another interesting finding on different aerosol properties between the ones found on February 12 (not shown here), 18, and the one on February 17 (shown in Figure 4.3). The cluster with the second highest mean *AOD* (0.63), SEA5-1, corresponded to the MODIS fire detection on February 18 and also the MODIS fire grids on February 12, but was less frequently found over the affected areas on February 17. This SEA5-1 had strong radiative scattering properties (*SSA* = 0.96, see Table 4.3). A factor potentially causing the different results could have been an influence of long-range transport polluted air masses. From air trajectories shown in Figure 4.3, on February 12 and 18, there were air masses originating from eastern Chinese industrial/urban areas that had been transported with prevalent northeasterly winds at 950 hPa to Mukdahan, NE Thailand. The long-range transport aerosol caused high radiative scattering aerosol (SEA5-1) to be present over SEA continent. This conclusion is consistent with the findings in Bridhikitti and Overcamp (2009), that high radiative scattering aerosol, possibly long-range transported from eastern China, was seasonally predominant over SEA continent.

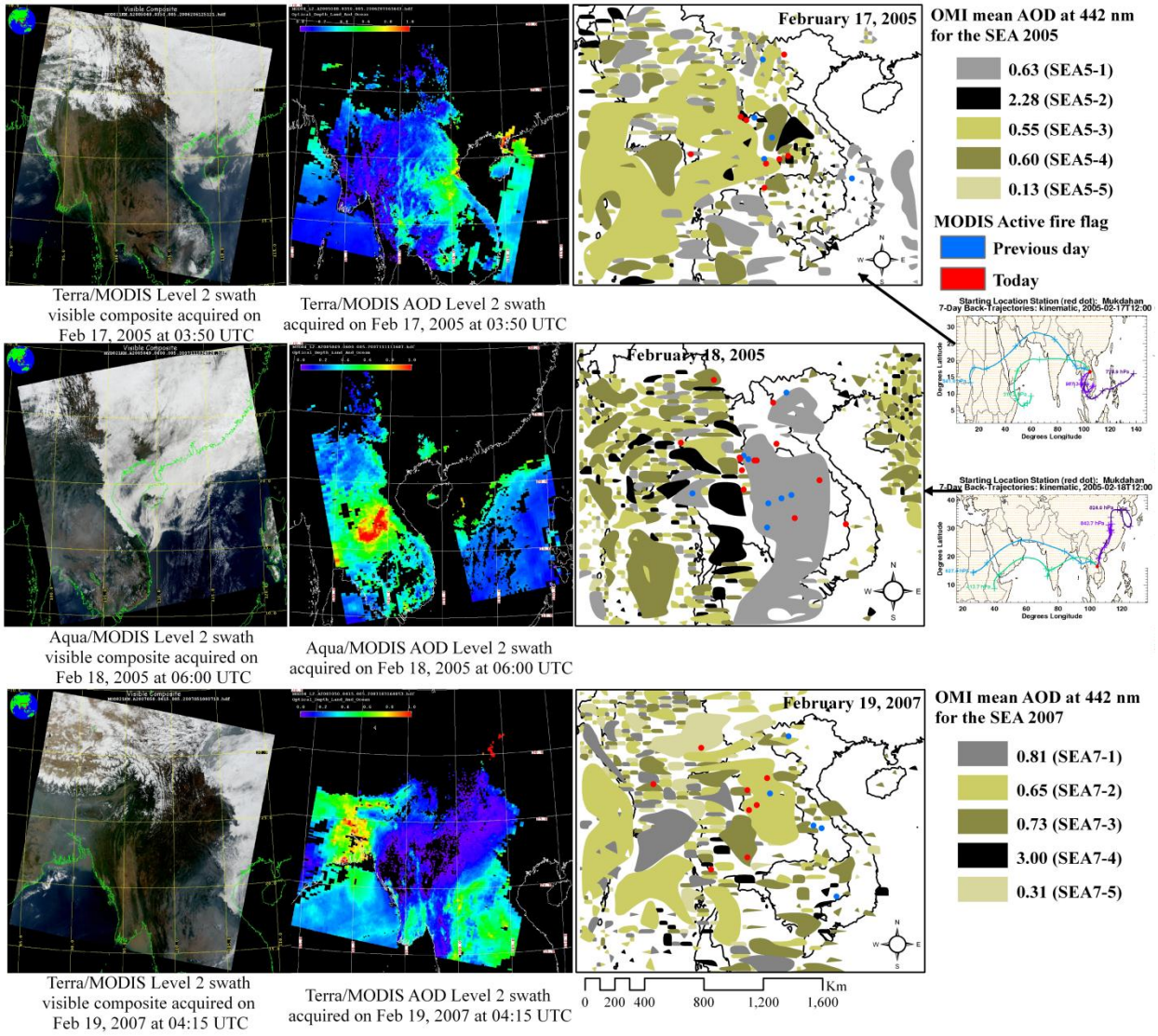

Figure. 4.3. MODIS Level 2 imagery in visible composite (left) and corresponding aerosol optical depth (*AOD*) ranging from 0 shown in violet to 1 shown in red (middle), and spatial aerosol clusters distribution overlaid with the MODIS active fire detections over the SEA biomass-burning affected areas on February 17 and 18, 2005, and February 19, 2007 (right). Note: White areas on the aerosol cluster maps indicate missing data.

Sources:The MODIS Level 2 imagery were acquired from L1 Atmosphere Archive and Distribution System (LAADS) website, available at http://ladsweb.nascom.nasa.gov/browse_images/l2_browser.html?form=AADS&browseType=Level+2. The air back trajectories at Mukdahan station were acquired from AERONET website, available at http://aeronet.gsfc.nasa.gov/cgi-bin/bamgomas_interactive.

2007 SEA Biomass-burning Aerosol

MODIS active fires coinciding with OMI SEA7-2 and SEA7-3 were observed. Neither cluster had very high *AODs*. As shown in Figure. 4.3, the SEA7-2 was found largely over NE Thailand, which is primarily rice paddies. The SEA7-3 cluster was largely found over central Thailand and extended into the lower part of northeastern and upper part of northern Thailand. All are urban/industrial lands or rice paddies. The SEA7-2 and SEA7-3 clusters had similar *AOD* levels (0.65 and 0.73, respectively) and similar size characteristic (OMI α_a = 1.17, 1.19, respectively), but their radiative forcing potentials were different. If an *SSA* of 0.9 indicates neutral radiative forcing, SEA7-2 exhibited positive forcing (OMI *SSA* = 0.87); whereas, SEA7-3 was negative (OMI *SSA* = 0.95). The optical properties of the lower *SSA* aerosol cluster, SEA7-2, were comparable to the local biomass-burning aerosol found in the 2005 SEA fire. The properties of the higher *SSA* aerosol cluster, SEA7-3, did not match well with any aerosol clusters observed during the 2005 SEA fire episode. In addition, SEA7-3 was not likely from China because the winds were not from the northeast. At this point, we are not sure what caused SEA7-3 to have higher *SSA* than that for typical biomass burning observed over SEA continent (Bridhikitti and Overcamp, 2009). This observing high OMI *SSA* might be simply a technical error associated with low *AOD*, as discussed earlier.

The cluster with the highest *AOD*, SEA7-4 (OMI *AOD* = 3), exhibited neutral radiative forcing (*SSA* = 0.91) and fine-mode size (α_a = 1.17). Its properties were similar to the highest-*AOD* cluster, SEA5-2, observed during the 2005 fire episode. This aerosol cluster

was scattered with small areas over SEA and its adjacency with the MODIS fire grids was not always obvious.

4.5. CONCLUSION

The appropriateness of using OMI/Aura aerosol products for biomass-burning aerosol detection and characterization was evaluated in this study from comparisons between the results obtained from the multivariate analyses of the OMI aerosol products and those obtained from ground-measured AERONET, AIRS/Aqua total column CO product, and MODIS active fire detections. The evaluations were done for four biomass burning episodes that occurred in two different regions: 2007/2009 Greek forest fires and 2005/2007 SEA fires. The Greek fires were small-scale fires; whereas, the SEA fires were large-scale fires.

Factor analysis was used to create three underlying factors from seventeen aerosol properties variables separately from the OMI and the AERONET. Factor loading patterns indicates similar variation and relationships among the aerosol variables from both data sets. Total communalities indicate similar high overall-permanence of using these factors to explain both aerosol data sets.

Frequencies of coincidence for each reciprocal pair between the clusters obtained from cluster analyses of the OMI aerosol products and the clusters from AERONET aerosol products are up to 69% for the Greek fires and 65% for the SEA fires. The calculated OMI absorbing Angström exponent, α_a, was used in this study to infer aerosol size characteristics. The OMI *AOD* tended to overestimate the AERONET *AOD* up to nearly

four times. Both AERONET and OMI provided similar properties (strong light scattering and dominated by fine-mode aerosols) of the aerosols observed in the early 2007 Greek fire episode, but not for the 2009 Greek fire episode. OMI *SSA*s did not significantly change during the Greek fire episodes, but the AERONET *SSA* did change. This inconsistency in *SSA* values results opposite conclusions on radiative forcing potential of the Greek forest fire aerosols based on the OMI versus the AERONET. In the SEA fires, good agreement on *SSAs* between the OMI and AERONET aerosol clusters was only acceptable when OMI *AOD* (442 nm) > 1. Under this condition, α_a values obtained from both data sets largely provided similar conclusions on dominant aerosol size characteristics.

Biomass-burning aerosol should have positive correlations between the OMI *AOD* and the AIRS total column CO. This evidence was only observed in a biomass-burning aerosol cluster for the 2005 SEA fire. Negative or poor correlations were observed in non-absorbing aerosol associated with high *AOD* levels. These could result from limitations of both OMI and AIRS instruments on detecting surface air pollutants due to interference by the aerosol. Therefore, *AOD* (442 nm) < 3 is recommended to minimize these effects.

For the SEA fires, spatial evaluation indicated good connections between MODIS active fire detection and OMI aerosol properties, including *AOD* and *SSA*. For the 2005 SEA fire episode, the changes in OMI aerosol optical properties corresponded with the changes of prevailing winds from southwesterly to northeasterly, causing higher *SSA* due

possibly to mixing with long-range transported Chinese urban/industrial aerosols. Similar OMI aerosol properties corresponding to the MODIS active fire detections were observed for both SEA fire episodes.

CHAPTER FIVE

REMOTE SENSING OBSERVATIONS OF THE OPTICAL PROPERTIES OF SOUTHEAST ASIAN FOREST-FIRE AEROSOLS

5.1. ABSTRACT

Previous studies have reported a range of optical properties for forest-fire aerosols. These have been attributed to environmental factors and burning characteristics. Roles of individual factors have not been statistically evaluated. This study determined optical properties of the aerosols from two forest-fire episodes: 2007 SEA continent and 2008 Indonesian fires, during two-month burning periods and investigated their dependencies on four limiting variables: wind speed/direction, relative humidity (RH), land use/cover, and age of aerosol. These variables were acquired or estimated from satellite retrievals and from meteorological model databases. Aerosol types with different optical properties were classified through multivariate analyses of Ozone Monitoring Instrument (OMI) aerosol variables, including aerosol optical depth (*AOD*), single-scattering albedo (*SSA*). Pearson Chi-square tests were used to test the independence of the forest-fire aerosol cluster membership and the limiting variables. Dependence between aerosol cluster membership and the limiting variables was significant for most cases, except for the Indonesian aerosol age factor. An age effect was not seen because of high wind speeds that blew off older aerosols out the study boundary. For the SEA continent aerosol, lower wind speeds were observed and the wind speed effect on the aerosol properties was more obvious. There was evidence that increasing atmospheric water content increased *AOD*

and *SSA*. For the SEA-continent aerosol, the increase in *SSA* did not have significantly hygroscopic growth. For Indonesian aerosol, increasing *SSA* was found with both increasing size, possibly from hygroscopic growth occurred in boundary layer, for very fine aerosol group and decreasing size for coarser aerosol group. In the residual layer, mixing biomass-burning aerosols with background aerosols limited by wind direction significantly caused to change in *SSA* for aerosols younger than two-day old. Influences from the background aerosol could change radiative forcing effects due to the forest-fire aerosols from positive (*SSA* < 0.9) to negative (*SSA* > 0.9) for the SEA-continent case and from negative to about neutral (mean *SSA* = 0.89) for the Indonesian case. With winds from the Indian Ocean and the SEA continent, size growth was often observed. When the winds were from the South China Sea/Indonesia and eastern Asia, the aerosols were finer in size. Strong association of the forest-fire aerosol properties with land use/cover were observed for Indonesian vegetation/peat lands, SEA-continent forests (evergreen and deciduous)/plantation lands, ocean surfaces, and Southeast Chinese territory.

5.2. INTRODUCTION

Forest-fire aerosols causing radiative cooling at the top of atmosphere were widely reported, such as during 2004 to 2005 forest fires in Portugal (Santos et al., 2008) and during 2003 Siberian forest fire (Jeong et al., 2008). A similar global impact was observed for the aerosols during the 1993 to 1994 Amazonian forest fires and during the 1994 to 1998 boreal forest fires in United States and Canada, indicated from the single scattering albedo (*SSA*, at 440 nm) of 0.94 (Dubovik et al., 2002). The forest-fire aerosols over Indonesia during 1997 El Nino year also exhibited strong radiative cooling

efficiency (Podgorny et al., 2003). Consistently, Gras et al. (1999) found that the Indonesian fire aerosols have high light scattering properties. In contrast, the Brazilian forest-fire aerosols collected by aircraft in the work of Reid (1998) exhibited low *SSA* at 550 nm values of 0.85 ± 0.02 (at Cuiabá, Mati Grosso) and 0.86 ± 0.05 (at Porto Velho, Rondônia), indicating their higher radiation absorbability and potential to cause global warming. This is similar to the results for aerosols from the Australian and African savanna fires (Dubovik et al., 2002; Gras et al., 1999).

These diverse conclusions have been attributed to aerosol aging, the state of their mixture with the background, ambient temperature, relative humidity (RH), moisture content of the fuel, and fire intensity (Dubovik et al., 2002; Fiebig et al., 2003). However, the qualitative roles of these variables on the aerosols from different forest-fire episodes had not been comparatively evaluated. This study determined optical properties of aerosols from the two Southeast Asian (SEA) forest-fire/biomass-burning episodes and investigated their dependence on wind speed/direction, RH, land cover as a surrogate of burning fuel type, and age of aerosol. Some of these spatial data sets were retrieved from Earth observation satellite sensors, including the Ozone Monitoring Instrument (OMI) and Moderate Resolution Imaging Spectroradiometer (MODIS).

5.3. METHODOLOGY

5.3.1. Site description

Two SEA fire episodes, the August to September 2008 Indonesian and the February to March 2007 SEA-continent fires, were considered in this study. Geographical locations

of the fire-affected areas are shown in Figure 5.1. The Indonesian fire-affected areas considered covered the areas of 92^{o}E to 119^{o}E longitude and 10^{o}S to 9^{o}N latitude and the SEA-continent fire affected areas covered the areas of 90^{o}E to 110^{o}E longitude and 8^{o}N to 30^{o}N latitude.

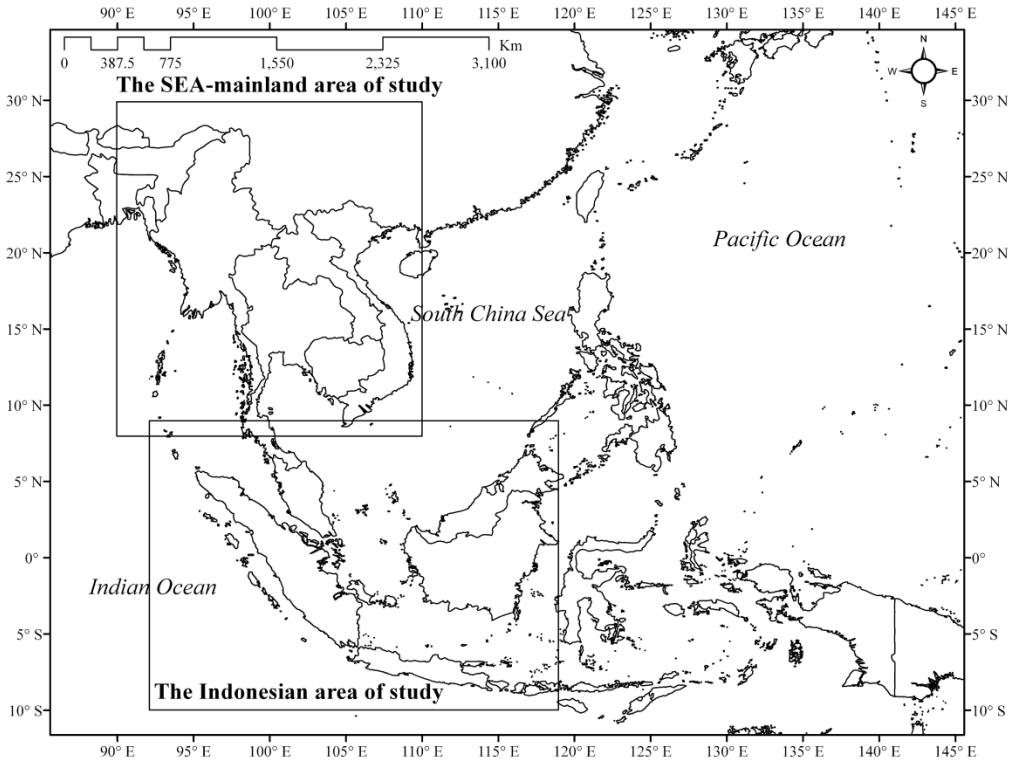

Figure 5.1. The forest fire-affected areas of study

Indonesian forest fires usually start over rice paddies, which are enriched with buried organic matter, causing peat fires. These fires typically burn slowly by smoldering and frequently extend to nearby tall, broad-leaved evergreen forests, and then develop to crown fires (Graham et al., 2004). In the dry season, the mixture of local biomass burning smoke, biogenic aerosols, and soil dust predominate over Indonesia (Guyon et al., 2003; Artaxo et al., 1998). The latter two aerosol types exhibited coarse-mode dominant size.

SEA-continent fires from both permanent agriculture and land clearing activities typically widely spread throughout the region in the late-dry season, February to April. Many of these fires occur within forest ecosystems, primarily deciduous broadleaf forest. Other land covers relating to SEA-continent forest-fire activities include open savanna woodlands, grasslands, paddy rice, and other permanent crops (Jones, 1998). Bridhikitti and Overcamp (2009) conducted a cluster analysis of the aerosol optical properties acquired from AERONET and found that the local biomass-burning aerosol was seasonally dominant over the SEA continent during this time of year. This aerosol exhibited *SSA* of approximately 0.90 and prevailing fine-mode size.

5.3.2. Data description

Satellite retrievals used in this study were from OMI onboard the Aura satellite and MODIS onboard the Terra satellites. Spatial wind speed/direction and relative humidity used in this study were from the National Centers for Environmental Prediction (NCEP). The details of these data sets are provided below.

OMI is a nadir-viewing spectrometer. It provides information on atmospheric composition, including aerosols, with a spatial resolution of 13×24 km^2 (swath level 2) at nadir and daily global coverage. The OMI data sets used in this study are the daily $0.25^o \times 0.25^o$ (~25 km for longitude, 27.8 km for latitude) level 3e aerosol product version 3, or OMAEROe.003 data set. An OMI level 3e is defined as the ensemble of all level 2 ground pixels whose centers have the same local calendar date on the ground. All of level 2 observations that overlap with each level 3e grid cell are considered and compared with several exclusion criteria given by Leonard (2009). The OMI aerosol

retrieval products acquired for this study include *AOD*, absorbing *AOD* (*AAOD*), and *SSA* for five wavelengths; 342.5, 388, 442, 463, and 483.5 nm. These products are estimated from the measured backscattering in the seventeen selected wavelength bands between 330 and 500 nm, from near UV to visible. In near UV, land surface reflectance, free of ice and snow, is minimized, and the UV absorbability of aerosol is increased due to increasing Rayleigh scattering by atmospheric gases. A set of two to three aerosol sub-types are first selected from aerosol indices (a measure of the change in spectral contrast), geographic location, and season. Then, an appropriate model yielding least square error with observed radiances is chosen (Torres et al., 2002). Bridhikitti et al. (2010) evaluated the appropriateness of using the OMI aerosol products for biomass-burning aerosol detection and characterization. Their findings suggest that the OMI products are appropriate for the studies concerning aerosols from large-scale biomass-burning areas, including SEA-continent and Indonesian fires. The OMI data set used in this study was acquired from the Web-based Giovanni online visualization and analysis tool available at http://disc.sci.gsfc.nasa.gov/giovanni.

Active fire detections in the MODIS Thermal Anomalies/Fire Daily Level 3 1-km resolution Global product were acquired for this study. The active fire has been evaluated from the variability of the surface brightness temperature, derived MODIS radiances at 4 and 11 μm, and surface reflectance by sunlight, compared to its background value. These fire observations are made twice a day from Terra at 10:30 am and 10:30 pm (Justice et al., 2006). Both these daytime and nighttime measurements were used to evaluate the daily active fires.

A land cover map used in this study was generated from the time-series analyses of the multi-wavelength from visible to near-infrared of MODIS surface reflectances. This MODIS surface reflectance product is 8-day L3 Global 500 m SIN Grid V005 retrieved from 2006 to 2007. Each grid value gives the percentage of the radiation energy in the specific bandwidth from the total energy integrated over entire spectrum. The methodology used to generate this land cover map is detailed in Chapter Two. The SEA-continent land covers classified to the map include 1) evergreen forests and perennial plantations, 2) deciduous forests and seasonal plantations, 3) wetland forests, wetlands, and mangrove forests, 4) rice paddies and other vegetation fields, 5) inland surface waters, 6) high-intensity urban areas, and 7) other. The time-series MODIS active fire and spectral surface reflectance products were acquired from the Land Processes Distributed Active Achieve Center (LPDAAC) website available at https://lpdaac.usgs.gov/lpdaac/get_data/data_pool.

The NCEP FNL (final) Operational Global Analysis data used in this study are wind speed/direction and relative humidity on $1^{o}\times1^{o}$ grid covering the study areas. This product is from the Global Data Assimilation System (GDAS), which collects observational data from many sources, including the Global Telecommunications System. The data are prepared every six hours and those at 6 UTC (1:00 pm local time) were used in this study. The data were acquired from the Research Data Archive (RDA) which is maintained by the Computational and Information Systems Laboratory (CISL) at the National Center for Atmospheric Research (NCAR) in Boulder, Colorado. The original data are available from RDA (http://dss.ucar.edu) as data set number ds083.2.

These NCEP metrological variables are at 700 hPa (approximately 2.8 km altitude). This altitude level was chosen because it is in the ranges of typical Indonesian forest-fire aerosols injection height (~2 to 3 km, Labonne et al., 2007), SEA smoke elevated layer observed over the Indian Ocean (< 3 km, Thampi et al., 2009), and SEA smoke elevated layer observed over East Asia (~2.5 to 4.5 km, Liu et al., 1999). Therefore, a 700-hPa altitude was assumed in this study to be the layer of polluted air masses attributed to both fire episodes and it is called in this dissertation the residual layer.

To evaluate properties of the aerosol from Indonesian peat fires, the spatial distribution of peat lands were acquired from a map of soil group Histosol (HS) in the World Reference Base (WRB) Map for World Soil Resources. This HS was defined as soils which are composed of organic materials, common in wetlands. Using HS from this WRB map would overestimate Indonesian peat lands by about half (Heil et al., 2007). However, the HS map corresponded well with the spatial distribution of the peat lands drawn in the literature (Heil et al., 2007). The map used in this study was in Arc/Info format and was acquired from Food and Agriculture Organization of the United Nations (FAO/AGL, 2003).

5.3.3. Data processing

The Angström exponent, α, indicates the spectral sensitivity of the aerosols and is considered an aerosol size-related variable. Two Angström exponents used in this study, extinction (α_e) and absorbing (α_a), were calculated from a spectral pair of *AOD* and *AAOD* measurements, respectively, using equation 1.

$$\alpha_{483.5:442} = -\frac{\ln\left[\frac{(A)AOD_{483.5}}{(A)AOD_{442}}\right]}{\ln\left(\frac{483.5}{442}\right)} \quad \text{(Eq.1)}$$

OMI α_e was calculated using OMI *AOD* at 442 and 483.5 nm and OMI α_a was similarly calculated using the OMI *AAOD* at the same wavelength pair. Spectral *AAOD* to *AOD* ratio, *AAR*, was calculated and used for multivariate analyses. Higher *AAR* indicates higher radiative absorption of aerosol plume. Higher α_e values indicate higher spectral dependence of *AOD* due to finer aerosols (Cheng et al., 2006).

Multivariate statistical analysis methods applied in this study include factor analysis of the aerosol variables obtained from OMI/Aura and cluster analysis of aerosol factors obtained from the previous factor analysis. The application of multivariate analyses for clustering different aerosol-types is briefly described below.

Factor analyses using the Varimax rotation method on correlation matrix of all the OMI/Aura aerosol variables, including five *AOD*s, five *AAR*s, five *SSA*s, and two αs, were performed to find a small number of uncorrelated functions, or underlying factors, that explain the relationship among the original aerosol variables. Only the observations with 1 < OMI *AOD* (442 nm) < 3 were used in the analyses because the OMI aerosol products were found to exhibit similar magnitude as the AERONET aerosol retrievals and have positive relationship with the AIRS column CO product (Bridhikitti et al., 2010). The analyses were run individually for each fire event. Hierarchical cluster analysis using the Ward-minimum variance method (Johnson, 1998) was used to identify the groups of different aerosol types dominating during the fire episodes. The number of

clusters was selected from the minimum number yielding a relatively high pseudo-F statistic together with relatively low pseudo-T^2 statistic compared with the nearby higher and lower cluster numbers (Johnson, 1998).

Six variables were retrieved daily over the fire-affected areas for two month period during the fire episodes. These variables include 1) the OMI-derived aerosol cluster, 2) the MODIS active fire, 3) the MODIS-derived land cover, 4) the NCEP relative humidity, 5) the NCEP wind speed, and 6) the NCEP wind direction. These spatial data sets were resampled to the grid interval, ~$0.01^o \times 0.01^o$, commensurate with the MODIS active fire product using the ArcGIS 9.2 data management tool.

The age of aerosol was determined from time-series analysis of the NCEP wind speed/direction and the MODIS active fire detections. Age zero was given to the observation found at MODIS active fire pixel. From this pixel, the location of one-day old aerosol was then estimated from the local wind speed and direction. The location of two-day old aerosol was estimated from the one-day old aerosol in the same manner, and so on until the location of three-day old aerosol is identified. Seven variables, including the six variables and age of aerosol, were collected daily along this lagrangian aerosol plume.

The wind speed and RH at 700 hPa were categorized into five levels; lower than 20^{th} percentile, 20^{th} to 40^{th} percentile, 40^{th} to 60^{th} percentile, 60^{th} to 80^{th} percentile, and higher than 80^{th} percentile. Pearson Chi-square tests were used to assess whether membership in an aerosol cluster and each categorical variable are statistically independent. Cell contribution to the overall Chi-square, later called the cell Chi-square statistic in this

dissertation, was used to evaluate where there were strong associations between the aerosol clusters and the limiting variables.

Several studies showed that some biomass-burning aerosols exhibited hygroscropic growth, which related their higher light scattering properties with increasing RH (Gras et al., 1999; Reid, 1998; Nessler et al., 2005). To illustrate this tendency and gain additional quantitative information, linear regression analysis was performed to assess the relationships between RH and α_a and between aerosol *SSA* (442 nm) and α_a. The analysis was done for selective aerosol clusters exhibiting strong associating with relative humidity. Outliers characterized by Studentized residual greater than |2| were removed before the analysis. All the statistical analyses were done via SAS 9.2 software (SAS Institute Inc., Cary, NC).

5.4. RESULTS AND DISCUSSION

The *AOD* and *SSA* referred in this discussion are at 442 nm. The size variable referred here is OMI-calculated α_a at 442 and 483.5 nm.

5.4.1. Factor and cluster analyses of the OMI aerosol variables

The factor analyses showed a similar factor pattern for the aerosols from both fire episodes. These analyses were run using three underlying factors, which were named: *SSA* factor (positively loaded on the *SSA*s and negatively loaded on *AAR*s), *AOD* factor (highly loaded on the *AOD*s), and α factor (highly loaded on α_e and α_a). The *SSA* factor accounted for the highest proportion of the total variability, followed by the *AOD* factor and the α factor, respectively.

The four clusters for the Indonesian aerosols and eight for the SEA-continent aerosols were chosen on the basic of maximizing pseudo-F statistic and minimizing pseudo-T^2 statistic. The number of clusters qualitatively agreed with tree diagrams obtained from the cluster analyses. Clusters were named 'I' for the Indonesian aerosols and 'S' for the SEA-continent aerosol, and followed by the cluster number. The OMI aerosol variables for these aerosol clusters are given in Table 5.1.

5.4.2 Pearson Chi-square tests

Independence between aerosol cluster membership and the limiting variables was rejected with significance level less than 0.01 for most cases, except for Indonesian aerosol age factor (p = 0.43). In addition, two- and three-day old aerosols were not found within the Indonesian boundary drawn in this study. This is because predominant high-speed wind blew aged aerosols out of the boundary quickly. Table 5.2 is the cross-comparison table showing the Chi-square test results between the aerosol clusters obtained from cluster analyses of the OMI aerosol variables for 1 < OMI *AOD* (442 nm) < 3 and their limiting variables. Strong associations were determined from a high value of the cell Chi-square statistic that contributed a large fraction to the overall Pearson Chi-square statistic. The value was flagged significant if the cell statistic was greater than 5% for the SEA case or 10% for the Indonesian case of total Chi-square statistic.

For better understanding of Table 5.2, cluster I1, as one example, strongly associates with fewer observations of easterly winds than expected, fewer with wind speed between 14 to 17 m s^{-1}, more observations for aerosols with all ages over ocean surfaces, and no preference for aerosol age, relative humidity level, and land use/cover for zero-day old

aerosol. The associations of the limiting variables on the aerosol properties are discussed below.

Table 5.1. Mean ±1 standard deviation of the selected OMI aerosol variables for each aerosol cluster obtained from the cluster analysis

Cluster	OMI variables*					Number of observations
	AAOD	*AOD*	*SSA*	α_e	α_a	
The Indonesian aerosols						
I1	0.06±0.02	1.28±0.19	0.96±0.02	1.38±0.32	1.25±0.41	12384
I2	0.16±0.06	1.51±0.45	0.89±0.02	1.46±0.34	1.14±0.17	9858
I3	0.11±0.04	2.14±0.39	0.95±0.02	1.50±0.35	1.18±0.15	11041
I4	0.13±0.09	1.63±0.52	0.92±0.04	3.65±2.59	9.70±7.57	189
The SEA-continent aerosols						
S1	0.13±0.02	1.16±0.12	0.89±0.02	1.36±0.35	1.17±0.55	7804
S2	0.06±0.02	1.28±0.20	0.96±0.02	1.27±0.31	1.27±0.53	7472
S3	0.20±0.04	1.49±0.26	0.86±0.02	1.40±0.34	1.16±0.58	7652
S4	0.16±0.03	1.76±0.26	0.91±0.02	1.38±0.32	1.19±0.70	9636
S5	0.10±0.02	1.21±0.14	0.92±0.01	1.32±0.29	1.12±0.50	5358
S6	0.27±0.06	2.44±0.30	0.89±0.02	1.48±0.72	1.28±1.16	8238
S7	0.11±0.04	2.23±0.39	0.95±0.01	1.39±0.34	1.21±0.44	6106
S8	0.15±0.08	1.70±0.54	0.91±0.03	1.41±0.27	1.14±0.12	1687

* *AAOD* is absorbing aerosol optical depth at 442 nm, *AOD* is aerosol optical depth at 442 nm, *SSA* is aerosol single scattering albedo at 442 nm, α_e is extinction Angström Exponent for 483.5 and 442 nm, and α_a is absorbing Angström exponent for 483.5 and 442 nm

Table 5.2. Pearson Chi-square-evaluated associations between the aerosol clusters and the limiting variables

Cluster	Aerosol age[a]	Wind direction	Wind speed[b]	Relative humidity[c]	Land use/cover[d]	
					zero-day old only	all ages
The Indonesian aerosols						
I1		**E**↓	**3**↓			**O**↑
I2		**E**↑, **NE**↑	**1**↓, **3**↑	**1**↑, **3**↓		**O**↑
I3		**E**↓, **NE**↓	**1**↑, **5**↓	**1**↓, **3**↑, **4**↑		**O**↑
I4			**2**↓, **4**↓, **5**↑	**2**↑	**V**↑, **DF**↓ (**P**↑)	**V**↑ (**P**↑)
The SEA-continent aerosols						
S1	**0**↑, 3↓	S↓, NW↑	5↓	**1**↑	**EF**↓, DF↑	DF↑, C↓
S2		S↓			EF↓	**O**↑
S3			1↑, 5↓			
S4						**C**↑
S5			1↓			**C**↑
S6	0↑			1↓, 3↑	**V**↓, **EF**↑	**C**↓, **EF**↑
S7		SE↑		**1**↓, 2↓, **5**↑	EF↑, DF↓	**C**↓
S8	**0**↓, 1↑, **3**↑	**S**↑,**SW**↓,**W**↓	**1**↓, 2↓, 4↑,**5**↑	**1**↑, **4**↓, **5**↓		**C**↑, EF↓,DF↓,**V**↓

[a] four category ages (day old) are [0,1, 2, 3]

[b] five category wind speeds at 700 hPa (m/s) are [< 11, 11 to 14, 14 to 17, 17 to 21, > 21] for the Indonesian case, and are [< 4, 4 to 6, 6 to 8, 8 to 10, > 10] for the SEA-continent case

[c] five category RH at 700 hPa (%) are [< 49, 49 to 64, 64 to 73, 73 to 82, > 82] for the Indonesian case, and are [< 25, 25 to 40, 40 to 53, 53 to 72, > 72] for the SEA-continent case

[d] DF = deciduous forests and seasonal plantations; EF = evergreen forests and perennial plantations, WF = wetland forests, wetlands, mangrove forests, V = rice paddies and other agricultural fields, O = Oceans, C = Chinese terrestrial, and P = peat lands (analyzed separately from other land use/cover types)

* **Bold fonts with underline** indicates that cell Chi-square statistic accounted for more than 20% of total Chi-square statistic; **Bold fonts without underline** indicates that cell Chi-square statistic accounted for more than 10% to 20% of the total; **Non-bolded fonts** indicates that cell Chi-square statistic accounted for more than 5% to 10% of the total; **Blank** indicates that cell Chi-square statistic accounted for less than 5% of the total; ↑ indicates more observations than the predicted from total population; ↓ indicates fewer observations than the predicted from total population.

Association with atmospheric relative humidity (RH)

There was evidence that increasing atmospheric water content increased aerosol loading (higher *AOD*) and aerosol scattering properties (higher *SSA*). From Table 5.2, cluster memberships in S1 and S7 are strongly associated with low and high RH, respectively. Cluster S1 exhibited significant lower *AOD* (1.16) and lower *SSA* (0.89) than the values for cluster S7 (*AOD* = 2.22; *SSA* = 0.95). A similar relationship was also found in cluster I2 (*AOD* = 1.51; *SSA* = 0.89) membership being strongly associated with low RH, and cluster I3 (*AOD* = 2.14; *SSA* = 0.95) membership strongly associated with high RH.

For SEA-continent aerosol clusters, a positive linear relationship (R^2 = 0.11, see Figure 5.2c) between RH and α_a for S1 and S7 does not indicate significant hygroscopic growth. In contrast, this suggests more fine aerosols with increasing RH and the production of these fine aerosols increased overall aerosol light-scattering efficiency (see Figure 5.2f). Little significant hygroscopic growth possibly resulted from two factors: a relatively low background RH in the residual layer and a hydrophobic primary aerosol. Fifty percent of RH observations in the residual layer observed over SEA continent during the fire episode were lower than 45%, which is considered low humidity. Carrico et al. (2005) found that hygroscopic growth of a carbon-dominated aerosol in Yosemite National Park was negligible for RH less than approximately 40%. Similarly, low RH could have inhibited the hygroscopic growth of the SEA-continent forest-fire aerosol. Chemical composition of primary biomass-burning aerosols were also felt to be dependent on the type of fuel which is discussed later. Higher production of fine aerosol with increased RH is possible if higher RH increases the formation of fine secondary water-soluble organic

aerosols via gas-to-particle processes, including direct photochemical reactions (Izumi et al., 1987) or photochemical-reaction-induced ozonolysis (Warren et al., 2009). This causes higher aerosol light-scattering properties.

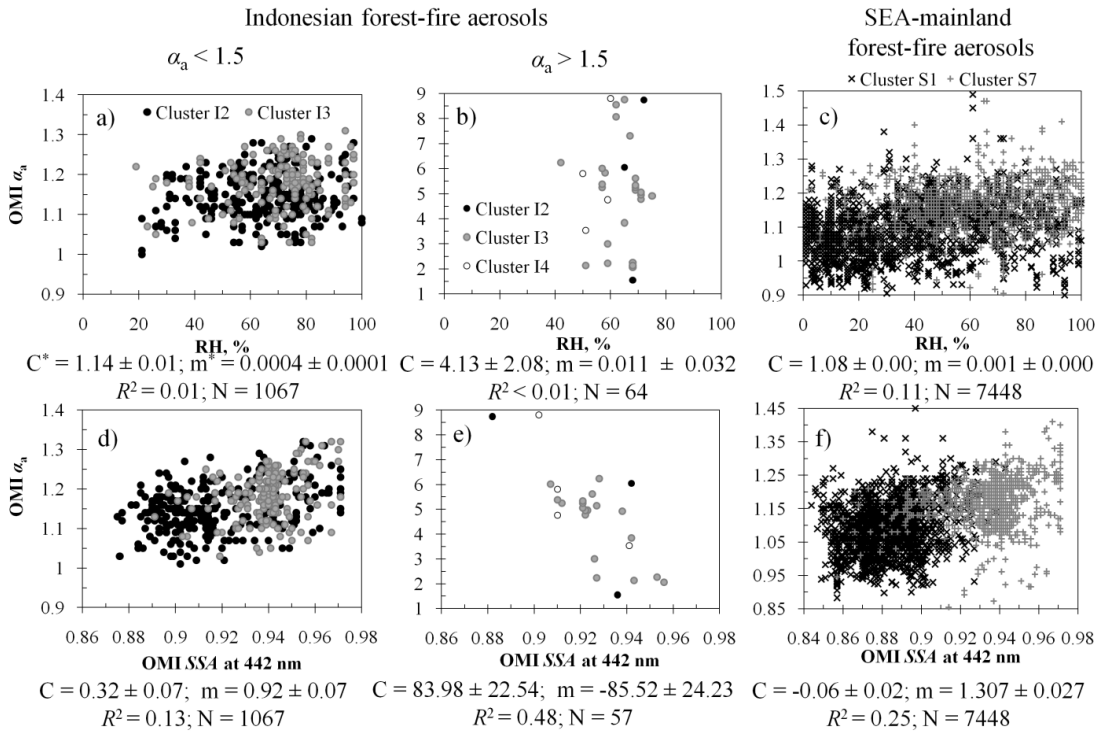

Figure 5.2. Scatter plots of OMI *AOD* (442 nm), OMI *SSA* (442 nm), and OMI α_a against the relative humidity and plots between the *SSA* and the α_a for all clusters (I2, I3, I4, S1 and S7), which are strongly associated with RH at 700 hPa (see Table 5.2). Estimates of linear regression model are under each plot.

$^*y = mx + C$; N = number of observations used for the regression analysis

Gras et al. (1999) found that smoke aerosols in Indonesia and tropical Australia during 1997 dry season showed increases in scattering efficiency with increasing RH. They also concluded that this increase in scattering efficiency was a result of hygroscopic growth. Reid (1998) also observed increases in both particle mass scattering efficiency and *SSA*

and decreases in α in the aged aerosols from 1995 Brazilian forest fire. Based on this evidence, Reid (1998) concluded that an increase in mass scattering efficiency was due to particle growth.

From the Chi-square tests, we also observed positive relationships between RH in the residual layer and aerosol scattering efficiency, but we did not see significant hygroscopic growth or any significant aerosol size dependences on RH in this layer (see Figure 5.2a and 5.2b). This suggests that hygroscopic growth in the residual layer was not significant. However, we found that aerosol size growth causing its higher light scattering efficiency was important for Indonesian very fine aerosol group ($\alpha_a > 1.5$, see Figure 5.2e). This growth of the Indonesian aerosol should occur in the boundary layer (Berg et al., 1998). In contrast to Indonesian coarser aerosol group ($\alpha_a < 1.5$), more fine-size aerosol caused overall higher aerosol scattering efficiency. These findings were drawn from linear relationships between *SSA* and α_a for I2, I3, and I4 which are shown in Figure 5.2d. The relationship for the Indonesian coarser aerosol group was similar with the observed for the SEA-continent aerosol (see Figure 5.2f) and similar processes were expected to play roles for both aerosols. These findings indicated more complex dynamic scattering properties of the Indonesian forest-fire aerosols than its connection to hygroscopic growth alone.

Association with wind speed/direction and implication to aging

Wind speed effect on the aerosol properties was best inferred from the properties of S3 aerosol cluster. From the Chi-square test, this S3 aerosol cluster was observed often with the lowest wind speed (< 4 m s^{-1}), less often with the highest wind speed (> 10 m s^{-1}), and

no preference for other limiting factors. Due to strong association with the low wind speed and no preference for aerosol age, this S3 cluster was less dynamic and could be a good proxy of pristine local forest-fire aerosol. Among SEA-continent aerosol clusters, this aerosol cluster had the lowest mean *SSA* of 0.86. This suggests that the original SEA-continent forest-fire aerosol had high light absorbability and had global warming potential. The wind speed effects on the aerosol dynamic properties were not obvious for the Indonesian aerosol. No aerosol age dependence could be found for this case. This could relate to occurrence of high wind speeds over the Indonesian region (> 11 m s^{-1} at 700 hPa for 80% of the observing time).

There was a finding supporting that aging changes in *SSA* are potentially from mixing with background aerosols limited by wind direction. The finding from Figure 5.3 demonstrates the significance of wind direction and aerosol age on the SEA-continent forest-fire aerosol properties. Differences in *SSA* and α_a values suggested dissimilar optical properties for all-ages aerosols found with different wind directions. Within the same wind direction, the *SSA* significantly increased from the values at zero-day old to those at one-day old. The difference was less significant among those at one-day old and older (drawn from the evidence found in the SEA-continent aerosol only). This indicates important external/internal mixing processes on dynamic scattering properties of the aerosols within less than two days after being injected into the residual layer.

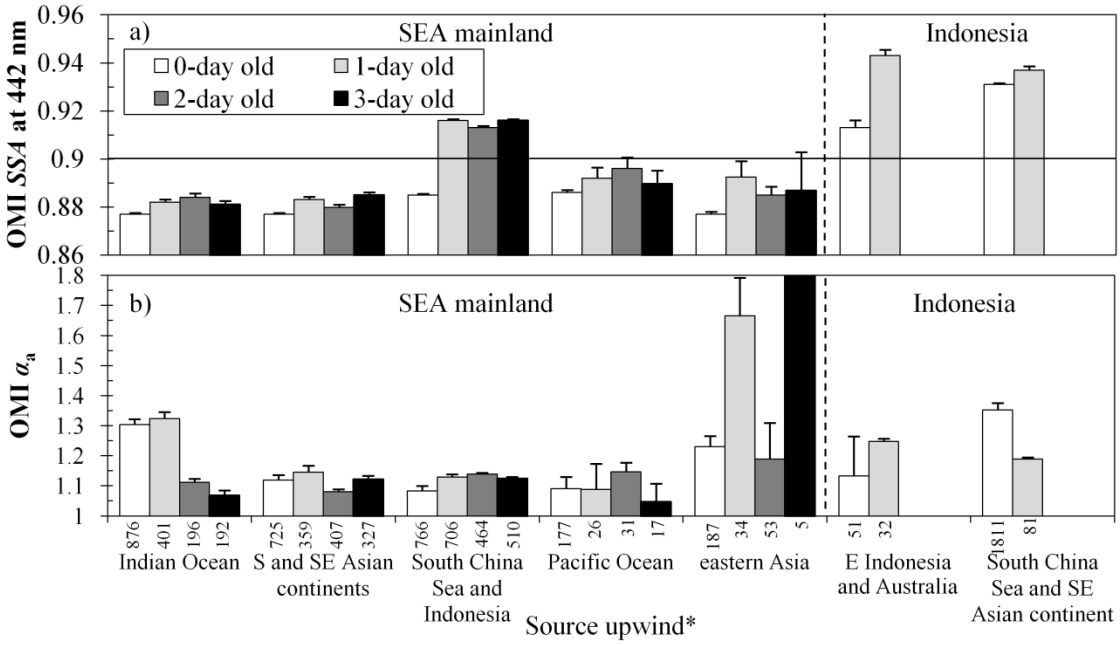

Figure 5.3. The mean and standard error of OMI *SSA* at 442 nm (a) and the calculated OMI absorbing Angström exponent (b) for different source contributors indicated from wind directions. Numbers above *x*-axis labels are number of observations for both (a) and (b).

* For sources upwind of SEA continent, Indian Ocean was inferred from southwesterly winds to SEA continent; S Asian and SEA continents were from westerly winds; South China Sea was from southerly winds; Pacific Ocean was from easterly winds, and E Asia was from northerly and northeasterly winds. Source contributors to Indonesia, E Indonesia and Australia were inferred from easterly winds to Indonesia and SEA continent were from northerly winds.

Overall zero-day-old SEA-continent aerosols exhibited positive radiative forcing potential due to their lower scattering efficiency suggested by mean *SSA* ranging 0.877 to 0.886 (*SSA* of ~0.9 indicates neutral radiative forcing). Mean *SSA*s increased to 0.882–0.916 when aerosols were one-day old. The observations having mean *SSA* higher than 0.9 were found with upwind sources from the South China Sea and from Indonesia. This

result corresponded with the observed overall high scattering efficiency (mean *SSA*s = 0.913 to 0.945) for the Indonesian aerosols (see Figure 5.3). Even though the transport from Indonesia to SEA continent could be limited by the influence of Intertropical Convergence Zone, the phenomena had occurred in many Indonesian fire episodes, such as the 1997 episode (Okada et al, 2001) and the 2006 episode (Hyer and Chew, 2010). This indicates a strong wind direction effect on radiative forcing efficiency of the SEA-continent forest-fire aerosols. Gras et al. (1999) measured the growth factor of aerosol light-scattering coefficient using integrating nephelometers over Kalimantan, the large island in Indonesian archipelago, during the 1997 Indonesian fire. They found that the aerosols exhibited a scattering growth similar to sea salt. They also observed that the aerosol exhibited a high *SSA* of 0.98. One hypothesis for high *SSA* is burning of Indonesian peat fuel. Another involved mixing with high-scattering marine aerosols. Both hypotheses are discussed later.

There is evidence showing significant wind direction effects on light scattering properties for Indonesian aerosol. Cluster I2 was observed often with winds from western Pacific Ocean region (E and NE winds in Table 5.2), including eastern Indonesia and northern Australia. This aerosol cluster had a significantly lower *SSA* value (0.89) than those with lower incidence of E and NE winds (mean *SSA* = 0.96 and 0.95 for I1 and I3, respectively). This aerosol cluster could have included UV-absorbing smoke aerosol from Australian savanna fires (Gras et al., 1999; Liley et al., 2003; O'Brien and Mitchell, 2003). These fires typically occur in northern Australia in dry seasons and potentially cause global radiative heating (O'Brien and Mitchell, 2003).

From Figure 5.3, the α_a, which is an aerosol size indicator, did not show a consistent pattern with aerosol age for all wind directions. Size growth was marked for the observations with upwind sources from the Indian Ocean for the SEA-continent case and those with upwind sources from SEA continent for the Indonesian case. The SEA-continent aerosols typically exhibited mean α_a less than 1.15. The observations exhibited mean $\alpha_a > 1.3$ and found with upwind source from the Indian Ocean for zero- and one-day old aerosols could be fine non-sea-salt marine aerosol and aerosols, primarily from biomass burnings, from Indian subcontinent and Indonesia (Rajeev et al., 2000; Lelieveld et al., 2001). The size growth could be a result of hygroscopic growth of mixed aerosols, which are internally/externally mixing between the aerosols from the Indian Ocean and the forest-fire aerosol. The size growth, however, was not found for upwind sources from the Pacific Ocean. Aerosols found over the northern Pacific Ocean are less influenced by anthropogenic emissions (Arimoto et al., 1996). These aerosols are primarily non-sea-salt marine aerosols and mineral aerosols related to Asian desert dust (Duce et al, 1980; Gao et al., 1992; Arimoto et al., 1996). However, the contribution of this desert dust to SEA-continent aerosols has not been reported elsewhere.

In contrast to the size growth, more fine-size aerosols observed in aged aerosol groups were associated with winds from the South China Sea and Indonesia for SEA-continent case. In addition, the observations that were observed with upwind sources from eastern Asia had very fine size (mean α_a = 1.15 to 3.47, see Figure 5.3). This very fine size aerosol could be secondary aerosol formed in pollution plumes transported from eastern

Asia, probably China, to SEA continent. Evidence of secondary aerosol formation was also shown in the work of Bridhikitti and Overcamp (2009).

Association with land cover/fuel type and implication to aging

Considering young (zero-day old only in Table 5.2) aerosols, high *AOD* clusters, S6 and S7 (mean *AOD* = 2.44 and 2.23, respectively), were observed often over evergreen forests. Lower *AOD* clusters, S1 and S2 (mean *AOD* = 1.16 and 1.28, respectively), were often observed over deciduous forest or less often over evergreen forest. Several factors could contribute to these differences. One factor was RH level. The aerosol clusters that strongly associated with higher RH (RH = 40% to 53% for S6 and > 72% for S7) were found often over evergreen forests. The aerosol cluster that strongly associated with lower RH (RH < 25% for S1) was found often over deciduous forests. Another limiting variable playing a role was mass density of organic matter, including vegetation, soil, and litter. Logically, burning more organic matter results in more aerosol loaded into the atmosphere. Evergreen forests in SEA continent can be considered as subtropical/tropical moist forest which could provide approximately 492 tons of organic matter per ha; whereas deciduous forests, which are drier, can only provide approximately one-third of the amount above (Brown and Lugo, 1982; Murphy and Lugo, 1986).

Type of fuel was another important factor affecting aerosol optical properties. The Indonesian I4 aerosol cluster was observed often over vegetation lands and peat lands. This aerosol cluster had very fine size (mean α_a = 9.7) which could grow and consequently exhibited higher light scattering efficiency (see Figure 5.2e). Mean *SSA* of this high peat land-associated I4 cluster was 0.92 which was larger than that observed

often over deciduous or evergreen forests (0.89 for both S1 and S6). Approximately 40% of hot spots observed in this study occurred on Histosol soil, relating to peat lands. Peat combustion contributed to the high-scattering Indonesian smoke, which resulted from increasing hygroscopicity for sulfate aerosols released from sulfur-rich peat fuel (Langmann and Graf, 2003). Peat combustion, for example for the 1997 forest fire, is largely a smoldering fire that generates more water-soluble organic aerosols and has higher scattering properties than a flaming fire (Gras et al., 1999). Okada et al. (2001) examined the inorganic composition of individual aerosol particles collected from an aircraft flying over Southern Kalimantan during the 1997 Indonesian fire and found that the individual aerosols were primarily an internal mixture of water-soluble organic materials and inorganic salt, primarily ammonium sulfate. The water-soluble organic components were hypothesized to be fatty acids produced from biomass burning (Okada et al., 2001). The inorganic sulfate salt component was possibly from sulfur-rich peat fuel. The mixed aerosols exhibit significant radiation scattering and cause global cooling effects (Adams et al., 2001).

SEA-continent biomass fires are not from peat fuel. Ma et al. (2003) examined the fine-particle inorganic composition of bio-smoke over SEA continent on a selected day in 2001 via aircraft collection. They found highly K-enriched absorbing aerosol in a biomass-burning aerosol layer with lower NO_3^- and SO_4^{2-} composition. The high-K salt in the SEA-continent aerosol agrees with the findings in biomass-burning aerosols from other regions, such as Brazil (Martins et al., 1998) and South Africa (Li et al., 2003). Martins et al. (1998) measured black carbon mass absorption efficiencies of Brazilian

smoke particles and found that a high concentration of K relates to high black carbon absorption efficiencies (Martins et al., 1998). Biomass-burning aerosols with high black-carbon fraction were generally observed in SEA continent and Southern China (Uno et al., 2003). These aerosols are light-absorbing and hydrophobic or moderately hygroscopic.

Light scattering properties of the aerosols also related to land cover at current aerosol locations. First evidence is from the I1, I3, and S2 clusters, which had very high *SSA* (mean > 0.95) and were not found often in a particular wind direction. These aerosol clusters were found often over ocean surfaces (See Table 5.2). The high-*SSA* aerosols were probably mixed with ultra-fine-size marine aerosols. These marine aerosols are nanometer size and serve as cloud condensation nuclei (O'Dowd et al., 2002; Charlson et al., 1987). Okada et al. (2001), found low Na- and Cl-components in the individual 1997 Indonesian forest-fire aerosols. This suggests that these mixed aerosols are probably not sea salt aerosol, but they are likely to be sulfate (non sea-salt) aerosol. This sulfate marine aerosol is caused by emissions of dimethyl sulphide produced by planktonic algae in sea water and is oxidized in the atmosphere (Charlson et al. 1987). Both sulfate marine aerosol and low-level clouds developed from the aerosols scatter incoming radiation and contribute a global cooling effect (O'Dowd et al., 2002; Charlson et al., 1987; Langmann et al., 1998). In addition, this observed high-*SSA* aerosol over the ocean could also be a result of production of new fine particles by gas-to-particle conversion processes. Deshpande and Kamra (2002) measured aerosol size distribution over the Indian Ocean between 1996 and 1997. They found production of new nucleation-mode (with maximum

at 133 nm diameter) particles, probably from the gas-to-particle conversion processes, when aerosols and trace gases from the Indian subcontinent were transported over the Indian Ocean. Therefore, similar processes could be found in the forest-fire aerosols as well.

Another indication is from S4 and S5 clusters, which was observed often over Chinese territory and had no preference for other limiting factors. Both aerosol clusters exhibited similar light scattering efficiency (mean *SSA* = 0.91 and 0.92 for S4 and S5, respectively) and also similar size characteristics (mean α_a = 1.19 and 1.12, respectively). This scattering efficiency was higher than the original local SEA-continent forest-fire aerosol, which had *SSA* of 0.86. Major land uses in Southeast China were forests and rice paddies (Wu et al., 2003). Fresh local agricultural waste burning, however, should not cause this higher light scattering because they generally emit black carbon-rich particles (Rose et al., 2010), which have high light absorbability. High anthropogenic sulfur emissions from coal fires in Southeast China should be more responsible for this aerosol characteristic. These emissions later produced sulfate particles via gas-phase reaction (Barth and Church, 1999). These particles exhibited high light scattering efficiency and significantly induced negative radiative forcing at the surface (Gu et al., 2006).

5.5. CONCLUSION

This study considers the residual layer aerosols from the two forest-fire episodes; 2007 SEA continent and 2008 Indonesian fires, during two-month burning periods and investigated the dependence of their optical properties on four variables. These variables

are 1) wind speed/direction, 2) relative humidity (RH), 3) land use/cover (as a surrogate of fuel type) estimated from time-series analysis of Moderate Resolution Imaging Spectroradiometer (MODIS) surface reflectance, and 4) age of aerosol estimated from spatial-temporal analysis of MODIS active fire and the wind characteristics. The first two variables were acquired from the National Centers for Environmental Prediction (NCEP). The forest-fire aerosols with different optical properties were classified into separated clusters through factor and cluster analyses of Ozone Monitoring Instrument (OMI) aerosol variables, including aerosol optical depth (*AOD*), single-scattering albedo (*SSA*), and absorbing Angström exponent (α_a) as an aerosol size indicator. Each limiting variable was categorized and was tested for association with the individual OMI aerosol cluster membership using Pearson Chi-square test for independence.

Dependence between aerosol cluster membership and the limiting variables was significant for most cases, except for Indonesian aerosol age factor. Due to high wind speeds, aerosols older than one day were not observed. Lower wind speed was observed over SEA continent and wind speed effect on the SEA-continent aerosol dynamic properties was more obvious. Lowest mean *SSA* (0.86 at 442 nm) and no age preference were found in the aerosol cluster that strongly associated with the lowest wind speed. This aerosol cluster should be an original SEA-continent forest-fire aerosol and it had global warming potential.

Results from the Pearson Chi-square test suggested significant positive effects of RH on *AOD* and *SSA* for the aerosols from both fire episodes. For the SEA-continent aerosol, hygroscopic growth was less significant due to relatively low background RH in the

residual layer and its dominant hydrophobic properties (Ma et al., 2003; Uno et al., 2003). For Indonesian aerosol, increasing *SSA* with increasing size was evident for very fine aerosol group and increasing *SSA* with deceasing size was found in the coarser aerosol group. This finding indicated more complex dynamic scattering properties of the Indonesian forest-fire aerosols than its connection to hygroscopic growth alone as hypothesized in previous studies (Gras et al, 1999; Reid, 1998; Nessler et al., 2005).

Mixing biomass-burning aerosols with background aerosols limited by wind direction significantly caused an aging change in *SSA* for mixed aerosol in the residual layer. Based on the SEA-continent case, the change was more important for aerosols younger than two-day old. Background aerosol related to upwind sources from Indonesia potentially changed radiative forcing effects due to SEA-continent forest-fire aerosol from positive (*SSA* < 0.9) to negative (*SSA* > 0.9). Background aerosol related to upwind sources from the western Pacific Ocean, including northern Australia, could lower mean *SSA* of local Indonesian forest-fire aerosol to 0.89 from 0.96 and 0.95 (for I1 and I3 clusters, respectively) when these winds were less often from those directions. Wind direction effects on size of the forest-fire aerosols did not show a similar pattern with aerosol age for all wind directions. Size growth was marked for the observations with upwind sources from Indian Ocean for the SEA-continent case and upwind sources from SEA continent for the Indonesian case. More fine-size aerosol observed in aged aerosol groups was found with upwind sources from the South China Sea and Indonesia for SEA-continent case. In addition, the observations that were found with upwind sources from

eastern Asia had very fine size, probably due to secondary aerosols (Bridhikitti and Overcamp, 2009).

For zero-day-old aerosol, high *AOD* aerosol clusters were often observed over evergreen forest. Lower *AOD* clusters were observed either more often over deciduous forest or less often over evergreen forest, or both. These attributed to differences in RH level and mass density of organic matters. Types of burning fuels (from peat lands and from deciduous/evergreen forests) also affected aerosol optical properties. The high peat land-associated aerosol cluster exhibited finer size (mean α_a for 483.5 and 442 nm = 9.7) and higher scattering efficiency (*SSA* = 0.92) than those found often over deciduous and evergreen forests. The light scattering property of the aerosols also related to land cover at current aerosol locations. Aerosol clusters having very high *SSA* (> 0.95) were often found over ocean surfaces. SEA-continent aerosol clusters having slightly higher *SSA* (0.91 and 0.92 for S4 and S5, respectively) than that for the undisturbed local forest-fire aerosol cluster (*SSA* = 0.86) were found often over Chinese territory. This higher scattering could relate to high sulfur emissions over Southeast China.

CHAPTER SIX

TROPOSPHERIC OZONE PROFILES AND THEIR EFFECTS ON EOS-AURA COLUMN OZONE FOR SURFACE OZONE IMPLICATION

6.1. ABSTRACT

This study determined sensitivity and inconsistency associated with using the satellite-based tropospheric column ozone (TCO) to infer daily surface ozone level. In this study, data used for TCO estimation were from the Ozone Monitoring Instrument (OMI) and Microwave Limb Sounder (MLS), both onboard the Earth Observing System (EOS) Aura satellite. The evaluation was based on results from linear regression analyses using this satellite-based TCO and coincident TCO estimated from balloon-based ozonesonde measurements. The evaluation was for different tropospheric ozone profile shapes and for different geographical regions. Spatial and seasonal variation of the ozone profiles, column abundance, and budgets were investigated and discussed. There was significant latitudinal dependence on the linear relationship between OMI/MLS TCO and sonde-based TCO. Estimates of sonde-based TCO at zero OMI/MLS TCO (intercept, c) increased from 11.9 to 41.6 DU for low-latitude Pacific stations to the Scandinavian station, respectively. Consistently, sensitivity of OMI/MLS TCO to the changes of sonde-based TCO (linear slope, m) and degree of linear relationship between both data sets (R^2) decreased from m = 0.49 to 0.25 and R^2 = 0.29 to 0.05, respectively. Induction of upper troposphere ozone (UO) was one factor responsible for these latitudinal differences. Zonal dependence (Pacific and Atlantic regions) was apparent but not strong. These were

attributed to zonally prevalent ozone profile characteristics. Regardless of the UO effect, the satellite retrievals could explain ~50% of total variation in the sonde TCO using linear models. The presence of residual layer ozone caused the sensitivity to be degraded slightly. In addition, OMI/MLS TCO was more comparable to sonde TCO when ozone-rich layers were found near the ground than when those were found in free troposphere. Based on these findings, sole satellite observations could not appropriately infer surface ozone concentration without corresponding information on tropospheric ozone profile.

6.2. INTRODUCTION

Retrievals from earth observation satellites are the only informative source of long-term global ozone trends. The ozone Monitoring Instrument (OMI) and Microwave Limb Sounder (MLS) are among many available satellite-based instruments taking measurements of atmospheric ozone. The OMI and MLS are onboard the Aura spacecraft launched in July 2004 under NASA's Earth Observing System (EOS). One of its major OMI missions is to detect global trends of total atmospheric column ozone. While the OMI measures ozone abundance on a total atmospheric column basis, MLS is capable of providing vertical information on the ozone. Compared to typical nadir viewing instruments, the limb viewing geometry of MLS has longer atmosphere viewing paths and stronger thermal contrast between the atmosphere and the cool-dark space. These conditions can maximize signal intensity and provide more accurate vertical information of many atmospheric gaseous species, including ozone. However, the accuracy of MLS vertical ozone retrieval degrades largely in the troposphere (Livesey et al., 2007) because

of reduced thermal contrast between the atmosphere and surface for typical infrared bands (Martin, 2008).

One technique to derive tropospheric column ozone (TCO) is subtracting measurements of stratospheric column ozone (SCO) retrieved from MLS from total column ozone retrieved from OMI. The complete global validation of the TCO acquired from this technique had been published in the work of Ziemke et al. (2006). In their study, TCO was compared with both seasonal average of ozonesonde measurements and results from the Global Modeling Initiative's Chemical Transport Model. Their results show good agreement with respect to zonal and seasonal variation, except over the Sahara desert. Kar et al. (2010) investigated the possibility of detecting urban signatures in the OMI/MLS TCO retrievals. Their finding indicated that these retrievals could detect higher ozone over polluted areas; including Beijing, New York, Sao Paulo, and Mexico City. Monthly average TCO was used in their study. These findings do not show sufficient sensitivity of the OMI/MLS-derived TCO to correlate with daily changes of the surface ozone level, which is crucial for using these retrievals to understand of surface ozone behavior.

In this study, the satellite sensitivity of the changes of surface ozone level was evaluated from the linear relationships between the satellite-based TCO and coincident TCO estimated from balloon-based ozonesonde measurements for different ozone profile shapes. These TCOs were integrated column ozone from the ground to tropopause layer. The tropospheric ozone profile helps identify vertical positions of any ozone-rich layer,

which accounts significantly to TCO. In addition, the ozone profile is one factor limiting accuracy of OMI total column ozone retrievals. OMI forward and inverse models in the ozone profile retrieval algorithm use a simulated radiance weighting functions in the ozone Hartley and Huggins bands (Worden et al., 2007). The simulations are based on prior knowledge of land surface reflectivity and the vertical distribution of ozone absorption cross-section, radiance scattering by cloud, aerosol, and other atmospheric gaseous molecules (Worden et al., 2007). Therefore, accuracy of OMI ozone retrievals can be improved if the modeled ozone profiles are good representations of the actual profiles.

The objectives of this study are 1) to investigate the temporal and spatial variation of tropospheric ozone profiles, column abundance, and budgets and 2) to determine linear regression models for the relationship of TCO derived from OMI/MLS retrievals and that from the ozonesonde measurements for different tropospheric ozone profile shapes. Results obtained from the models were then used to evaluate the sensitivity of the OMI/MLS TCO on daily changes of the surface ozone level and to evaluate effects of the ozone profile shape on this sensitivity.

6.3. METHODOLOGY

6.3.1. Site description

A map and details of ten ozonesonde stations considered in this study are in Figure 6.1 and Table 6.1, respectively. To explain spatial variations of the tropospheric ozone characteristics, these stations were classified to represent the data for low, mid, and high

latitudes. In addition, differences in ozone profile shapes observed at Pacific and Atlantic stations were also discussed. The Southern Hemisphere tropospheric ozone is not included here due to limited ozonesonde data sets available.

The three low-latitude stations are in Watukosek, Indonesia; Sepang Airport, Malaysia; and Maxaranguape (Natal), Brazil. These locations have humid tropical climates. These areas have less annual variation of sunshine hours and temperature, but the amount of seasonal rainfall varies resulting wet-and-dry climate system. The Watukosek station is surrounded by agricultural lands, primarily rice paddies. The Sepang Airport station is surrounded by plantations and forests. Both stations are influenced by easterly winds from the Pacific Ocean. Typically the driest period for both Pacific stations is between June and August and the wet period is between December and April. The Natal station is coastal environment surrounded by forest and mangroves and is adjacent to Atlantic Ocean. Its typical wet period occurs in March to July and its dry period is from September to January (Logan and Kirchhoff, 1986).

There are five mid-latitude stations, three of which are in the United State (US) and two are in East Asia. The US stations are in Houston (TX, in the South), Huntsville (AL, in the Southeast), and Narragansett (RI, in the Northeast). Data acquired from these US stations represented Atlantic ozone. Houston is populated urban city, which frequently experienced high-level ozone. Huntsville is more rural and surrounded by deciduous trees. Narragansett is characterized as rural area adjacent to Atlantic Ocean. The East

Asian stations are located in populated urban areas in Naha (Okinawa), Japan and Hong Kong Observatory. Data acquired from both stations represented Pacific ozone.

Two high-latitude stations are in De Bilt, Netherlands and Ny Alesund, Norway. The De Bilt station is located in a farming-based municipality. The Ny Alesund station is located in an undisturbed area west of the Norwegian Sea. Both stations have coastal influences.

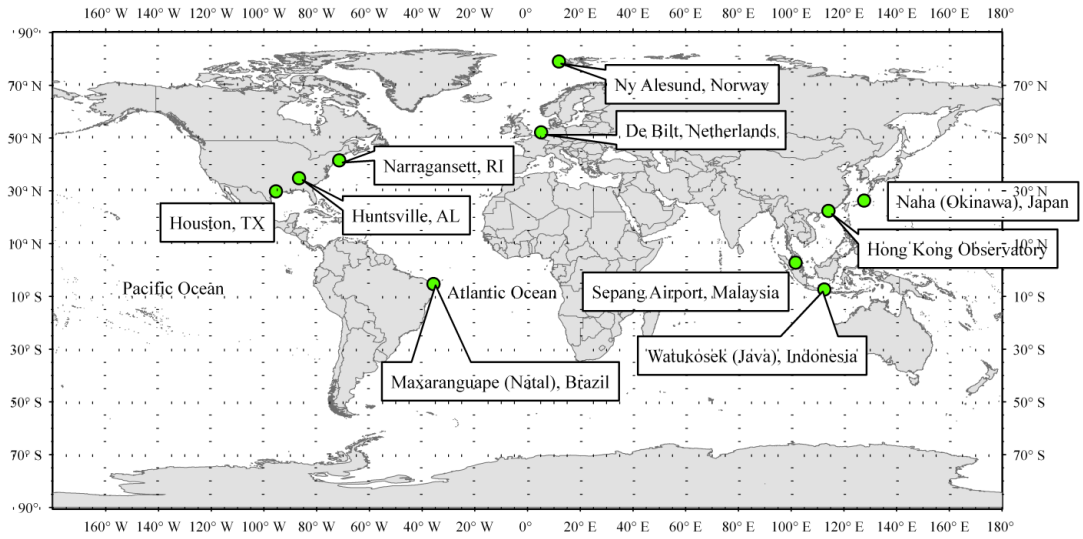

Figure 6.1. Map of ten ozonesonde stations considered in this study

6.3.2. Data description

Satellite retrievals used to derive the tropospheric column ozone (TCO) were from Microwave Limb Sounder (MLS) and Ozone Monitoring Instrument (OMI). Both MLS and OMI are onboard the Aura spacecraft which has a near-polar sun-synchronous orbit at 705-km altitude, crossing the equator (for ascending orbit) at approximately 1:45 pm.

Table 6.1. Details on ten ozonesonde stations considered in this study

Station name	Latitude, Longitude	Elevation from mean sea level, m	Spatial classifications	Data period	Number of observations				WOUDC ozonesonde citation
					DJF	MAM	JJA	SON	
Watukosek (Java), Indonesia	7.50° S, 112.60° E	50	Low latitude/ Pacific	2005-2008	9*	7	12*	10	Hokkaido U. & NASDA. Retrieved Nov 1, 2010
Sepang Airport, Malaysia	2.73° N, 101.70° E	17	Low latitude/ Pacific	2005-2006	6	7	6	5	MMS. Retrieved Nov 1, 2010
Maxaranguape (Natal), Brazil	5.43° S, 35.64° W	14	Low latitude/ Atlantic	2005-2010	30	27	37	34	INPE & NASA-WFF. Retrieved Nov 30, 2010
Huntsville, AL	34.72° N, 86.64° W	196	Mid latitude/ Atlantic	2005-2007	12	12	24	18	UAH. Retrieved Nov 29, 2010
Houston, TX	29.72° N, 95.4° W	19	Mid latitude/ Atlantic	2006	0	14	17	0	Valparaiso U. Retrieved Nov 1, 2010
Narragansett, RI	41.49° N, 71.42° W	21	Mid latitude/ Atlantic	2006	0	9	19	0	U. Rhode Island. Retrieved Nov 4, 2010
Naha (Okinawa), Japan	26.21° N, 127.69° E	28	Mid latitude/ Pacific	2009-2010	4	6	3	5	JWA. Retrieved Nov 7, 2010
Hong Kong Observatory	22.31° N, 114.17° E	66	Mid latitude/ Pacific	2005-2009	22	26	21	25	HKO. Retrieved Nov 12, 2010
De Bilt, Netherlands	52.10° N, 5.18° E	4	High latitude	2005-2009	26	29	30	24	KNMI. Retrieved Nov 4, 2010
Ny Alesund, Norway	78.93° N, 11.95° E	11	High latitude	2005-2006	15	15	13	9	AWI-NA. Retrieved Nov 4, 2010

* Without underline indicates dry period; with underline indicates wet period

Winter Spring Summer Fall

OMI is nadir-viewing near-UV/Visible solar backscatter spectrometer, which provides nearly global coverage in one day. OMI total column ozone level 2 (L2, swath) data with a spatial resolution of 13×24 km^2 at nadir were acquired for this study. This product is from the Total Ozone Mapping Spectrometer (TOMS) algorithm, using two spectral bands centered at 317.5 nm and 331.2 nm to derive the ozone. Overall the quality of this OMI total ozone is similar to that from TOMS, having root-mean squared error of 1-2%, depending on solar zenith angle, aerosol amount, and cloud cover (Ozone Processing Team-NASA/GSFC, 2008).

The MLS instrument is a thermal-emission microwave limb sounder that measures vertical profiles of ozone from the upper tropospheric layer through the upper mesosphere. With its forward viewing, MLS measurements are taken about seven minutes before OMI nadir views. However both can be referred as collocated data sets. The ozone profile is taken from the 240-GHz band with vertical resolution of 3 km for the standard ozone product in the upper troposphere and stratosphere, and 4 to 6 km in the upper mesosphere. The ozone volume mixing ratio product L2 version 2.2 was acquired to this study. Its estimated single-profile precision varies from 0.1 to 0.3 ppm_v (2 to 15%) from 46 to 0.5 hPa (approximately 20 to 50 km). The estimated precision for MLS column ozone abundances from pressures of 215 to 100 hPa (approximately 12 to 16 km) is 2% or less, based on simulated MLS retrievals (Livesey et al., 2007). Froidevaux et al. (2008) show good agreement in the latitudinal distributions obtained from MLS and from coincident profiles from other satellite instruments, as well as from

coincident aircraft lidar data. Retrievals at pressure from 215 hPa to 0.02 hPa are recommended for use (Livesey et al., 2007).

Vertical profiles of ozone partial pressure and relative humidity at the ten stations were acquired from the World Ozone and Ultraviolet Radiation Data Centre (WOUDC), Environment Canada (available at http://www.woudc.org/index_e.html). The ozone measurements are made with balloon-borne ECC (electrochemical concentration cell)-type sonde. This is based on the reaction of potassium iodide with ozone (Logan, 1999). The comparison of ECC sondes with an accurate UV photometer in a laboratory chamber shows less than ± 5% bias (Logan, 1999). For tropospheric ozone measurements, the sonde accuracies are about 10%, but the accuracy may be degraded to about 15% in the case of low ozone concentrations, <10 ppb_v (Logan, 1999).

All available data acquired between noon to 2:00 pm local time, close to Aura satellite's overpass time, from year 2005 to 2010 were used for the analyses. The number of observations used in this study is shown in Table 6.1. The satellite data sets used here correspond to the ten ozonesonde stations. The OMI L2 data set was acquired from Mirador, an Earth Science data search tool (available at http://mirador.gsfc.nasa.gov/), and the MLS L2 data set was from Giovanni web-based data application (available at http://disc.sci.gsfc.nasa.gov/giovanni). Both tools were developed by Goddard Earth Sciences Data and Information Services Center, National Aeronautics and Space Administration (NASA).

6.3.3. Data analysis

Tropospheric column ozone (TCO) calculations

The satellite-based TCO was calculated by subtracting MLS-derived SCO from OMI total column ozone. The MLS SCO was estimated by the method of pressure integration of ozone volume mixing ratio from 0.46 hPa to 215 hPa, approximately at the tropopause, using equation 1,

$$\text{MLS SCO (Dobson Unit, DU)} = \frac{\sum_{i=215hPa}^{0.46hPa}\left(x_{v,i}\frac{P_i N_A}{10\times g\times M_r}\ln\left[\frac{\sqrt{P_{i+1}}}{\sqrt{P_{i-1}}}\right]\right)}{2.69\times10^{16}}, \quad \text{(Eq.1)}$$

where $x_{v,i}$ is MLS ozone volume mixing ratio at i (unitless), i is MLS pressure level, P_i is pressure i in Pa (for uppermost pressure level, P_{i+1} = 21.5 Pa. for lowermost pressure level, P_{i-1} = 31,623 Pa), N_A is number of molecule mole^{-1} = 6.022×10^{23} molecule mole^{-1}, M_r = air molecular weight which set to 29 g mole^{-1}, and g = 9.81 m s^{-2}. The TCO is in Dobson Unit (DU) which is the unit of ozone column density. At standard temperature and pressure, one DU is 2.69×10^{16} ozone molecules cm^{-2}.

Similarly, sonde-based TCO was calculated from integrating ozone partial pressure from the ground level to the level at approximately 215 hPa using equation 2,

$$\text{Ozonesonde TCO (Dobson unit, DU)} = \frac{\sum_{j=\text{ground}}^{\sim215hPa}\left(\frac{P_{O_3,j}N_A}{10\times g\times M_r}\ln\left[\frac{\sqrt{P_{j+1}}}{\sqrt{P_{j-1}}}\right]\right)}{2.69\times10^{16}}, \quad \text{(Eq.2)}$$

where j is ozonesonde pressure level and $P_{O_3,j}$ is ozone partial pressure at j in Pa. For uppermost pressure level, $P_{O_3,j+1}$ is approximately 21,500 Pa. For lowermost pressure level, $P_{O_3,j-1}$ is the pressure at ground.

In this study, the tropopause level is fixed at 215 hPa, which is approximately 10 to 12 km altitude. This level might not represent the actual tropopause level, where ozone concentration abruptly increases with altitude. For the Northern Hemisphere, the actual tropopause level varies from approximately 15 to 17 km for low latitudes, 7 to 15 km for mid-latitudes, and 7 to 12 km for high-latitudes (Lamsal et al., 2004). Therefore, the TCO pronounced in this study could either include contribution from lower stratosphere ozone, especially for higher latitudes, or exclude partial contribution of upper troposphere ozone, especially for low latitude. However, this study investigated agreement between the satellite-derived column ozone and the measurements from ozonesonde and focuses on surface ozone implications. Therefore, the definition of the tropopause height should not be a vital constraint here.

Identification tropospheric ozone layers

In this study, the surface-contributed column ozone was the integrated column ozone from the ground to the top of boundary layer (BL), which here was defined by the first height above ground that had significant increasing (or '+*r*') or decreasing (or '-*r*') of sonde ozone partial pressure with height. The layer with significant '+*r*' and '-*r*' were evaluated from significant changes of the sonde ozone vertical profiles between these observed in three atmospheric layers (averaged over 10 hPa interval) above and these

observed in three layers below. The significant changes are either more than 0.5 mPa ($\Delta[O_3] > 0.5\,\mathrm{mPa}$) or more than three times changing of the rate ('+*r*' or '-*r*'). In this study, top of BL was assumed to be at least 1 km from the ground in order to eliminate effects of stable BL on surface ozone removals via dry deposition and titration by oxides of nitrogen, NO_x (Zhang and Rao, 1999). The top altitude of BL defined here was determined from the sonde ozone gradient alone and it might not be the same with those evaluated using temperature and/or relative humidity gradients.

The middle troposphere was simply defined as the layer above BL to 7 km above ground. The upper troposphere was defined by the layer from 7 km to 215 hPa, which is set as the tropopause height in this study. The 7-km cut-point was the lowest estimate of global tropopause height from the literature (Lamsal et al., 2004; Stajner et al., 2008); therefore, the layer above this height tends to incorporate stratospheric ozone.

Tropospheric ozone budgets are mainly from four processes: (1) stratrospheric intrusion; (2) photochemical reactions from lightning-generated NO; (3) boundary layer photochemistry; and (4) advective transport of aged ozone or its precursors (Thompson et al., 2007). The first and second processes play roles in middle to upper troposphere. The third process directly contributes to surface-borne ozone. The fourth process could contribute to surface ozone. This process is associated with formation of nocturnal residual layer, the stable surface layer forming at night. The ozone can be transported in the nocturnal residual layer aloft during the night over long distances with the prevailing winds. In the morning with the growth of BL reaching the residual layer (called

fumigation), the pollutant can be entrained downward into the ground (Zhang and Rao, 1999). All observations used for the analysis were acquired from noon to 2:00 pm local time, when both photochemistry and vertical mixing should control surface ozone concentration (Zhang and Rao, 1999). However, there is a possibility that the BL does not reach into the residual layer and that ozone is persistently trapped in the residual layer during the time of observations.

Categorization sonde ozone partial pressure profiles

In this study, sonde ozone partial pressure profiles were classified into four categories (see Figure 6.2 for illustration). These are 1) those lacking both pronounced surface enhanced ozone (SO) and residual layer ozone (RO), 2) with SO and without RO, 3) with RO and without SO, and 4) with both SO and RO. The first category was classified as observations having no significant changes of ozone partial pressure from the ground to at approximately 7 km or higher. This indicates high vertical mixing that suppresses the formation of surface-borne ozone. The presence of SO was determined from observing significant '-*r*' without '+*r*' found in its lower altitude. This presence of SO indicates high BL photochemical activity. This SO could also include fumigation-breakup RO (or its precursor). SO is mixed in the confined layer from the ground; therefore, it has more potential to impact human health than the first ozone profile category. The presence of RO was determined by observing '+*r*' above 1 km from ground and '-*r*' at higher altitude. The sensitivity of the satellite-based TCO for each ozone profile category was investigated.

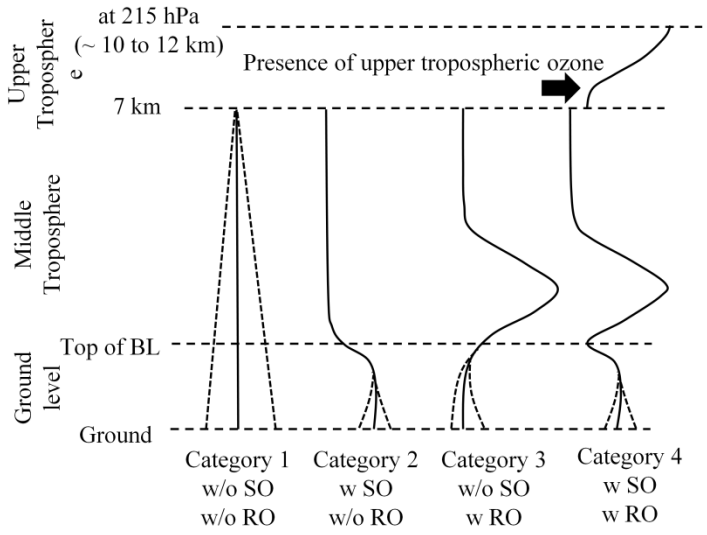

Figure 6.2. Four ideal ozone vertical profile categories referred into this study. Note: SO is surface enhanced ozone, RO is residual layer ozone, "w/o" is "without", "w" is "with"

For each ozone profile category, observations with and without major contribution of upper troposphere ozone (UO) were also analyzed separately. This UO contribution was evaluated from a presence of significant increases of ozone concentration without significant decreases from 7 km altitude to 215 hPa. This UO could be from stratospheric ozone intrusion, convection of photochemistry-induced ozone influenced by lightning-generated NO, and/or advection of polluted air masses from an outside area. The stratospheric air mass is dry, thus air masses with stratospheric ozone should have low relative humidity. Because of this, stratospheric ozone intrusion could be identified with a dry air mass. In this study, stratospheric ozone signature was assigned to observations with decreasing averaged relative humidity in three layers (10 hPa interval) above a base of UO-rich layer by 8 percentage units (%) or more from those averaged in three layers below ($\Delta RH_{U\text{-}L} = RH_{upper} - RH_{lower} \leq -8\%$).

6.4. RESULTS AND DISCUSSION

6.4.1. Spatial and seasonal variations of tropospheric ozone profiles, column abundance, and budgets

Examples of these ozone profiles in each category are shown in Figure 6.3. Climatology of these tropospheric ozone profiles together with their column abundance and budgets are discussed separately for each geographical region.

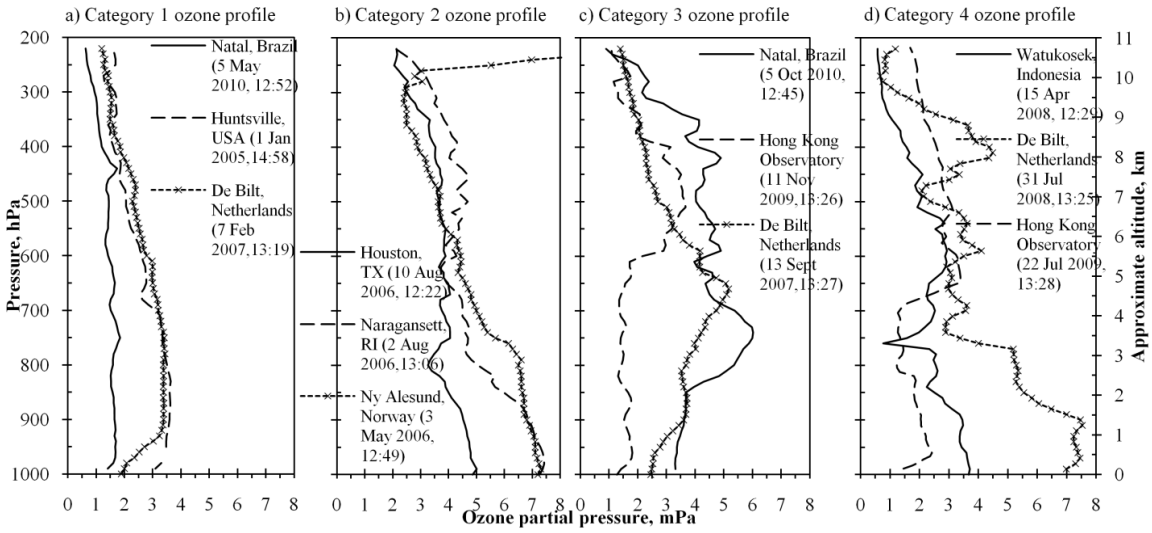

Figure 6.3. Examples of sonde ozone partial pressure profiles classified into the four categories. Note: Time is shown in local time.

Low-latitude Pacific region

Mean TCO for the low-latitude Pacific stations, shown in Table 6.2, did not show much seasonal variation. The lowest TCO, 19 DU, was observed in the driest periods from June to August (JJA). The highest TCO, 24 DU, was found later from September to November (SON), when local biomass burning over Java is common (Komala et al., 1996).

Typical ozone profile categories shown in Figure 6.4 indicate that surface enhanced ozone, SO, predominated at both low-latitude Pacific stations in all seasons (83% to 88%, categories 2 + 4, of total seasonal observations). In low latitudes, monthly sunshine hours and temperature do not vary significantly, therefore active photochemical production of ozone can be observed throughout the year. It is even more pronounced when local biomass burning emissions are active. This SO was likely observed with residual layer ozone, RO, (category 4) from June to February, covering the driest period, and was often observed without RO (category 2) in the wet periods from March to May (MAM). Komala (1996) observed tropospheric ozone behavior in Indonesia via analyzing ozonesonde measurements. They also found more of a category-4 ozone profile in the dry periods and hypothesized that long-range transport of biomass burning emissions could be responsible for the ozone enhancement in the middle troposphere.

The residual layer ozone, RO, contributed an all-season higher fraction to TCO, from ~37% in SON and DJF to ~48% in MAM, than the surface ozone (see Table 6.3). Apparent RO can be also found in the wet periods in higher altitude as a result of long-range transport of ozone-rich air masses produced by biomass burning emissions in the Asian continent (Komala et al., 1996; Thompson et al., 2003).

The stratospheric ozone signature of a significant decrease in relative humidity with altitude was not observed at these stations. This should be attributed to a lower upper boundary at 215 hPa, ~10 to 12 km, than the typical tropopause level, ~15 to 17 km for low latitudes (Lamsal et al., 2004).

Table 6.2. Estimates TCOs (in DU) from OMI/MLS retrievals and from ozonesonde measurements for different stations

		Low latitude		Mid latitude				High latitude	
	Month	Watukosek (Java), Indonesia / Sepang Airport, Malaysia	Maxaranguape (Natal), Brazil	Houston, TX	Narragansett, RI	Huntsville, AL	Naha (Okinawa), Japan / Hong Kong Observatory	De Bilt, Netherlands	Ny Alesund, Norway
OMI Total column ozone, DU	DJF	247 ± 1.3 (13)*	266 ± 4.1 (29)	-	-	293 ± 11.1 (12)	252 ± 4.5 (25)	305 ± 10.0 (26)	-
	MAM	255 ± 2.5 (14)	268 ± 5.2 (27)	276 ± 5.4 (14)	356 ± 14.2 (9)	316 ± 8.4 (12)	287 ± 5.5 (32)	360 ± 7.5 (28)	385 ± 11.6 (15)
	JJA	254 ± 1.6 (18)	275 ± 4.3 (37)	296 ± 2.5 (16)	306 ± 2.5 (19)	307 ± 2.3 (24)	285 ± 5 (24)	332 ± 7.2 (30)	306 ± 8.0 (13)
	SON	252 ± 1.9 (15)	275 ± 3.1 (34)	-	-	282 ± 4.5 (18)	265 ± 3.6 (30)	274 ± 4.4 (24)	274 ± 5.4 (9)
MLS-integrated stratospheric column ozone, DU	DJF	229 ± 1.8 (15)	232 ± 1.2 (30)	-	-	266 ± 9.5 (12)	218 ± 2.3 (26)	292 ± 8.7 (26)	299 ± 17.3 (15)
	MAM	236 ± 1.8 (14)	233 ± 1.5 (27)	240 ± 4.6 (14)	312 ± 10.3 (9)	286 ± 7.6 (12)	246 ± 2.4 (32)	326 ± 7.0 (29)	362 ± 11.0 (15)
	JJA	234 ± 1.7 (18)	238 ± 1.6 (37)	262 ± 2.2 (16)	274 ± 3.9 (19)	263 ± 2.9 (24)	251 ± 1.5 (24)	298 ± 4.5 (30)	279 ± 7.9 (13)
	SON	233 ± 1.2 (15)	242 ± 1.5 (34)	-	-	251 ± 3.6 (18)	234 ± 3.3 (30)	252 ± 3.4 (24)	255 ± 3.6 (9)
OMI/MLS-derived TCO, DU	DJF	19.2 ± 2.0 (15)	34.4 ± 4.3 (29)	-	-	27.1 ± 4.4 (12)	34.8 ± 3.8 (23)	18.7 ± 2.7 (26)	-
	MAM	19.3 ± 1.5 (14)	34.8 ± 5.6 (27)	35.9 ± 3.4 (14)	51.0 ± 6.9 (8)	32.8 ± 5.0 (11)	41.2 ± 4.9 (28)	33.1 ± 2.8 (32)	24.7 ± 3.5 (14)
	JJA	20.0 ± 1.7 (18)	37.1 ± 4.5 (37)	34.0 ± 1.8 (16)	33.7 ± 2.6 (18)	44.0 ± 2.4 (24)	33.3 ± 5.3 (29)	37.1 ± 4.5 (24)	27.3 ± 2.5 (13)
	SON	19.1 ± 1.9 (15)	34.1 ± 1.6 (34)	-	-	31.1 ± 2.0 (18)	32.7 ± 2.4 (21)	27.3 ± 2.5 (30)	21.7 ± 3.8 (8)
Ozonesonde-integrated TCO, DU	DJF	20.4 ± 1.0 (15)	26.9 ± 0.9 (30)	-	-	32.2 ± 2.4 (12)	29.6 ± 0.9 (26)	33.1 ± 1.5 (26)	37.8 ± 3.4 (15)
	MAM	22.3 ± 1.9 (14)	21.2 ± 1.0 (27)	29.9 ± 1.0 (14)	45.8 ± 3.7 (9)	43.1 ± 2.1 (12)	38.7 ± 1.2 (32)	43.2 ± 2.2 (29)	53.5 ± 3.1 (15)
	JJA	18.9 ± 1.0 (18)	27.1 ± 1.0 (37)	41.0 ± 1.6 (17)	39.2 ± 1.0 (19)	44.4 ± 1.5 (24)	27.3 ± 1.0 (24)	42.4 ± 1.4 (30)	44.3 ± 1.7 (13)
	SON	23.6 ± 1.4 (15)	35.3 ± 0.8 (34)	-	-	30.9 ± 0.7 (18)	31.6 ± 1.2 (30)	31.9 ± 1.0 (24)	42.3 ± 1.8 (9)

* Mean ± Standard error (Number of observations)

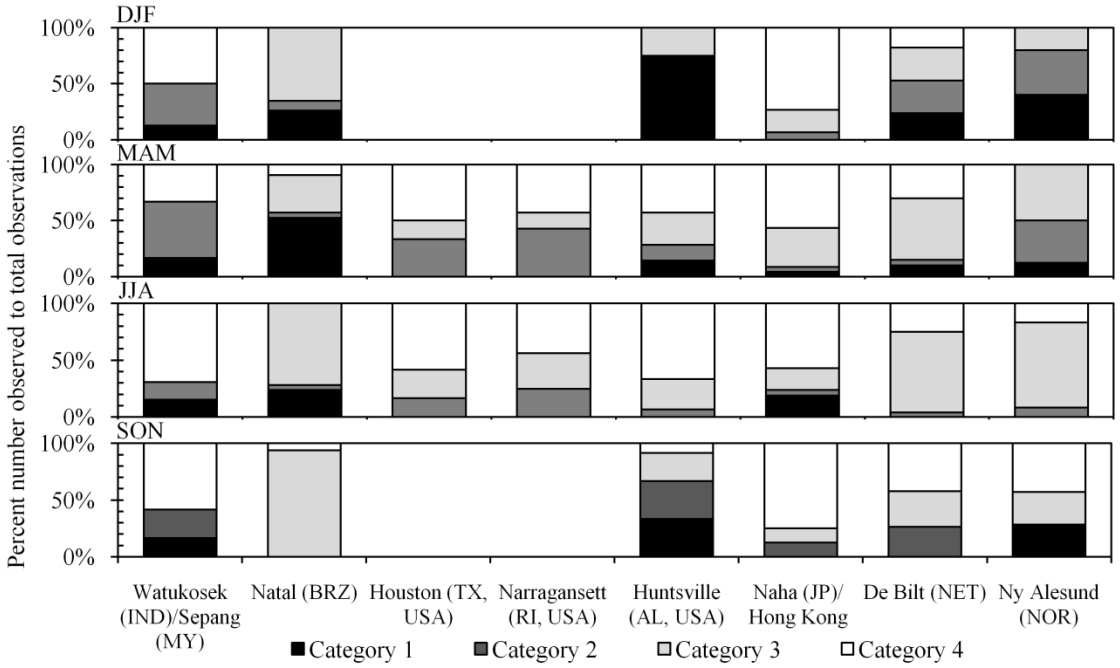

Figure 6.4. Seasonal distributions of four ozone profile categories

Low-latitude Atlantic region

From Table 6.2, mean TCO observed at the low-latitude Atlantic station (Natal, Brazil) had a minimum of 21 DU in the early wet seasons (MAM) and a maximum of 35 DU in the early dry seasons (SON). All-season largest contribution to the TCO was RO, which provided from ~26% of TCO in the later wet seasons (JJA) to ~37% in the early wet season (see Table 6.3). The presence of RO without SO (category 3 in Figure 6.4) predominated (65% to 94% of total seasonal observations) in all seasons; except in the early wet seasons in which the vertically mixed ozone profile (category 1) was more frequent (52%).

Table 6.3. Seasonal distributions of surface-contributed ozone, residual layer ozone (RO), and upper troposphere ozone (UO) fractions in tropospheric column ozone (TCO, in DU) estimated from sonde ozone partial pressure profiles for different stations

Month	Locations	Fraction of ozonesonde TCO[a], DU		
		Surface ozone	RO	UO
DJF	Watukosek (IND)/Sepang Airport (MY)	0.19±0.06 (8)[b]	0.37±0.06 (7)	NO
	Natal (BRZ)	0.17±0.04 (17)	0.27±0.03 (32)	0.18±0.03 (5)
	Houston (USA)		ND	
	Narragansett (USA)		ND	
	Huntsville (USA)	0.08±0.02 (2)	0.23±0.08 (4)	0.18±0.04 (3)
	Naha (JP)/ Hong Kong	0.19±0.03 (15)	0.49±0.08 (21)	0.17±0.05 (3)
	De Bilt (NET)	0.27±0.06 (13)	0.33±0.04 (14)	0.18±0.02 (14)
	Ny Alesund (NOR)	0.33±0.07 (6)	0.24±0.08 (5)	0.24±0.03 (8)
MAM	Watukosek (IND)/Sepang Airport (MY)	0.26±0.04 (5)	0.48±0.06 (2)	NO
	Natal (BRZ)	0.14±0.02 (10)	0.37±0.04 (9)	0.15±0.09 (3)
	Houston (USA)	0.34±0.06 (6)	0.27±0.07 (4)	0.22±0 (1)
	Narragansett (USA)	0.28±0.07 (7)	0.34±0.05 (4)	0.21±0.05 (4)
	Huntsville (USA)	0.20±0.04 (5)	0.27±0.05 (5)	0.08±0.03 (3)
	Naha (JP)/ Hong Kong	0.12±0.02 (21)	0.50±0.12 (20)	0.15±0.07 (3)
	De Bilt (NET)	0.18±0.02 (18)	0.28±0.04 (17)	0.21±0.03 (16)
	Ny Alesund (NOR)	0.29±0.06 (7)	0.10±0.01 (4)	0.26±0.04 (11)
JJA	Watukosek (IND)/Sepang Airport (MY)	0.30±0.09 (11)	0.41±0.14 (9)	NO
	Natal (BRZ)	0.18±0.03 (19)	0.26±0.04 (18)	0.08±0.03 (2)
	Houston (USA)	0.20±0.03 (12)	0.46±0.07 (10)	0.32±0 (1)
	Narragansett (USA)	0.21±0.03 (16)	0.35±0.04 (12)	0.16±0.02 (8)
	Huntsville (USA)	0.24±0.03 (15)	0.23±0.02 (14)	0.13±0.04 (3)
	Naha (JP)/ Hong Kong	0.17±0.06 (17)	0.39±0.16 (16)	0.20±0.08 (2)
	De Bilt (NET)	0.19±0.02 (24)	0.29±0.04 (23)	0.19±0.03 (13)
	Ny Alesund (NOR)	0.24±0.07 (12)	0.17±0.03 (11)	0.23±0.03 (9)
SON	Watukosek (IND)/Sepang Airport (MY)	0.24±0.04 (10)	0.37±0.06 (7)	NO
	Natal (BRZ)	0.12±0.01 (32)	0.27±0.03 (32)	0.14±0.02 (4)
	Houston (USA)		ND	
	Narragansett (USA)		ND	
	Huntsville (USA)	0.24±0.04 (8)	0.22±0.08 (4)	0.10±0.03 (3)
	Naha (JP)/ Hong Kong	0.19±0.03 (24)	0.49±0.08 (21)	0.11±0.02 (2)
	De Bilt (NET)	0.27±0.03(19)	0.33±0.04 (14)	0.12±0.01 (11)
	Ny Alesund (NOR)	0.19±0.04 (5)	0.24±0.08 (5)	0.30±0.03 (9)

[a] Measured from noon to 2:00 pm local time; [b] Mean ± Standard error (Number of observations)

ND = No data; NO = Not observed

This RO should be influenced by a combination of local and long-range transport biomass burning from northern Africa. The northern African air masses are transported through interaction of the Harmattan flow toward the Southwest and the Intertropical Convergence Zone. This interaction creates a zonal wave-one feature in the middle to lower upper troposphere (Sauvage et al., 2006). The wave-one persists throughout the year over the Atlantic (Thompson et al., 2003; Sauvage et al., 2006). This agrees with our observing the dominant contribution of RO in all seasons. The biomass burning emissions, including NO_x, CO, and hydrocarbons, could enter the wave-one system and induce production of ozone in the residual layer as they are transported to the Natal station (Logan and Kirchhoff, 1986).

Besides exhibiting a seasonal maximum of TCO, in SON, overall peak ozone mixing ratios was also highest seasonal value ranging from 60 ppb_v to 102 ppb_v (see Figure 6.5-c.4); whereas its seasonal mean at the ground was 25 ppb_v (see Figure 6.6-b). Figure 6.5-c.4 shows that all the peak ozone values found in SON were at elevations 1.4 km to 5 km.

Upper troposphere ozone, UO, was found in all seasons; but its contribution to TCO was the highest, 18%, in the late dry seasons (DJF). UO observed in the wet seasons, however, was not likely from stratospheric-tropospheric air mass exchange because it was not found with the stratospheric ozone signature (observed $\Delta RH_{U-L} = -1.3\%$ to +1.2%). In the dry seasons, three out of nine UO observations were likely from the stratospheric intrusion because they had the stratospheric ozone signature of very dry air.

Mid-latitude Pacific region

Mean TCO in Table 6.2 shows a spring maximum (~39 DU) and summer minimum (~27 DU) pattern, which is typically found over Hong Kong and lower latitudes of Japan (Chan et al., 1998; Chan et al., 2003; Liu et al., 1999; Liu et al., 2002). In our study, RO (categories 3 + 4) was observed in ~92% of the total springtime observations and this ozone contributed ~50% to the TCO. The RO could be long-range transport photochemical ozone produced from biomass burning emissions over the Southeast Asian (SEA) continent (Chan et al., 1998; Chan et al., 2003; Liu et al., 1999; Liu et al., 2002). Peak ozone mixing ratios for spring were often at elevations from 3 km to 4.5 km (see Figure 6.5-d.2). This finding corresponded with evidence from back trajectory analysis. In one case on 8 April 2009 at 13:00 local time, shown in Figure 6.7-b, the air mass at 3 km elevation observed over the Hong Kong station had a trajectory at low altitudes over SEA continent before moving over the station. Therefore, the long-range transport SEA biomass burning emissions could be responsible for the peak ozone at this elevation.

RO fraction predominated in all seasons (> 75% of seasonal observations—see Figure 6.4). However, this ozone fraction in TCO was at a minimum in summer. This can be explained by seasonal wind directions, which were often from the Pacific Ocean in summer. One case of this wind characteristic is illustrated in Figure 6.7-c.

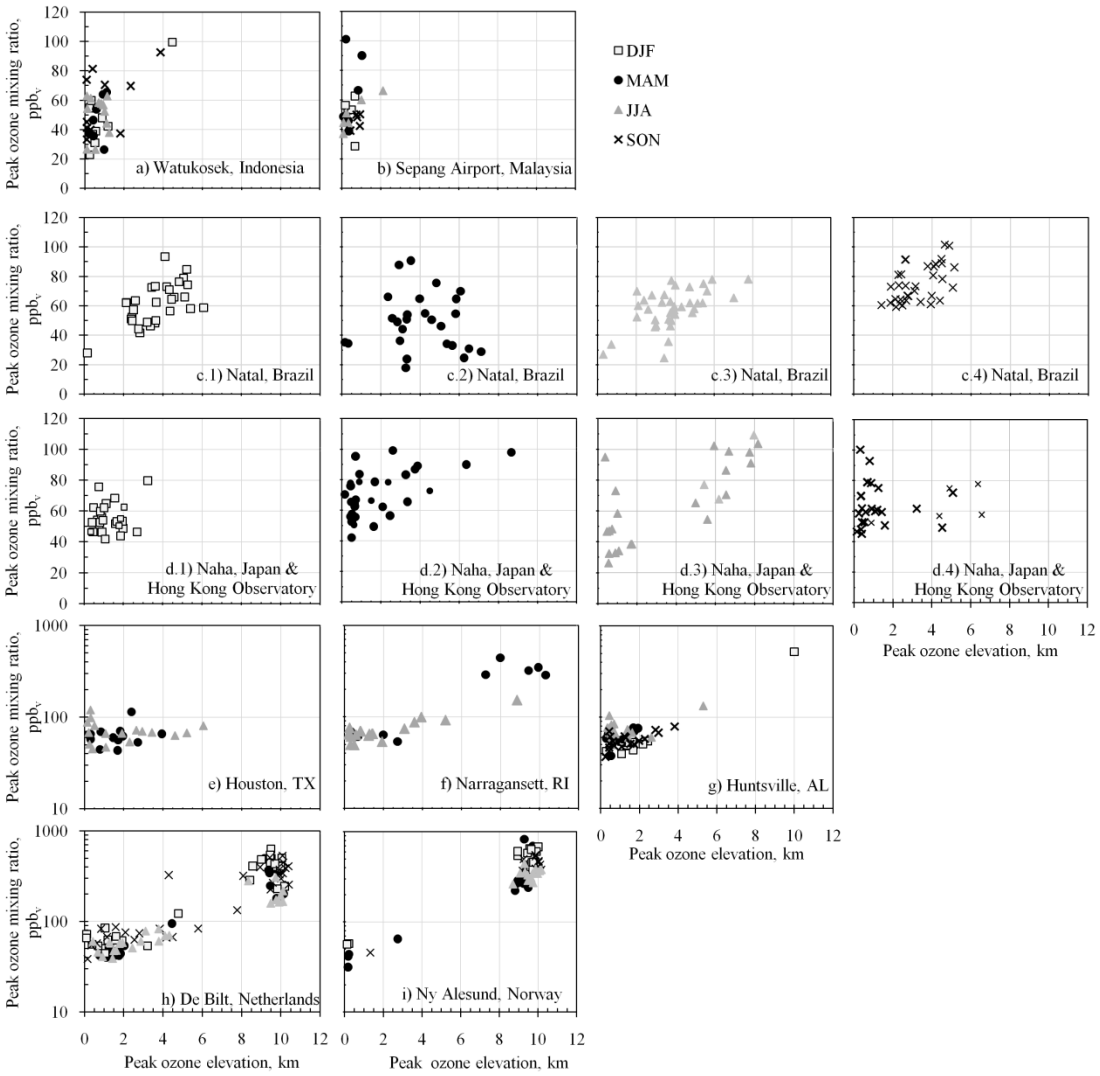

Figure 6.5. Scatter plots between peak sonde-based ozone mixing ratio and its observed altitude by season and by station. Note: there are no sonde observations available for the Houston and the Narragansett stations from September to February

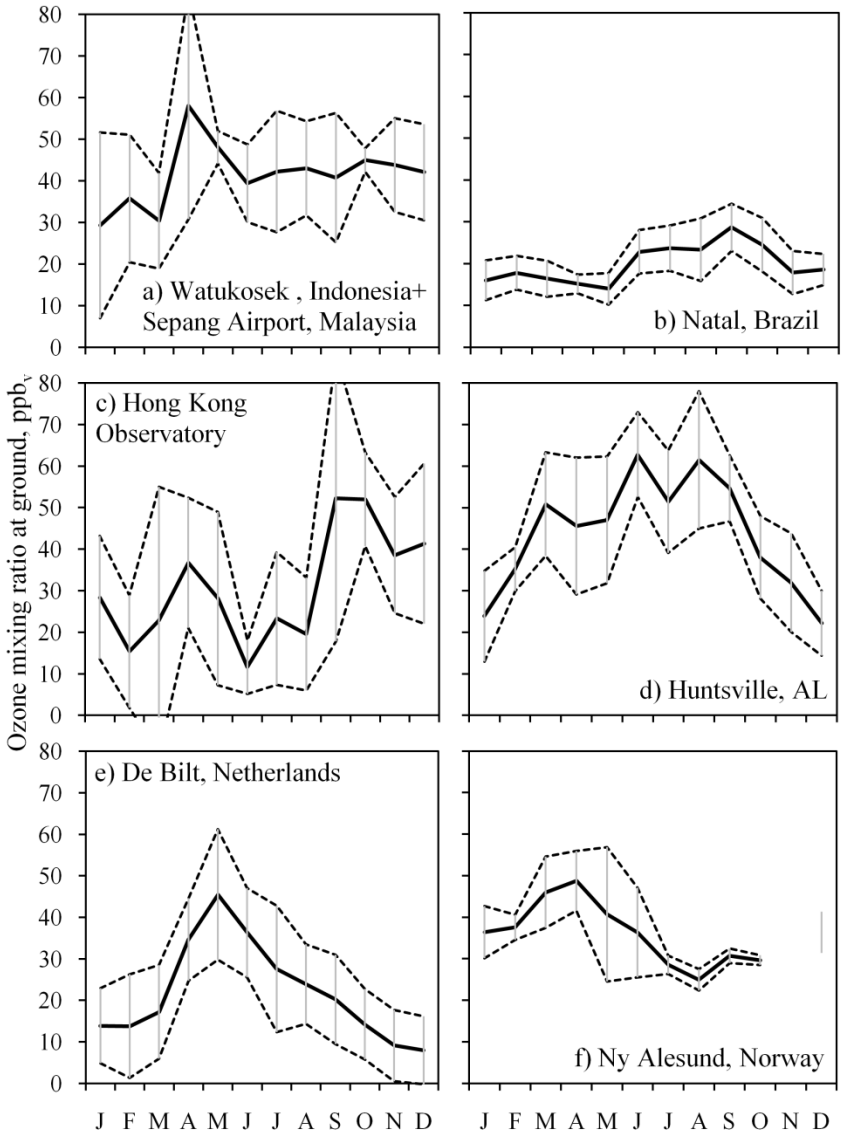

Figure 6.6. Monthly variation of ground-level sonde-based ozone mixing ratio by station. Solid lines show mean value. Dash lines show one standard deviation from the mean

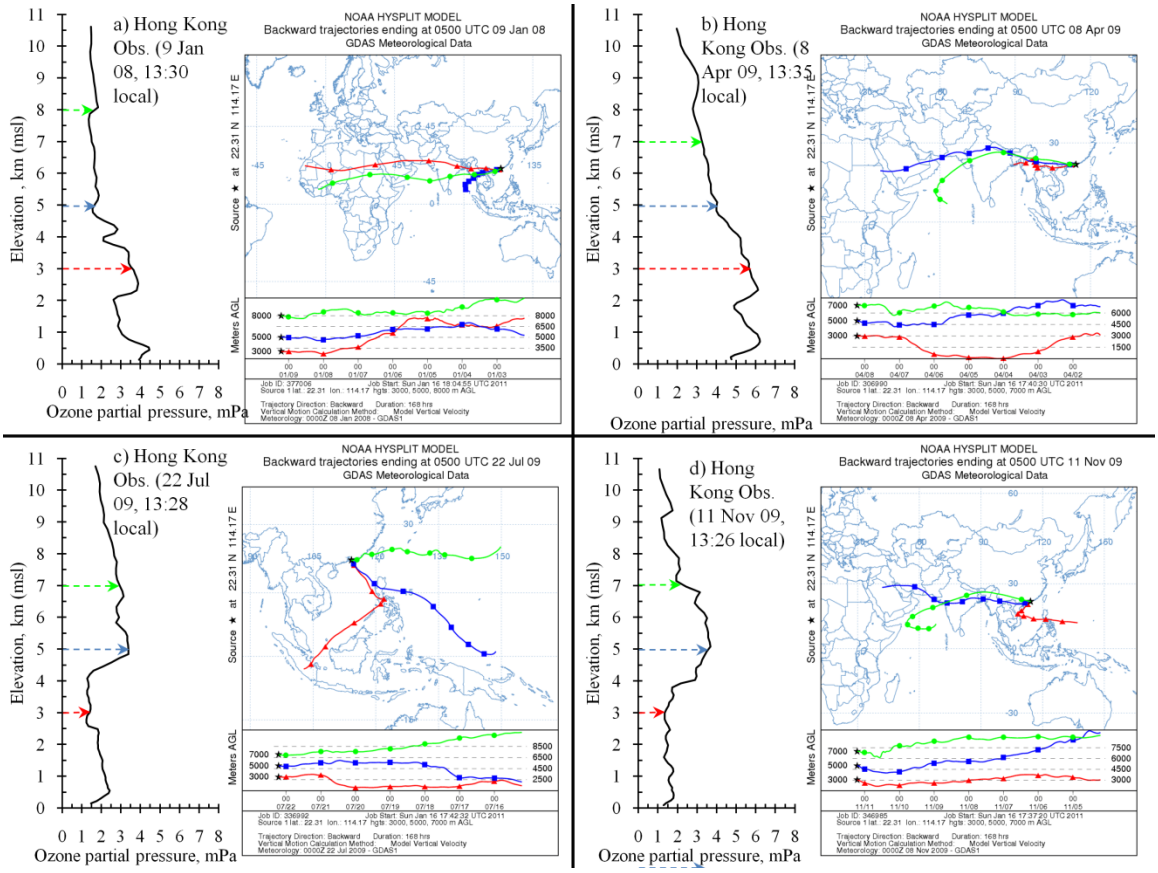

Figure 6.7. Sonde ozone profiles and their corresponding 7-days air back trajectories observed over Hong Kong Observatory station on a) 9 January 2008 at 13:30 local, b) 8 April 2009 at 13:35 local, c) 22 July 2009 at 13:28 local, and d) 11 November 2009 at 13:26 local. The air back trajectories were generated from the web-based HYSPLIT model using meteorological data from Global Data Assimilation System (GDAS).

Photochemical production could often cause high peak ozone levels occurring near the ground in spring (42 to 99 ppb_v, see Figure 6.5-d.2) compared to those in winter (42 to 80 ppb_v, see Figure 6.5-d.1). Photochemical reactions could also be responsible for high peak ozone mixing ratios (45 to 102 ppb_v, see Figure 6.5-d.4) near the ground (mainly < 1.6 km) in the fall. High peak values near the ground in spring and fall were also observed by Liu et al. (2002). They hypothesized that the photochemical activities were

promoted by a seasonal strong high pressure system over the Asian continent. Consistently, from Figure 6.6-c monthly average ground-level ozone mixing ratio was also high in spring and fall and low in summer and winter. This indicates that SO partially contributed to overall springtime TCO maxima and summertime TCO minima. The summertime minima can be explained by local photochemical climatology as described below.

Comparing among seasons, summer RO was least frequent and its fraction in TCO was also lowest; whereas the more vertically mixed ozone profile (category 1) was observed (see Figure 6.4). This indicates stronger surface convection enhancing vertical mixing processes. From Figure 6.5-d.3, peak ozone mixing ratios were found in two distinct altitude ranges; near the ground to 1.7 km and from 5 km to 8.2 km. While those found near the ground exhibited the lowest seasonal peak values, the ones found at the higher altitude exhibited elevated peak values, 55 ppb_v to 103 ppb_v. In addition, the ozone profile observed on 22 July 2009 (see Figure 6.7-c) showed a major increase in ozone partial pressure at ~5 km. This ozone was unlikely from long-range transport polluted air mass because of no apparent air back trajectories over polluted areas.

Chan et al. (1998) suggested that the low surface ozone concentration for the East Asia in the summertime resulted from seasonal increase in photochemical ozone destruction by strong UV radiation and high concentration of water vapor influenced by summer monsoon (see Figure 6.7-c), which brings relatively moist clean air from the South China Sea to the region (Chan et al., 1998). In contrast to the destruction, the photochemical production of ozone over eastern Asia in summer becomes stronger in the upper

troposphere because of rapid convective transport of ozone precursors from the boundary layer along the East Asian coast (Liu et al., 2002). This mechanism can explain our findings of summertime elevated peak ozone mixing ratios in higher altitudes.

There were observations with UO found in all seasons; however, only one out of eleven observations was found with the stratospheric ozone signature. Therefore, the majority of these ozone-rich air masses were probably not recently transported from stratosphere. However, they might be influenced by the stratospheric intrusion. Figure 6.7-a and -c shows a low concentration ozone inversion layer at approximately 8 km and 7 km, respectively and the corresponding air back trajectories indicate their 5-day old paths at altitude above 8.5 km. Therefore, it was possible that advection of aged stratospheric ozone could be responsible for the presence of UO over these stations.

Mid-latitude Atlantic region

Climatology of tropospheric ozone for the Houston and Narragansett stations from September to February is not discussed here due to lack of observations.

Houston is one of US cities that has experienced high-level surface ozone. The level regularly exceeds a National Ambient Air Quality Standards from March to November, covering spring-summer-fall (Morris et al., 2010). In contrast with the observations at the mid-latitude Pacific urban stations, the Houston station showed higher mean TCO in summer, 41 DU, than that in spring, 30 DU. From Table 6.3, the Houston summertime RO contributed ~46% to TCO and was frequently found in 83% (categories 3 + 4, shown in Figure 6.4) of total summertime observations. This predominance of RO agrees with

the findings from MILAGRO (Megacities Initiative: Local and Global Research Observations)/Intercontinental Transport Experiment in the work of Thompson et al. (2008) using aircraft to follow pollutant transport into and out of North America. From that experiment, TCO was found increasingly from spring to summer, particularly at levels between 5 km and 12 km. They show that the increase corresponded to more advected ozone, including imported and/or re-circulated aged ozone (and its precursors). In addition, from Figure 6.8 photochemical ozone production in the advected air masses could also be enhanced by predominant low-speed winds over the southern US in summer rather than those in spring which are influenced by higher wind speeds.

Compared with that in summer, surface-contributed ozone in spring provided higher contribution to TCO (~34% for spring and ~20% for summer). Correspondingly, SO was also more predominant with 83% (categories 2 + 4) of the total springtime observations. The higher surface ozone fraction related to a thicker mid-day boundary layer in spring (~4.3 km) than that in summer (~2.7 km). There were only two observations, one for each of the spring and the summer months, exhibiting UO characteristics and they indicated that the UO contributed 22% and 32% to TCO, respectively. Both observations clearly showed strong stratospheric ozone signature (observed ΔRH_{U-L} = -33% and -14%, for spring and summer, respectively).

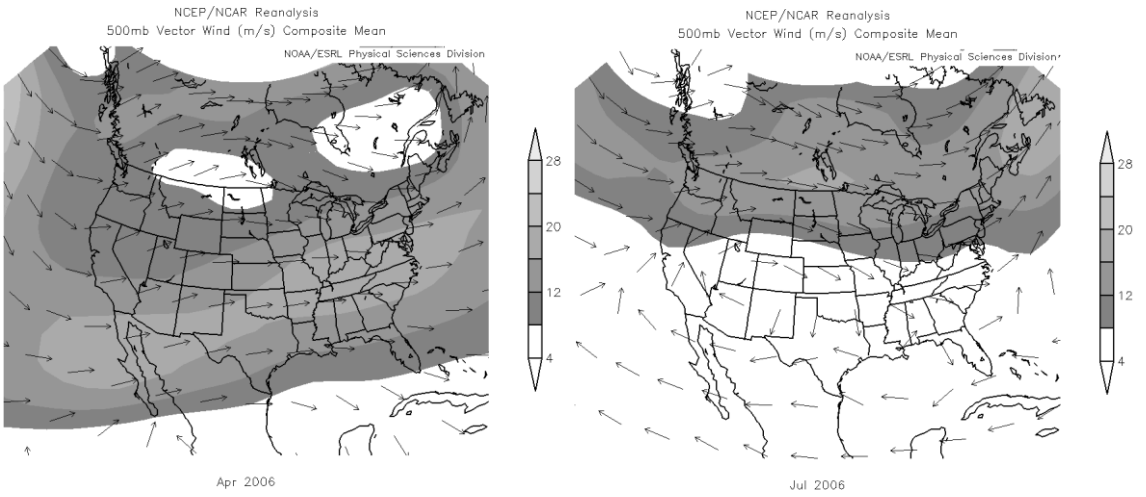

a) April 2006 b) July 2006

Figure 6.8. Monthly average wind speeds (m s^{-1}) and directions at 500 mbar over USA for a) April 2006 and b) July 2006. These maps were generated from the web-based monthly/seasonal climate composite plotting tool available at http://www.esrl.noaa.gov/psd/cgi-bin/data/composites/printpage.pl. Note: The data set was NCEP/NCAR Reanalysis derived data provided by the NOAA/OAR/ESRL PSD, Boulder, Colorado, USA.

The mean TCO observed at the Houston station was not significantly higher than that observed at the other two US stations, at Huntsville and Narragansett, in summer and showed a lower mean value in spring. The Houston ozone is more confined in the mixed layer because of a high-pressure system leading stagnant air and/or recirculation of pollution via a local sea breeze circulation between the Houston area and the Gulf of Mexico (Morris et al., 2010). In good agreement with these weather patterns, no observation with a vertically mixed ozone profile (category 1) was found at the Houston station. These conditions also allow higher pollutant concentration to accumulate near the

ground. However, this ground-level ozone did not cause to significantly higher TCO than observed at the other US sites.

Mean TCO at the Narragansett station was highest among three US stations in spring, 46 DU, and lowest in summer, 39 DU. From Figure 6.5-f, the springtime peak ozone mixing ratios were more frequent at higher altitudes (up to 10.3 km, close to at 215 hPa) and had higher values (up to 441 ppb_v) compared to those observed at other two US stations in the summer. From Table 6.3, UO fraction at this station was also higher in spring (21%) than in summer (16%). All four of these springtime UO observations were found with negative ΔRH_{U-L}, and two exhibited the stratospheric ozone signature. On the other hand, five out of total eight summertime UO observations showed positive ΔRH_{U-L}, and only one exhibited the signature. A persistent low-pressure system developing over the northern Atlantic during spring causes strong subsidence air masses with high pressure systems. This leads to more frequent stratosphere-troposphere air mass exchanges (Thompson et al., 2007; Moody et al., 1995). These findings bring us to a conclusion that stratospheric-tropospheric ozone exchange should be one factor contributing to the high springtime mean TCO at the Narragansett station; whereas the exchange process was less effective in summer.

At the Narragansett station, spring-to-summertime ozone mixing ratio at the ground was 39.6 ± 16 ppb_v, which was lower than the other two US stations (47.6 ± 22 ppb_v and 56.0 ± 15 ppb_v for the Houston and the Huntsville stations, respectively). However, Thompson et al. (2007) showed that the surface ozone at the Narragansett station was higher than those observed over nearby stations in the Gulf of Maine in the summer of 2004. Among

all the US stations, summer-to-springtime SO (category 2) was the most frequent at the Naragansett station (see Figure 6.4). From Figure 6.5-f, the peak spring-summertime ozone mixing ratios below 3 km found at this station narrowly ranged from 49 to 74 ppb_v, whereas larger variation was observed for the Houston and the Huntsville stations (44 to 120 and 38 to 104 ppb_v, respectively).

The Huntsville station had the highest mean TCO, 44 DU, among the three US stations in summer. This level was slightly increased from that in spring (43 DU). Newchurch et al. (2003) compared the tropospheric ozone concentration during 1995 to 2002 among four US non-urban stations, including Huntsville. They found that over Huntsville at approximately 700 hPa to 800 hPa, ozone concentrations exceed the mean of the other three stations by as much as 25-30% in August and September. As shown in Figure 6.4, SO (categories 2 + 4) was more predominant at the Huntsville station from spring (57%) to summer (74%) than those from fall (41%) to winter (0%). Surface ozone also contributed approximately 20% to 24% to TCO during spring through fall, and it contributed only ~8% in winter. Moreover, peak ozone mixing ratios were typically found at altitudes lower than 3 km (see Figure 6.5-g). These findings can be explained by Huntsville's geography, which is surrounded by deciduous trees. These trees are a substantial source of isoprene emissions and contribute to the spring-to-summer elevated TCO. This hypothesis is consistent with the conclusion drawn by Newchurch et al. (2003).

Vertically mixed ozone (category 1) was predominant for 75% of total wintertime observations. The natural isoprene emissions from biomass are also less pronounced in

this season. This caused an even vertical ozone distribution and smaller surface ozone fraction in TCO observed in the winter months (see Table 6.3).

High-latitude region

At the De Bilt (in Netherlands) station, mean TCOs were similar between for spring (43 DU) and for summer (42 DU) and between for fall (33 DU) and winter (32 DU). Mean TCOs observed at Ny Alesund (in Norway) showed more seasonal variation. The highest (54 DU) was found in spring, followed by 44 DU in summer, 42 DU in fall, and the lowest (38 DU) in winter. The springtime maxima observed at these high-latitude remote stations were also observed in a previous study conducted by Scheel et al. (1997). They hypothesized that stratospheric ozone intrusion and active photochemical production after the wintertime accumulation of ozone precursors could contribute to these spring maxima. This hypothesis is supported by our findings as described below.

From Figure 6.5-h and -j, peak ozone mixing ratios were observed in two discrete altitude ranges. The active photochemical production should be more responsible for peak ozone mixing ratios, ranging from 38 to 122 ppb_v, at the lower altitude range (0.1 to 5.8 km). Those at the higher altitudes (7.8 to 10.4 km) exhibited higher values from 133 to 826 ppb_v, and they should be attributed to stratospheric ozone. Tropopause height for this region typically ranges from 7 to 12 km (Lamsal et al., 2004). Therefore, the ozone found at these higher altitudes could include stratospheric ozone. Stratospheric intrusion is common at these higher latitude stations due to influence of polar jets (Colette and Ancellet, 2005). The evidence was evenly found in all seasons; however, the stratospheric ozone signature was more pronounced from spring to fall for Ny Alesund

and from spring to summer for De Bilt. Based on these findings, the stratospheric ozone intrusion should be one factor responsible for the springtime maxima.

Another factor responsible for the springtime maxima was seasonal photochemical activity. From Table 6.3 and Figure 6.4 for De Bilt (52^{o}N), the RO (categories 3 + 4) was predominant in spring and summer (85% and 96% of total seasonal observations, respectively). Its fraction in TCO (28% and 29%, respectively) was larger than surface-contributed ozone (18% and 19%, respectively) and UO (21% and 19%, respectively). Colette and Ancellet (2005) investigated long-term ozone profiles from many European sites, including the De Bilt station. They found that the lifetime of the residual layer increased in summer, which caused enhanced photochemical production in aged tropospheric air masses in the layer. This stable condition occurred as a result of a high pressure system and clear skies over Europe in late spring to summer (Beck and Grennfelt, 1994). For the Ny Alesund station (79^{o}N), the RO was also often in spring and summer (50% and 92%, respectively, see Figure 6.4), but its contribution to TCO was lower (~10% and ~17%, respectively, see Table 6.3) than that from the other two ozone types. This is possibly because of its location being farther from regional polluted source, central Europe; therefore the ozone contribution from long-range transport polluted air masses in the residual layer can be moderated.

SO (categories 2 + 4) was more pronounced in fall (68% and 43% of total observations in fall, for De Bilt and Ny Alesund, respectively) and winter (47% and 40%) than that in spring (35% and 37.5%) and summer (29% and 25%). Surface-contributed ozone fraction in TCO was also more marked for winter (27% and 33% of TCO, for De Bilt and Ny

Alesund, respectively) than that for summer (19% and 24%). These findings resulted from less photochemical ozone destruction by titration with oxides of nitrogen, NO_x (Scheel et al., 1997; Beck and Grennfelt, 1994). Both stations are in coastal remote areas where local NO sources are limited. Due to their coastal locations, the surface ozone budget in these areas was not likely affected by dry deposition, ozone advection, and boundary layer-to-free troposphere air mass exchange (Beck and Grennfelt, 1994). Therefore the surface ozone should be mainly restricted by photochemical destruction and production. Even though surface ozone was dominant in fall and winter, the ground-level ozone mixing ratio (see Figure 6.6-e and -f) observed during these seasons was still lower than those in summer and spring.

6.4.2. Linear regression models between OMI/MLS TCO and ozonesonde TCO for different tropospheric ozone profile shapes

Scatter plots in Figure 6.9 were between OMI/MLS TCO and sonde TCO, both integrated from the ground to 215 hPa, for four geographical regions. These plots indicate latitudinal dependence on linear relationships between both data sets. If the observations exhibiting OMI/MLS TCO greater than 50 DU are ignored, low latitude stations were closer to one-to-one relationship. For the high latitude, the satellite-based TCO were significantly lower than those from the ozonesonde measurements.

Table 6.4 shows latitudinal dependence on the linear regression models using the satellite retrievals to estimate ozonesonde TCO. Intercept (*c*) is an estimate of ozonesonde TCO at zero OMI/MLS TCO. It suggests inconsistency between the ozonesonde TCO and OMI/MLS TCO at low TCO levels. The values clearly increased with higher latitude (*c*

from 11.9 DU for low-latitude Pacific stations to 41.6 DU for the Scandinavian station). Slopes (m) indicate sensitivity of OMI/MLS TCO to the changes of sonde TCO. Coefficient of determination (R^2) indicates degree of linear relationship between TCO from both data sets. Both m and R^2 were higher for the low latitude observations than those for the higher latitudes (m = 0.49 and 0.25, R^2 = 0.29 and 0.05 for low-latitude Pacific stations and the Scandinavian station, respectively).

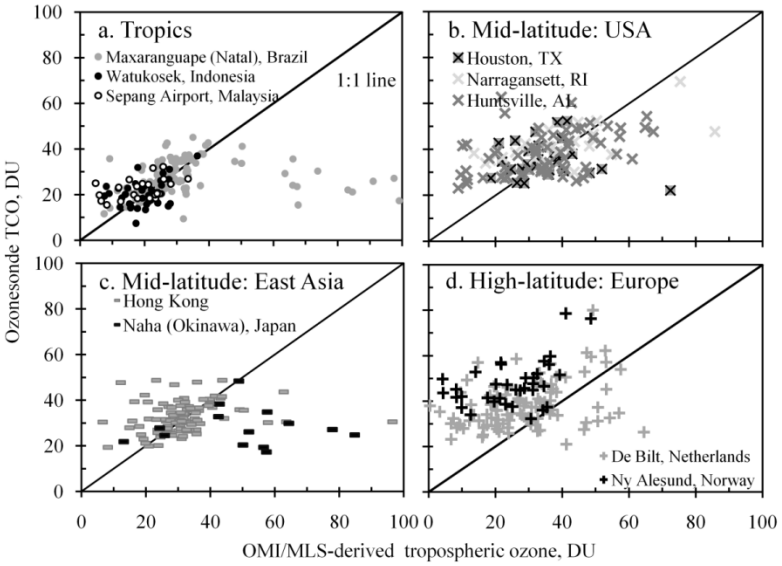

Figure 6.9. Scatter plots between OMI/MLS TCO and sonde TCO for a) tropic stations, b) mid-latitude Atlantic stations, c) mid-latitude Pacific stations, and d) high-latitude stations

Induction of upper troposphere ozone (UO) was one factor contributing to these latitudinal differences. From Figure 6.10 and Table 6.5, compared with those without UO, the observations with UO showed distinctly lower R^2, poorer OMI/MLS TCO sensitivity (indicated by lower m), and larger inconsistency between OMI/MLS TCO and predicted sonde TCO at low TCO levels (indicated by higher c). Observations with

category-3 ozone profile were prone to serious UO effect. In this case, the presence of UO degraded R^2 from 0.49 (without UO) to < 0.001 (p = 0.86–very poor linear relationship). For observations in category-4 ozone profile, the UO effect was milder. This is possibly because surface tropospheric ozone weighed higher on TCO. In this case, the R^2 decreased to 0.37 (with UO), the OMI/MLS TCO sensitivity decreased by 24% (from m = 0.58 to 0.44), and the inconsistency at low TCO levels increased by 79% (from c = 14.4 to 25.9 DU).

Table 6.4. Linear regression models between OMI/MLS TCO (x) and sonde TCO (y) for different geographical region

Regions	Locations	Number of Obs.	Estimate		R^2	p for testing $m = 0$
			Slope, m[a] (unitless)	Intercept, c[a] (DU)		
Low-latitude Pacific	Watukosek (Java), Indonesia / Sepang Airport, Malaysia	35	0.49 [0.22,0.76][b]	11.89 [5.89,17.89]	0.29	<0.001
Low-latitude Atlantic	Maxaranguape (Natal), Brazil	90	0.36 [0.23,0.49]	18.71 [14.75,22.67]	0.26	<0.001
Mid-latitude Pacific	Naha (Okinawa), Japan / Hong Kong Observatory	75	0.25 [0.12,0.37]	24.69 [20.63,28.75]	0.17	<0.001
Mid-latitude Atlantic-southern and southeastern USA	Houston, TX / Huntsville, AL	58	0.34 [0.21,0.48]	24.19 [19.07,29.30]	0.32	<0.001
Mid-latitude Atlantic-northeastern USA	Naragansett, RI	23	0.23 [0.03,0.43]	32.36 [24.92,39.81]	0.21	0.03
High-latitude western Europe	De Bilt, Netherlands	76	0.22 [0.08,0.37]	32.57 [27.99,37.15]	0.12	0.003
High-latitude Scandinavia	Ny Alesund, Norway	34	0.25 [-0.09,0.39]	41.55 [35.41,47.68]	0.05	0.22

[a] $y = m(x)+c$; [b] estimate [95% confidence interval for the parameters]

Compared among the different regions, observations from the high latitude often had high-level UO and showed more of the category-3 characteristics than the category-4 (see

Figure 6.4). These caused significant underestimating of sonde TCO using the satellite retrievals for higher latitudes.

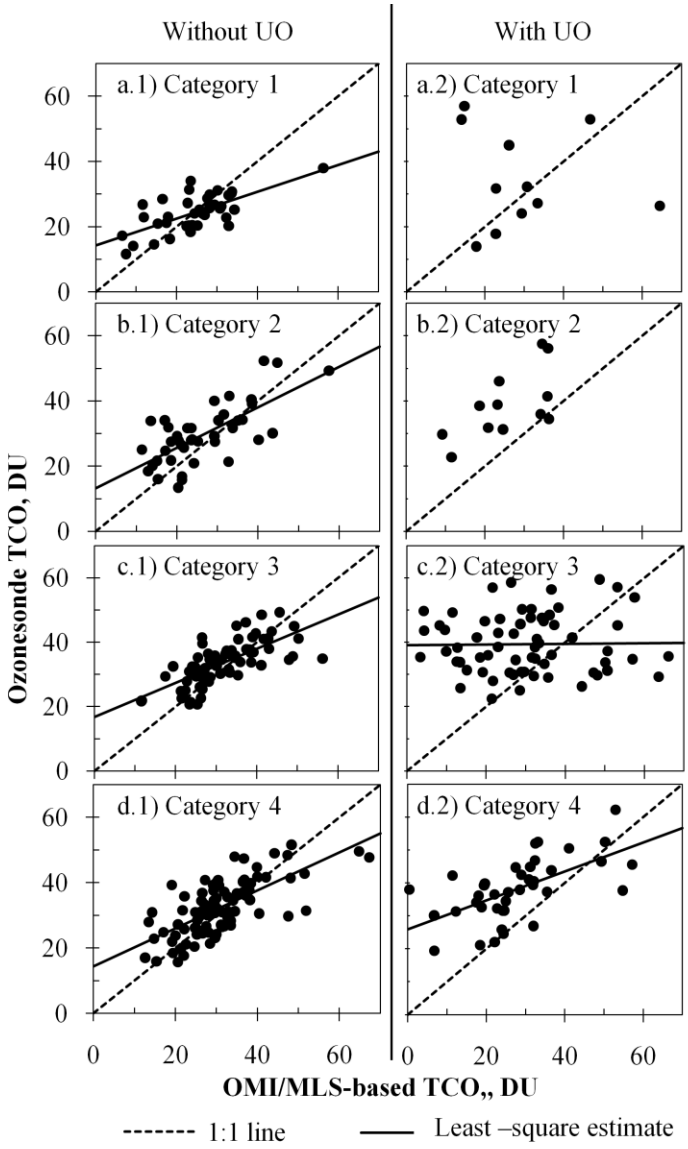

Figure 6.10. Scattering plots between OMI/MLS TCO and sonde TCO for different ozone profile categories and for with and without upper troposphere ozone (UO). Solid line shows least-square estimate from linear regression models detailed in Table 6.5.

Table 6.5. Linear regression models between OMI/MLS-based TCO (x) and sonde-based TCO (y) for different ozone profile categories and for with and without upper troposphere ozone (UO)

Ozone profile categories	Number Observations	Estimate		R^2	p for testing $m = 0$
		Slope, m[a] (unitless)	Intercept, c[a] (DU)		
Category 1 (without SO[b] and without RO[b])					
Without UO	37	0.41 [0.25, 0.56][c]	14.30 [10.27, 18.34]	0.45	<0.001
With UO	12	No linear model estimation due to too few observations			
Category 2 (with SO and without RO)					
Without UO	41	0.62 [0.42, 0.83]	13.22 [7.42, 19.03]	0.49	<0.001
With UO	13	No linear model estimation due to too few observations			
Category 3 (without SO and with RO)					
Without UO	76	0.53 [0.40, 0.66]	16.80 [12.60, 21.00]	0.49	<0.001
With UO	64	0.01 [-0.14, 0.17]	39.07 [33.78, 44.36]	<0.001	0.86
Category 4 (with SO and with RO)					
Without UO	87	0.58 [0.45, 0.71]	14.42 [10.23, 18.61]	0.49	<0.001
With UO	39	0.44 [0.25, 0.63]	25.88 [20.04, 31.72]	0.37	<0.001

[a] $y = m(x)+c$

[b] SO = surface enhanced ozone; RO = residual layer ozone

[c] Mean [95% confidence interval of the mean]

Regardless of the UO effect, R^2 values for all ozone profile categories (~0.5, see Table 6.5) were similar. This indicates that the satellite retrievals could explain ~50% of total variation in the sonde TCO using the linear regression models. The presence of SO without RO provided the highest satellite-based TCO sensitivity (m = 0.62) and the lowest intercept (c = 13.2 DU) among all ozone profile categories. This sensitivity was increased markedly by ~51% and this intercept was decreased slightly by ~7.5% from the case without SO (from m = 0.41 and c = 14.3 DU, respectively for category 1). Presence of RO had minor impact on using this satellite-based TCO to predict sonde TCO under

the presence of SO. In this case, having RO caused its sensitivity slightly degraded by ~6% and its intercept increased by ~9% (to m = 0.58 and c = 14.4 DU, respectively for category 4). The strongest sensitivity found in the category-2 observations indicated that the satellite retrievals performed better under conditions without both UO and RO.

Observations with ozone-rich air masses at higher elevations (mainly in free troposphere) showed higher inconsistency at low TCO levels and lower sensitivity than those observed at lower elevation (mainly in boundary layer). These conclusions were drawn from observing ~27% higher intercept value and ~14.5% fewer linear slope in the category-3 ozone profile compared with those in the category 2. This finding indicates that there were better TCO estimates from the satellite data when the ozone profile shape was more weighted near the ground.

From Figure 6.9, the satellite retrievals tended to overestimate sonde TCO when its TCO value was high (> 50 DU). This study used all possible observations from the satellite retrievals that were coincident with the ozonesonde measurements, regardless of quality of the data sets. Observations with OMI/MLS TCO greater than twice of those of ozonesonde measurements and greater than 50 DU were considered to be outliers. These were not included into the analyses of linear regression models (Table 6.4 and 6.5). The OMI ozone retrieval from TOMS algorithm is based on backscattering in two UV spectral bands, 317.5 nm and 331.2 nm. Accuracy on OMI ozone retrieval can be degraded markedly in the troposphere because the backscattering UV is largely interfered by cloud, aerosols, and high surface reflectivity, mainly over snow, ice, and sea glint (Bhartia and Wellemeyer, 2002). Therefore, data with quality flag of 0 (good sample) or

1 (glint contamination corrected) were recommended for use (Ozone Processing Team-NASA/GSFC, 2008). Incorporating poor quality data into the analyses could affect the results shown here. However, these recommended quality flags inappropriately identified outlier observations as good data. In this study, approximately forty percent (17 out of 43) of the outliers had an acceptable quality flags.

Based on the most recent version of the OMI total ozone retrieval algorithm, TOMS-V8, a total 1,512 *a priori* ozone profiles were constructed to represent ozone profiles for each combination of 12 months and 18 latitudes (10^o wide). These choices were designed to capture variation of tropospheric ozone (0-10 km) with season and latitude (Bhartia and Wellemeyer, 2002). However, the findings from this study indicate that the tropospheric ozone profile still significantly affects accuracy of using the satellite retrievals to estimate TCO.

Stajner et al. (2008) pointed out that ignoring zonal dependence in the OMI ozone retrieval algorithm could partially cause high bias on assimilated TCO. As shown in the earlier part of this work, there are differences between ozone profile characteristics observed at Pacific and Atlantic stations that show that tropospheric ozone is not zonal symmetric. From Table 6.4, the zonal dependence (Pacific and Atlantic regions) on relationships between TCOs from satellite retrievals and from ozonesonde measurements was apparent, but it was not as strong as the latitudinal dependence. For the low latitude stations, higher sensitivity and lower inconsistency at low TCO levels in the linear models were seen for the Pacific stations (m ~0.49, c ~11.9, and R^2 =0.29) compared to the Atlantic station (m ~0.36, c ~18.7, and R^2 = 0.26). In contrast, for mid latitudes the

linear model for the Atlantic stations had higher sensitivity and higher R^2 (m ~0.34, c ~24.2, and R^2 = 0.32 for the South and the Southeast US stations) than those for the Pacific stations (m ~0.25, c ~24.7, and R^2 = 0.17). These zonal differences can be explained by zonally prevalent ozone profile characteristics. As discussed earlier, the observations with higher SO yielded better sensitivity and lower inconsistency at low TCO levels on estimating TCO from the OMI/MLS retrievals. From Figure 6.4, approximately 83% to 88% of seasonal ozone profile observations at the low-latitude Pacific stations were with SO (category 2 or 4); whereas these ozone profiles were only found 4% to 14% of the observations at the low-latitude Atlantic station. For the mid-latitude observations, higher surface ozone fraction and/or lower RO fraction in TCO were found for the Atlantic stations than for the Pacific stations (see Table 6.3).

In summary, even though we found some good sensitivities of the tropospheric column ozone, TCO, retrievals from OMI/MLS-Aura in correlation with those from ozonesonde measurements; this OMI/MLS TCO could not indicate the surface ozone level unless local tropospheric ozone profile shape is known. Since the current Aura sensors could not accurately measure the ozone profile, using sole satellite retrievals to infer the surface ozone level was not appropriate.

6.5. CONCLUSION

This study aims to evaluate sensitivity of tropospheric column ozone (TCO) retrieved from Earth Observing System (EOS) Aura satellite on daily changes of surface ozone concentration. The satellite-based TCO was calculated by subtracting stratospheric

column ozone retrieved from Microwave Limb Sounder (MLS, L2 version 2.2) from total column ozone retrieved from Ozone Monitoring Instrument (OMI, TOMS L2). The sensitivity was evaluated from linear relationships between this satellite-derived TCO and coincident TCO estimated from balloon-based ozonesonde measurements for different tropospheric ozone profile shapes. These shapes account for the ozone profiles with and without the presences of surface enhanced ozone (SO), residual layer ozone (RO, long-range transported in free troposphere), or upper troposphere ozone (UO, observed above 7 km altitude). In addition, seasonal variations of the ozone profiles, column abundance, and budgets were investigated and discussed. To explain spatial variations of the tropospheric ozone; all available ozone data from years 2005 to 2010 at ten ozonesonde stations, mainly in the Northern Hemisphere, were acquired and classified to represent the data for low, mid, and high latitudes and for Pacific and Atlantic regions.

Results from the analyses of ozone partial pressure profiles taken from ozonesonde measurements showed seasonal variations of tropospheric ozone characteristics for the different geographical regions. The major findings are summarized below:

- For low-latitude Pacific stations, seasonal mean TCOs did not change significantly. SO was observed in all seasons, but RO contributed a larger fraction of TCO. Both types of ozone were often found together from June to February, covering the annual driest periods. Biomass burning emissions could be responsible for these occurrences (Komala et al., 1996; Thompson et al., 2003).

- Mean TCO observed at the low-latitude Atlantic station in Brazil was at lowest in the early wet season and at highest in the early dry season. RO was the largest contribution to TCO for all seasons and it was predominant, except in the early wet seasons. RO should be influenced by a combination of local and long-range transport biomass burning aerosols from northern Africa (Logan and Kirchhoff, 1986). Upper troposphere ozone (UO) was found in all seasons; however, more stratospheric ozone intrusion signature was found in the dry season.

- For mid-latitude Pacific stations, mean TCO showed a spring maximum and summer minimum pattern. In spring, RO was predominant and it contributed approximately half to the TCO. This ozone was possibly long-range transport photochemical ozone produced from biomass burning emissions over the Southeast Asian continent (Chan et al., 1998; Chan et al., 2003; Liu et al., 1999; Liu et al., 2002). In addition, high peak ozone mixing ratios were also observed near the ground in spring. In summer, RO fraction minimized and more peak ozone mixing ratio found at the higher altitude due to rapid convective transport of ozone precursors from the boundary layer (Liu et al., 2002). Observations with UO were found in all seasons and these could be from advected aged stratospheric ozone.

- The Houston station, mid-latitude Atlantic urban, had higher TCO in summer than that in spring. This related to the persistent high pressure system over the southern US in the summer months. Compared to the other two US stations, more high ozone events at the Houston station were observed at the surface level, but they did not contribute the major fraction of TCO. The Huntsville station, surrounded by

deciduous trees with seasonal high natural isoprene emissions, experienced the highest mean TCO among the US stations in the summer. The Narragansett station, in the Northeast US adjacent to Atlantic Ocean, had the springtime highest mean TCO among the US stations. This could be credited to stratospheric-tropospheric ozone exchange.

- For the high-latitude European stations, which are located in remote areas, springtime TCO maxima were observed and these were attributed to stratospheric ozone intrusion and photochemical activity. In the spring and summer months, RO often occurred and its fraction of the TCO was also dominant. This could be resulted from enhanced photochemical production by development of a high pressure system and clear skies over Europe (Colette and Ancellet, 2005; Beck and Grennfelt, 1994). SO was more pronounced in fall and winter. This could be resulted from less photochemical ozone destruction by titration with oxides of nitrogen, NO_x (Scheel et al., 1997; Beck and Grennfelt, 1994).

There was significant latitudinal dependence on linear relationships between OMI/MLS TCO and sonde TCO. Linear intercept (c) suggests inconsistency between the ozonesonde and OMI/MLS TCOs at low TCO levels and it increased with higher latitude (c =11.9 DU for low-latitude Pacific stations to 41.6 DU for the Scandinavian station). Sensitivity of OMI/MLS TCO to the change in sonde TCO (linear slope, m) and degree of the linear relationship between both data sets (R^2) were also higher for the low latitude than those for the high latitude (m = 0.49 and 0.25, R^2 = 0.29 and 0.05 for low-latitude Pacific stations and the Scandinavian station, respectively). Induction of UO was one

factor responsible for these latitudinal differences. In the case that ozone profiles weighed higher in the free troposphere, the presence of UO caused very poor linear relationships. For the case that ozone profiles weighed higher at lower troposphere, the UO decreased the OMI/MLS TCO sensitivity by ~24% and increased the intercept by ~79%.

Zonal dependence (Pacific and Atlantic regions) was apparent on relationships between the OMI/MLS TCO and the sonde TCO, but it was not as strong as the latitudinal dependence. The zonal differences can be explained by zonally prevalent ozone profile characteristics as described earlier.

Regardless of the UO effect, the satellite retrievals could explain ~50% of total variation in the sonde-TCO observations using the linear regression models. The strongest sensitivity was found in the observations having SO without RO. The presence of RO caused the sensitivity to be degraded slightly by ~6% and the intercept increased by ~9%. In addition, the OMI/MLS TCO was more comparable to that from ozonesonde measurements when ozone-rich layers were found nearer to the ground than when those were found in the free troposphere. These findings indicate that the OMI/MLS TCO could not be used as a standalone indicator of surface ozone concentration. Corresponding information about tropopsheric ozone profile was required to improve performance of using these satellite retrievals on surface ozone implication.

CHAPTER SEVEN

CONCLUSIONS AND FUTURE RESEARCH

7.1. RESEARCH OVERVIEW

Satellite remote sensing is widely used for Earth observations to collect information about global dynamic systems. In this work, we used retrievals from three Earth observation satellites, Terra, Aqua, and Aura. These satellites are launched under NASA Earth Observing System (EOS). They are positioned at an altitude of 705 km and have a near-polar orbit in synchronization with the Sun; with their paths crossing the same location at the same local time every day. The satellite retrievals used in this study have moderate resolutions with spatial resolution ranging from hundred meters to ten kilometers.

This study evaluates the performance of using the moderate-resolution satellite retrievals to facilitate understanding characteristics of Southeast Asia (SEA) surface air pollution from biomass burning and urban activities. The moderate-resolution satellite retrievals were used for three applications, which are the following.

1. Using surface reflectance from Moderate Resolution Imaging Spectroradiometer (MODIS) onboard the Terra satellite to map potential air pollution sources, including forests, rice paddies, and high-intensity urban areas.
2. Using aerosol optical properties retrieval from Ozone Monitoring Instrument (OMI) onboard the Aura satellite incorporating spatial information from the first

task and retrievals from other remote sensors to facility understanding dynamic optical characteristics of SEA biomass-burning aerosols.

3. Using tropospheric column ozone (TCO) estimated from the retrievals from OMI and Microwave Limb Sounder (MLS), both onboard the Aura satellite, to infer surface ozone concentrations.

7.2. MAJOR RESEARCH FINDINGS

In responding to the first application, algorithms used for the SEA land cover classification using the time-series satellite imagery were developed and their results were either compared with national statistical databases or with commensurate high-resolution satellite imagery. Details on this work are in Chapter Two. These imagery were generated from the 500-m resolution MODIS/Terra spectral surface reflectance (MOD09A1) acquired from 2006 to 2007. The estimated forest combination areas, including forests and plantations, were similar in magnitude to the provincial forest areas reported in the national forest statisitical databases after corrected plantation areas. With the exception of beaches, deserts, and permanent bare soils, large urban areas can be easily identified. In this study, MODIS urban areas greater than 80 km^2 were observed in seven cities. These were 1) Bangkok, Thailand; 2) Kuala Lumpur, Malaysia; 3) Manila, Philippines; 4) Jakarta, Indonesia; 5) Ho Chi Minh City, Vietnam; 6) Bandung, Indonesia; and 7) Surabaya, Indonesia. The algorithm for mapping rice paddy areas could distinguish different rice ecosystems and provides rice-cropping frequency. The total estimated rice area for SEA was 42×10^6 ha, which agrees with published values.

Comparison between the estimated rice paddy area and the national rice statistics on the provincial or state level showed high correlations over the areas dominated by rainfed rice. The high correlations were also found with irrigated rice but the model tended to underestimate the paddy areas. For the areas dominated by upland rice, the correlations were good, but the MODIS rice areas were overestimated. Overall, high coefficients of determinations (R^2) indicate that the spatial distribution of these MODIS rice areas was consistent with the actual distribution. In addition, These R^2 values are either similar in magnitude or larger than those reported in literature, regardless the rice ecosystem. However, poor correlation was found for deepwater rice.

The second application used the satellite retrievals to facilitate understanding optical characteristics and their changes with time of SEA biomass-burning aerosols. Prior to evaluating this application, the characteristics of background SEA aerosols should be understood. In Chapter Three, optical characteristics of SEA regional aerosols had been investigated through the multivariate analyses of long-term ground-based aerosol measurements acquired from Aerosol Robotic Network (AERONET). The results of this study showed that high aerosol exposure events were most frequently observed with seasonal NE prevailing winds from mid-September to December. The aerosol observed during this time exhibited a single scattering albedo, *SSA*, of approximately 0.95 (440 nm), a relatively low refractive index, and a larger fine-mode size, suggesting it had the characteristics of urban/industrial aerosols. These aerosol sources were probably at eastern China. From January to April, the aerosol exhibited a lower *SSA* of approximately 0.90, a higher refractive index, and a smaller fine-mode size, suggesting biomass-burning

smoke. The SEA urban aerosol exhibited a mean *SSA* of approximately 0.90 (440 nm) or lower and more coarse-mode size, possibly attributed to road dust or soil dust, played a role from October to January when seasonal winds are strongest.

Using MODIS aerosol retrieval for the second application was first proposed. However comparing MODIS aerosol variables, including aerosol optical depth (*AOD*) and aerosol type, with AERONET ground-measured aerosol variables showed disagreement in several cases. Details about this comparison are in Appendix A. This suggests that the MODIS retrieval was not appropriate for the biomass-burning aerosol characterization. Next, OMI aerosol retrieval was chosen. Appropriateness of using this OMI aerosol retrieval to infer the biomass-burning aerosol properties was evaluated along three lines of evidence. These are comparisons between the results obtained from multivariate analyses of the OMI products and those obtained from the ground-measured AERONET data, from Atmospheric Infrared Sounder (AIRS) total column CO, and from MODIS active fire detections. Details on the evaluation and results are given in Chapter Four. In summary the OMI aerosol retrieval for the large-scale fires could be confirmed by the three approaches. However, this was limited to observations with 1 < OMI *AOD* (442) < 3. This result indicates that OMI aerosol retrieval can be appropriately used for the studies of regional SEA biomass-burning aerosol optical properties.

In Chapter Five, the second application was evaluated by considering the aerosols from the two forest-fire episodes; 2007 SEA-continent and 2008 Indonesian fires. Dependence of the aerosol optical properties on four variables was investigated: 1) wind speed/direction, 2) relative humidity (RH), 3) land use/cover (as a surrogate of fuel type)

estimated from time-series analyses of MODIS surface reflectance, and 4) age of aerosol estimated from spatial-temporal analysis of MODIS active fire and the wind characteristics. The aerosol optical variables that were used for the evaluation were retrieved from OMI and these include *AOD, SSA,* and absorbing Angström exponent (α_a) as an aerosol size indicator. Results from Pearson Chi-square tests for independence showed that the dependence between aerosol groups with different optical properties and the limiting variables was significant for most cases, except for the Indonesian aerosol age factor. This is probably due to few observations of aerosols older one day. These dependences agreed well with a prior knowledge on regional burning conditions (types of fuel and relative humidity) and aerosol chemical/physical properties (chemical composition related to aerosol optical properties and hygroscopicity) in literature. One limitation of using the OMI aerosol retrieval for the aerosol dynamic study is that this retrieval lacks vertical information. This study considers a typical SEA aerosol elevated layer altitude of approximately 2.8 km, consistent with literature. At this height, hygroscopic growth (decreasing α_a with increasing RH in the residual layer) for the Indonesian aerosol was not evident, probably because this growth process mainly occurred at lower altitudes in the boundary layer.

The last application, using EOS-Aura tropospheric column ozone (TCO) to infer surface ozone level, was evaluated from linear relationships between OMI/MLS TCO and coincident TCO from balloon-based ozonesonde measurements for different tropospheric ozone profile shapes. Details on this work are in Chapter Six. The ozone data from many locations, including in SEA, were acquired and classified to represent the data for low,

mid, and high latitudes and for Pacific and Atlantic regions. There was significant latitudinal dependence on linear regression models using OMI/MLS TCO and sonde TCO. A better linear relationship, which is closer to one-to-one, was found in the low-latitude cases and the poorest relationship was observed in the high-latitude cases. Induction of UO was one factor responsible for these latitudinal differences. Zonal dependence (Pacific and Atlantic regions) was apparent, but it was not strong. The zonal differences can be explained by zonally prevalent ozone profile characteristics. The presence of RO caused model sensitivity to be slightly degraded by ~6% and model inconsistency at low TCO levels increased by ~9%. The OMI/MLS TCO had the strongest linear relationship with the ozonesonde measurements under the absences of RO and UO and when ozone-rich layers were found nearer to the ground. However, this OMI/MLS TCO could not appropriately imply the ground-level ozone concentration unless local tropospheric ozone profile shapes are known.

7.3. SUGGESTIONS FOR FUTURE RESEARCH

Spatial land cover information obtained from the analyses of surface reflectance retrieval from the moderate-resolution EOS satellite can be incorporated into the estimation of spatial air pollutant emissions related to land activities. In one case, the information can be used for estimating methane emissions from rice paddies. The emissions are significant (Barnet et al., 2003) and they are dependent on rice ecosystems. Methane is the most abundant hydrocarbon in the atmosphere and contributes to the greenhouse effect. Since it has a long atmospheric lifetime of ~8 to 10 years, it is quite homogeneously distributed in the vertical tropospheric column and more horizontally

concentrated in the vicinity of sources (Ashcroft and Morel, 1995; Pfister et al., 2005). The research conducted in this dissertation has shown that satellite retrievals can be potentially used to distinguish different rice ecosystems. In addition, methane measurements can be taken from satellites sensors. Current EOS has three instruments that are designed for the observation of tropospheric methane distribution. These are the Measurements of Pollution In The Troposphere (MOPITT) on the Terra satellite, the Tropospheric Emission Spectrometer (TES) on the Aura satellite, and the AIRS on the Aqua satellite. Methane typically can be measured by satellite observations in long-wave infrared absorption bands. There are high uncertainties associated with remote sensing-based methane retrievals attributed to strong water absorption, temperature dependency, inconsistency of surface reflectance in methane spectral bands, and small spatial variation of total atmospheric column methane (Barnet et al., 2003; Ashcroft and Morel, 1995; Pfister et al., 2005). However, several previous global-scale methane measurements taken from the EOS satellite agreed that methane emissions from SEA is considerable and is attributed to biomass burnings and rice cultivations (Xiong et al., 2008; Payne et al., 2009).

In this study, we showed that the moderate-resolution satellite retrievals can be used to facilitate understanding dynamic optical characteristics of SEA biomass-burning aerosols. However, the analyses conducted in this dissertation did not account for vertical variation of the aerosol distribution and the aerosols were assumed to exist in a specific elevated layer height. This assumption could neglect some of the aerosol dynamic processes that occurred in different atmospheric layers. Incorporating aerosol profile

information will resolve altitude-dependency on dynamic characteristics of the aerosols. In one way, this information could be obtained from Cloud-Aerosol Lidar and Infrared Pathfinder Satellite Observations (CALIPSO). CALIPSO carries active lidar which is used to measure profiles of atmospheric aerosols and clouds. The CALIPSO orbits seven minutes ahead of Aura spacecrafts and both are members of A-train constellation. Thus, the aerosol profile retrieval from CALIPSO can be considered as collocated with the OMI/Aura aerosol retrieval. CALIPSO aerosol profile algorithm also includes a model distinguishing biomass-burning aerosols from other aerosol types (Omar et al., 2009). Therefore, incorporating the aerosol retrieval from CALIPSO into the atmospheric aerosol studies should improve understanding of dynamic characteristics of the biomass-burning aerosols in the future.

Based on the findings in this dissertation, EOS-Aura tropospheric column ozone (TCO) estimated from the OMI and MLS retrievals are more appropriately used to infer daily changes in surface ozone concentration in the absence of upper troposphere ozone and when the ozone is near the ground. Comparison among the results obtained for different latitudinal regions, the satellite-based TCO sensitivity to the changes of sonde-based TCO was highest and its inconsistency with the ozonesonde TCO at low TCO levels was lowest for the low-latitude region. SEA is in low latitude and here the presence of stratospheric ozone intrusion in upper troposphere (~215 hPa) is rare. Thus, OMI/MLS TCO retrievals may appropriately infer surface ozone concentration in SEA urban cities, where the high-level ozone is often found near the ground. This OMI/MLS TCO might also be capable of providing better understanding of urban ozone production

mechanisms. Several works suggest the plausibility of using satellite-based TCO to evaluate the mechanisms driving urban ozone formations. Martin et al. (2004) applied the concept of relationships among ozone, oxides of nitrogen (NO_x), and volatile organic compounds (VOC) to diagnose NO_x-limited versus VOC-limited conditions using the ratio of formaldehyde (HCHO) column (as a surrogate of VOC) to the tropospheric NO_2 column (as a surrogate of NO_x) from Global Ozone Monitoring Experiment (GOME) observations. Their findings indicate that the diagnosis from the space-based observations is highly consistent with *in situ* observations. Duncan et al. (2010) applied the same technique with OMI observations, which had finer spatial resolution compared to those from GOME (~40 × 320 km^2). Their result shows more NO_x-limited areas than in the *in situ* studies. Both studies were conducted in the mid-latitude Northern Hemisphere in the summertime. Witte et al. (2011) employed this OMI HCHO-to-NO_2 ratio technique to determine a major ozone production mechanism during the 2008 Beijing Olympic Games and found that NO_x-limitations played a role.

Another possible application of the satellite-based TCO is to monitor weekday-to-weekend changes of urban ozone concentrations and its precursors. Traffic volume reduction from weekdays to weekends causes a decrease in mean concentration of ozone precursors (Blanchard et al., 2008). The precursors include NO_x, VOC, and carbon monoxide (CO). However, weekend ozone concentration might be comparable, or even higher, with weekday ozone concentration. This was observed in many large US cities (Blanchard et al., 2008). Factors and mechanisms limiting weekend ozone concentrations are not fully understood. One factor could be weekend decreases of nitrogen oxide (NO)

emissions from automobile exhausts which minimizes destruction of ozone and allows more ozone to accumulate to reach higher concentration (Blanchard et al., 2008).

In conjunction with the main studies conducted in this dissertation, we also conducted a preliminary study using data acquired for Thailand to investigate the sensitivities of satellite-estimated TCO. The sensitivities were on the spatial changes of surface ozone concentration responding to advective ozone formation and on temporal changes of the ozone level responding to traffic volume changes from weekdays to weekends. Details and results of this study are in Appendix B. In this study, level 2G (L2G) OMI data binned to $0.25^{o}\times0.25^{o}$ spatial grid (~25 × 27.8 km^2) were used. These data, however, exhibited coarser spatial resolution than the level 2 (L2) data used for the study in Chapter Six. In summary, the L2G OMI/MLS TCO showed similar seasonal trends with ground-measured surface ozone concentration. However, only 4.5 to 10.6% of total variation of the daily average surface ozone concentration can be explained by its linear relationship with the TCO. Meteorological factors affected significantly on the relationship. This L2G TCO had strong latitudinal dependence and it was not useful for monitoring advection and formation of the ozone in the Bangkok Metropolitan Region in Thailand. The ground measurements consistently showed similar reductions of ozone precursors' concentrations from weekdays to successive weekends for the different dry seasons. However, the reductions were not observed from the satellite retrievals. In addition, we investigated further the capability of L2G OMI retrievals, including TCO, tropospheric column nitrogen dioxide (NO_2), and total column HCHO, on the evaluation

of major surface ozone formation mechanisms. Disappointedly, the OMI retrievals resulted in different conclusion from that evaluated from ground measurements.

Even though results from this preliminary study suggests that the L2G OMI retrievals were not appropriate for the studies concerning urban ozone behaviors, for future studies we highly recommend experimenting with quality-checked L2 OMI retrievals and incorporating information about local tropospheric ozone climatology into the analyses.

APPENDIX A

COMPARISON OF THE MODIS AEROSOL AND THE AERONET AEROSOL AND THEIR DEPENDENCES ON A LAND SURFACE BRIGHTNESS AND AN AEROSOL TYPE: THE STUDY IN SOUTHEAST ASIA

(Published as "Bridhikitti, A., & Overcamp, T. J. (2009). Comparison of the MODIS aerosol and the AERONET aerosol and their dependences on a land surface brightness and an aerosol type: the study in Southeast Asia. In Proceeding of the Air and Waste Management Association's 102nd Annual Conference and Exhibition, Detroit, MI, USA")

A.1. ABSTRACT

MODIS (Moderate Resolution Imaging Spectroradiometer) onboard the Terra and Aqua satellites has the capability of monitoring long-term daily atmospheric aerosols over the globe. However, recent reports showed that the validation of its aerosol data sets was occasionally poor, which could be related to surface conditions and aerosol types. Understanding the factor limiting the estimation of aerosol properties is essential for future improvement of the MODIS aerosol algorithm and is useful for MODIS users. In this study, the collection 5 MODIS aerosol products, including aerosol optical depth (*AOD*), Angström exponent, and aerosol type, were compared with ground-based measurement acquired from four Southeast Asian (SEA) AERONET stations during 2003 to 2007. The results showed significant effects of the aerosol type and land surface brightness on the correlation of the MODIS and the AERONET products. The cluster analysis of AERONET data suggested two major classes of aerosols: the higher single scattering albedo, *SSA*, and the lower *SSA*. For *AOD*, better linear correlation was found for the higher *SSA* aerosol (mean *SSA* ~0.94; R^2 = 0.81 at 470 nm) and over the brightest

surfaces, bare soils and plateaus (mean reflectance at 660 nm > 0.128; R^2 = 0.81 at 470 nm). Approximately 55% to 65% of the *AOD* observations fall within the uncertainty limit for the land algorithm. MODIS Angström exponent was not correlated with the value from AERONET. The MODIS aerosol type was also not in agreement with the aerosol types determined from the analysis of AERONET data. MODIS reported two aerosol types dominated: sulfate aerosol (87%) and heavy absorbing smoke (13%). This sulfate aerosol was mainly classified in this study as the lower *SSA* aerosols and half of the MODIS heavy absorbing smoke was reported in the higher *SSA* cluster instead of the lower *SSA* cluster as expected.

Index Terms— Aerosol Robotic Network (AERONET), aerosol optical depth, Angström exponent, aerosol single scattering albedo, Moderate Resolution Imaging Spectroradiometer (MODIS) aerosol,

A.2. INTRODUCTION

Satellite-observing atmospheric aerosol helps scientists understand the role of aerosols on global radiation and climate. Satellite observations can be used for monitoring regional transport of polluted air masses. Aerosol retrieval products from the satellites include aerosol optical depth, *AOD*, and various aerosol optical properties. *AOD* is a measure of the extinction of solar radiation by aerosol scattering and absorption between the point of observation and the top of the atmosphere. It indicates the aerosol amount in the total atmospheric column. Optical properties of aerosol, such as size, sphericity, light scattering/absorbing properties, can be used to infer its chemical composition and its

potential sources. These properties can be determined from the inversion of the radiance/irradiance retrieved from satellites or ground-based sensors based on minimizing fitting error of the observed with the results.

Since the launching of MODIS on the Terra satellite in 1999 and the Aqua satellite in 2002, its estimates of aerosol properties have been widely applied in regional aerosol studies (Levy et al., 2009). The most recent aerosol retrieval algorithm, version 5.2 released in April 2006, has been used to generate collection 5 (C005) aerosol products. A comparison of MODIS aerosol C005 products over land with the ground-based sun photometer measurements from AERONET, conducted by Levy et al. (2009), included more than 6,300 global and seasonal representative data sets. AERONET (AErosol RObotic NETwork) program is a federation of ground-based remote sensing aerosol networks established by NASA and PHOTONS, from France. The program, with many international collaborators, provides standard observations with global coverage of spectral *AOD* and aerosol inversion products. Levy et al. (2009) reported that MODIS *AOD* at 550 nm was linearly related to AERONET *AOD* by $AOD_{\mathrm{MODIS}} = 0.029 + 1.01 \times AOD_{\mathrm{AERONET}}$ with $R = 0.894$, indicating a good correlation. However, the correlation for the other aerosol products, such as fine model weighting and Angström exponent, were not as good (Levy et al., 2009). An independent comparison of the MODIS *AOD* C004 data with ground-based measurements of the Chinese Sun Hazemeter Network (CSHNET), found that the MODIS *AOD* retrievals did not always correlate with these observations. It was suggested that these inaccuracies could be related to surface conditions and aerosol types (Wang et al., 2007).

This study reported here compared *AOD*, Angström exponent, and aerosol type retrieved from MODIS with the ground-based measurements acquired from four Southeast Asian AERONET stations. In addition, the effects of aerosol type and land surface condition on the validation of the MODIS aerosol algorithm, focusing on a regional air quality over Southeast Asia (SEA), were evaluated.

The results from this study provide information for MODIS users helping them to understand the limitations or uncertainties of using MODIS aerosol products. Understanding the factors limiting product validation is also essential for future improvement of the MODIS aerosol algorithm.

A.3. RESEARCH METHODOLOGY

A.3.1. Data description

MODIS aerosol products

Due to a difference in the spatial-temporal retrieval for level 2 MODIS aerosol products and AERONET aerosol products, the MODIS data used here have been collocated in time and space with the AERONET data. The MOD04/MYD04 (short name of the MODIS aerosol products data set) level 2 has been processed using MAPSS (MODIS Aerosol and associated Parameters Spatio-temporal Statistics) based on the approach developed by Ichoku et al. (2002). In summary, 10 km × 10 km at nadir MODIS level 2 aerosol products are averaged over 50 km radius centered at the ground station. The value of subset center, its mean (used in this study), local spatial variability, the spatial slope

and associating azimuth, including multiple correlation coefficients were computed (Ichoku et al., 2002). These products can be accessed at http://modis.atmos.gsfc.nasa.gov/mapss.html.

There are two main aerosol retrieval algorithms in the version 5.2. One is applied over land and another is applied over ocean. The land and ocean algorithm is the union of the "best" value for the over ocean pixels and the "corrected" value for the over land pixels. The "best" value is the value retrieved from the solution with the least fitting error. In the MODIS aerosol C005, the "corrected" value is the value estimated by fitting an MODIS aerosol optical model (classify aerosol into 3 categories: 'neutral', 'non-absorbing', and 'absorbing'), associated with a particular region and season (Levy et al., 2009).

The five co-spatial-temporal subset MOD04/MYD04 level 2 products over land acquired for this study include:

I. the corrected *AOD* at 470, 550, 660, and 1020 nm using the land algorithm;

II. the *AOD* at 550 nm using the ocean algorithm (best) and using the land algorithm (corrected);

III. the Angström exponent, aerosol-size related parameter for 470:670 nm using the land algorithm; This value less than 0.8 indicates coarse-size dominated aerosol (Cheng et al., 2006);

IV. the aerosol type from the land algorithm, including five standard aerosols: mixed aerosol, dust (coarse-dominated), sulfate, smoke, and heavy absorbing smoke;

V. the mean reflectance (the mean of the remaining pixels after removing too dark, too bright, and cloudy pixels), the fraction of the upward radiance over a specified spectra band to a total incoming radiance, at 470, 550, 660, 870, 1200, 1600, and 2100 nm using the land algorithm.

Except for the mean reflectance, all these products were compared with the AERONET aerosol products in this study. The mean spectral reflectance was used to evaluate the interaction of the MODIS aerosol products with land surface condition.

AERONET inversion products

The AERONET products, ground-based sun photometers data, used in this study are level 2 (cloud-screened and quality-assured) daily average *AOD* at 440, 500, 660, and 1020 nm and the Angström exponent for 870:440 nm. These data sets were downloaded from AERONET website (http://aeronet.gsfc.nasa.gov/). Twenty-six AERONET inversion products, as detailed in Bridhikitti and Overcamp (2009), were also used in this study in a cluster analysis to determine the dominant aerosol types. The effects of these aerosol types on the validation of the MODIS aerosol products were later evaluated.

A.3.2. AERONET site descriptions

The data from four AERONET sites over SEA, shown in Figure A.1, were retrieved during 2003 to 2007 for this study: Bac Giang, Vietnam (BG); Mukdahan, Thailand (MU); Pimai, Thailand (PI); Silpakorn University, Thailand (SU). BG, PI, and MU are characterized as the rural environment surrounded by agricultural fields, primarily rice

paddies. SU is more urban and located at about 50 km west of Bangkok, the capital of Thailand. Two prevailing winds dominate over these areas: northeasterly winds during October to April, which includes the typical dry seasons, and southwesterly winds during May to September, which includes the typical rainy season.

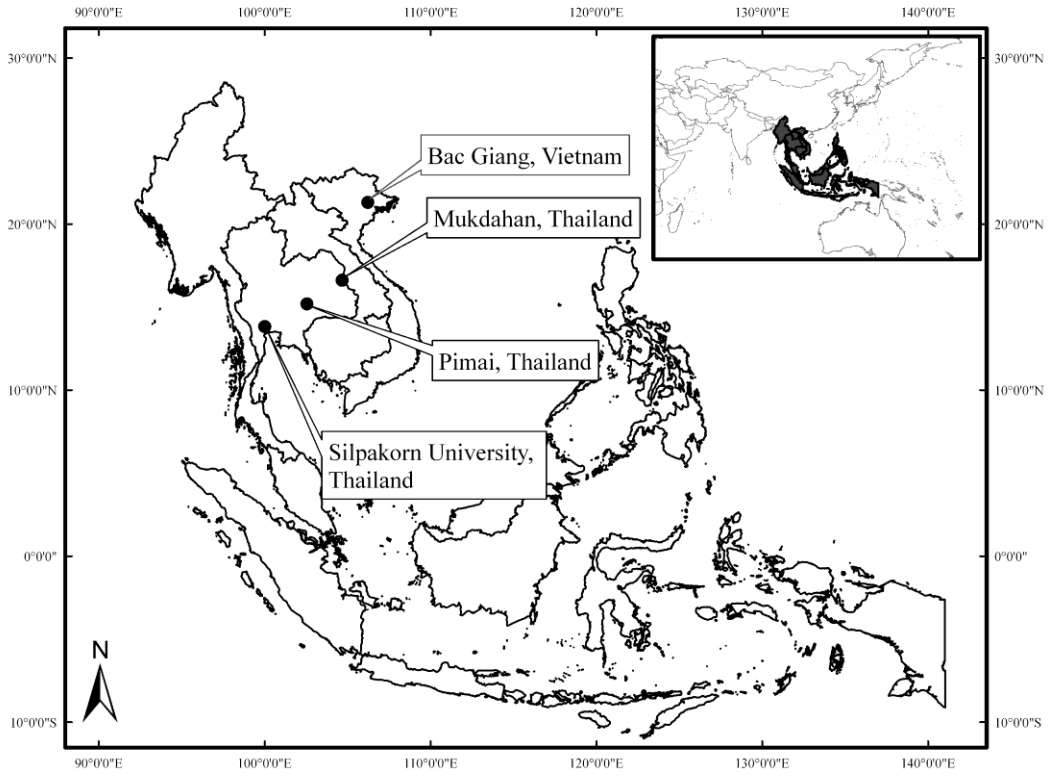

Figure A.1. Locations of the four AERONET stations considered in this study

A.3.3. Data processing

The AERONET *AOD* at 440, 500, 660, and 1020 nm were interpolated to the corresponding value at 470, 550, 674, and 2120 nm, respectively by using the Angström exponent relationship in equation 1 as

$$AOD_A = AOD_B\left(\frac{\mathrm{A}}{\mathrm{B}}\right)^{-\alpha_{avg}} \quad \text{(Eq.1)}$$

$$\alpha_{\mathrm{C-D}} = -\frac{\ln\left(\frac{AOD_{\mathrm{C}}}{AOD_{\mathrm{D}}}\right)}{\ln\left(\frac{\mathrm{C}}{\mathrm{D}}\right)} \quad \text{(Eq.2)}$$

Where AOD_{A} = calculated AERONET *AOD* at wavelength A = 470, 550, 674, and 2120 nm; AOD_{B} = AERONET *AOD* at wavelength B = 440, 500, 660, and 1020 nm, when paired with the wavelength A, respectively; and α_{avg} = the average among the AERONET Angström exponents for wavelengths C: wavelengths D, 440: 870, 440:674, 380:500, and 500:870 nm calculated using equation 2.

Remer et al. (2005) suggests that the MODIS *AOD* validation is satisfactory over land if these two collocated data sets fall within the uncertainty of $\Delta AOD = \pm 0.05 \pm 0.15 AOD$.

The mean comparisons of these Angström exponents using the analysis of variance (ANOVA) failed to reject the equal means assumption with a 0.05 significance level, indicating that the Angström exponent was independent of the choice of wavelength pairs. The MODIS Angström exponent for 470:670 nm, therefore, was compared to the AERONET Angström exponent for 870:440 nm.

In this study, the MODIS mean reflectance at 660 nm was used to characterize the light scattering of the land surfaces. The preliminary analysis in this study found that there was no significant mean reflectance difference at 660 nm among the different AERONET aerosol types; however, the difference was significant at a 0.05 significance level from

site to site. Dark surfaces, including most vegetated land surfaces, have a lower mean reflectance due to stronger radiative absorption than bright surfaces, including bare soils and paved surfaces.

Cluster analysis is designed to group the set of objects into classes so that those having similar properties are in the same class. Cluster analysis using the average linkage method was performed in this study via SAS 9.2 software for grouping dominant aerosols at the monitoring sites. The analysis is useful for solving the problems with unknown number of classes. This average linkage method, averaging distance between pairs of observations (one in each cluster), tends to be less influenced by the extreme values (SAS Institute Inc., 2002). In this study, the appropriate number of cluster level was chosen at the peak of pseudo-*F* value as typically suggested for this analysis (SAS Institute Inc., 2002).

A linear regression analysis, a linear contrast analysis, and/or an analysis of variance (ANOVA) to compare the means were performed using SAS 9.2 software on the two dominant aerosol clusters and separately for four mean reflectance levels at 660 nm [$\leq$ 0.110: first quartile (SR1); 0.110-0.128: second quartile (SR2); 0.128-0.146: third quartile (SR3); and $\geq$ 0.146 (SR4)].

A.4. RESULTS AND DISCUSSION

A.4.1. Cluster analysis of the AERONET aerosol inversion products

Cluster analysis of the AERONET inversion products showed that 92% of the total observations over the four sites were dominated by two aerosol clusters which are named a higher single scattering albedo, *SSA*, (mean *SSA* ~0.94 at 440 nm) aerosol and a lower *SSA* (*SSA* ~0.91 at 440 nm) aerosol. The effects of these two aerosol types and different surface reflectance levels on the validation of the MODIS aerosol algorithm are discussed here for *AOD*, Angström exponent, and aerosol types.

The selection of MODIS aerosol inversion model in the version 5.2 is based on the results from AERONET aerosol clustering by Levy et al. (2009) as well. For SEA, the spherical non-absorbing (*SSA* ~0.95) aerosol model is applied from June to December, and a spherical neutral model (*SSA* ~0.9) is for the rest of the year [implied from the Figure. 10 in Levy et al. (2009)]. Figure A.2 shows two aerosol clusters found in this study from the cluster analysis versus time. The higher *SSA* aerosol cluster was frequently observed at BG from September to December and the lower *SSA* aerosols cluster was observed from December to April. This roughly corresponds to the choice of the aerosol models in the MODIS aerosol algorithm.

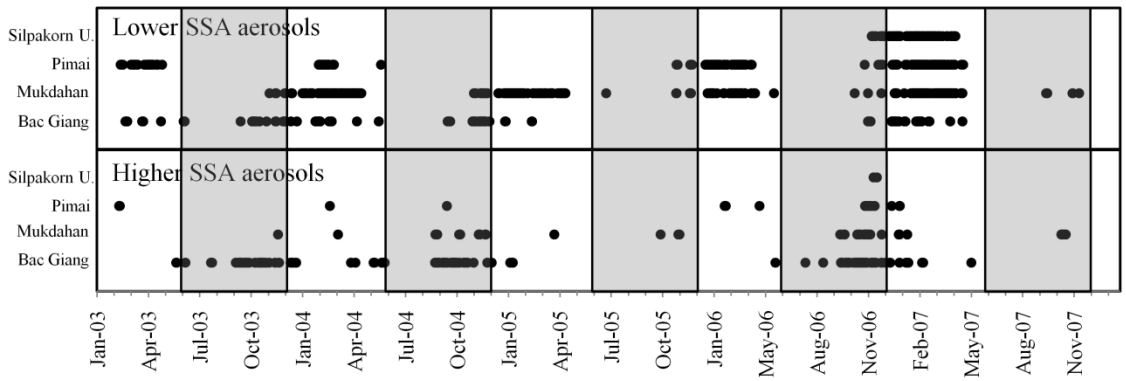

Figure A.2. Time series of two aerosol clusters [the higher *SSA* and the lower *SSA*] observed for each site. The gray area and white area show the period which the non-absorbing model and the neutral model, respectively, are used for estimating Southeast Asian MODIS aerosol (Levy et al., 2009)

A.4.2. MODIS *AOD* products comparison

The results from the linear regression analysis of the AERONET *AOD* and the MODIS *AOD* are given in Table A.1 and A.2. The land-ocean algorithm gave a lower R^2 and fewer observations than the land algorithm alone because some observations were eliminated during the quality assurance and the quality control processing. The *AOD* at 470 nm using the land algorithm gave the best correlation than those for longer wavelengths for both aerosol types and all mean reflectance levels. Comparing both aerosol types, as seen in Table A.1, the higher *SSA* aerosol resulted in higher linear correlation than a lower *SSA* aerosol. At 470 nm, the slope [higher *SSA* and lower *SSA*] was 1.068 ± 0.043 (N = 146) and 0.854 ± 0.026 (N = 541); while the intercept was –0.067 ± 0.044 and 0.041 ± 0.019; and R^2 = 0.81 and 0.67. In this study, approximately 55% to 65% of the observations fell within the uncertainty limit for the land algorithm for both aerosol types (in Table A.1) and for all mean reflectance levels (in Table A.2).

Table A.1. Linear regression equations of the MODIS spectral *AOD* and the AERONET spectral *AOD* for individual aerosol type and the percentage observed in the uncertainty limit

AOD Wavelength	Aerosol clusters	$AOD_{MODIS} = A \times (AOD_{AERONET}) + B$			
		A	B	R^2	% observed within uncertainty limit[a]

470 nm (L[b])	Lower *SSA*	0.854±0.025[¤]	0.041±0.019	0.68	57
	Higher *SSA*	1.068±0.043	-0.067±0.044	0.81	59
550 nm (L)	Lower *SSA*	0.823±0.027	0.051±0.017	0.63	57
	Higher *SSA*	0.969±0.041	-0.008±0.036	0.80	59
660 nm (L)	Lower *SSA*	0.824±0.032	0.081±0.015	0.55	57
	Higher *SSA*	0.969±0.045	0.041±0.032	0.76	60
550 nm (L-O[b])	Lower *SSA*	0.750±0.032	0.097±0.019	0.52	57
	Higher *SSA*	0.968±0.042	-0.021±0.037	0.79	58

[a] Uncertainty of $\Delta AOD = \pm 0.05 \pm 0.15 AOD$ over land [6]; [¤] Mean ± Standard error

[b] L = land algorithm, L-O = Land algorithm (corrected) and Ocean algorithm (best)

As shown in Table A.2, the brightest surface, SR4, provided a higher linear correlation than the darker surfaces with a slope closer to unity [$AOD_{MODIS} = 1.07 \times AOD_{AERONET} - 0.07$ at 470 nm, N = 185, $R^2 = 0.81$]. The percentage of observations falling within the uncertainty limit was also higher in the brighter surface classes (SR3 and SR4). Wang et al. (2007) reported that the MODIS *AOD* retrievals performed well over dark surfaces but poorly over bright surfaces. However, the bright surfaces considered in Wang et al. (2007) are the areas in the deserts, arid regions and plateaus of China. These surfaces are expected to exhibit higher surface reflectance than the surfaces observed in this study. Based on the MODIS mean reflectance at 2100 nm (expected to be similar with that at 2130 nm), 95% of the observations found this study were dark pixels as defined by the MODIS land algorithm.

Table A.2. Linear regression equations of the MODIS spectral *AOD* and the AERONET spectral *AOD* for individual mean reflectance level and the percentage observed in the uncertainty limit

AOD	Surface	$AOD_{MODIS} = A \times (AOD_{AERONET}) + B$

Wavelength	reflectance at 660 nm	A	B	R^2	% observed within uncertainty limit[a]
470 nm (L[b])	≤ 0.110	0.84±0.03[*]	0.03±0.01	0.63	55
	0.110-0.128	0.87±0.04	0.03±0.02	0.72	56
	0.128-0.146	0.94±0.03	-0.01±0.03	0.80	64
	>0.146	1.07±0.04	-0.07±0.04	0.81	59
550 nm (L)	≤ 0.110	0.82±0.03	0.03±0.01	0.58	55
	0.110-0.128	0.85±0.04	0.04±0.02	0.70	56
	0.128-0.146	0.88±0.03	0.02±0.02	0.78	63
	>0.146	1.00±0.04	-0.02±0.03	0.80	61
660 nm (L)	≤ 0.110	0.87±0.04	0.04±0.01	0.51	55
	0.110-0.128	0.89±0.04	0.05±0.02	0.63	55
	0.128-0.146	0.90±0.04	0.05±0.02	0.75	66
	>0.146	0.99±0.04	0.04±0.02	0.79	58
550 nm (L-O[b])	≤ 0.110	0.83±0.03	0.02±0.01	0.58	49
	0.110-0.128	0.75±0.04	0.10±0.02	0.59	49
	0.128-0.146	0.87±0.04	0.06±0.03	0.70	51
	>0.146	0.94±0.04	0.01±0.03	0.75	51

[*] Mean ± Standard error

[a] Uncertainty of $\Delta AOD = \pm 0.05 \pm 0.15 AOD$ over land (Remer et al., 2005)

[b] L = land algorithm, L-O = Land algorithm (corrected) and Ocean algorithm (best)

Since there was no significant effect of the type of aerosol on the mean reflectance at 660 nm, any change in this reflectance is probably due to the land surface conditions alone. As seen in Table A.2 and the corresponding plots for 470 nm in Figure A.3, mean *AOD* increased as the mean reflectance increased with a lower mean *AOD* being observed over darker surfaces, including crop lands. This trend, found in both MODIS land *AOD* and AERONET *AOD*, probably resulted from surfaces brightness affecting the *AOD* algorithm. An alternative hypothesis is that higher aerosol loadings were emitted from brighter surfaces and a lower one was emitted from darker surfaces. However, this was

not hypothesized here because it is contradicted by the seasonal observations of aerosol exposure from burning agricultural residues over the SEA continent (Liu et al., 1999; Tipayarom, 2004).

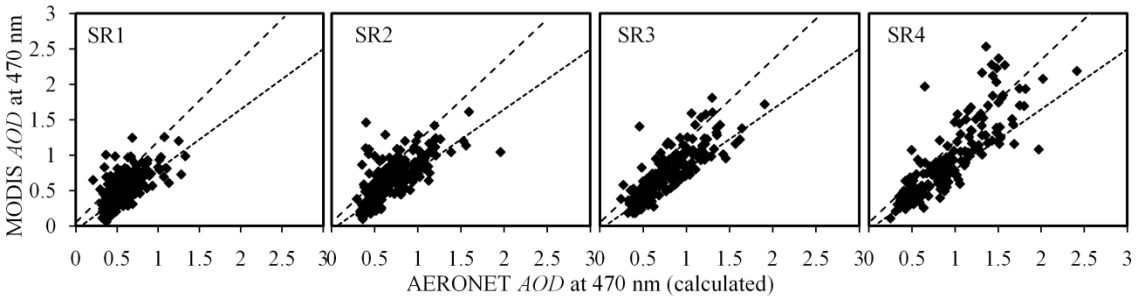

Figure A.3. The plots of the calculated AERONET *AOD* at 470 nm (*x*) versus MODIS *AOD* at 470 nm (*y*) for four mean reflectance at 660 nm [≤ 0.11 (SR1); 0.11-0.13 (SR2); 0.13-0.15 (SR3); and ≥ 0.15 (SR4)]. The short dash line is the lower uncertainty limit and the coarse dash line is the upper uncertainty limit

A.4.3. MODIS Angström exponent comparison

The MODIS and AERONET mean Angström exponent for individual aerosol types and mean reflectance levels are shown in Table A.3. The mean Angström exponents from both data sets were significantly different. Mean AERONET values were higher in all cases. Distributions of the MODIS Angström exponent, shown in Figure A.4, exhibited an upper bound of 1.8 and a lower bound of 0.5, whereas, most of the values from AERONET ranged between 1 and 2.

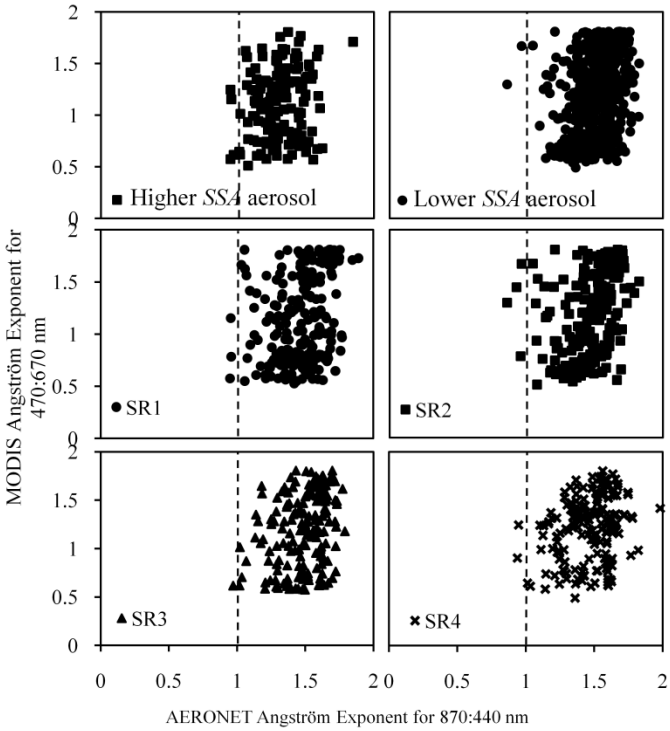

Figure A.4. The plots between AERONET Angström exponent for 840:440 nm (*x*) and MODIS mean Angström exponent at 470:670 nm (*y*) for two aerosol types [higher *SSA* aerosols and lower *SSA* aerosols] and for four mean reflectance at 660 nm [≤ 0.11 (SR1); 0.11-0.13 (SR2); 0.13-0.15 (SR3); and ≥ 0.15 (SR4)]

Table A.3. Mean ± 1 Standard deviation of the MODIS Angström exponent at 470-:670 nm, and the AERONET Angström exponent at 870:440 nm for individual aerosol type and individual mean reflectance level

Aerosol clusters	MODIS Angström exponent at 470:670 nm	L2 AERONET Angström exponent at 870:440 nm
Lower *SSA* aerosols	1.26±0.37, N=317[a]	1.52±0.14, N=580
Higher *SSA* aerosols	1.11±0.32, N=92	1.31±0.17, N=260
Surface reflectance at 660 nm		
≤ 0.110	1.15±0.41, N=212	1.43±0.20, N=292
0.110-0.128	1.18±0.40, N=200	1.47±0.17, N=200
0.128-0.146	1.21±0.38, N=168	1.49±0.16, N=168

>0.146	1.22±0.33, N=173	1.47±0.17, N=173

[a] Mean ± 1 standard deviation, N is total number observation

A.4.4. MODIS aerosol type comparison

Table A.4 shows the cross-frequency of the MODIS aerosol type and the aerosol type obtained from a cluster analysis of AERONET aerosol products. MODIS assigns an integer value to indicate aerosol type (0 = mixed, 1 = dust, 2 = sulfate, 3 = smoke, 4 = heavy absorbing smoke). In the collocation with AERONET data, these integer values are average over the cells within a 50 km radius. When the MODIS aerosol type varies over the cells of interest, a non integer value can be reported. Since these values are ambiguous, only integer data were compared to AERONET cluster type. These were 88% of the total observations.

Table A.4. Cross-frequency between the MODIS aerosol type (land algorithm) and the AERONET aerosol type resulted from the preliminary aerosol clustering analysis over SEA (Total observation = 620)

		AERONET aerosol type resulted from the preliminary aerosol clustering analysis		Total percentage
		Lower *SSA* aerosols	Higher *SSA* aerosols	
MODIS aerosol type*	Sulfate	Total Percent =70.00 Row Percent=80.37 Column Percent=92.14	17.10 19.63 71.14	87.10
	Heavy absorbing smoke	5.97 46.25 7.86	6.93 53.75 28.86	12.90
Total percentage		75.97	24.03	100.00

* The observation reported here was considered only the integer values of the mean MODIS aerosol type subset. These values were accounted for 88% of total observation.

Of the total MODIS aerosol type observations, 87% were reported to be a sulfate aerosol and 13% a heavy absorbing smoke. No MODIS mixed aerosol, dust, and smoke classes were observed in this study. If the aerosols are dominated by sulfate, they are likely from long-range transport (Bridhikitti and Overcamp, 2009; Pongkiatkul and Oanh, 2007). Eighty percent of this sulfate aerosol was classified as a lower *SSA* aerosol and the rest as higher *SSA* aerosol. The lower *SSA* aerosol had mean *SSA* of 0.91 (440 nm), within in the range of the biomass burning smoke reported in the literature (Dubovik et al., 2002; Oanh et al., 2006). Heavy absorbing smoke, enriched with a black carbon, has a naturally low *SSA*. In contrast, 54% of the MODIS heavy absorbing smoke observed in this study was found to be a higher *SSA* aerosol.

A.5. CONCLUSION

The results from this study are summarized as following:

- Cluster analysis of the AERONET aerosol inversion products showed two aerosol clusters, the higher *SSA* (mean *SSA* ~0.94 at 440 nm) aerosol and the lower *SSA* (*SSA* ~0.91 at 440 nm) aerosol, dominated at the SEA sites. Temporal observation of these aerosols roughly corresponded to the seasonal choice of the aerosol models in the MODIS aerosol algorithm for SEA.

- The *AOD* correlation depended on surface brightness and aerosol type. Higher linear correlation between the MODIS *AOD* and the AERONET ground-based measurement *AOD* was found for higher *SSA* aerosols (mean *SSA*~0.94) with an R^2 of 0.81 (470 nm) and for *AOD* over the brighter surfaces (soil and plateau; mean reflectance

at 660 nm > 0.128) with an R^2 = 0.81 (470 nm). According to the MODIS aerosol algorithm version 5.2 for dark-bright pixel definition, 95% of the observations in this study were assigned to dark pixels.

- Approximately 55% to 65% of the *AOD* observations fell within the uncertainty limit defined in Remer et al. (2005) for the land algorithm without significant differences for both aerosol types and for all *AOD* spectra.

- Based on the MODIS algorithm version 5.2, the MODIS Angström exponent was significantly different from the one acquired from AERONET.

- The MODIS aerosol type did not correspond to the aerosol types determined from the AERONET aerosol cluster analysis. The MODIS aerosols observed in this study were either a sulfate aerosol (87%) or a heavy absorbing smoke (13%). This sulfate aerosol was primary coupled to a lower *SSA* aerosol having a *SSA* similar to the biomass burning smoke reported in the literature. The heavy absorbing smoke enriched with a black carbon naturally has a low *SSA*. However, approximately half of the MODIS heavy absorbing smoke was found to be a higher *SSA* aerosol.

APPENDIX B

IMPLICATIONS FROM OZONE MONITORING INSTRUMENT (OMI) RETREVALS ON URBAN OZONE BEHAVIORS: CASE OF THAILAND

B.1. INTRODUCTION

Ozone Monitoring Instrument (OMI) onboard Aura spacecraft was launched in July 2004 with one of its missions to continue detecting global ozone trends. Its predecessors include the Total Ozone Mapping Spectrometer (TOMS), the Global Ozone Monitoring Experiment (GOME), and the Scanning Imaging Absorption Spectrometer for Atmospheric Cartography (SCIAMACHY). Compare to these former instruments, the OMI has more advance capabilities; including global coverage with higher spatial resolution, which could enhance its detection of tropospheric air pollution at urban scales (Levelt et al., 2006). Kar et al. (2010) investigated the possibility of detecting urban signatures in the tropospheric column ozone (TCO) derived from OMI and Microwave Limb Sounder (MLS) retrievals. Their finding indicated fairly significant sensitivity to the lower troposphere over the polluted land areas; including Beijing, New York, Sao Paulo, and Mexico City. Monthly average TCO was used in their study. This study investigated further sensitivities of the satellite-based TCO on the spatial changes of surface ozone responding to downwind ozone formation and on temporal changes of the ozone level responding to weekday-to-weekend traffic volume changes. In addition, we explored the possibility of using OMI products, including tropospheric column NO_2, total column formaldehyde (HCHO), to evaluate urban ozone formation mechanisms.

Traffic volume reduction from weekdays to weekends causes decreases mean concentration of ozone precursors (Blanchard et al., 2008). The precursors include oxide of nitrogen (NO_x), volatile organic compounds (VOC), and carbon monoxide (CO). However, weekend ozone concentration might be comparable, or even higher, with weekday ozone concentration. This evidence was observed in many large US cities (Blanchard et al., 2008). Factors and mechanisms limiting weekend ozone concentrations are not fully acknowledged. One factor could be weekend reductions of nitrogen oxide (NO) emissions from automobile exhausts which minimizes destruction of ozone and allows more ozone to accumulate to reach higher concentration (Blanchard et al., 2008).

Currently, urban ozone control strategy has been focused on control of volatile organic compounds (VOC) and NO_x. NO_x includes NO and NO_2; however, NO rapidly reacts with ozone and forms NO_2. NO_2 consume hydroxyl radical (OH) by oxidizing VOC and form nitric acid (HNO_3). NO_2 also uses photolyzed ozone for NO_2-to-nitrate radical (NO_3) conversion. At high NO_x-to-VOC ratios, the ozone used for NO_2-to-NO_3 conversion play more important role in the reaction paths for NO_x. Therefore, decreasing NO_x can lead to an increase in ozone (Finlayson-Pitts and Pitts Jr., 1997). In this case (called VOC-limited condition), control of VOC is the most effective. At high VOC-to-NO_x ratios, ozone can only form as much as there is NO to be oxidized to NO_2, the source of free oxygen atom to form ozone under photochemical reaction (Finlayson-Pitts and Pitts Jr., 1997). In this case (called NO_x-limited condition), control of NO_x is the most effective.

Martin et al. (2004) applied the ozone-NO_x-VOC relationship concept to diagnose NO_x-limited versus VOC-limited conditions using the ratio of HCHO column (as a surrogate of VOC) to the tropospheric NO_2 column (as a surrogate of NO_x) from Global Ozone Monitoring Experiment (GOME) observations. Their finding indicates that the diagnosis from the space-based observations is highly consistent with *in situ* observations. Duncan et al. (2010) applied the same technique using the OMI observations, which had finer spatial resolution compared to those from GOME (~40 × 320 km^2). Their result shows more NO_x-limited areas than in the *in situ* studies. Both studies were conducted on the mid-latitude Northern Hemisphere in the summertime. This study, we applied this satellite-based indicator for a tropical urban area of Bangkok Metropolitan Region (BMR).

B.2. METHODOLOGY

B.2.1. Site description

In this study, ground-measured data and satellite retrievals were acquired at thirty-eight locations, shown in Figure B.1, in Thailand. These locations are mainly categorized to seven land environments based on the guideline from the work of Bennet and Engardt (2008). These are Bangkok Metropolitan Region, BMR, roadside, BMR residential area, cement industrial, seaside industrial, coal-fired power plant, inland city, and seaside city. The BMR is consisted of Bangkok, the capital of Thailand, and its surrounding five provinces. This region is an area characterized by high traffic volume and high industrial

development. Strong evidence of ozone pollution in BMR had been shown in previous studies (Zhang and Oanh, 2002; Oanh and Zhang, 2004).

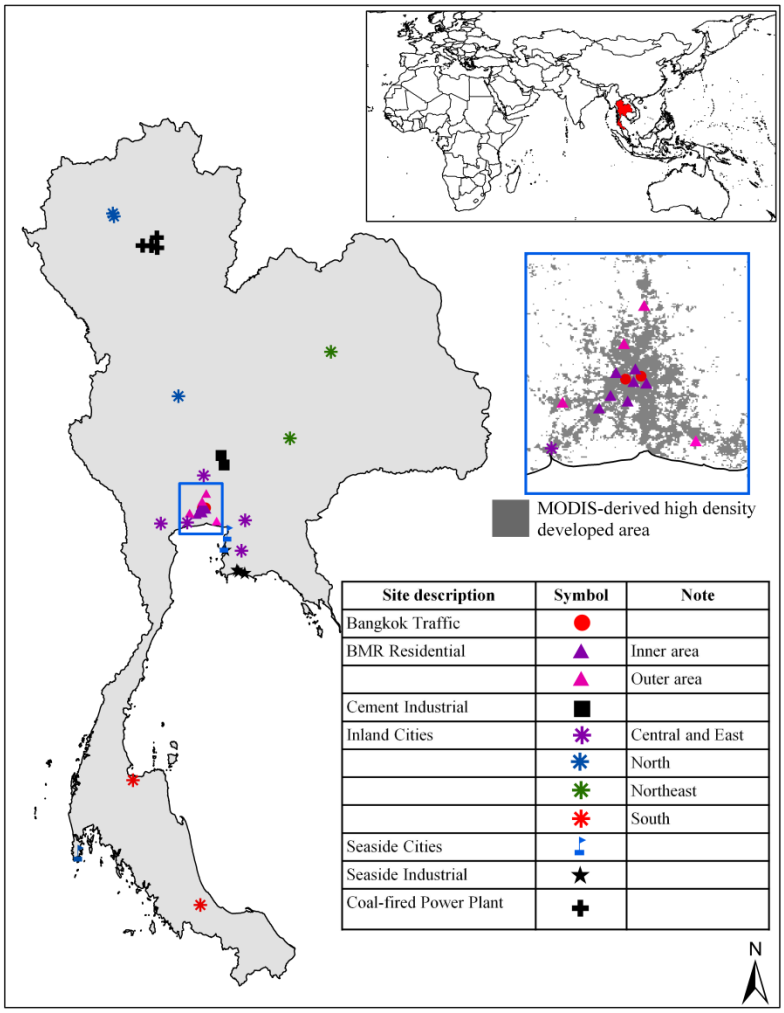

Figure B.1. Thirty-eight locations of Thailand ambient air monitoring stations considered in this study

Thailand has a tropical-monsoon climate dominated by three seasons, rainy from mid-May to October, winter from November to February, and summer from March to mid-May. The South, however, experiences only wet and dry conditions with minor annual

temperature changes. The wet condition is from April to October on its west coast and from September to December on its east coast.

B.2.2. Data description

Tropospheric column ozone (TCO) was be estimated from stratospheric column ozone (SCO) retrieved from Microwave Limb Sounder (MLS) and total column ozone retrieved from Ozone Monitoring Instrument (OMI). Both MLS and OMI are onboard Aura spacecraft, which has a near-polar sun-synchronous orbit at 705-km altitude and crosses an equator (for ascending orbit) at approximately 1:45 pm.

OMI is nadir-viewing near-UV/Visible solar backscatter spectrometer, which provides nearly global coverage in one day, with a spatial resolution of 13×24 km^2 at nadir. The level 2G data binned to $0.25^o \times 0.25^o$ spatial grid (~27.8×27.8 km^2 at the equator) were acquired for this study. The products include OMI total column ozone from Differential Optical Absorption Spectroscopy (DOAS) algorithm, previously applied to GOME total column ozone retrieval, and that from Total Ozone Mapping Spectrometer (TOMS) algorithm. Spectral window used for DOAS fit is 331.1 to 336.1 nm, minimizing sensitivity to atmospheric temperature; whereas, two spectral bands centered at 317.5 nm and 331.2 nm are used to derived the TOMS ozone. Mean differences in ozone column estimates derived by both algorithms vary from 0 to 9 Dobson Unit, DU, (0 - 3%), and their correlation coefficients vary between 0.89 and 0.99 with latitude and season. The OMI-TOMS data are shown to be high overall quality with no significant solar zenith

angle or latitude dependences, whereas, the OMI-DOAS shows latitudinal independence in most cases but significant dependence on solar zenith angle (NASA OMI Team, 2009).

OMI tropospheric NO_2 and total column formaldehyde (HCHO) were also acquired for the evaluation of urban ozone formation. These products have the same spatial resolution with the OMI ozone. The method to determine OMI NO_2 slant column (column along the light path of photons that reach the detector) abundances is DOAS. Spectral windows for the DOAS fit, a least squares fit of a modeled spectrum to the natural log of a measured reflectance spectrum, is 405 to 465 nm. The vertical column density is then determined from empirical air mass factor (AMF), which is the ratio between the DOAS-fit slant column densities and the radiative transfer model-derived vertical column density. The AMF is calculated using specific NO_2 profiles for polluted and unpolluted columns. The amount of the tropospheric NO_2 is calculated from these column amounts with the assumed NO_2 profile shapes. The estimated accuracy of the OMI tropospheric NO_2 algorithm is ±30% in polluted case under clear sky (Chance, 2002). The HCHO retrieval algorithm is similar to the one for the NO_2; but it used spectral fitting window of 327.5 to 356.5 nm (Kurosu, 2008). The vertical column HCHO is assumed being primarily in troposphere and its accuracy is highly dependent on an *a priori* HCHO vertical profile and geophysical conditions. The HCHO uncertainty is estimated to ±25% under biogenically-enhanced conditions (Chance, 2002).

The MLS instrument is a thermal-emission microwave limb sounder that measures vertical profiles of temperature, ozone, and other constituents in upper tropospheric layer to the upper mesosphere. Since the measurements are taken about seven minutes before

OMI views, they can be referred as collocated data sets. The ozone profile is taken from the 240 GHz retrieval with vertical resolution of 3 km for the standard ozone product in the upper troposphere and stratosphere, and 4 to 6 km in the upper mesosphere. Ozone volume mixing ratio product level 2 (L2, swath) version 2.2 was acquired to this study. Its estimated single-profile precision varies from 0.1 to 0.3 ppm_v (2 to 15%) from 46 to 0.5 hPa (~20 to 50 km). The estimated precision for MLS column ozone abundances down to pressures of 215 to 100 hPa (~12 to 16 km) is 2% or less, based on simulated MLS retrievals (Livesey et al., 2007).

Hourly surface ozone mixing ratio at 2:00 pm and temporal-correspondent CO and NO_2 ambient mixing ratios at the 38 stations was acquired from the Bureau of Air Quality and Noise Management, Pollution Control Department (PCD) of Thailand. The ozone was measured using API Photometric Ozone analyzer model 400 (Bennet and Engardt, 2008), which is an EPA designated equivalent method, US EPA EQOA-0992-087 (US EPA, August 24, 2010). The CO and NO_2 measured using non-dispersive infrared detection and chemiluminescence, respectively. Results from analyses of these ground measurements were then used to evaluate the sensitivities of the atmospheric column-based satellite retrievals.

Tropospheric column ozone (TCO) derived from OMI total column ozone data using Convective Cloud Differential (CCD) method (Ziemke et al., 1998) was acquired from NASA/GSFC Atmospheric Chemistry and Dynamics Branch, available online at http://acdb-ext.gsfc.nasa.gov/Data_services/cloud_slice/new_data.html. The data used in this study are monthly averaged for 2005 to 2008 using all available daily OMI data and

have 1^o for latitude (~111 km) ×1.25^o for longitude (~139 km) resolution. Magnitudes of this CCD-derived TCO were compared with those of the OMI/MLS TCO estimated in this study.

Meteorological parameters, which are total column water vapor, surface skin temperature, surface air temperature, and tropopause height, were acquired from Atmospheric Infrared Sounders (AIRS) on Aqua satellite. These parameters were retrieved from the thermal infrared radiation in the 4.2 and the 15 μm CO_2 bands, and the 6.3 μm water bands. The data are averaged and binned into $1^o \times 1^o$ grid cells (Olsen, 2007). The data used in this study are the global daily Level 3 (L3) product for the ascending orbit from Southern Hemisphere to Northern Hemisphere, crossing an equator at approximately 1:30 pm local time (Olsen, 2007). Only daytime data was used in this study because they are more accurate due to higher surface-air thermal contrast than for nighttime data. In this study, these parameters were used to investigate roles of meteorological factors on relationships between the satellite-based TCO and the ground-measured surface ozone concentration.

The data sets from 2005 to 2008 were used for the analysis. The OMI L2G, MLS L2, and AIRS L3 data sets covering the information at the 38 stations were acquired using the GES-DISC Interactive Online Visualization ANd aNalysis Infrastructure (Giovanni) online tool as part of the NASA's Goddard Earth Sciences (GES) Data and Information Services Center (DISC).

B.2.3. Data analysis

The TCO was calculated by subtracting MLS-derived SCO from OMI total column ozone. The MLS SCO was estimated by the method of pressure integration of ozone volume mixing ratio from 0.46 hPa (~34 km attitude) to 215 hPa (~11 km attitude), approximately at tropopause, using equation 1.

$$\text{MLS-derived SCO (Dobson Unit, DU)} = \frac{\sum_{i=215hPa}^{0.46hPa}\left(x_{v,i}\frac{P_i N_A}{10\times g\times M_r}\ln\left[\frac{\sqrt{P_{i+1}}}{\sqrt{P_{i-1}}}\right]\right)}{2.69\times10^{16}} \quad \text{(Eq.1)}$$

Where $x_{v,i}$ is MLS ozone volume mixing ratio at i (unitless), i is MLS pressure levels, P_i is pressure i in Pa (for uppermost pressure level, P_{i+1} = 21.5 Pa. for lowermost pressure level, P_{i-1} = 31,623 Pa), N_A is number of molecule per mole = 6.022×10^{23} molecule $mole^{-1}$, M_r = air molecular weight which set to 29 g $mole^{-1}$, and g = 9.81 m s^{-2}. The TCO is in Dobson Unit (DU) which is the unit of ozone column density. At standard temperature and pressure, one DU is 2.69×10^{16} ozone molecule cm^{-2}.

The TCO is in Dobson Unit (DU) which is the unit of ozone column density. The surface ozone level is daily averaged shown in volume fraction unit of ppb_v. Temporal resolutions of both data sets are not compatible and tropospheric ozone vertical profile is not equally weighted through atmospheric height. The profile relates to mixing height limiting by meteorological conditions and to ozone source strength relating to both land uses and meteorological conditions. In this study, stratospheric ozone intrusion was assumed to be negligible. This assumption should be appropriate here because Thailand

is in low latitude, which is dominated by upward ozone and occurrence of large-scale eddy convection driving stratospheric ozone intrusion at 215 hPa is unlikely. More details on SE Asian ozone climatology are in Chapter Six.

Linear relationships between the satellite-derived TCO and the surface ozone concentration were analyzed separately for OMI TOMS- and DOAS-algorithm products. The product that showed higher linear correlation with the surface ozone concentration was used in next-step of analyses. Dependences of meteorological conditions on the relationships were also evaluated from correlation matrix among the surface ozone concentration (y), the satellite-estimated TCO (x), the individual meteorological variables ($\vec{\mathbf{u}}$), and $\vec{\mathbf{u}}$-x interaction variables ($\vec{\mathbf{u}}^T \times x$). The appropriate variables among x, $\vec{\mathbf{u}}$, and $\vec{\mathbf{u}}^T \times x$ were selected from stepwise regression analysis using 0.05 significance level for the variables to be entered and 0.10 significance level for the variables to be removed. The selected satellite retrieval variables measured in 2005 and 2007 were used for developing linear model for surface ozone estimation. This model was then tested with 2006 and 2008 data sets.

Principal component analysis was used to determine linear combinations, called effective principal components, of surface ozone's and its precursors' concentrations. These effective principal components account for high variations of the observations and they significantly associate with the amount of those gaseous components. Surface ozone, therefore, should be effectively controlled by controlling these principal components. In

addition, the principal component patterns indicate associations among ozone and its precursors, which signify the mechanisms controlling surface ozone formation.

B.3. RESULTS AND DISCUSSION

B.3.1. Comparing the OMI TCOs from TOMS and DOAS alogorithms

As shown in Figure B.2, with more observations having linear correlation coefficient, *R*, closer to positive unity, performance of the tropospheric column ozone (TCO) derived from TOMS algorithm on estimating surface ozone concentration was better than that from DOAS algorithm. Thus, this TOMS TCO variable was later used as OMI/MLS TCO in the following analyses. The TOMS TCO estimated in this study was also comparable in magnitude with the monthly average TCO estimated from Convective Cloud Differential method (see Figure B.3). However, the determination of correlation, R^2, for the TOMS TCO observations indicates that only 4.5% to 10.6% of total variation of the surface ozone concentration can be explained by its linear relationship with this estimated TOMS TCO.

B.3.2. Dependences of the OMI/MLS TCO and the surface ozone concentration on meteorological conditions

From the stepwise linear regression analysis, four variables were suggested to be useful for surface ozone estimation. These variables are 1) AIRS surface skin temperature, 2) AIRS total column water vapor, 3) interaction between AIRS surface air temperature and the TCO, and 4) interaction between surface skin temperature and the TCO. Minimum and maximum daily mean values of the total column water vapor for all studied locations

were 17 and 53 kg m^{-2}, respectively, and the values of the surface skin temperature were 300 and 312 K, respectively. Results from linear regression analysis of these selected variables and the surface ozone concentration, shown in equation 2, indicate that there was less inconsistency between the predicted and the observed surface ozone when the water vapor increased and the skin temperature decreased. This condition is typical in rainy season when surface ozone level is minimized by rain-scavenging ozone precursors. The relationship in equation 2 also suggests higher intercept value, up to 48 ppb_v, for observations in summer (exhibiting high surface skin temperature and low water vapor).

Higher TCO's sensitivity on the changes of surface ozone concentrations were with higher contrast between the surface skin and air temperature. This condition was frequently found from March to June (summer to beginning of rainy) and from September to October (ends of rainy). The tropopause height variable poorly correlated with the ground-measured ozone concentration (R^2 < 0.05); therefore, it was not introduced into the surface ozone estimation model.

$$\text{OMI/MLS surface ozone} = -238 + 0.95T_{skin} - 0.61W + 0.01(T_{skin} - T_{air}) \times \text{TCO} \qquad \text{(Eq. 2)}$$

Where, OMI/MLS surface ozone is in ppb_v; T_{skin} and T_{air} are surface skin temperature and surface air temperature in K, respectively; and W is AIRS total column water vapor in kg m^{-2}. The TCO in Dobson Unit (DU) is estimated from TOMS OMI total column ozone and the MLS-derived SCO.

The equation 2 consistently yielded R^2 of 0.26 for both modeled data set, for observations in 2005 and 2007 (number of observations = 6819), and tested data set, for observations

in 2006 and 2008 (number of observations = 7029). This suggests that the using TCO to explain the variability of surface ozone is improved at least 15% after corrected the water vapor, the surface skin temperature, and the surface air temperature.

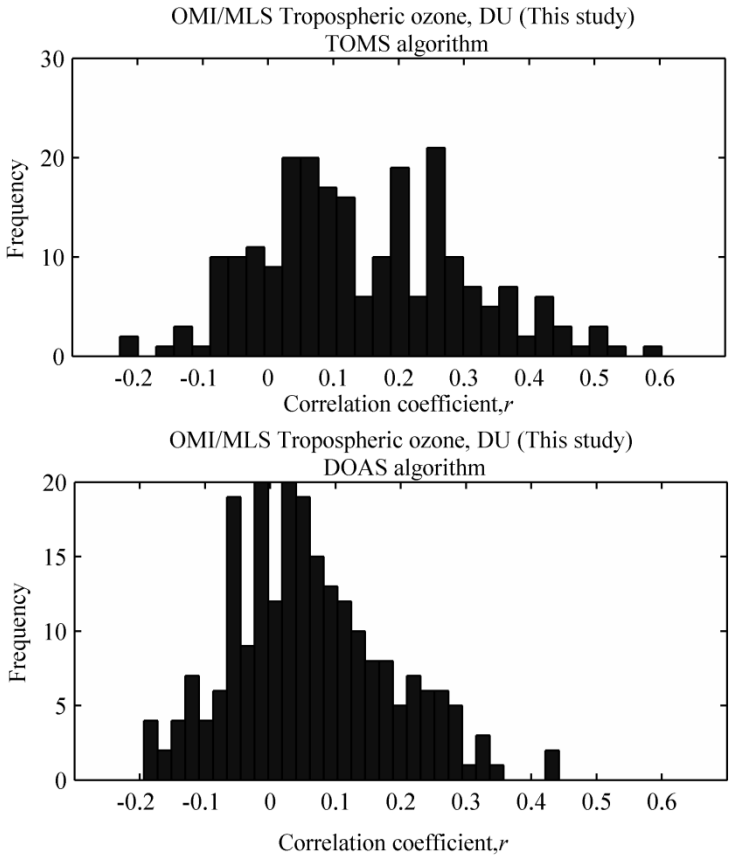

Figure B.2. Distribution of linear correlation coefficient, *R*, between the estimated tropospheric column ozone obtained from OMI TOMS and DOAS algorithms and the surface ozone concentration. The coefficients were for each station and for each two-month intervals from 2005 to 2008.

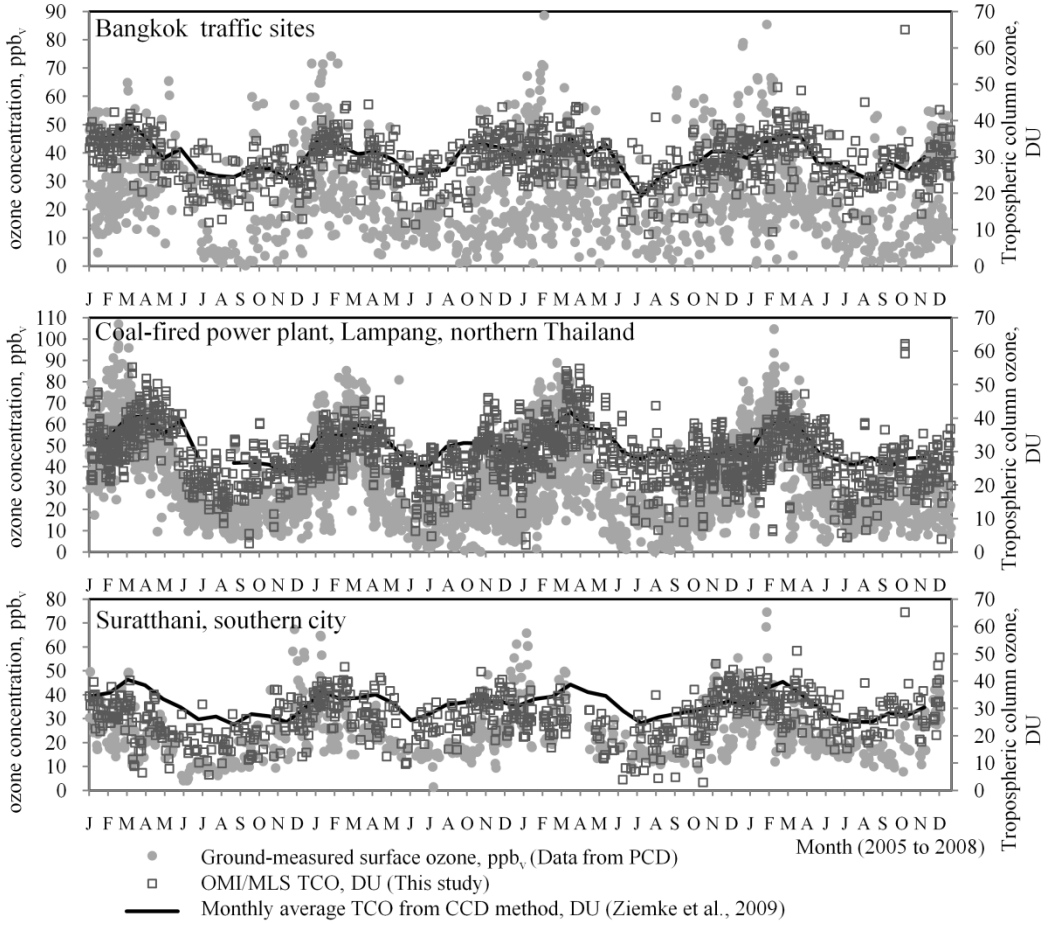

Figure B.3. Temporal profiles of daily-average ground-measured surface ozone concentration, the estimated daily OMI/MLS TCO from this study, and the monthly average TCO from CCD method acquired from Ziemke et al. (2009).

B.3.3. Sensitivity of the OMI/MLS TCO on spatial changes of surface urban ozone concentration

Figure B.4.a) shows means of the OMI/MLS TCO and ground-measured ozone concentration for BMR and its adjacent inland cities. The ground measurements showed increasing in surface ozone concentrations with the distance from the BMR traffic sites to

toward BMR outer bounds. This increase should be a result of ozone formations in the polluted air masses during their advection downwind. Both the OMI/MLS TCO and the surface ozone concentration data sets were collected about at the same times and covering the same locations; however, the OMI/MLS TCO did not show spatial changes. Spatial smoothness of the satellite retrievals should not be fully responsible for this poor spatial sensitivity. From Figure B.4.b), both TCOs that observed over a coal-fired power plant and those over a populated urban city of Chiangmai, approximately 200 km apart, were in similar magnitude. The spatial smoothness aspect should not be an issue in this case. This evidence indicates domination of latitudinal dependence over the local TCO variations driven by different land use activities. Based on these findings, the OMI/MLS TCO was not useful for the studies concerning advective urban ozone formation.

B.3.4. Sensitivity of the OMI/MLS TCO on weekday-to-weekend changes of urban surface ozone concentration

Based on the Bangkok traffic volume data collected by Oanh et al. (2008), the traffic volume decreased from the levels on weekdays to the levels on the Saturdays by up to 10.5%. The traffic volume was the lowest on the Sundays which the levels was decreased by 14.7% to 25.7% from the levels observed on the Saturdays (Oanh et al., 2008). Even vehicular emissions are the major sources of ozone precursors in Bangkok (Oanh and Zhang, 2004); in this study ground-measured surface ozone mixing ratio at 2:00 pm did not significantly show days-of-week variations associated with traffic volume changes.

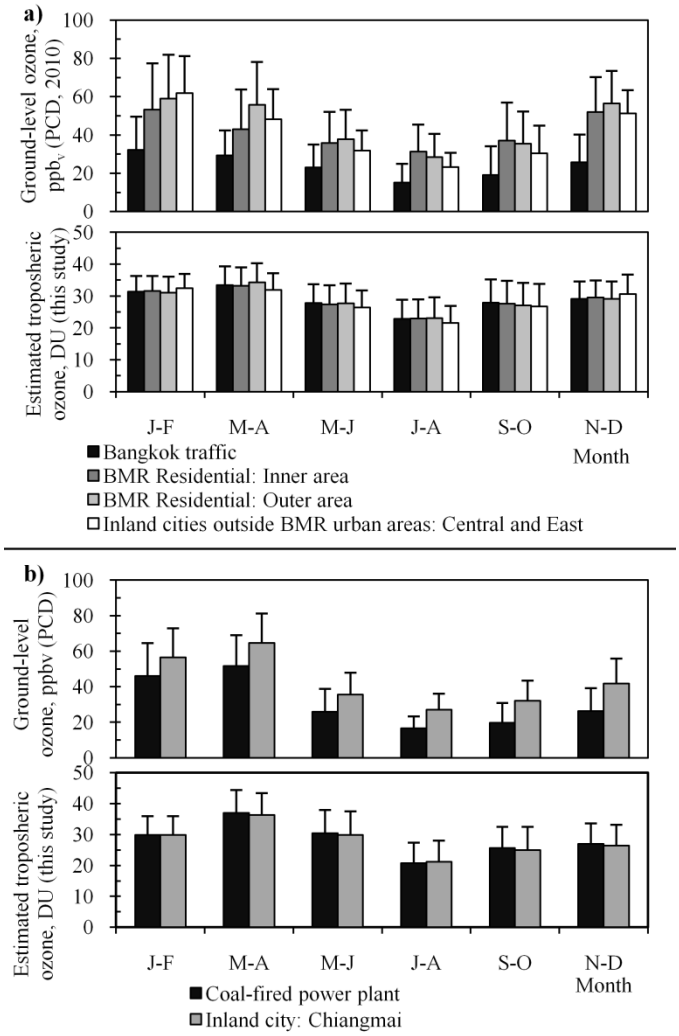

Figure B.4. Two-monthly averages of the surface ozone concentration measured at 2:00 pm (from PCD, Thailand) and the coincident OMI/MLS TCO (from this study) for a) BMR and its adjacent areas and b) two selected locations in the northern Thailand. Error bar indicates one standard deviation

Note: number observations are 142 to 328 for Bangkok traffic, 523 to 1089 for BMR residential, 50 to 129 for Central/East inland cities, 303 to 666 for coal-fired power plant, and 255 to 468 for Chiangmai.

From Table B.1, concentrations of surface ozone observed on the high-traffic volume weekdays, represented by Friday, and those on the lower-traffic volume Saturdays and Sundays were in similar magnitude. Median ozone mixing ratio (ppb_v) was from 46.8 to 50.1, 33.3 to 36.2, and 46.6 to 50, for the January–February, the March–April, and the November–December, respectively.

The surface ozone precursors showed slight decreasing from the levels on the weekdays to the levels on the successive weekends. Considering in the dry periods, two-monthly median concentration reductions from the weekdays to the successive Sundays were approximately 7% to 10 % for CO and 12% to 24% for NO_2. For NO_2, significant reductions from the Saturdays to the successive Sundays were also found. These reductions, however, were in lower magnitudes than those were previously observed in large US cities by Blanchard et al. (2008). In their study, ~28% and ~49% reductions for CO and NO_x, respectively, were found and these decreases were mainly occurred in the early of the day. The data used in our study, however, were taken at the late afternoon when Blanchard et al. (2008) observed less day-of-week mean surface ozone concentration variations.

From the weekday-to-weekend comparisons in Table B.1, two-monthly median surface ozone and NO_2 concentrations at 2:00 pm in the dry seasons were lowest on March to April. One possibly causing the less building-up ozone and NO_2 concentrations was seasonally increasing mean wind speeds from ~0.88 m s^{-1} (averaged from the values

observed at 2:00 pm at all BMR stations from 2005 to 2008) for the November–December to ~1.03 m s^{-1} for the March–April.

Table B.1. Median concentrations of surface ozone and its precursors in the BMR on the Fridays and the weekends during the two-month intervals in the dry periods (November to April) from 2005 to 2008

	Ground measurements at 2:00 pm (data from PCD)								
	Ozone, ppb_v			CO, ppm_v			NO_2, ppb_v		
	Friday	Saturday	Sunday	Friday	Saturday	Sunday	Friday	Saturday	Sunday
Jan–Feb	47.4 (292)*	51.4 (322)	46.8 (322)	0.7 (305)	0.72 (330)	0.68 (327)	18.9 (304)	17.6 (333)	15.2 (327)
Mar–Apr	34.8 (283)	33.4 (295)	36.2 (298)	0.6 (308)	0.58 (328)	0.5 (316)	16.1 (296)	14.4 (312)	13.2 (310)
Nov–Dec	49.8 (375)	48.6 (401)	46.6 (382)	0.62 (365)	0.6 (395)	0.6 (383)	19.6 (366)	16.8 (394)	13.7 (386)
	Satellite retrievals (This study)								
	OMI/MLS-estimated surface ozone, ppb_v			OMI total column HCHO, × 10^{15} molecules cm^{-2}			OMI tropospheric NO_2, × 10^{15} molecules cm^{-2}		
	Friday	Saturday	Sunday	Friday	Saturday	Sunday	Friday	Saturday	Sunday
Jan–Feb	46.6 (221)	47.2 (246)	46.9 (287)	17.3 (256)	14.1 (248)	17.5 (297)	6.8 (344)	6.2 (403)	6.4 (352)
Mar–Apr	42.8 (208)	42.1 (154)	43.5 (195)	17.1 (257)	20.4 (278)	15.6 (253)	4.9 (376)	4.2 (312)	4.2 (307)
Nov–Dec	37.7 (182)	41.2(238)	38.8 (233)	14.5 (243)	14.5 (262)	16.5 (255)	6.2 (359)	6.9 (356)	5.8 (369)

* Median (number of observations)

Consistent with the observed from the ground measurements, changes of the satellite-estimated surface ozone concentrations from the weekdays to the weekends were not apparent. The two-monthly median OMI tropospheric NO_2 levels in Table B.1 slightly reduced (5%, 14%, and 6% for the January–February, the March–April, and the November–December, respectively) from the Fridays to the Sundays and had the lowest value on the March–April. These findings were consistent with the observed from the

ground measurements. This seasonal variation was likely influenced by meteorological changes rather than the changes related to land use activities.

However, from Table B.1 as the ground observations showed consistently the reductions of NO_2 from the Saturdays to the successive Sundays, the satellite retrieval was not. Even though the OMI NO_2 showed some weekday-to-weekend reductions, the changes were within typical same-day-of-week variations. Therefore in summary, the satellite retrievals were not quite useful for the studies concerning daily of surface ozone and its precursors in BMR.

Daily changes of OMI tropospheric column NO_2, however, were found to be useful as a measurable indicator for evaluating implementation of urban traffic restrictions. Significant reduction of the OMI NO_2 were observed during the 2006 Sino-African Summit in Beijing (Wang et al., 2007) and the 2008 Beijing Olympic Games (Witte et al., 2011), when the traffic restrictions were in place.

B.3.5. The OMI retrievals for evaluation of urban ozone formation mechanisms

Carbon monoxide could be a surrogate for traffic-derived formaldehyde, HCHO (Rappenglück et al. 2010). Tropospheric HCHO is largely as a product of VOC oxidation through photoreactions with hydroxyl radical (OH). Thus, the HCHO serves as a major proxy for VOC (Fishman et al., 2008). Inferring VOC from CO is not appropriate for the residential areas, where more VOC is contributed from area sources, including biogenic emissions, anthropogenic biomass burning, and industrial emissions.

Coefficient of determination, R^2, between the NO_2 and CO concentrations for combined observations collected at the roadside and at the residential sites was 0.69. This suggests major contributions of the CO and the NO_2 from vehicular emissions. As discussed earlier, the CO was expected as vehicular-attributed VOC indicator (Rappenglück et al. 2010). However, vehicles only account for 56% of VOC; whereas they account for 81% and 71% of NO_x and CO, respectively, in Bangkok (Milt et al., 2009). Based on this estimation, the CO was can only explain approximately 40% of VOC at most. Since the CO was not well representing the VOC, in this study, the condition limiting urban ozone formation was evaluated from the ground measurements by focusing on relationships between the surface ozone and the NO_2 alone.

Ozone isopleths shown in Figure B.5 indicate that ground-measured ozone concentration at the roadside sites was overall lower than the levels observed at the residential sites and its magnitude tended to decrease with increasing NO_2 level, following the first principal component (G-PC1). From the principal component pattern shown in Table B.2, the surface ozone concentration was positively weighted into the G-PC1. Negative correlation (eigenvector = -0.67) between G-PC1 score and the NO_2 concentration indicates that increasing surface ozone concentration at the Bangkok roadside corresponded with decreasing NO_2 level. This implies VOC-limited condition on the surface ozone formation. The predomination of VOC-limited condition in the BMR was previously reported in the work of Oanh and Zhang (2004) based on simulated ozone formations using ground-measured anthropogenic emissions acquired from PCD. Generally, more VOC-limited condition for urban ozone formation is observed near

traffic locations, where NO_x from vehicular emissions is high (Finlayson-Pitts and Pitts Jr., 1997).

Table B.2. Results from Principal Component Analyses on correlation matrices of the ground-measured variables and of the satellite retrievals for all BMR sites in the dry periods (November to April) for 2006 and 2008

Ground-measurement (PCD, 2010)		Eigenvector		
Number of observations = 6243	Mean ± 1 Stdev	G-PC1	G-PC2	G-PC3
NO_2 at 2:00 pm, ppb_v	21.12 ± 16.59	-0.67	0.21	0.72
CO at 2:00 pm, ppm_v	0.71 ± 0.44	-0.65	0.31	-0.69
Ozone at 2:00 pm, ppb_v	47.31 ± 22.58	0.37	0.93	0.07
	Eigenvalue	1.81	0.88	0.31
Satellite-based (this study)		Eigenvector		
Number of observations = 2849	Mean ± 1 Stdev	S-PC1	S-PC2	S-PC3
OMI tropospheric NO_2, $\times 10^{15}$ molecule cm^{-2}	8.21 ± 4.87	0.71	0.03	-0.70
OMI total column HCHO, $\times 10^{15}$ molecule cm^{-2}	15.86 ± 7.60	0.69	-0.24	0.68
OMI/MLS-estimated surface ozone, ppb_v	45.21 ± 8.10	0.15	0.97	0.19
	Eigenvalue	1.34	1.00	0.66

At the Bangkok residential sites, the surface ozone level was effectively decreased by decreasing NO_2 level, following the second principal component, G-PC2 (See Figure B.5). This indicates that the major ozone formation in the residential areas was NO_2-limited. These areas are the downwind of vehicular emission sources and have more ozone production influenced by biomass burning (Pochanart et al., 2001). The biomass burning causes VOC abundance that promotes to more the NO_2-limited condition. To decrease the surface ozone by 1 ppb_v, the NO_2 should be decreased by approximately

0.31 ppb_v [= (0.21/16.59) ÷ (0.93/22.58)], equivalent to approximately 1.5% of the current mean surface NO_2 mixing ratio.

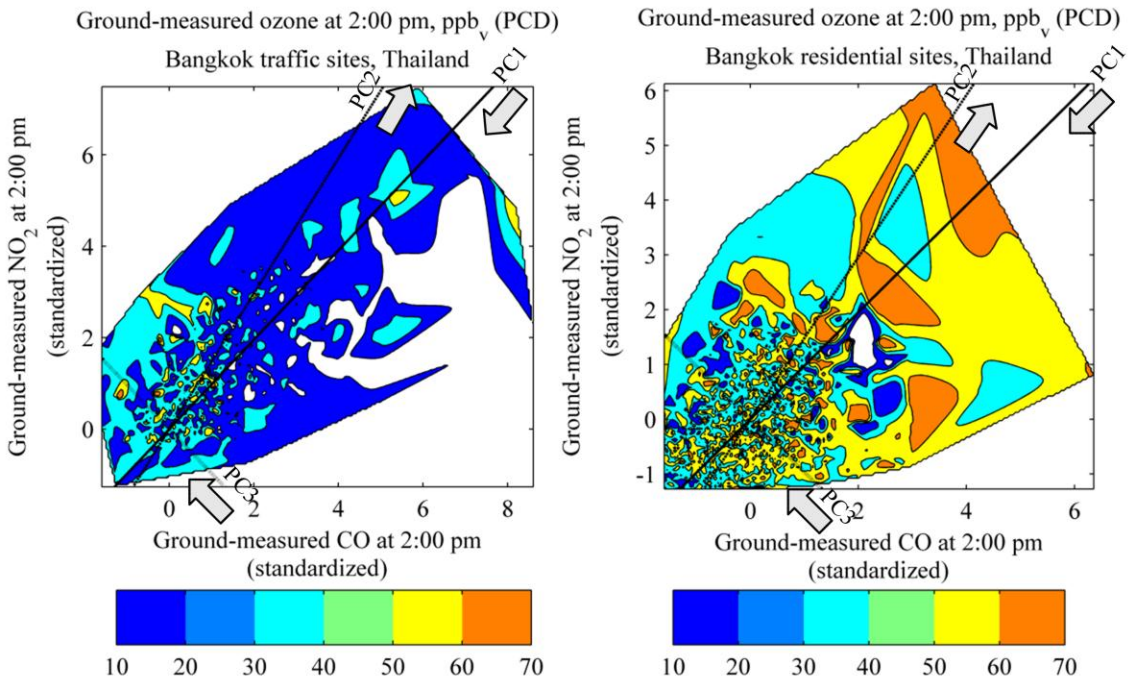

Figure B.5. Ground-measured surface ozone concentration isopleths (in ppb_v) with coincident ground-measured NO_2 and CO distributions for the Bangkok roadside sites and the Bangkok residential sites in the dry periods (November to April) from 2005 to 2008. Arrows show positive ozone component vector for each of three principal components (G-PCs). More details on the principal components are in Table B.2.

The satellite-estimated surface ozone concentration isopleths were shown in Figure B.6. From temporal distribution of principal component scores in Figure B.7, S-PC2 and S-PC3 are not useful for the evaluation of the ozone formation mechanisms because these components were dependent on degrees of the atmospheric water vapor and the surface air temperature, respectively; whereas those for the ground measurements (not shown

here) did not exhibited the dependence. There were two possible explanations for these dependences. One is that the satellite-estimated surface ozone used here was derived from TCO with corrected both meteorological factors. Another explanation is that variations of the satellite-based NO_2 and HCHO are also inherent by meteorological changes. Therefore, the meteorological factors could influent on the O_3-NO_2-HCHO relationships and the abundances of the NO_2 and the HCHO.

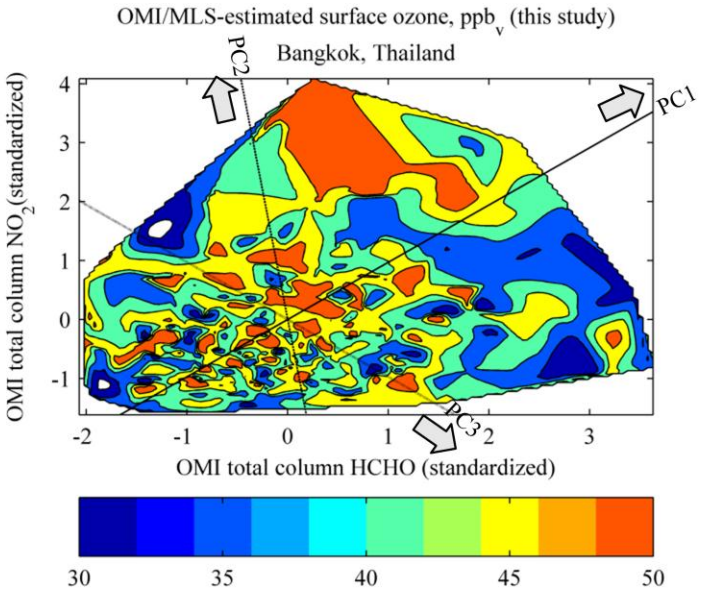

Figure B.6. OMI/MLS-estimated surface ozone concentration isopleths (in ppb_v) with OMI tropospheric column NO_2 and OMI total column HCHO distributions for all BMR sites in the dry periods (November to April) for 2006 and 2008. Arrows show positive ozone component vector for each of three principal components (S-PCs). More details on the principal component patterns are in Table B.2.

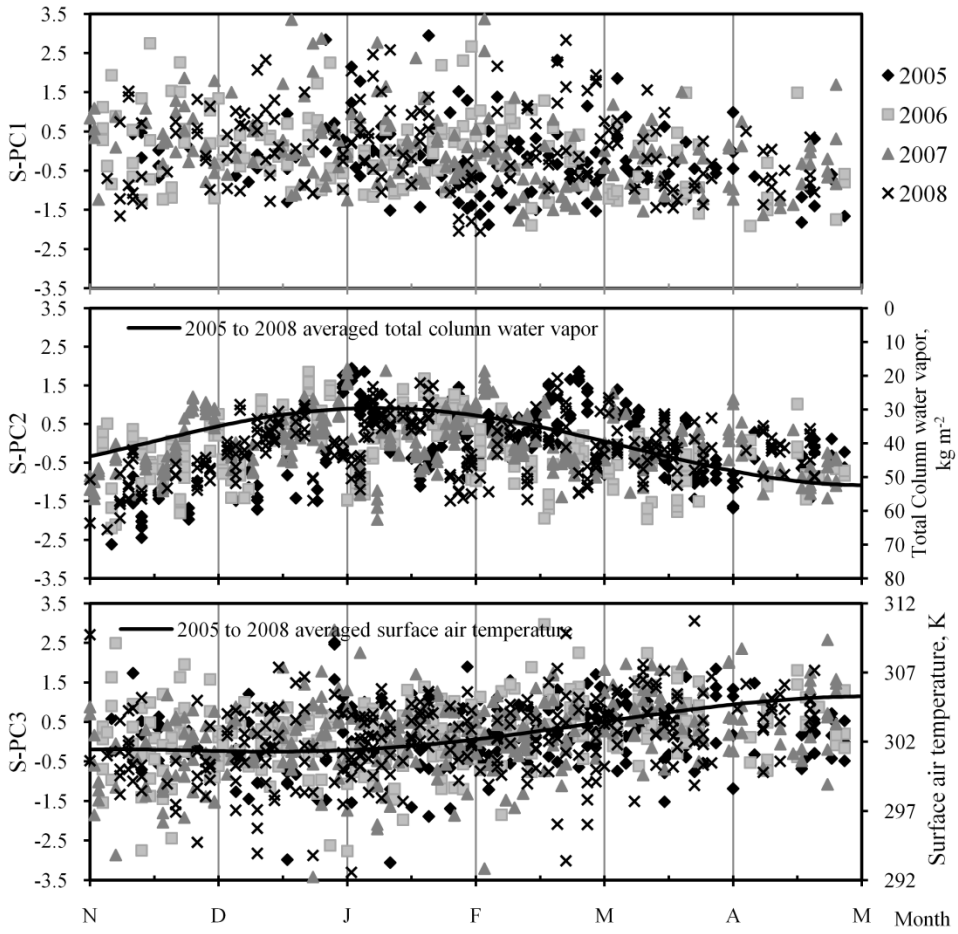

Figure B.7. Temporal distributions of AIRS total column water vapor, AIRS surface air temperature, and principal component scores resulted from the principal component analyses of the satellite retrievals. The detailed on the principal component patterns are in Table B.2. Note: the analysis was for the observations at BMR stations and for the dry periods from November to April in 2005 to 2008.

The S-PC1 did not exhibit meteorological (or temporal) dependence; thus it was an only O_3-NO_2-HCHO relationship that was used to evaluate the ozone formation mechanisms.

From the principal component patterns shown in Table B.2, the estimated surface ozone mixing ratio was positively correlated with the S-PC1. From eigenvector of this S-PC1,

both OMI NO_2 and OMI HCHO played roles on the surface ozone formation. The surface ozone was effectively decreased by decreasing both OMI NO_2 and OMI HCHO with the NO_2 and HCHO ratio of approximately 1.6 [= (0.71/4.87) ÷ (0.69/7.60)]. In this case, decreasing the surface ozone by 1 ppb_v required decreasing tropospheric NO_2 and total column HCHO by approximately 8×10^{15} molecule cm^{-2} [= (0.71/4.87) ÷ (0.15/8.10)] and 5×10^{15} molecule cm^{-2} [= (0.69/7.6) ÷ (0.15/8.10)], respectively. This means that approximately 97% of the current mean OMI NO_2 and 31% of the current mean OMI HCHO should be eliminated in order to meet 1-ppb_v surface ozone reduction. From this estimation, the surface ozone formation was more NO_2-limited. This conclusion was consistent with the results from the ground measurements taken at the BMR residential sites, but not for the BMR roadsides. However, this conclusion might be an instrumental bias. Duncan et al. (2010) found that the OMI observations tended to provide more NO_x-limited than in the *in situ* studies.

Regardless the bias, the ozone control strategies implied from both data sets were significantly different. In order to decrease surface ozone by 1 ppb_v, the satellite retrievals suggested more laborious attempt to decrease the OMI NO_2 abundance by 97% of its current mean value; whereas the ground-measurement suggested 1.5% reduction of the current mean of surface NO_2 mixing ratio. This implies poor capability of using the OMI retrievals as a tool for urban ozone pollution control.

B.4. CONCLUSION

This study investigated sensitivities of the satellite-estimated tropospheric column ozone (TCO) on the spatial changes of ground-measured surface ozone concentration

responding to advective ozone formation and on the temporal changes of the ozone concentration responding to traffic volume changes from weekdays to weekends. This TCO was estimated by subtracting concurrent measurements of stratospheric column ozone (SCO) derived from Microwave Limb Sounder (MLS) from total column ozone measured by Ozone Monitoring Instrument (OMI). Both MLS and OMI are onboard Aura spacecraft. The TCOs covered information at 38 ground monitoring stations in Thailand, which include a populated urban area of the Bangkok Metropolitan Region, BMR. Both the satellite retrievals and the ground measurements were acquired at approximately the same local time at about 2:00 pm. Interactions of meteorological factors, retrieved from Atmospheric Infrared Sounders (AIRS) on Aqua satellite, on the relationships between the satellite-based TCO and the surface ozone concentration were also investigated. In addition, we explored the possibility of using OMI retrievals; including tropospheric column NO_2, total column formaldehyde (HCHO), to evaluate major urban ozone formation mechanisms.

Results from this study suggest that the OMI ozone from the Total Ozone Mapping Spectrometer (TOMS) algorithm was more appropriate for estimating the surface ozone concentration than that from the Differential Optical Absorption Spectroscopy (DOAS) algorithm. However, only 4.5 to 10.6% of total variation of the daily average surface ozone concentration can be explained by its linear relationship with this estimated TOMS TCO. This percentage increased at least by 15% after corrected the meteorological factors. This TOMS OMI/MLS TCO was later used in following analyses.

Spatial variation of this TCO was more latitudinal dependence than driven by different land use activities. Daily changes of the surface ozone concentration responding to weekday-to-weekend traffic volume changes were not observed from both the ground measurements and the satellite retrievals. The ground measurements, however, consistently showed reductions of median concentrations of ozone precursors, CO and NO_2, from the weekdays to the successive weekends in the different dry seasons. However, the reductions were not observed from the satellite retrievals. These findings indicated that the OMI/MLS TCO was not useful for the studies concerning advective surface ozone formation.

In this study, multivariate analyses of the satellite retrievals resulted NO_2-limited condition for the BMR ozone formation. This conclusion was consistent with a result from the analyses of the ground measurements using observations from the BMR residential sites; but it was different from that for the BMR roadside sites. Meteorological condition was one factor limiting capability of using the satellite retrievals to evaluate surface ozone formation mechanisms. Excluding this meteorological interference, two sets of results from the analyses of the satellite retrievals and the ground measurements still suggest significantly different ozone control strategies. Thus, in conclusion the OMI retrievals were not appropriate for using as a tool for the BMR ozone pollution control.

REFERENCES

Adams, P.J., Seinfeld, J.H., Koch, D., Mickley, L., Jacob, D., 2001. General circulation model assessment of direct radiative forcing by the sulfate-nitrate-ammonium-water inorganic aerosol system. Journal of geophysical research 106, 1097-1111.

AERONET, 2010. Aerosol robotic network web page. Accessed June 27, 2010. http://aeronet.gsfc.nasa.gov/

Ahmadi, N., 2004. Upland rice for highlands: new varieties and sustainable cropping systems for food security Promising prospects for the global challenges of rice production? In: Proceedings of the FAO Rice Conference. Rice is Life. International Rice Conference. Rome (Italy), 12th-13th February 2004.

Arimoto, R., Duce, R.A., Savoie, D.L., Prospero, J.M., Talbot, R., Cullen, J.D., Tomza, U., Lewis, N.F., Ray, B.J., 1996. Relationships among aerosol constituents from Asia and the North Pacific during PEM-West A. Journal of Geophysical Research 101, 2011-2023.

Artaxo, P., Fernandes, E.T., Martins, J.V., Yamasoe, M.A., Hobbs, P.V., Maenhaut, W., Longo, K.M., Castanho, A., 1998. Large-scale aerosol source apportionment in Amazonia. Journal of Geophysical Research 103, 31837-31847.

Ashcroft, P. and Morel, B., 1995. Limits of space-based remote sensing for methane source characterization. IEEE Transactions on Geoscience and Remote Sensing 33, 1124-1134.

Badan Pusat Statistik (BPS), Statistics Indonesia web page. Accessed July 2008. http://dds.bps.go.id/eng/ 5

Badarinath, K.V.S., Kharol, S.K., Sharma, A.R., Krishna Prasad, V., 2009. Analysis of aerosol and carbon monoxide characteristics over Arabian sea during crop residue burning period in the Indo-Gangetic plains using multi-satellite remote sensing data sets. Journal of Atmospheric and Solar-Terrestrial Physics 71, 1267-1276.

Balis, D.S., Amiridis, V., Zerefos, C., Gerasopoulos, E., Andreae, M., Zanis, P., Kazantzidis, A., Kazadzis, S., Papayannis, A., 2003. Raman lidar and sunphotometric measurements of aerosol optical properties over Thessaloniki, Greece during a biomass burning episode. Atmospheric Environment 37, 4529-4538.

Barnet, C.D., Datta, S., Strow, L., 2003. Trace Gas measurements from the Atmospheric Infrared Sounder (AIRS). In: Optical Remote Sensing, OSA Technical Digest (Optical Society of America 2003), paper OWB2.

Barth, M.C. and Church, A.T., 1999. Regional and global distributions and lifetimes of sulfate aerosols from Mexico City and Southeast China. Journal of Geophysical Research 104, 30231-30239.

Beck, J.P. and Grennfelt, P., 1994. Estimate of ozone production and destruction over northwestern Europe. Atmospheric Environment 28, 129-140.

Bennet, C. and Engardt, M., 2008. A regional model for surface ozone in Southeast Asia. Tellus B 60, 718-728.

Berg, O.H., Swietlicki, E., Krejci, R., 1998. Hygroscopic growth of aerosol particles in the marine boundary layer over the Pacific and southern oceans during the first aerosol characterization experiment (ACE 1). Journal of Geophysical Research 103, 16535-16545.

Bhartia, P.K. and Wellemeyer, C.W. 2002. TOMS-V8 Total O3 Algorithm. In: Bhartia, P.K. (Ed.), OMI Algorithm Theoretical Basis Document Volume II (OMI-ATBD-02), NASA Goddard Space Flight Center, Greenbelt, MD, 15-32.

Blanchard, C.L., Tanenbaum, S., Lawson, D.R., 2008. Differences between weekday and weekend air pollutant levels in Atlanta, Baltimore, Chicago, Dallas-Fort worth, Denver, Houston, New York, Phoenix, Washington, DC, and surrounding areas. Journal of the Air and Waste Management Association 58, 1598-1615.

Bowers, S.A. and Hanks, R.J., 1965. Reflection of radiant energy from soils. Soil Science 100, 130.

Bridhikitti, A. and Overcamp, T.J., 2009. Understanding optical characteristics of the Southeast Asia's regional aerosol. In: Proceedings of the Air and Waste Management Association's 102nd Annual Conference and Exhibition, Detroit, MI.

Bridhikitti, A., Overcamp, T.J., Gerard, P.D., 2010. Ozone Monitoring Instrument (OMI) sensor for biomass-burning aerosol optical properties. In: Proceedings of the Air and Waste Management Association's 103rd Annual Conference and Exhibition, Calgary, Canada.

Brown, S. and Lugo, A.E., 1982. The storage and production of organic matter in tropical forests and their role in the global carbon cycle. Biotropica 14, 161-187. 11

Carrico, C.M., Kreidenweis, S.M., Malm, W.C., Day, D.E., Lee, T., Carrillo, J., McMeeking, G.R., Collett Jr., J.L., 2005. Hygroscopic growth behavior of a carbon-dominated aerosol in Yosemite national park. Atmospheric Environment 39, 1393-1404.

Chan, C.K. and Yao, X., 2008. Air pollution in mega cities in China. Atmospheric Environment 42, 1-42.

Chan, C.Y., Chan, L.Y., Harris, J.M., Oltmans, S.J., Blake, D.R., Qin, Y., Zheng, Y.G., Zheng, X.D., 2003. Characteristics of biomass burning emission sources, transport, and chemical speciation in enhanced springtime tropospheric ozone profile over Hong Kong. Journal of Geophysical Research 108, 4015.

Chan, L.Y., Liu, H.Y., Lam, K.S., 1998. Analysis of the seasonal behavior of tropospheric ozone at Hong Kong. Atmospheric Environment 32, 159-168.

Chance, K. 2002. OMI Algorithm Theoritical Basis Document, Volume IV: OMI Trace Gas Algorithms. In: Anonymous Smithsonian Astrophysical Observatory, Cambridge, MA, USA,

Charlson, R.J., Lovelock, J.E., Andreae, M.O., Warren, S.G., 1987. Oceanic phytoplankton, atmospheric sulphur, cloud albedo and climate. Nature 326, 655-661.

Chen, C., Son, N., Chang, L., Chen, C., 2011. Monitoring of soil moisture variability in relation to rice cropping systems in the Vietnamese Mekong Delta using MODIS data. Applied Geography 31, 463-475.

Cheng, A.Y.S., Chan, M.H., Yang, X., 2006. Study of aerosol optical thickness in Hong Kong, validation, results, and dependence on meteorological parameters. Atmospheric Environment 40, 4469-4477.

Chow, J.C., Watson, J.G., Kuhns, H., Etyemezian, V., Lowenthal, D.H., Crow, D., Kohl, S.D., Engelbrecht, J.P., Green, M.C., 2004. Source profiles for industrial, mobile, and area sources in the Big Bend regional aerosol visibility and observational study. Chemosphere 54, 185-208.

Christopher, S.A., Gupta, P., Haywood, J., Greed, G., 2008. Aerosol optical thicknesses over North Africa: 1. development of a product for model validation using ozone monitoring instrument, Multiangle Imaging Spectroradiometer, and Aerosol Robotic Network. Journal of Geophysical Research 113, D00C04.

Chuang, M., Fu, J.S., Jang, C.J., Chan, C., Ni, P., Lee, C., 2008. Simulation of long-range transport aerosols from the Asian continent to Taiwan by a southward Asian high-pressure system. Science of The Total Environment 406, 168-179.

Chueinta, W., Hopke, P.K., Paatero, P., 2000. Investigation of sources of atmospheric aerosol at urban and suburban residential areas in Thailand by positive matrix factorization. Atmospheric Environment 34, 3319-3329.

CIP, Centro Internacional de la Papa: GIS data. Accessed January 2008. http://research.cip.cgiar.org/gis/modules.php?name=Downloads&d_op=viewdownload&id=1

Cohen, D.D., Crawford, J., Stelcer, E., Bac, V.T., 2010. Characterisation and source apportionment of fine particulate sources at Hanoi from 2001 to 2008. Atmospheric Environment 44, 320-328.

Colette, A. and Ancellet, G., 2005. Impact of vertical transport processes on the tropospheric ozone layering above Europe. part II: Climatological analysis of the past 30 years. Atmospheric Environment 39, 5423-5435.

Deshpande, C.G. and Kamra, A.K., 2002. Aerosol size distributions in the north and South Indian Ocean during the northeast monsoon season. Atmospheric Research 65, 51-76.

Dimitrakopoulos, A.P., 2002. Mediterranean fuel models and potential fire behaviour in Greece. International Journal of Wildland Fire 11, 127-130.

Dixon, J.A., Gibbon, D.P., Gulliver, A., 2001. Farming Systems and Poverty: Improving Farmers' Livelihoods in a Changing World. FAO and World Bank, Rome and Washington, D.C, 412 pp.

Dubovik, O. and King, M.D., 2000. A flexible inversion algorithm for retrieval of aerosol optical properties from sun and sky radiance measurements. Journal of Geophysical Research 105, 20676.

Dubovik, O., Holben, B., Eck, T.F., Smirnov, A., Kaufman, Y.J., King, M.D., Tanré, D., Slutsker, I., 2002. Variability of absorption and optical properties of key aerosol types observed in worldwide locations. Journal of the Atmospheric Sciences 59, 590-608.

Duce, R.A., Unni, C.K., Ray, B.J., Prospero, J.M., Merrill, J.T., 1980. Long-range atmospheric transport of soil dust from Asia to the tropical North Pacific: Temporal variability. Science 209, 1522-1524.

Duncan, B.N., Yoshida, Y., Olson, J.R., Sillman, S., Martin, R.V., Lamsal, L., Hu, Y., Pickering, K.E., Retscher, C., Allen, D.J., 2010. Application of OMI observations to a space-based indicator of NOx and VOC controls on surface ozone formation. Atmospheric Environment 44, 2213-2223. .

FAO/AGL, 2003. WRB map of world soil resources, Land and Water Development Division, Food and Agriculture Organization of the United Nations, Rome, Italy. Accessed January/31 2011. http://www.fao.org/ag/agl/agll/wrb.soilres.stm

FAOSTAT, 2006. Statistical database of the food and agricultural organization of the United Nations. Accessed December 2008. http://faostat.fao.org/site/377/default.aspx#ancor

Fiebig, M., Stohl, A., Wendisch, M., Eckhardt, S., Petzold, A., 2003. Dependence of solar radiative forcing of forest fire aerosol on ageing and state of mixture. Atmospheric Chemistry and Physics Discussions 3, 1273-1302.

Finlayson-Pitts, B.J. and Pitts Jr, J.N., 1997. Tropospheric air pollution: Ozone, airborne toxics, polycyclic aromatic hydrocarbons, and particles. Science 276, 1045-1051.

Fishman, J., Bowman, K.W., Burrows, J.P., Richter, A., Chance, K.V., Edwards, D.P., Martin, R.V., Morris, G.A., Pierce, R.B., Ziemke, J.R., 2008. Remote sensing of tropospheric pollution from space. Bulletin of the American Meteorological Society 89, 805-821.

FMBP, Forest management bureau of Philippines web page. Accessed July 2008. http://forestry.denr.gov.ph/

Forest Administration of Cambodia web page. Accessed November 2008. http://www.forestry.gov.kh/Statistic/Forestcover.htm

Forestry Department Brunet Darussalam web page. Accessed November 2008. http://www.forestry.gov.bn

Froidevaux, L., Jiang, Y.B., Lambert, A., Livesey, N.J., Read, W.G., Waters, J.W., Browell, E.V., Hair, J.W., Avery, M.A., McGee, T.J., 2008. Validation of AURA Microwave Limb Sounder stratospheric ozone measurements. Journal of Geophysical Research 113, D15S20.

FWI/GFW, 2002. The State of the Forest: Indonesia. Emily Bogor, Indonesia: Forest Watch, and Washington DC: Global Forest Watch, 104.

Gao, Y., Arimoto, R., Zhou, M.Y., Merrill, J.T., Duce, R.A., 1992. Relationships between the dust concentrations over eastern Asia and the remote North Pacific. Journal of Geophysical Research 97, 9867-9872.

Graham, R.T., McCaffrey, S., Jain, T.B. 2004. Science basis for changing forest structure to modify wildfire behavior and severity. U.S. Department of Agriculture Forest Service. RMRS-GTR-120. 52pp.

Gras, J.L., Jensen, J.B., Okada, K., Ikegami, M., Zaizen, Y., Makino, Y., 1999. Some optical properties of smoke aerosol in Indonesia and tropical Australia. Geophysical Research Letters 26, 1393-1396.

GSO, General statistics office of Vietnam web page. Accessed July 2008. http://www.gso.gov.vn/default_en.aspx?tabid=491

Gu, Y., Liou, K., Xue, Y., Mechoso, C., Li, W., Luo, Y., 2006. Climatic effects of different aerosol types in China simulated by the UCLA general circulation model. Journal of Geophysical Research 111, D15201.

Guo, J., Zhang, J., Zhang, Y., Cao, Y., 2008. Study on the comparison of the land cover classification for multitemporal MODIS images. In: 2008 International Workshop on Earth Observation and Remote Sensing Applications, 1-6.

Guyon, P., Boucher, O., Graham, B., Beck, J., Mayol-Bracero, O.L., Roberts, G.C., Maenhaut, W., Artaxo, P., Andreae, M.O., 2003. Refractive index of aerosol particles over the Amazon tropical forest during LBA-EUSTACH 1999. Journal of Aerosol Science 34, 883-907.

Hayes, D.J. and Cohen, W.B., 2007. Spatial, spectral and temporal patterns of tropical forest cover change as observed with multiple scales of optical satellite data. Remote Sensing of Environment 106, 1-16.

Hays, M.D., Fine, P.M., Geron, C.D., Kleeman, M.J., Gullett, B.K., 2005. Open burning of agricultural biomass: Physical and chemical properties of particle-phase emissions. Atmospheric Environment 39, 6747-6764.

Heil, A., Langmann, B., Aldrian, E., 2007. Indonesian peat and vegetation fire emissions: Study on factors influencing large-scale smoke haze pollution using a regional atmospheric chemistry model. Mitigation and Adaptation Strategies for Global Change 12, 113-133.

Hidy, G.M., Brook, J.R., Chow, J.C., Green, M., Husar, R.B., Lee, C., Scheffe, R.D., Swanson, A., Watson, J.G., 2009. 2009 critical review discussion: Remote sensing of particulate pollution from space: Have we reached the promised land? Journal of the Air and Waste Management Association 59, 1130-1139.

Hoff, R.M. and Christopher, S.A., 2009. Remote sensing of particulate pollution from space: Have we reached the promised land? Journal of the Air and Waste Management Association 59, 645-675.

Huete, A., Didan, K., Miura, T., Rodriguez, E.P., Gao, X., Ferreira, L.G., 2002. Overview of the radiometric and biophysical performance of the MODIS vegetation indices. Remote Sensing of Environment 83, 195-213.

Huke, R.E. and Huke, E.H., 1997. Rice Area by Type of Culture: South, Southeast, and East Asia. International Rice Research Institute, Los Banos, Laguna, Philippines, 59.

Hyer, E.J. and Chew, B.N., 2010. Aerosol transport model evaluation of an extreme smoke episode in Southeast Asia. Atmospheric Environment 44, 1422-1427.

ICEM 2003. Lao PDR National Report on Protected Areas and Development. In: Anonymous Review of Protected Areas and Development in the Lower Mekong River Region, International Centre for Environmental Management, Indooroopilly, Queensland, Australia.

Ichoku, C., Chu, D.A., Mattoo, S., Kaufman, Y.J., Remer, L.A., Tanré, D., Slutsker, I., Holben, B.N., 2002. A spatio-temporal approach for global validation and analysis of MODIS aerosol products. Geophysical Research Letters 29, 8006, 4 pp.

IRRI, 1975. Major Research in Upland Rice. International Rice Research Institute, Los Banos , Philippines, 255.

Izumi, K., Mizuochi, M., Murano, K., Fukuyama, T., 1987. Humidity effects on photochemical aerosol formation in the SO2-NO-C3H6-air system. Atmospheric Environment (1967) 21, 1541-1553.

Jeong, J.I., Park, R.J., Youn, D., 2008. Effects of Siberian forest fires on air quality in East Asia during May 2003 and its climate implication. Atmospheric Environment 42, 8910-8922.

Jeong, M.J. and Hsu, N.C., 2008. Retrievals of aerosol single-scattering albedo and effective aerosol layer height for biomass-burning smoke: Synergy derived from "A-train" sensors. Geophysical Research Letters 35, L24801.

Johnson, D.E., 1998. Applied multivariate methods for data analysis. Duxbury Press Pacific Grove, CA. 567 pp.

Johnson, L.A. and Dearden, P. 2009. Fire Ecology and Management of Seasonal Evergreen Forests in Mainland Southeast Asia. In: Chochrane, M.A. (Ed.), Tropical Fire Ecology:Climate Change, Land use, and Ecosystem Dynamics, Springer-Praxis Publishing, Chichester, UK, 289-310.

Jones, S.H., 1998. Vegetation fire and land use in Southeast Asia: The interpretation of remotely sensed data for Cambodia. Geocarto International 13, 63-73.

Justice, C.O., Giglio, B., Korontzi, S., Owens, J., Morisette, J.T., Roy, D.P., Descloitres, J., Alleaume, S., Petitcolin, F., Kaufman, Y., 2006. Algorithm technical background document: The MODIS fire products, Version 2.3. EOS ID#2741. Accessed July/31 2010. http://modis.gsfc.nasa.gov/data/atbd/atbd_mod14.pdf.

Kar, J., Fishman, J., Creilson, J.K., Richter, A., Ziemke, J., Chandra, S., 2010. Are there urban signatures in the tropospheric ozone column products derived from satellite measurements? Atmospheric Chemistry and Physics 10, 5213-5222.

Kaskaoutis, D.G., Nastos, P.T., Kosmopoulos, P.G., Kambezidis, H.D., Kharol, S.K., Badarinath, K.V.S., 2010. The Aura–OMI aerosol index distribution over Greece. Atmospheric Research 98, 28-39.

Kaskaoutis, D.G., Kharol, S.K., Sifakis, N., Nastos, P.T., Sharma, A.R., Badarinath, K.V.S., Kambezidis, H.D., 2011. Satellite monitoring of the biomass-burning aerosols during the wildfires of August 2007 in Greece: Climate implications. Atmospheric Environment 45, 716-726.

Kim, J., Yoon, S., Jefferson, A., Kim, S., 2006. Aerosol hygroscopic properties during Asian dust, pollution, and biomass burning episodes at Gosan, Korea in April 2001. Atmospheric Environment 40, 1550-1560.

Komala, N., Saraspriya, S., Kita, K., Ogawa, T., 1996. Tropospheric ozone behavior observed in Indonesia. Atmospheric Environment 30, 1851-1856.

Kurosu, T.P., 2008. OMHCHO Readme File. Accessed June 2010. https://www.cfa.harvard.edu/~tkurosu/SatelliteInstruments/OMI/PGEReleases/READMEs/OMHCHO_README.pdf

Labonne, M., Bréon, F.M., Chevallier, F., 2007. Injection height of biomass-burning aerosols as seen from a spaceborne Lidar. Geophysical Research Letters 34, L11806.

Lamsal, L.N., Weber, M., Tellmann, S., Burrows, J.P., 2004. Ozone column classified climatology of ozone and temperature profiles based on ozonesonde and satellite data. Journal of Geophysical Research 109, D20304.

Langmann, B. and Graf, H.F., 2003. Indonesian smoke aerosols from peat fires and the contribution from volcanic sulfur emissions. Geophysical Research Letter 30, 1547.

Langmann, B., Herzog, M., Graf, H.F., 1998. Radiative forcing of climate by sulfate aerosols as determined by a regional circulation chemistry transport model. Atmospheric Environment 32, 2757-2768.

Lelieveld, J., Crutzen, P.J., Ramanathan, V., Andreae, M.O., Brenninkmeijer, C.A.M., Campos, T., Cass, G.R., Dickerson, R.R., Fischer, H., De Gouw, J.A., 2001. The Indian Ocean experiment: Widespread air pollution from South and Southeast Asia. Science 291, 1031-1036.

Leonard, P.J.T., 2009. README for OMAEROe (OMI daily L3e for OMAERO): OMAEROe high level overview. Accessed November/11 2009. http://disc.sci.gsfc.nasa.gov/Aura/data-holdings/OMI/omaeroe_v003.shtml

Levelt, P.F., Hilsenrath, E., Leppelmeier, G.W., van den Oord, G.H.J., Bhartia, P.K., Tamminen, J., de Haan, J.F., Veefkind, J.P., 2006. Science objectives of the ozone monitoring instrument (OMI). IEEE Transactions on Geoscience and Remote Sensing 44, 1199-1208.

Levy, R.C., Remer, L.A., Tanré, D., Mattoo, S., Kaufman, Y.J., February 2009. Algorithm for remote sensing of tropospheric aerosol over dark targets from MODIS Collections 005 and 051: Revision 2. Accessed Mar/11 2011. http://modis-atmos.gsfc.nasa.gov/_docs/ATBD_MOD04_C005_rev2.pdf

Li, J., Posfai, M., Hobbs, P.V., Buseck, P.R., 2003. Individual aerosol particles from biomass burning in southern Africa: 2. compositions and aging of inorganic particles. Journal of Geophysical Research 108, 8484.

Liley, J.B., Baumgardner, D., Kondo, Y., Kita, K., Blake, D.R., Koike, M., Machida, T., Takegawa, N., Kawakami, S., Shirai, T., Ogawa, T., 2003. Black carbon in aerosol during BIBLE B. Journal of Geophysical Research 107, 8399.

Liu, H., Chang, W.L., Oltmans, S.J., Chan, L.Y., Harris, J.M., 1999. On springtime high ozone events in the lower troposphere from Southeast Asian biomass burning. Atmospheric Environment 33, 2403-2410.

Liu, H., Jacob, D.J., Chan, L.Y., Oltmans, S.J., Bey, I., Yantosca, R.M., Harris, J.M., Duncan, B.N., Martin, R.V., 2002. Sources of tropospheric ozone along the Asian Pacific rim: An analysis of ozonesonde observations. Journal of Geophysical Research 107, 4573.

Liu, Y., Kahn, R.A., Chaloulakou, A., Koutrakis, P., 2009. Analysis of the impact of the forest fires in august 2007 on air quality of Athens using multi-sensor aerosol remote sensing data, meteorology and surface observations. Atmospheric Environment 43, 3310-3318.

Livesey, N.J. et al., 2007. Earth Observing System (EOS), Aura Microwave Limb Sounder (MLS), Version 2.2 Level 2 Data quality and description document. JPL D-33509. Jet Propulsion Laboratory, California Institute of Technology, Pasadena, CA, 115.

Logan, J.A. and Kirchhoff, V., 1986. Seasonal variations of troposheric ozone at Natal, Brazil. Journal of Geophysical Research 91, 7875-7881.

Logan, J.A., 1999. An analysis of ozonesonde data for the troposphere: Recommendations for testing 3-D models and development of a gridded climatology for tropospheric ozone. Journal of Geophysical Research 104, 16115.

LPDAAC, Land processes distributed active archive center web page. Accessed March 2008. http://lpdaac.usgs.gov/datapool/datapool.asp

Ma, Y., Weber, R., Lee, Y., Orsini, D., Maxwell-Meier, K., Thornton, D., Bandy, A., Clarke, A., Blake, D., Sachse, G., 2003. Characteristics and influence of biosmoke on the fine particle ionic composition measured in Asian outflow during the transport and chemical evolution over the Pacific (TRACE-P) experiment. Journal of Geophysical Research 108, 8816.

Mallet, M., Roger, J.C., Despiau, S., Dubovik, O., Putaud, J.P., 2003. Microphysical and optical properties of aerosol particles in urban zone during ESCOMPTE. Atmospheric Research 69, 73-97.

Manly, B.F.J., 1994. Multivariate Statistical Methods: A Primer. Chapter and Hall/CRC Press.

Martins, J.V., Artaxo, P., Liousse, C., Reid, J.S., Hobbs, P.V., Kaufman, Y.J., 1998. Effects of black carbon content, particle size, and mixing on light absorption by aerosols from biomass burning in Brazil. Journal of Geophysical Research-Atmospheres 103, 32041-32050.

Martin, R.V., Fiore, A.M., Van Donkelaar, A., 2004. Space-based diagnosis of surface ozone sensitivity to anthropogenic emissions. Geophysical Research Letters 31, 1-4.

Martin, R.V., 2008. Satellite remote sensing of surface air quality. Atmospheric Environment 42, 7823-7843.

Mayaux, P., Achard, F., Malingreau, J.P., 1998. Global tropical forest area measurements derived from coarse resolution satellite imagery: A comparison with other approaches. Environmental Conservation 25, 37-52.

Milt, A., Milano, A., Garivait, S., Kamens, R., 2009. Effects of 10% biofuel substitution on ground level ozone formation in Bangkok, Thailand. Atmospheric Environment 43, 5962-5970.

Ministry of Agricultural and Irrigation Union of Myanmar web page. Accessed March 2010. http://www.myanmar.gov.mm/ministry/agri/statistics.htm

MODIS Land. Accessed March 2008. http://modis-land.gsfc.nasa.gov/tools.htm

Moody, J.L., Oltmans, S.J., Levy, H.I., Merrill, J.T., 1995. Transport climatology of tropospheric ozone: Bermuda, 1988–1991. Journal of Geophysical Research 100, 7179-7194.

Morris, G.A., Ford, B., Rappenglück, B., Thompson, A.M., Mefferd, A., Ngan, F., Lefer, B., 2010. An evaluation of the interaction of morning residual layer and afternoon mixed layer ozone in Houston using ozonesonde data. Atmospheric Environment 44, 4024-4034.

MTC, Malaysian timber council web page. Accessed November 2008. www.mtc.com.my

Murphy, P.G. and Lugo, A.E., 1986. Ecology of tropical dry forest. Annual Review of Ecology and Systematics 17, 67-88.

NASA OMI Team, 2009. Ozone Monitoring Instrument (OMI): Data User's Guide. OMI-DUG-3.0. Accessed December 2009. http://disc.sci.gsfc.nasa.gov/Aura/additional/documentation/README.OMI_DUG.pdf

Nessler, R., Weingartner, E., Baltensperger, U., 2005. Effect of humidity on aerosol light absorption and its implications for extinction and the single scattering albedo illustrated for a site in the lower free troposphere. Journal of Aerosol Science 36, 958-972.

Newchurch, M.J., Ayoub, M.A., Oltmans, S., Johnson, B., Schmidlin, F.J., 2003. Vertical distribution of ozone at four sites in the United States. Journal of Geophysical Research 108, 4031.

NSC, National statistics center of the Lao PDR web page. Accessed July 2008. http://www.nsc.gov.la/

NSOP, National statistics office of Philippines web page. Accessed July 2008. http://www.census.gov.ph/data/sectordata/dataagri.html

NSOT, National statistical office of Thailand web page. Accessed July 2008. http://web.nso.go.th/eng/index.htm

Oanh, N.T.K. and Zhang, B., 2004. Photochemical smog modeling for assessment of potential impacts of different management strategies on air quality of the Bangkok metropolitan region, Thailand. Journal of the Air and Waste Management Association 54, 1321-1338.

Oanh, N.T.K., Upadhyay, N., Zhuang, Y.H., Hao, Z.P., Murthy, D.V.S., Lestari, P., Villarin, J.T., Chengchua, K., Co, H.X., Dung, N.T., Lindgren, E.S., 2006. Particulate air pollution in six Asian cities: Spatial and temporal distributions, and associated sources. Atmospheric Environment 40, 3367-3380.

Oanh, N.T.K., Martel, M., Pongkiatkul, P., Berkowicz, R., 2008. Determination of fleet hourly emission and on-road vehicle emission factor using integrated monitoring and modeling approach. Atmospheric Research 89, 223-232.

O'Brien, D.M. and Mitchell, R.M., 2003. Atmospheric heating due to carbonaceous aerosol in northern Australia–confidence limits based on TOMS aerosol index and sun-photometer data. Atmospheric Research 66, 21-41.

O'Dowd, C.D., Jimenez, J.L., Bahreini, R., Flagan, R.C., Seinfeld, J.H., Hämeri, K., Pirjola, L., Kulmala, M., Jennings, S.G., Hoffmann, T., 2002. Marine aerosol formation from biogenic iodine emissions. Nature 417, 632-636.

Okada, K., Ikegami, M., Zaizen, Y., Makino, Y., Jensen, J.B., Gras, J.L., 2001. The mixture state of individual aerosol particles in the 1997 Indonesian haze episode. Journal of Aerosol Science 32, 1269-1279.

Olsen, E.T. 2007. AIRS/AMSU/HSB Version 5 Level 3 Quick Start Version 1.1. In: Anonymous Jet Propulsion Laboratory, California Institute of Technology, Pasadena, CA.

Omar, A.H., Winker, D.M., Vaughan, M.A., Hu, Y., Trepte, C.R., Ferrare, R.A., Lee, K.P., Hostetler, C.A., Kittaka, C., Rogers, R.R., 2009. The CALIPSO automated aerosol classification and lidar ratio selection algorithm. Journal of Atmospheric and Oceanic Technology 26, 1994-2014.

Ozone Processing Team-NASA/GSFC, 2008. OMTO3 README file. Accessed February/6 2011. http://jwocky.gsfc.nasa.gov/omi/OMTO3_README_v8_5.pdf

Payne, V.H., Clough, S.A., Shephard, M.W., Nassar, R., Logan, J.A., 2009. Information-centered representation of retrievals with limited degrees of freedom for signal: Application to methane from the tropospheric emission spectrometer. Journal of Geophysical Research 114, D10307.

PCA, Philippines coconut authority web page. Accessed July 2008. http://pca.da.gov.ph/cocostat.php

Pfister, G., Gille, J.C., Ziskin, D., Francis, G., Edwards, D.P., Deeter, M.N., Abbott, E., 2005. Effects of a spectral surface reflectance on measurements of backscattered solar radiation: Application to the MOPITT methane retrieval. Journal of Atmospheric and Oceanic Technology 22, 566-574.

Pingali, P.L. and Xuan, V.T., 1992. Vietnam: Decollectivization and rice productivity growth. Economic Development and Cultural Change 40, 697-718.

Pochanart, P., Kreasuwun, J., Sukasem, P., Geeratithadaniyom, W., Tabucanon, M.S., Hirokawa, J., Kajii, Y., Akimoto, H., 2001. Tropical tropospheric ozone observed in Thailand. Atmospheric Environment 35, 2657-2668.

Podgorny, I.A., Li, F., Ramanathan, V., 2003. Large aerosol radiative forcing due to the 1997 Indonesian forest fire. Geophysical Research Letters 30, 1028.

Pongkiatkul, P. and Oanh, N.T.K., 2007. Assessment of potential long-range transport of particulate air pollution using trajectory modeling and monitoring data. Atmospheric Research 85, 3-17.

Provincial statistics center of Thailand web page. Accessed July 2008. http://service.nso.go.th/nso/nsopublish/contact/provcenter.html

Rajeev, K., Ramanathan, V., Meywerk, J., 2000. Regional aerosol distribution and its long-range transport over the Indian Ocean. Journal of Geophysical Research 105, 2029-2043.

Rappenglück, B., Dasgupta, P.K., Leuchner, M., Li, Q., Luke, W., 2010. Formaldehyde and its relation to CO, PAN, and SO2 in the Houston-Galveston airshed. Atmospheric Chemistry and Physics 10, 2413-2424.

Reid, J.S., 1998. Emission, evolution, and radiative properties of particles from biomass burning in Brazil. PhD dissertation, University of Washington,

Remer, L.A., Y.J. Kaufman, D. Tanre, S. Mattoo, D.A. Chu, J.V. Martins, R.-R. Li, C. Ichoku, R.C. Levy, R.G. Kleidman, T.F. Eck, E. Vermote, B.N. Holben, 2005. The MODIS aerosol algorithm, products, and validation. Journal of the Atmospheric Sciences 62, 947-973.

Rose, D., Nowak, A., Achtert, P., Wiedensohler, A., Hu, M., Shao, M., Zhang, Y., Andreae, M.O., Pöschl, U., 2010. Cloud condensation nuclei in polluted air and biomass burning smoke near the mega-city Guangzhou, China- part 1: Size-resolved measurements and implications for the modeling of aerosol particle hygroscopicity and CCN activity. Atmospheric Chemistry and Physics 10, 3365-3383.

Sakamoto, T., Yokozawa, M., Toritani, H., Shibayama, M., Ishitsuka, N., Ohno, H., 2005. A crop phenology detection method using time-series MODIS data. Remote Sensing of Environment 96, 366-374.

Sakamoto, T., Van Phung, C., Kotera, A., Nguyen, K.D., Yokozawa, M., 2009. Analysis of rapid expansion of inland aquaculture and triple rice-cropping areas in a coastal area of the Vietnamese Mekong Delta using MODIS time-series imagery. Landscape and Urban Planning 92, 34-46.

Santos, D., Costa, M.J., Silva, A.M., 2008. Direct SW aerosol radiative forcing over Portugal. Atmospheric Chemistry and Physics 8, 5771-5786.

SAS Institute Inc, 2002. SAS OnlineDoc® 9.1.3. Cary, NC. Accessed May 2008.

Sauvage, B., Thouret, V., Thompson, A.M., Witte, J.C., Cammas, J.P., Nédélec, P., Athier, G., 2006. Enhanced view of the "tropical Atlantic ozone paradox" and "zonal wave one" from the in situ MOZAIC and SHADOZ data. Journal of Geophysical Research 111, D01301.

Scheel, H.E., Areskoug, H., Geiss, H., Gomiscek, B., Granby, K., Haszpra, L., Klasinc, L., Kley, D., Laurila, T., Lindskog, A., 1997. On the spatial distribution and seasonal variation of lower-troposphere ozone over Europe. Journal of Atmospheric Chemistry 28, 11-28.

Stajner, I., Wargan, K., Pawson, S., Hayashi, H., Chang, L.P., Hudman, R.C., Froidevaux, L., Livesey, N.J., Levelt, P., Stubi, R., 2008. Assimilated ozone from EOS-aura: Evaluation of the tropopause region and tropospheric columns. Journal of Geophysical Research 113, D16S32.

Thampi, B.V., Rajeev, K., Parameswaran, K., Mishra, M.K., 2009. Spatial distribution of the Southeast Asian smoke plume over the Indian Ocean and its radiative heating in the atmosphere during the major fire event of 2006. Geophysical Research Letters 36, L16808.

Thompson, A.M., Stone, J.B., Witte, J.C., Miller, S.K., Oltmans, S.J., Kucsera, T.L., Ross, K.L., Pickering, K.E., Merrill, J.T., Forbes, G., 2007. Intercontinental chemical transport experiment ozonesonde network study (IONS) 2004: 2. Tropospheric ozone budgets and variability over northeastern North America. Journal of Geophysical Research 112, D12S13.

Thompson, A.M., Witte, J.C., Oltmans, S.J., Schmidlin, F.J., Logan, J.A., Fujiwara, M., Kirchhoff, V., Posny, F., Coetzee, G.J.R., Hoegger, B., 2003. Southern Hemisphere additional ozonesondes (SHADOZ) 1998–2000 tropical ozone climatology: 2. tropospheric variability and the zonal wave-one. Journal of Geophysical Research 108, 8241.

Thompson, A.M., Yorks, J.E., Miller, S.K., Witte, J.C., Dougherty, K.M., Morris, G.A., Baumgardner, D., Ladino, L., Rappenglueck, B., 2008. Tropospheric ozone sources and wave activity over Mexico City and Houston during MILAGRO/Intercontinental transport experiment (INTEX-B) ozonesonde network study, 2006 (IONS-06). Atmospheric Chemistry and Physics 8, 5113-5125.

Tingting, L. and Chuang, L., 2010. Study on extraction of crop information using time-series MODIS data in the Chao Phraya basin of Thailand. Advances in Space Research 45, 775-784.

Tipayarom, D., 2004. Source characterization for air pollution emission from rice-straw open burning in Thailand, M.S. Thesis, Asian Institute of Technology, Pathumthani, Thailand

Torres, O., Decae, R., Veefkind, P., de Leeuw, G. 2002. OMI Aerosol Retrieval Algorithm. In: Stammes, P. (Ed.), OMI Algorithm Theoretical Basis Document Volume III: Clouds, Aerosols, and Surface UV Irradiance, ATBD-OMI-03, Version 2. 47-69. Accessed February/3 2011. http://eospso.gsfc.nasa.gov/eos_homepage/for_scientists/atbd/docs/OMI/ATBD-OMI-03.pdf

United States Environmental Protection Agency website.2010. List of Designated Reference and Equivalent Methods. National Exposure Research Laboratory, Human Exposure and Atmospheric Sciences Division, Research Triangle Park, NC. http://www.epa.gov/ttn/amtic/criteria.html

Uno, I., Carmichael, G.R., Streets, D., Satake, S., Takemura, T., Woo, J.H., Uematsu, M., Ohta, S., 2003. Analysis of surface black carbon distributions during ACE-Asia using a regional-scale aerosol model. Journal of Geophysical Research 108, 8636.

Wang, L., Xin, J., Wang, Y., Li, Z., Liu, G., Li, J., 2007. Evaluation of the MODIS aerosol optical depth retrieval over different ecosystems in China during EAST-AIRE. Atmospheric Environment 41, 7138-7149.

Wang, Y., McElroy, M.B., Boersma, K.F., Eskes, H.J., Veefkind, J.P., 2007. Traffic restrictions associated with the Sino-African summit: Reductions of NO_x detected from space. Geophysical Research Letters 34, 8814.

Wangkiat, A., Harvey, N.W., Garivait, H., Okamoto, S., 2004. Source contribution of atmospheric aerosols in Bangkok metropolitan area by CMB 8 receptor model. International Journal of Environment and Pollution 21, 80-96.

Wardlow, B.D. and Egbert, S.L., 2008. Large-area crop mapping using time-series MODIS 250 m NDVI data: An assessment for the US central Great Plains. Remote Sensing of Environment 112, 1096-1116.

Warren, B., Malloy, Q.G.J., Yee, L.D., Cocker III, D.R., 2009. Secondary organic aerosol formation from cyclohexene ozonolysis in the presence of water vapor and dissolved salts. Atmospheric Environment 43, 1789-1795.

Wassmann, R., Neue, H.U., Lantin, R.S., Makarim, K., Chareonsilp, N., Buendia, L.V., Rennenberg, H., 2000. Characterization of methane emissions from rice fields in Asia. II. Differences among irrigated, rainfed, and deepwater rice. Nutrient Cycling in Agroecosystems 58, 13-22.

Witte, J.C., Duncan, B.N., Douglass, A.R., Kurosu, T.P., Chance, K., Retscher, C., The unique OMI $HCHO/NO_2$ feature during the 2008 Beijing Olympics: Implications for ozone production sensitivity. Atmospheric Environment, In Press, Accepted Manuscript, Accepted date: 2 March 2011.

Worden, J., Liu, X., Bowman, K., Chance, K., Beer, R., Eldering, A., Gunson, M., Worden, H., 2007. Improved tropospheric ozone profile retrievals using OMI and TES radiances. Geophysical Research Letters 34, L01809.

Wu, H., Guo, Z., Peng, C., 2003. Land use induced changes of organic carbon storage in soils of China. Global Change Biology 9, 305-315.

Xanthopoulos, G., 2009. Lessons learned from the dramatic fires of 2007 and 2009 in Greece. In: Proceedings of Technical meeting of the fire service: Capacity for managing forest fires, 18^{th}-19^{th} November 2009, Catalonia, Spain.

Xiao, X., Boles, S., Frolking, S., Li, C., Babu, J.Y., Salas, W., Moore III, B., 2006. Mapping paddy rice agriculture in South and Southeast Asia using multi-temporal MODIS images. Remote Sensing of Environment 100, 95-113.

Xiao, X., Boles, S., Liu, J., Zhuang, D., Frolking, S., Li, C., Salas, W., Moore III, B., 2005. Mapping paddy rice agriculture in southern China using multi-temporal MODIS images. Remote Sensing of Environment 95, 480-492.

Xiong, X., Barnet, C., Maddy, E., Sweeney, C., Liu, X., Zhou, L., Goldberg, M., 2008. Characterization and validation of methane products from the atmospheric infrared sounder (AIRS). Journal of Geophysical Research 113, G00A01.

Yui, X., Zhuang, D., Chen, H., Hou, X., 2004. Forest classification based on MODIS time series and vegetation phenology. In: IGARSS'04 Proceedings of Geosciences and Remote Sensing Symposium, 2369-2372.

Zha, Y., Gao, J., Ni, S., 2003. Use of normalized difference built-up index in automatically mapping urban areas from TM imagery. International Journal of Remote Sensing 24, 583-594.

Zhang, B.N. and Oanh, N.T.K., 2002. Photochemical smog pollution in the Bangkok Metropolitan Region of Thailand in relation to O3 precursor concentrations and meteorological conditions. Atmospheric Environment 36, 4211-4222.

Zhang, J. and Rao, S.T., 1999. The role of vertical mixing in the temporal evolution of ground-level ozone concentrations. Journal of Applied Meteorology 38, 1674-1691.

Ziemke, J.R., Chandra, S., Bhartia, P.K., 1998. Two new methods for deriving tropospheric column ozone from TOMS measurements: Assimilated UARS MLS/HALOE and convective-cloud differential techniques. Journal of Geophysical Research 103, 22115-22127.

Ziemke, J.R., Chandra, S., Duncan, B.N., Froidevaux, L., Bhartia, P.K., Levelt, P.F., Waters, J.W., 2006. Tropospheric ozone determined from Aura OMI and MLS: Evaluation of measurements and comparison with the global modeling Initiative's chemical transport model. Journal of Geophysical Research 111 , D19303, 18 pp.

Ziemke, J.R., 2009. Tropospheric ozone data from aura OMI/MLS. Accessed March/8 2010. http://acdb-ext.gsfc.nasa.gov/Data_services/cloud_slice/new_data.html 3.